The Diagnosis of Extrapulmonary Tuberculosis (EPTB): Scanning Protocols and Innovative Methods for Image Quality Improvement of FDG PET/CT Imaging

A thesis submitted in fulfilment of the requirements for the degree of

Doctor of Philosophy

Submitted by

Hairil Rashmizal Abdul Razak

B. Sc (Hons)

School of Medical Sciences

College of Science, Engineering and Technology

RMIT University

August 2011

DECLARATION

I certify that except where due acknowledgement has been made, the work is that of the author alone; the work has not been submitted previously, in whole or in part, to qualify for any other academic award; the content of the thesis is the result of work which has been carried out since the official commencement date of the approved research program; any editorial work, paid or unpaid, carried out by a third party is acknowledged; and, ethics procedures and guidelines have been followed.

Hairil Rashmizal Abdul Razak

4th of August 2011

ACKNOWLEDGEMENTS

First and foremost, I would like to address my sincere thanks to my primary supervisor, A/Prof Moshi Geso, who had given me the necessary freedom in bringing forward my own idea in my PhD studies, as well as for all the advice, help, supervision, support, and trust throughout my PhD journey. Also, I would like to acknowledge my co-supervisor Prof Abdul Jalil Nordin from the Nuclear Imaging Centre, Faculty of Medicine and Health Sciences, University Putra Malaysia, for being a good mentor especially in helping up with the important clinical issues during my PhD studies.

I would also like to acknowledge our collaborators; A/Prof Claudio Rossetti and his team from the Advanced Technology Department, Division of Nuclear Medicine at Ospedale Niguarda Ca' Granda, Milan, Italy, and Dr. Luigi Bertolazzi and his team from the Nuclear Medicine Department at Ospedale Santa Corona, Pietra Ligure, Italy, for providing us with the FDG PET/CT imaging data of the twelve EPTB patients.

My sincere thanks go to Dr Noraini Abdul Rahim, Consultant Radiologist at Diagnostic Imaging Department, Serdang Hospital, Selangor, Malaysia, for her assistance in the recruitment of the patients during the clinical trial of this research.

A special vote of thanks is due to Bruce Van Every and Ruth Martin from the Nuclear Medicine Department of Alfred Hospital, and Trevor Ackerly from the William Buckland Radiotherapy Centre, Alfred Hospital, for so graciously providing facilities and assistance in PET/CT imaging and the irradiation works.

I would also like to thanks Dr Adrian Schembri and Dr Anthony Bedford from the School of Mathematical and Geospatial Sciences, RMIT University for their assistance in the statistical analyses. Special thanks too to the University Technology MARA and the Ministry of Higher Education Malaysia for providing me with a scholarship throughout my PhD studies. I also want to acknowledge the financial support given by the School of Medical Sciences, RMIT University.

I wish to thank all my colleagues from the Medical Radiation Physics and Biology Research Group; Dr Pradip Dep, Dr Price Jackson, Dr Wan Nordiana Rahman, Nathan Annabell and Mamdooh Alqathami.

My special thanks must go to Damian D'Souza and Kristi Milley, PhD students at the School of Medical Sciences, RMIT University for their assistance in proofreading this thesis.

Finally, I dedicate this thesis to my beloved wife; Wan Ismawati Ismail, parents, brothers and sisters for their prayers, support, encouragement and love.

CONTENTS

LIST OF FIGURES

CHAPTER 2

CHAPTER 3

CHAPTER 4

CHAPTER 5

CHAPTER 6

LIST OF TABLES

CHAPTER 2

CHAPTER 3

CHAPTER 4

CHAPTER 5

CHAPTER 6

ABBREVIATIONS AND ACRONYMS

Abbreviation	Meaning
2-D	Two-dimensional
3-D	Three-dimensional
AEC	Automatic Exposure Control
AFB	Acid Fast Bacilli
BaF_2	Barium fluoride
BGO	Bismuth germinate
BMI	Body Mass Index
CECT	Contrast Enhanced CT
CMI	Cell Mediated Immunity
CSF	Cerebrospinal Fluid
CT	Computed Tomography
CTDI	Computed Tomography Dose Index
CXR	Chest X-ray
DLP	Dose Length Product
DOTS	Directly Observed Treatment Short-course
DSCT	Dual Source CT
DTH	Delayed Type Hypersensitivity
EC	Electron Capture
EPTB	Extrapulmonary Tuberculosis
FDG	Fluorodeoxyglucose
FOV	Field of View
FPR	False Positive Rate
GSO	Gadolinium oxyorthosilicate doped with cerium
HIV	Human Immunodeficiency Virus
HRCT	High Resolution CT
HU	Hounsfield Unit
ICRP	International Commission on Radiological Protection
LOR	Line of Response

LSO	Lutetium oxyorthosilicate doped with cerium
MDCT	Multi Detector CT
MIP	Maximum Intensity Projection
MRI	Magnetic Resonance Imaging
NaI(Tl)	Sodium iodide doped with thalium
OSEM	Ordered Subset Expectation Maximisation
PCR	Polymerase Chain Reaction
PET	Positron Emission Tomography
PET/CT	Positron Emission Tomography/Computed Tomography
PMT	Photo Multiplier Tube
PPD	Purified Protein Derivative
PTB	Pulmonary Tuberculosis
RAMLA	Row Action Maximum Likelihood Algorithm
ROC	Receiver Operating Characteristic
ROI	Region of Interest
SNR	Signal Noise Ratio
SPECT	Single Photon Emission Tomography
SPECT/CT	Single Photon Emission Tomography/Computed Tomography
SUV	Standardised Uptake Value
SUVmax	Maximum Standardised Uptake Value
SUVmean	Mean Standardised Uptake Value
SXRT	Superficial X-ray Radiotherapy
TB	Tuberculosis
Tc-99m	Technetium-99m
TOF	Time of Flight
TU	Tuberculin Unit
VOI	Volume of Interest
WHO	World Health Organisation
WPR	Western Pacific Region
YSO	Yttrium oxyorthosilicate doped with cerium

SUMMARY

Positron emission tomography/computed tomography (PET/CT) is a hybrid imaging system that integrates the functional imaging modality known as PET with multi-slice CT scanning. PET scan can provide detailed information about functional abnormality, particularly when it is associated with the metabolic activity of a disease, but the anatomical data (size, shape and location) is usually inadequate. In contrast, multi-slice CT scan offers high spatial resolution anatomical imaging. Thus, by combining these two imaging modalities into one scanner, the acquisition of both functional and anatomical data can be obtained in a single imaging session, and any functional abnormalities can also be accurately localised.

Fluorodeoxyglucose (FDG) is the most widely and routinely used radiopharmaceutical for PET/CT imaging. Numerous studies have demonstrated that FDG PET/CT offers synergistic clinical advantages during the initial staging, re-staging and therapeutic response assessment of a wide variety of cancers, as compared to other conventional imaging modalities including a dedicated PET scanner. In addition, the use of FDG PET/CT imaging has expanded into the diagnostic evaluation and treatment follow-up of the infectious disease of tuberculosis (TB). However, there is still a lack of evidence concerning the utilisation of this imaging technique in the detection of extrapulmonary tuberculosis (EPTB) lesions. Therefore, this gap is the primary motivating theme of this thesis.

The major aim of this research is to determine the feasibility of the application of FDG PET/CT for detecting EPTB lesions. A clinical study was prospectively conducted on a series of sixteen Malaysian patients who were either highly suspected or confirmed with EPTB infectious disease. FDG PET/CT scans were performed during

the diagnostic processes of all patients. Of these sixteen patients, nine were positively diagnosed with EPTB through the histopathological findings of the sample sputum/aspirate/tissue and/or clinical/radiological assessments during their periodical follow-up visits, whilst the rest were categorised as non-EPTB patients. All detected extrapulmonary lesions were visually and semiquantitatively (by measuring the maximum standardised uptake value; SUVmax) analysed and evaluated, and no significant difference was observed between the SUVmax values of EPTB and non-EPTB lesions (7.0 ± 2.3 vs. 8.8 ± 4.6, P=0.07). This may indicate that the SUVmax value cannot be used to differentiate between EPTB and non-EPTB lesions. Nevertheless, when comparing the imaging findings of FDG PET/CT scans with the other conventional imaging modalities, this hybrid imaging system has shown a relatively higher in the imaging diagnosis of EPTB patients. Therefore, FDG PET/CT is a reliable and practical imaging modality, and can feasibly be used to detect EPTB lesions.

Dual time point imaging (DTPI) of FDG PET/CT scan has been found to be a practical imaging method that could enhance the differentiation between malignant and inflammatory/infectious lesions by assessing the SUVmax values of the lesions at two different imaging times. This special imaging technique had been successfully carried out during the FDG PET/CT scans in thirteen of our patients. However, due to a slight variation in the scanning protocols, the proper PET/CT image analyses could only be performed on eleven patients. Two sets of the SUVmax values were obtained for each patient: SUVmax1 and SUVmax2 values were from initial and delayed images. All EPTB lesions exhibited a statistically significant increasing pattern in their SUVmax values of both imaging time points (6.8 ± 2.5 vs. 7.9 ± 3.2, P=0.001). The SUVmax

values of non-EPTB lesions were also increased, but the change was less significant and smaller in amplitude as compared with those of EPTB lesions (6.2 ± 2.6 vs. 6.5 ± 2.8, P=0.044). In addition, when comparing the percentage difference of the SUVmax values (%ΔSUVmax) from both types of lesions (EPTB and non-EPTB), the result showed that there was no statistically significant difference (P=0.06). This might indicate that DTPI technique was not a useful method in distinguishing between EPTB and non-EPTB lesions, thus, the initial whole body FDG PET/CT imaging may be sufficient for differentiating the EPTB from other infectious diseases.

Another interesting aspect of FDG PET/CT imaging is the application of non-ionic iodine-based contrast media during its CT image acquisition. Many clinical studies have postulated that iodine-based contrast media can be used in FDG PET/CT imaging without affecting the diagnostic interpretation, but this data was only well documented for cancer patients. Thus, this research also aimed to verify this effect on all EPTB patients. This clinical study was conducted by measuring the SUVmax values of five different tissues (heart, liver, spleen, urinary bladder and EPTB lesion) from two different sets of PET/CT fusion images (PET/contrast-enhanced CT and PET/unenhanced CT). None of the changes in the SUVmax values of any of the tissues were found to be statistically significant. Based on this study, it is accepted that iodine-based contrast media could potentially be used in FDG PET/CT imaging of EPTB patients, without producing any significant effects on the SUVmax values. To strengthen this conclusion, an experimental phantom study has also been executed to isolate the expected effect in the absence of the variability inputs prevalent in a clinical study. This phantom study was specially designed to closely mimic the *in vivo* FDG PET/CT imaging, by inserting saline bags and bony structures, as well as two test tubes

that contained two different concentrations of iodine-based contrast media. The results showed that iodine-based contrast media can be safely applied during the CT scan of PET/CT imaging, without affecting the diagnostic accuracy of this integrated imaging modality.

A radiation dose arising from FDG PET/CT imaging plays an important role as it could provide a rational framework for the justification and optimisation of this imaging scan, and because of that, this research has determined the dosimetric component of FDG PET/CT imaging. The FDG PET/CT radiation dose is estimated through the calculations of the effective dose from each scan (FDG PET and CT), by using the administered radioactivity of FDG and $CTDI_{vol}$ data. These two effective doses are then summed in order to calculate the FDG PET/CT effective dose. The results of this dosimetric study exhibit that the largest fraction of the radiation dose comes from the CT portion of the FDG PET/CT imaging, which contributes to more than 60% of the entire FDG PET/CT effective dose. Cumulatively, this data demonstrates that our mean PET/CT effective dose is still in accordance with the previously reported values, even if the additional delayed CT scan has been performed.

In conclusion, it has been shown that FDG PET/CT is a useful imaging tool for detecting EPTB lesions, although our results suggest that the DTPI technique is ineffective in distinguishing between EPTB and non-EPTB lesions. In addition, iodine contrast media could potentially be applied during FDG PET/CT imaging of EPTB patients, while maintaining a considerably low effective dose value. These observations, taken together, provide the beginnings of a suitable body of evidence upon which a clinician can make a diagnostic decision on whether use of FDG PET/CT is indicated for the detection of EPTB lesions.

CHAPTER 1

INTRODUCTION

1.1. Problem statement

Whole body scanning using fluorodeoxyglucose (FDG) on an integrated PET/CT imaging modality has been routinely used in the diagnosis and staging of a wide variety of cancers [1-3]. In addition, FDG PET/CT scan is proven to be an important imaging tool for detecting inflammatory and infectious lesions [4]. The rationale for the high accumulation of FDG in these inflammatory/infectious lesions is mainly due to the elevated glycolytic activity of the activated inflammatory cells such as neutrophils and macrophages [5]. In an inflammatory/infectious tissue, it has been shown that these two cell types utilise large amount of glucose as the main energy source for their chemotaxis and phagocytosis processes [6]. Hence, this could elucidate the capability of FDG PET/CT imaging in depicting inflammation/infection diseases.

Tuberculosis (TB) is a systemic infectious disease caused by *Mycobacterium tuberculosis* [7]. It is one of the most common causes for false positive findings on FDG PET/CT imaging in the diagnosis of malignant tumours [8, 9]. The reason for this occurrence is due to the essential role of macrophages; particularly of alveolar macrophages, as these cells are the first line of defence in combating the *Mycobacterium tuberculosis* infection in humans [10]. In addition, a previous study has demonstrated that the macrophages could have higher FDG uptake than the viable malignant cells although they are located in the same sample of tissue [11]. Therefore, the high accumulation of FDG in tuberculous lesions is expected and could augment the effectiveness of FDG as a suitable tracer for infection imaging using an integrated PET/CT imaging system.

TB can spread to virtually any tissue or organ in the human body [12]. While pulmonary tuberculosis (PTB) is the most common presentation, extrapulmonary

tuberculosis (EPTB) is also significantly important clinical problem [13]. EPTB occurs due to dissemination via the lymphohaematogenous route during the early stage of the pulmonary infection [14, 15]. The symptoms of this disease are usually non-specific [15] and vary depending on the affected sites or tissues [16]. For this reason, the diagnosis procedure of EPTB is typically complicated [8], and to establish a definite/confirmed diagnosis of EPTB, it may require invasive and expensive serological/radiological investigations [17]. In addition, prompt and accurate diagnoses of EPTB are the key elements for an effective treatment [16], but they are often delayed primarily due to the difficulty in isolating the small number of *Mycobacterium tuberculosis* present in the affected tissues [13]. Therefore, it is of high clinical importance to predetermine and detect the EPTB lesions using non-invasive techniques in highly suspected patients, in order to avoid unnecessary invasive and sophisticated/expensive procedures.

In standard clinical practice, a chest radiograph is the primary imaging technique for the detection of both PTB and EPTB lesions [18]. However, due to its limited sensitivity and specificity, other imaging modality like computed tomography (CT) has been found to be more helpful especially in localising and determining these two lesions [12, 16, 18]. Similarly, the usefulness of FDG PET/CT imaging in detecting EPTB lesions has been highlighted in a few recent studies [7, 19, 20]. However, these observations are mostly derived from the findings of the patients who have also concomitantly presented with an underlying malignancy [19] and/or immunosuppression diseases such as human immunodeficiency virus; HIV [20], and active PTB infection disease [7]. Thus, there are insufficient evidence-based reports in the current literature which exclusively describe the utilisation of FDG PET/CT imaging

in a series of either confirmed or highly suspected EPTB patients. Hence, this leads to the requirement for conducting a prospective study that aims at definitively detecting and characterising the EPTB lesions using FDG PET/CT imaging. This novel approach should be undertaken as an effort to shorten the diagnostic procedure of EPTB infection disease, which then may provide a better prognosis for patients with this disease.

The utilisation of dual time point imaging (DTPI) technique during FDG PET/CT imaging has been proposed as a method of choice in distinguishing between malignancy and inflammations/infections [21-23]. Again, there is scarce data on the application of this special imaging technique for differentiating EPTB lesions from malignant and/or other inflammatory/infectious lesions [7]. On the other hand, several studies have shown that by performing the CT component of FDG PET/CT imaging as for the diagnostic scanning protocol; contrast-enhanced CT (CECT) scan, it could result to higher diagnostic values of this integrated imaging system [24-27]. However, there are no studies in the literature that particularly employ this type of scanning protocol for FDG PET/CT imaging of EPTB patients. Thus, it would be valuable to conduct a study that could properly address and document both of these issues.

1.2. Hypotheses and aims of the research

The purpose of the research presented in this thesis is to test the following hypotheses:

- *Hypothesis 1*

  EPTB lesions exhibit high intensity uptake of FDG, which can clearly be depicted on PET and PET/CT fusion images.

- *Hypothesis 2*

  The utilisation of the dual time point imaging (DTPI) technique during FDG PET/CT scan can increase the diagnostic value of this integrated imaging modality in detecting EPTB lesions.

- *Hypothesis 3*

  The application of iodine-based contrast media during the CT scan of FDG PET/CT imaging will not cause any significant image artifacts on PET/CT fusion images.

- *Hypothesis 4*

  The effective radiation dose of EPTB patient who has undergone FDG PET/CT imaging is considerably low as compared with the previously reported values.

The specific aims of all designed studies in this research are:

1. To evaluate the role of FDG PET/CT imaging in the detection of the EPTB lesions.
2. To define the mean value of FDG uptake in a series of patients who are either highly suspected or confirmed for EPTB infection disease using the semiquantitative measurement (Maximum Standardised Uptake Value; SUVmax).
3. To investigate the usefulness of DTPI technique of FDG PET/CT scan in depicting EPTB lesions, and distinguishing this type of lesion from other inflammatory/infectious lesions.
4. To identify the potential value of FDG PET/CT imaging for assessing the therapeutic response of EPTB patients.

5. To determine the effects of iodine-based contrast media on PET/CT fusion images through the clinical imaging findings and the experimental results of the phantom study.
6. To estimate the PET/CT effective dose for a series of patients who have undergone the scanning using the established calculation methods and the published data.

1.3. Thesis outline

This thesis is divided into 3 different sections, according to the conducted studies:

1. Section A: Clinical imaging study
2. Section B: Phantom study
3. Section C: Dosimetric study

In addition, here are the brief descriptions on the remainder chapters of this thesis:

- Chapter 2 reviews the operating principle for PET, CT and PET/CT scanners, and briefly explains about FDG, SUV and common PET/CT image artifacts. Furthermore, the current issue regarding tuberculosis disease in Malaysia together with the essential information on the pathogenesis, diagnosis and treatment of tuberculosis are presented in this chapter.
- Chapter 3 details the FDG PET/CT scanning protocols that have been used during the imaging session of all our patients, including the utilisation of dual time point imaging (DTPI) technique and an intravenous injection of iodine-based contrast media during the CT scan of FDG PET/CT imaging. Fundamentally, two different types of data are obtained in this clinical study;

the prospective data of sixteen Malaysian patients and twelve Italian patients for the retrospective data. In addition, out of all Malaysian patients, six of them have undergone a repeat FDG PET/CT imaging with an interval of six months from the initial scan and upon the completion of 24 weeks of anti-tuberculous drugs treatment.

- Chapter 4 describes and discusses the results of FDG PET/CT scans from both Malaysian and Italian patients. Based on the image analysis and interpretation, all EPTB lesions demonstrate high accumulation of FDG with the maximum standardised uptake value (SUVmax) as high as 20.8. This imaging finding clearly indicates that FDG PET/CT imaging could offer a diagnostic potential in detecting EPTB lesions. On the other hand, the utilisation of DTPI technique may not be a useful method in distinguishing between EPTB and non-EPTB lesions. Thus, for diagnostic purposes, initial whole body FDG PET/CT scan seems to be sufficient for depicting and differentiating EPTB from other infection diseases. Furthermore, this study has found that iodine-based contrast media can be safely applied during the CT scan of FDG PET/CT imaging, in which it will not cause any significant changes on the SUVmax values of PET/CT fusion images. In the last section of this chapter, a few technical recommendations that have been believed to improve the quality of PET/CT fusion images are also addressed.
- Chapter 5 quantifies the amount of changes in the standardised uptake values (SUVs) of PET/CT fusion images caused by the utilisation of iodine-based contrast media during the CT scan of FDG PET/CT imaging. This experimental study had been conducted using an anthropomorphic phantom, in

which the set-up was aimed to replicate the true *in vivo* imaging situation. The results of this phantom study showed that none of the changes in the SUVs were found to be statistically significant. Therefore, this finding supports and augments the results from our clinical imaging study, as described in the previous chapter; Chapter 4.

- Chapter 6 estimates the total PET/CT effective dose by slightly modifying the established calculation methods and published data. The experimental attempts for measuring the PET/CT effective dose using a sensitive type gafchromic film are also explained in this chapter.
- Chapter 7 summarises all the findings of this research work. From these findings, then the conclusion remarks have been drawn. Two future studies that can be developed from this research are also suggested in the last section of this final chapter.

CHAPTER 2

LITERATURE REVIEW

Radiological imaging plays an essential role in the disease management: diagnosing, treatment monitoring and follow-up assessment. Conventional imaging modalities like general radiography, computed tomography (CT) scan, magnetic resonance imaging (MRI) and ultrasonoraphy can be categorized as morphological imaging modalities; they have the capability of identifying the anatomical patterns and provide basic information regarding location, size and shape of the lesion.

Nuclear medicine, a branch of radiological imaging, also plays an important role in the detection of the lesions. It could act as a complement to morphological imaging by integrating biology and *in vivo* imaging data in order to acquire the pathophysiological information of a disease. Generally, nuclear medicine images are quite 'noisy' and the spatial resolution is low compared to radiographs, CT and/or MRI images. Several imaging modalities are commonly used in a nuclear medicine department like gamma camera, single photon emission tomography (SPECT), positron emission tomography (PET) and the latest are the hybrid imaging scanners; PET/CT and SPECT/CT. However, in this chapter, the main focus is only for PET, CT and PET/CT scanners; as these three modalities are fundamentally related with this research, which will be further discussed in the following sections.

2.1. Positron Emission Tomography (PET)

The first PET scanner was commercially introduced in 1980, but only after a decade it was established as an important imaging modality and widely used in the oncology field [3]. PET is a dedicated imaging modality that could map the radiopharmaceutical distribution and quantify the cellular metabolic activities by measuring the intensity of the accumulated radiopharmaceutical in a particular region of the human body [28]. The

operating principle is based on the detection of the coincident photons that have originated from the annihilation process between the emitted positrons and the electrons of the surrounding tissues [29].

Positron emitters are produced using a circular particle accelerator, known as a cyclotron. The stable (non-radioactive) isotope is bombarded with protons, which then will create an unstable isotope with an excess of protons in its nucleus [28]. Thus, in re-achieving of its stability stage, a proton (p) will be converted into a neutron (n) through the nuclear transmutation process [3]. This results in the emission of a positron (β^+); a positively charged electron emitted from nuclei that have an excess of protons, and a neutrino (ν); a particle that has a very small mass and zero charge [30, 31].

$$ {}^{1}_{1}p^{+} \longrightarrow {}^{1}_{0}n + {}^{0}_{1}\beta^{+} + \nu \qquad (2.1) $$

After being emitted from the nucleus, the positron loses kinetic energy by interactions with the surrounding matter. When nearly all of its kinetic energy has been lost, then positron will combine with an electron, forming a metastable intermediate species called positronium; it is a non-nuclear, hydrogen like element composed of the positron and electron that spin around their combined centre of mass. This positronium will quickly undergo an annihilation process, thus creating two photons of 511 keV gamma rays; the energy of the gamma rays is equivalent to the rest mass of the electron and positron. These two gamma rays are emitted in diametrically opposite directions (180^{o}) to each other for conserving the momentum, which is close to zero before the occasion of an annihilation process [30, 31] (refer to Fig. 2.1).

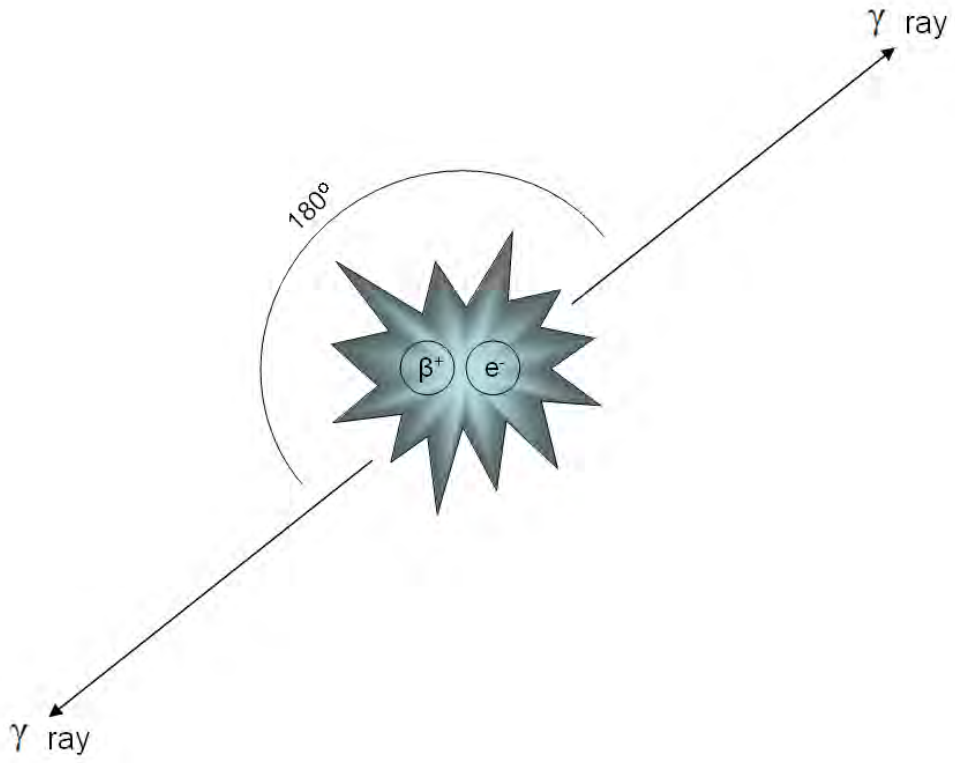

Figure 2.1: Positron- electron annihilation reaction (β^+; positron, e^-; electron, and γ; gamma ray).

The emission of these two gamma rays are simultaneously captured in a single coincident event by PET detector system, within a very short period of time; a few nanoseconds, this is called coincidence time window [3]. Therefore, by surrounding the patient with a ring detector system, the pairs of coincident photons can be detected. The origin of the emission of these coincident photons is assumed to lie within the line joining the two points at which the photons hit the detector; this joined line is called the line-of-response (LOR). The projection data from the integral activity of sets of LORs will be reconstructed to generate an image of the distribution of positron emitter within the object [31]. However, in general, there are three different categories of coincident

events involved in PET imaging [30], in which each of these coincidences could affect the production of PET images in a different way (refer to Fig. 2.2):

1. True coincidences

   True coincidences (Fig. 2.2a) are emissions from single annihilation points that enter the PET detector without undergoing any significant interactions within the imaging field-of-view (FOV).

2. Random coincidences

   Random coincidences (Fig. 2.2b) occur due to the accidental detection of two unrelated single events within the coincidence time window. These coincidences only add to the image background that may result in reducing the image contrast.

3. Scatter coincidences

   Scatter coincidences (Fig. 2.2c) are true coincidence events from single annihilation points, however one or both of the photons undergo Compton scattering reaction (Fig. 2.3) within the imaging FOV before entering the PET detector. These coincidences can lead to mispositioning of LOR, which may incorrectly represent the true activity distribution within the FOV and worsen the image contrast.

Apart from the true coincidences, all others will result in incorrect spatial information [31]. Thus, several techniques that utilise sophisticated correction models and complex electronic systems have been developed and designed to remove these unwanted coincidences [3, 31].

2.1.1. PET detectors

As mentioned earlier, the coincident events are captured by PET detectors. These detectors are dedicatedly engineered to operate with the high energy photons; 511 keV, and because it is designed in a ring shape system, it has a capability to acquire a tomographic image without requiring the rotation of the detectors [32]. In general, radiation detectors can be divided into three groups: gas chambers, semiconductor detectors, and scintillation detectors. However, in PET imaging, the scintillation detectors are the most common and successful method, mainly due to the following four paramount properties [30]:

1. Stopping power for 511 keV photons

   The stopping power of a scintillator is characterised by the average distance travelled by the photon before it deposits its energy within the scintillator crystal. This means that a scintillator with a short attenuation length will provide a high efficiency in stopping the 511 keV photons. Additionally, the attenuation length of a scintillator depends upon its density (ρ) and the effective atomic number (Z_{eff}).

2. Signal decay time

   A short signal decay time of a scintillator is important for individually processing each detected pulse at high counting rates. This property can also help in reducing the number of random coincidence events.

3. Light output

   A high light output of a scintillator facilitates for attaining good spatial and energy resolutions.

4. Intrinsic energy resolution

   The intrinsic energy resolution of a scintillator arises due to inhomogeneties in the crystal growth process as well as non-uniform light output for the interactions within it. Combination of this property with the light output plays a role in determining the energy resolution of a scintillator. A good energy resolution is necessitated to an efficient rejection of scatter coincidences.

Several scintillator cystals are commonly used in PET imaging like sodium iodide doped with thalium: NaI(Tl), bismuth germanate: BGO, lutetium oxyorthosilicate doped with cerium: LSO, yttrium oxyorthosilicate doped with cerium: YSO, gadolinium oxyorthosilicate doped with cerium: GSO, and barium fluoride: BaF_2 [30]. Some of these scintillators physical properties are listed in Table 2.1.

Table 2.1: Physical properties of commonly used scintillators in PET imaging [30].

Property	NaI(Tl)	BGO	LSO	YSO	GSO	BaF_2
Density (g/cm^3)	3.67	7.13	7.4	4.53	6.71	4.89
Effective atomic number (Z_{eff})	50.6	74.2	65.5	34.2	58.6	52.2
Attenuation length (cm)	2.88	1.05	1.16	2.58	1.43	2.2
Decay time (ns)	230	300	40	70	60	0.6
Light output (photons/keV)	38	6	29	46	10	2
Light output; relative to NaI(Tl) (%)	100	15	75	118	25	5
Wavelength, λ (nm)	410	480	420	420	440	220
Intrinsic energy resolution (%)	5.8	3.1	9.1	7.5	4.6	4.3
Energy resolution (%)	6.6	10.2	10	12.5	8.5	11.4
Index of refraction	1.85	2.15	1.82	1.8	1.91	1.56
Linear attenuation coefficient, μ (cm^{-1}); measured at 511 keV	0.3411	0.9496	0.8658	0.3875	0.6978	0.4545
Mass attenuation coefficient, μ/ρ (cm^2/g); measured at 511 keV	0.0948	0.1332	0.117	0.853	0.104	0.0929

NaI(Tl): sodium iodide doped with thalium, BGO: bismuth germanate, LSO: lutetium oxyorthosilicate doped with cerium, YSO: yttrium oxyorthosilicate doped with cerium, GSO: gadolinium oxyorthosilicate doped with cerium, and BaF_2: barium fluoride.

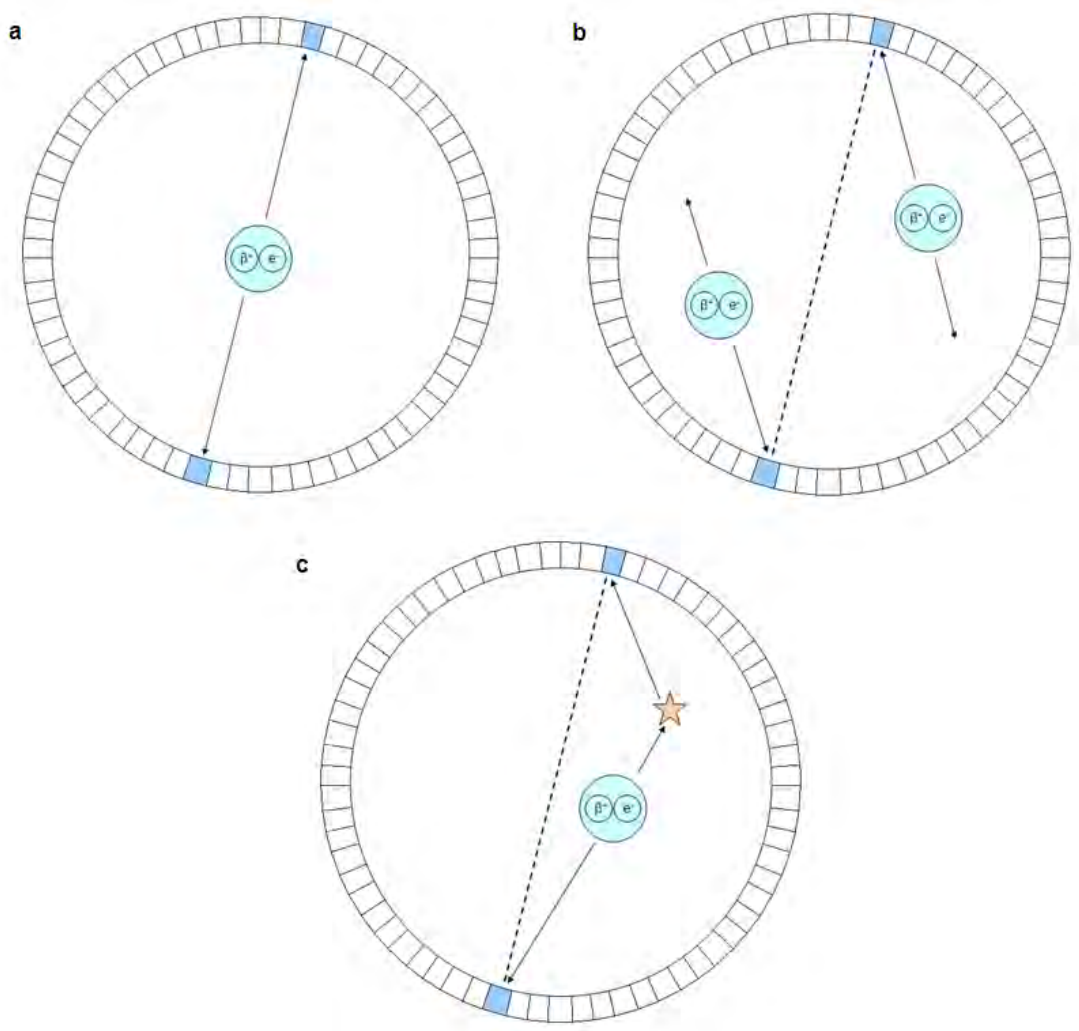

Figure 2.2: Three different types of coincidences detected in a PET imaging system. (a) True coincidence from a single positron-electron annihilation process is captured by a pair of PET detector systems. (b) Random coincidence; two photons from different positron-electron annihilation processes are detected within the coincidence time window, which appears to form a true coincidence event. (c) Scatter coincidence; one of the photons has undergone Compton scattering (star shape) prior to being detected by the PET detectors. ***The dashed line represents the line-of-response (LOR).***

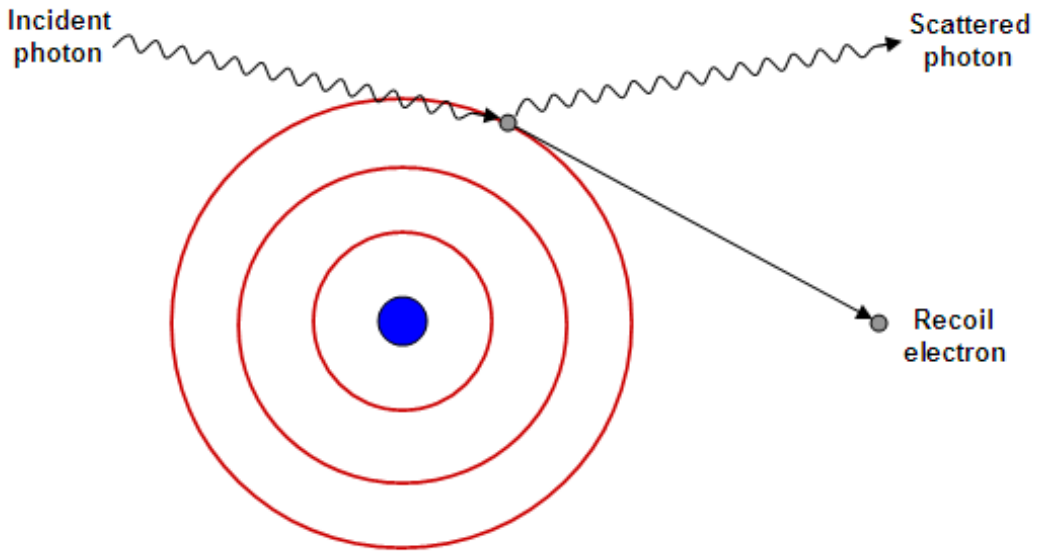

Figure 2.3: Illustration of Compton scattering reaction. Part of the energy from incident photon is transferred to an atomic electron. After this interaction, the incident photon undergoes a change in direction and the electron is ejected from the atom. The deflected photon and the ejected electron are known as scattered photon and recoil electron, respectively. This effect dominates in human tissue at energies above approximately 100 keV and less than ~ 2 MeV [30].

The first PET scanners were developed with various geometric configurations of NaI(Tl) crystals; a common scintillator material for the standard nuclear medicine gamma cameras. NaI(Tl) provides a high light output, which leads to good energy and spatial resolutions. This crystal has low stopping power mainly due to its low density [30]. Thus, NaI(Tl) is not quite suitable to be used as a scintillator for PET [3]. In the late 1970s, a denser scintillator known as bismuth germanate (BGO) with greater stopping power than NaI(Tl) had been considered as a prospective material for PET detectors [3]. Its excellent stopping power contributes to an enhanced sensitivity of PET

scanners, by increasing the ability of the scanner to detect the coincident photons emitted within its imaging FOV [30]. This crystal was established as the material of choice and has been the most widely used scintillator in PET detector system for more than 25 years [3, 29].

The introduction of new and faster scintillators such as LSO and GSO has been found to improve the performance of PET scanners in the clinical imaging; both of these scintillators have shorter decay times than BGO by a factor of 6 to 7 [3]. In addition, LSO appears to be an ideal scintillator crystal with a combination of the high light output and the high stopping power. For the last type of scintillator crystal; in this case is BaF_2, it has an extremely short decay time: 0.6 ns (refer Table 2.1). Thus, this special feature makes it ideal to be used as a detector material in time-of-flight (TOF) PET scanner; a newer generation of PET scan that is able to estimate the location of the annihilation point within an object [30].

The operating principle of PET imaging is primarily based on coincidence detection, which starts when an incoming photon hits its scintillation detector. This process results in the emission of visible light or often refers as luminescence reaction. The emitted visible light is then detected by a photo-detector. The photo-detectors that are commonly utilised in PET detector system can be divided into two categories: the photo-multiplier tubes (PMTs) and the semiconductor based photodiodes. However, the most reliable technique to measure and detect the emitted visible light photons from the scintillation detectors is using the PMTs. Basic construction of a PMT is shown in Fig. 2.4, which consists of a vacuum enclosure with a thin photo-cathode layer at the entrance window [30].

A signal detection mechanism begins once the emitted visible light hits the photo-cathode, where the light photon will deposit its energy into the photo-cathode and trigger for an ejection of a photo-electron by the photo-cathode. In the presence of an electrical field, the photo-electron is accelerated to a nearby electrode called the dynode. This acceleration increases the energy of the photo-electron, and results in the emission of multiple secondary electrons. These acceleration and emission processes continue through several dynodes in increasing electrical potentials, and this leads to a gain of photo-electrons of more than a million at the anode side (refer to Fig. 2.4). This high gain generates a very good signal-to-noise ratio (SNR) which can easily be measured by an external circuit. Hence, this is the primary reason for the widespread success and applicability of the PMTs in scintillation detectors system [30].

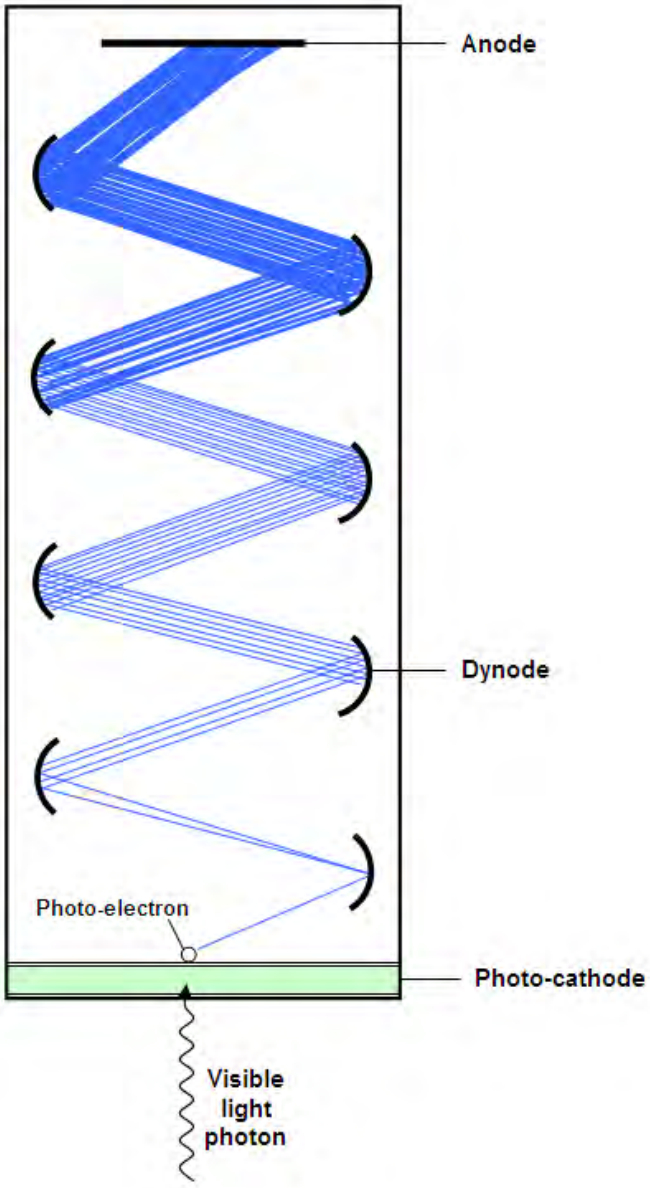

Figure 2.4: Schematic diagram of a photo-multiplier tube; consists of a vacuum enclosure with a thin photo-cathode layer at the entrance window. When the emitted visible light hits the photo-cathode, it will eject a photo-electron. This photo-electron is then accelerated to a nearby electrode called dynode. The increase in kinetic energy acquired by this process will produce a number of electrons at the next dynode, and so on, causing large amplification of the signal at the anode.

Nowadays, most dedicated PET scanners employ an array of block detectors for identifying coincident events. Each of these block detectors typically consists of an array of scintillator crystals (between 8 x 8 and 13 x 13 distinct crystal elements) and bonds to four PMTs [31] (Fig. 2.5). This special design allows for improved spatial resolution of PET system and reduced dead time of the scintillator detector [30].

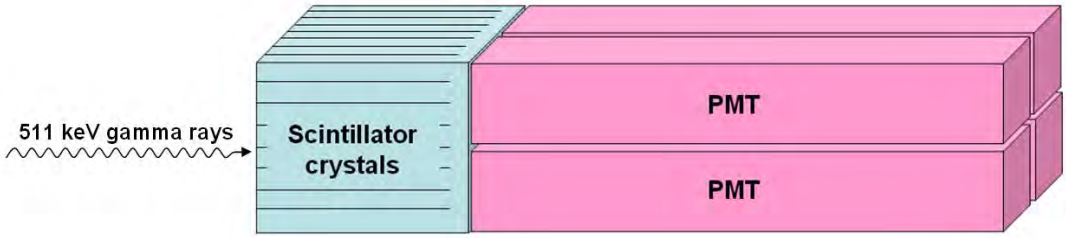

Figure 2.5: Schematic representation of a block detector for PET system. It consists of 8 x 8 scintillator crystals and bonds to four photomultiplier tubes (PMTs).

2.1.2. Attenuation correction of PET

For nuclear medicine, the term attenuation usually refers to a decrease in the energy intensity of a photon, as it passes through a medium/matter either by absorption or scatter reactions [32]. Accordingly, as highlighted before at the PET energy level, the dominant interaction between photon and human tissue belongs to Compton scattering [30]. This means that in PET imaging system, most of the emitted annihilation photons are actually being attenuated in tissue, rather than directly entering the scintillation detectors [29].

The attenuation of the emitted annihilation photons follows the low of exponential absorption [3], outlined in the following equation:

$$I_x = I_o e^{-\mu x} \tag{2.2}$$

where, *I* represents the photon beam intensity, the subscriptions of '0' and '*x*' refer respectively to the unattenuated beam intensity and the intensity measured through a thickness of medium of thickness *x*, and μ refers to the linear attenuation coefficient of the medium. The linear attenuation coefficient (μ) is a measure of the probability that a photon will be attenuated by a unit length of the medium, and it has a unit of cm^{-1} [30]. However, when an annihilation reaction occurs at a depth of 'a' from one detector (refer to Fig. 2.6), in a medium of total thickness of D, the number of photons recorded by detector A; N_a, would be as of the equation below:

$$N_a = N_o e^{-\mu a} \tag{2.3}$$

where N_o represents the number of emitted photons, and μ is the linear attenuation coefficient of the medium (assumed to be a constant). Based on the above equation, it can clearly be seen that the number of detected photons changes with the depth of 'a'[31]. On the other hand, for the opposite detector; detector B, the recorded number of photons is equal to:

$$N_b = N_o e^{-\mu(D-a)} \tag{2.4}$$

where the depth of b = D − a. Thus, as in PET imaging system, the number of annihilation photons (N) that can be detected by the two opposed detectors would be:

$$
\begin{aligned}
N &= (N_o e^{-\mu a}) \cdot (N_o e^{-\mu(D-a)}) \\
&= N_o (e^{-\mu a} \cdot e^{-\mu(D-a)}) \\
&= N_o e^{-\mu[a+ (D-a)]} \\
&= N_o e^{-\mu D}
\end{aligned} \tag{2.5}
$$

Based on the above equation, it shows that the detected number of annihilation photons depends upon the linear attenuation coefficient of the medium, μ, and the total thickness of the medium/object, D [31]. In addition, this value is independent of the depth [3] or the location of the annihilation reaction within the medium/object [30, 31].

For a dedicated PET imaging system, the attenuation can be corrected by performing a transmission scan using an external source of 511 keV photons such as Germanium-68 (^{68}Ge), in either a ring or rod shape [31]. During the transmission scan, usually three ^{68}Ge sources are used to rotate around the patient, to fully cover the axial extent of PET scanner [3]. With this transmission data, an attenuation map of the patient can be derived from the ratio between the known (true) and measured (attenuated) intensity of the external sources [29]. This patient-specific attenuation map is then used to correct the emission data [31], and it happens before the PET image reconstruction [3]. In spite of the fact that transmission scan is essential for PET imaging, this scan is also a time consuming technique [33], which may represent about 40% or more of the total duration of PET imaging [3]. Thus, the application of transmission scan during PET imaging results in a long total acquisition time, ranging between 50 – 70 min [34].

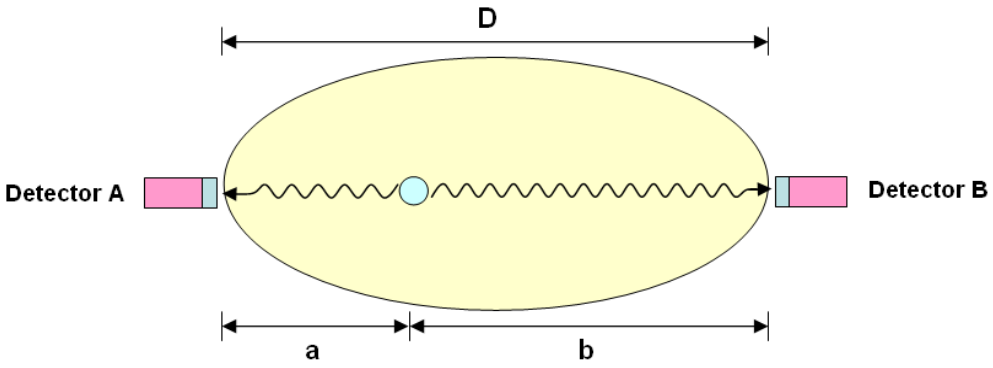

Figure 2.6: Detectors A and B record a pair of photons from an annihilation reaction that is located at 'a' depth from detector A and 'b' depth from detector B. For each annihilation reaction, the probability of detecting both photons is the product of the individual photon detection probabilities. Thus, the number of annihilation photons recorded by both detectors (A and B) is depth independent, and the total attenuation is only determined by the total thickness of the medium, D and the linear attenuation coefficient of the medium, μ (as in the Equation 2.5).

In general, PET imaging consists of two different scans, which are the transmission and the emission scans. Each of these scans generates a set of images that correspond to its scanning; the transmission and the emission images. Usually, the PET image acquisition commences with the transmission emission scan then followed by the emission scan [3]. As mentioned earlier, the emission data are corrected for attenuation using the transmission data prior to the PET image reconstruction. This enables the PET scanner to create a new set of images, the so called attenuation corrected images [31], which have been found to demonstrate less evident of image artifacts [3]. However, PET images can occasionally also be reconstructed without the attenuation correction due to two reasons: to identify the presence of the motion artifact and to determine the additional anatomical information that is available in the uncorrected image [33].

Therefore, it can be considered that the imaging information provided by these two scans are complementary to one another [33].

Although PET imaging can successfully provide the functional information of various diseases, several limitations of this imaging technique have been identified. These include:

- The attenuation map from the transmission is usually noisy and sensitive to the emission activity in the injected patient [33].
- A long acquisition time may limit the throughput capability of the PET scanner [35].
- The spatial resolution of PET images is generally poor compared with radiographs, CT or MRI images [35].
- The cost of all PET instruments and facilities is relatively high as compared to other conventional imaging modalities [31, 35].
- The cost of each PET imaging is also high, which mainly depends on the cost of radiopharmaceuticals used [35].
- Patient may suffer to an internal whole body exposure with a non-uniform distribution [35, 36].
- The radiation dose largely depends on the amount of injected radioactivity [35].

However, with the evolution in technology, most of these limitations have been resolved. For example, the introduction of a new PET imaging system that is capable of acquiring the imaging data in either a two-dimensional (2-D) or three dimensional (3-D) mode [3]. The acquisition of PET images in a 3-D mode can increase the sensitivity of the scanner at least by a factor of 6 [3]. Thus, this new imaging technique may decrease

the total acquisition time and/or allow for reducing the amount of injected radioactivity to the patient [35]. In addition, the performance characteristics of PET scanner have shown a dramatic improvement from the introduction of new and faster scintillator crystals, and the advances in computer and electronic systems [3, 35].

2.2. Multi-slice CT scanner

The technology of CT scanners is more rapidly developed when compared with dedicated PET imaging systems [3]. The first CT scanner was commercially introduced in 1972 [3, 37]. About two decades later, the era of the helical/spiral CT scanner emerged [37], in which the images/projections are acquired continuously while the patient/table is translated at a constant speed [38] (Fig. 2.7). This type of scanning offers three main advantages: 1) complete organ coverage in a single breath hold, 2) uniform sampling density as a result from the translation of patient/table at a constant speed and 3) the ability of producing overlapped images without overlapped scans [38] also known as volume data acquisition [37]. Interestingly, by utilising these overlapped images or volume data, the scanner can reconstruct the images in 3-D [37, 38]. Thus, this helical/spiral scanning has also paved the way for the development of 3-D image processing techniques, which have become a vital component in newer generations of the CT scanners [37].

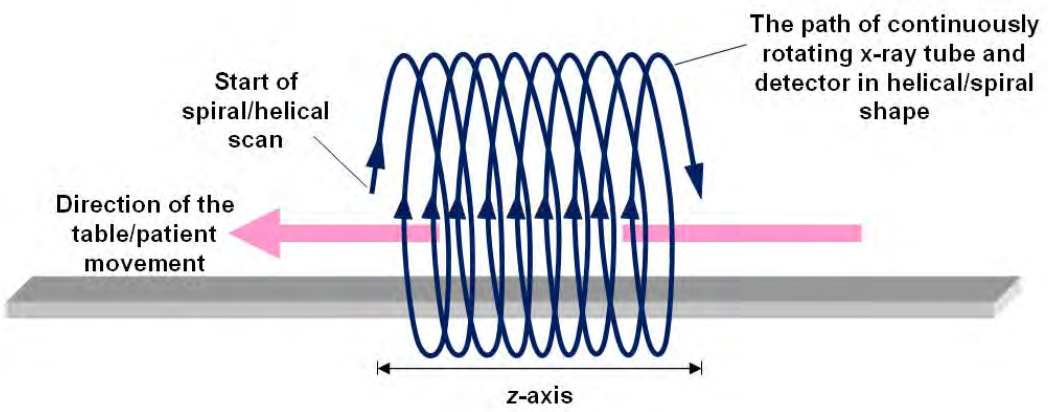

Figure 2.7: The basic principle of a helical/spiral CT scan. The table/patient is translated at a constant speed while the volume data are acquired. The x-ray tube and detector system are continuously rotated in a helical/spiral shape. The images could be reconstructed at any point along the longitudinal axis; *z*-axis.

In 1998, a four-slice CT system was invented, the technology of which solved two major problems with single-slice helical/spiral CT scanner: 1) insufficient volume coverage within a single breath hold, and 2) missing spatial resolution in the longitudinal axis due to wide collimation [37]. The four-slice CT system can acquire larger volume coverage in shorter scanning times with an improvement in the longitudinal resolution. In this new CT system, four rows of detector have been used instead of a single detector row as its predecessor (Fig. 2.8), and hence, it can also be named as a multi-detector CT; MDCT, scanner.

Currently, the detectors for modern CT systems are made from radiation-sensitive solid state materials. These detectors convert the attenuated x-rays into visible lights, which then will be detected by silicon photodiodes. Similar to the PMTs in PET imaging system, the photodiodes convert visible lights into electrical currents, and these electrical currents are amplified and converted into digital signals. In addition, the x-ray

tube for MDCT scanner requires larger heat storage capacity of the anode plate. This characteristic can be achieved either by using the thick graphite layers attached to the backside of the anode plate or the rotating envelope x-ray tube. In a rotating envelope tube, the anode plate constitutes an outer wall of the x-ray tube, and thus, it has direct contact with the cooling oil in the tube housing which allows for very efficient heat dissipation [37]. An example of a rotating envelope x-ray tube is shown in Fig. 2.9.

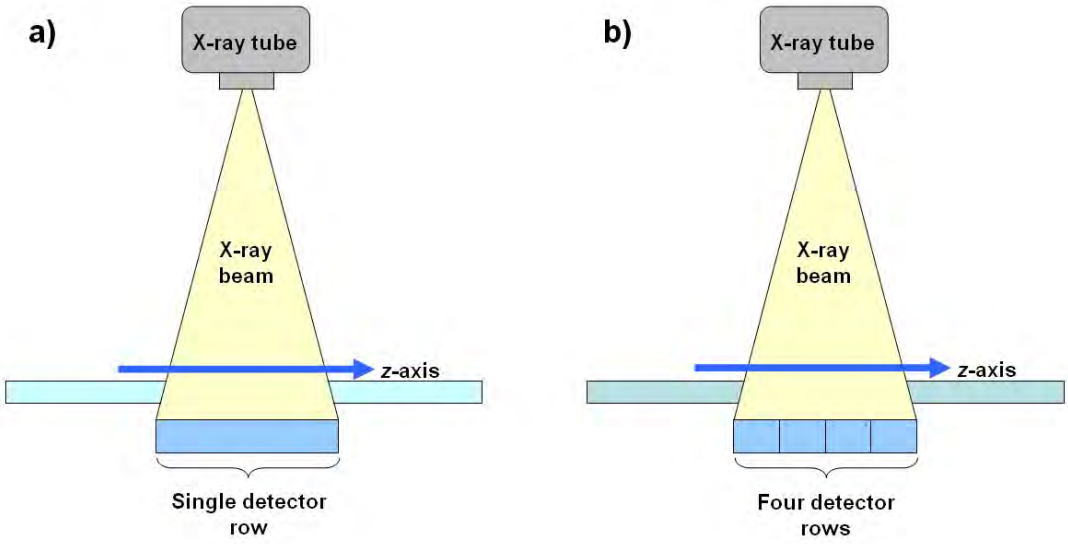

Figure 2.8: Schematic diagrams of a) a single-slice CT system with one detector row, and b) a four-slice CT system with four detector rows.

Figure 2.9: A rotating envelope x-ray tube. The anode plate constitutes an outer wall of the x-ray tube and it is in direct contact with the cooling oil in the tube housing (blue arrow). This design allows for efficient heat dissipation via thermal conduction. In addition, rotating envelope tubes have no moving parts and no bearing in the vacuum [37].

With the development of MDCT system, the technology in CT imaging has tremendously changed. In 2007, a scanner with the capability of acquiring 320 slices during one tube rotation was introduced. However, prior to this, the first dual-source CT (DSCT) system was developed in 2005. This DSCT system has two x-ray tubes and two corresponding detectors, or in other words it has two acquisition systems that are mounted onto the rotating gantry with an angular offset of 90^{o}, as shown in Fig. 2.10. In DSCT, both x-ray tubes can either be operated simultaneously or at different kV settings. The later technique allows for dual energy acquisitions which may provide additional functional information to the morphological information, based on the differences in x-ray attenuation coefficients [37]. In addition, the timeline of the technological advancements in CT scanning systems is summarised in Fig. 2.11.

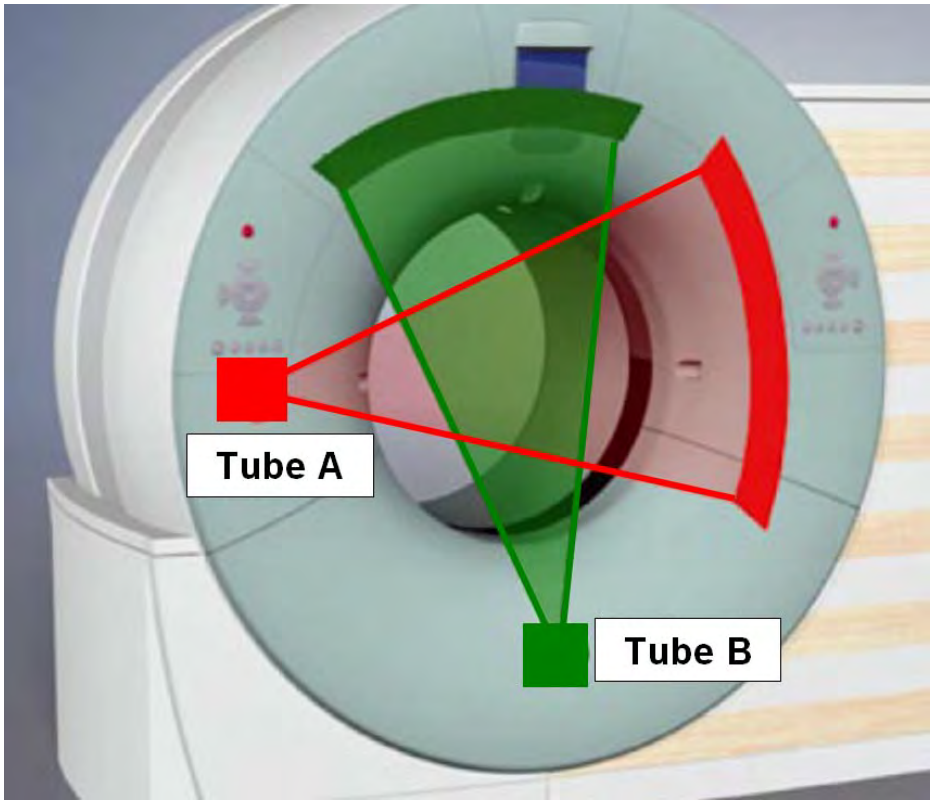

Figure 2.10: Schematic illustration of a dual-source CT (DSCT) system using two x-ray tubes (A and B) and two corresponding detectors offset by 90^{o} [37].

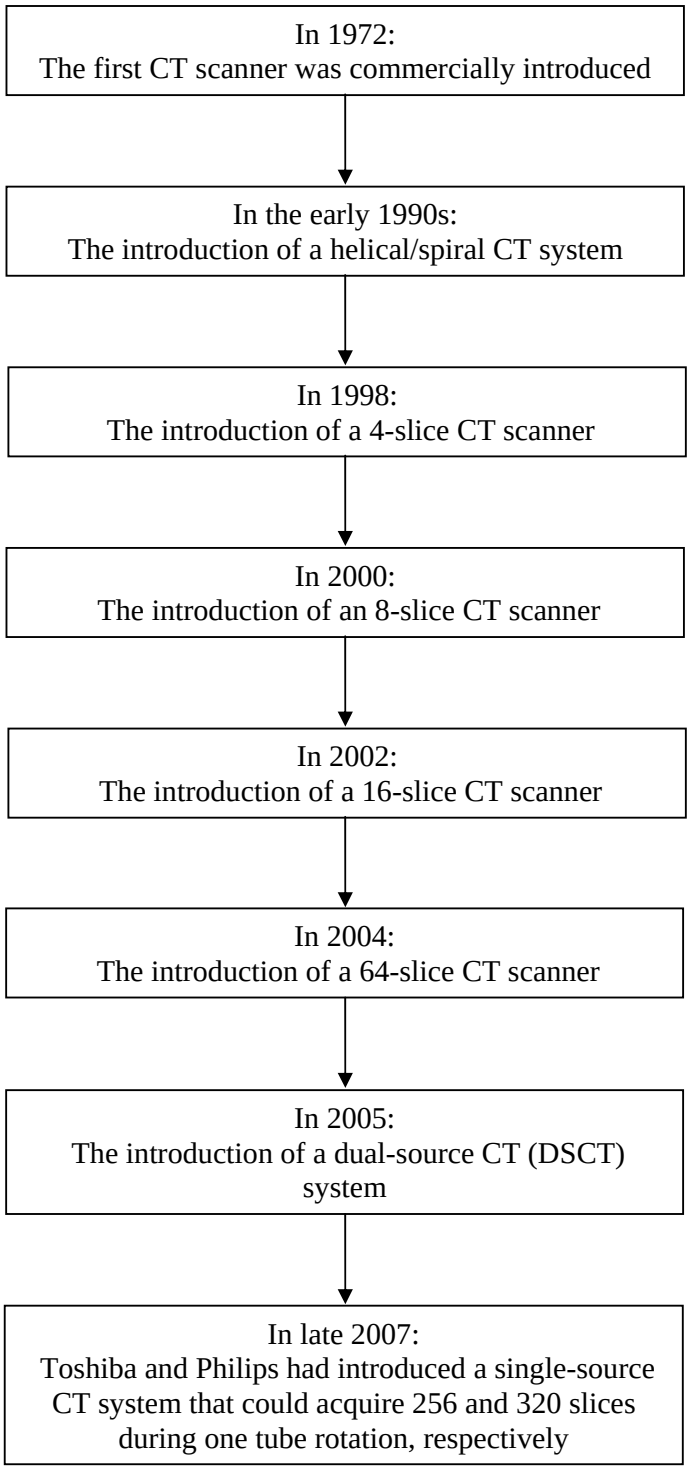

Figure 2.11: Summary of the technology developments in CT scanning system.

2.3. Positron Emission Tomography/Computed Tomography (PET/CT)

In the imaging diagnosis of a disease, CT images are primarily used for detecting anatomical or morphological changes, whereas PET imaging provides functional or metabolic information that is associated with the disease. The utilisation of both anatomical and functional information may facilitate for more accurate lesion detection and differentiating between normal and abnormal tissues. Thus, this issue demands the integration of these two images into a single display system, regardless of either using software or hardware fusion techniques.

The first attempt of integrating the images from different modalities began in the 1980s [39]. It started with the fusion of the metabolic emission images from PET to the much higher resolution anatomic images from either MRI or CT scans by using a software based image fusion technique. At that time, this technique was successful for the brain, whereas for the other parts of the body, it was seemed to be complicated mainly due to the synchronisation problems [39-41]. The drawbacks for this software based image fusion technique are addressed in Table 2.2.

Table 2.2: A comparison of advantages and disadvantages between software and hardware based image fusion techniques [39].

Software fusion	Hardware fusion
Image retrieval from different archives	Image available from one device
Repeated patient positioning	Single patient positioning
Different scanner bed profiles	One bed for both scans
Uncontrolled internal organ movement between scans	Consecutive scans with little internal organ movement in between scans
Disease progression in time between scans	Scans acquired close in time
Limited registration accuracy	Improved registration accuracy
Less convenient for patient (two scans)	Single, integrated exam
Labour-intensive registration algorithms	No further image alignment required

To resolve the problems associated with the software fusion technique (refer to Table 2.2), a combination of CT and PET systems in one scanner was proposed. This approach is referred to the hardware based image fusion technique [3]. The development of the first integrated PET/CT prototype was initiated in 1992 and took about six years until the prototype became fully operational allowing for clinical trials of more than 300 cancer patients. These studies emphasised of the following advantages [3]:

- an accurate localisation of functional abnormalities,
- a clear differentiation between the normal uptake and the pathological uptake,
- a minimisation on the effects of both external and internal patient movements, and
- a significant reduction in scanning time and an increase in patient throughput from the utilisation the CT based PET attenuation correction factors.

The first integrated PET/CT imaging modality was commercially made available to be used for clinical imaging in early 2001 [2, 39]. In this first PET/CT scanner, CT and PET scans were acquired and reconstructed on separate consoles, while the image fusion display system was only installed on the PET console [3, 39] (Fig. 2.12). However, with the advances in technology, all PET/CT imaging systems can now be operated and displayed from a single console, and five major vendors offer this integrated imaging system: a) Philips Healthcare Systems, b) Siemens Healthcare Solutions, c) General Electrics (GE) Healthcare, d) Toshiba Medical Systems, and e) Hitachi Medical Systems. Indeed, over 5000 PET/CT imaging systems have been installed worldwide [3, 29].

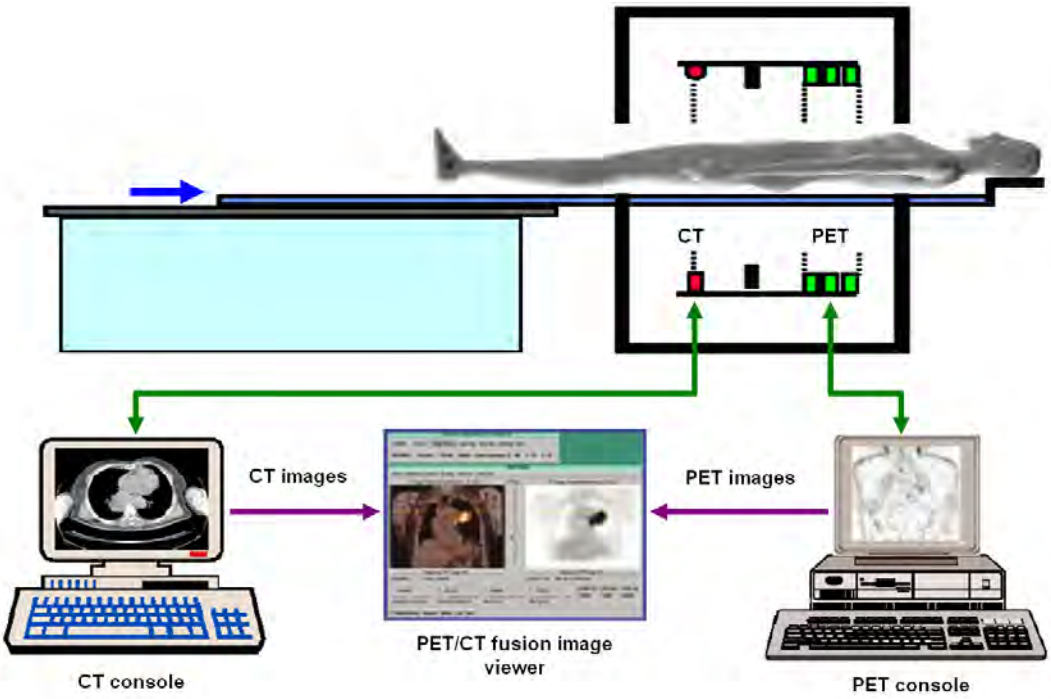

Figure 2.12: Schematic representation of the first PET/CT scanner, where PET components were mounted on the rear of a common rotating support. Both CT and PET scans were acquired and reconstructed on separate consoles, but the image fusion display was only installed in PET console [39].

Currently, PET/CT imaging modality consists of the combination between a whole-body dedicated PET system and a standard multi-slice CT scanner, which have been incorporated into a single gantry [29] (Fig. 2.13). Usually, the CT scanner is mounted in front of the gantry, then followed by the PET imaging system [42]. This design allows for the acquisition of functional PET and morphological CT images in a single imaging session without positional change of the patient, and with very minimal delay in time between those two scans [43]. These two sets of images can be intrinsically co-registered using an automated PET/CT image registration technique, which offers several advantages such as convenience and fast method, observer

independence, and well tolerate with all respiratory phases either during CT or PET scan [44]. Thus, PET/CT fusion images can result in more accurate anatomical localisation of both normal tissues and pathologic lesions [45].

Figure 2.13: Biograph 6 PET/CT imaging system from Siemens Healthcare Solutions, which incorporates PET and CT scanners into a single gantry setting. The PET imaging system consists of a multi LSO detector ring system, whereas the CT scanner is the SOMATOM Emotion 6; that enables for an acquisition of 6 slices per one revolution. ***Image courtesy from Prince Court Medical Centre, Kuala Lumpur, Malaysia.***

The most recent development in PET/CT imaging is the incorporation of a PET system with a MDCT scanner of up to 128 detector rows [29, 46]. This new PET/MDCT integration has improved the capability of the imaging system, in which it can potentially be used in the standard acquisition protocols for imaging of the heart

[47]. However, instead of functioning as an integrated imaging modality, PET/CT scanner can also be operated as two different modalities, either a dedicated PET system or a CT scanner [45].

2.3.1. PET/CT detectors

The scintillator materials for PET/CT detector are basically the same as in a dedicated PET imaging system. The first PET/CT prototype utilised the BGO detector, however, presently most of PET/CT detectors are made of LSO [29]. The LSO material has fast timing properties with a high light output and good stopping power for 511 keV gamma ray photons [48] (refer to Table 2.1).

2.3.2. Attenuation correction of PET/CT

Unlike a dedicated PET scanner, in PET/CT imaging system, the information on the attenuation correction of the PET emission data can be derived by using CT data [43, 49], in which it may eliminate the need for a separate and lengthy PET transmission scan [39]. With this CT-based attenuation correction technique, the overall whole body PET/CT scanning time can substantially be reduced by about 30% – 40% [3, 42]. In addition, this data provides essentially noiseless attenuation correction factors as compared to those from PET transmission scan [3, 39]. Therefore, this novel approach has been found to increase the throughput capability of a PET/CT scanner with less patient discomfort [42].

As highlighted in section 2.1.2, the attenuation correction of PET emission data depends upon the linear attenuation coefficient value of the medium; μ, and the total thickness of the medium; D [31]. Of these two factors, only the linear attenuation

coefficient values can be effectively determined from the CT images, and these values are energy dependent [3, 30]. To calculate the PET attenuation correction factors, CT numbers (represent in Hounsfield Units; HU) that are acquired at a mean photon energy of 70 keV (the mean energy of the polychromatic x-ray beam produced by CT scan) must be converted and scaled to the linear attenuation coefficient values of 511 keV PET energy level [3, 39]. This process can be done by applying the scaling algorithms to the HU data of the CT images, in which the algorithms use a bi-linear function to transform the HU data to the linear attenuation coefficient values above and below a threshold with different factors [43, 49]. Accordingly, all biological tissues on the CT images are classified into two different compositions of either the air-water mixture or the water-bone mixture, with an optimal threshold is found to be at around 100 HU [3] (refer to Fig. 2.14). These bi-linear scaling algorithms have been widely used and accepted in the clinical PET/CT imaging [49].

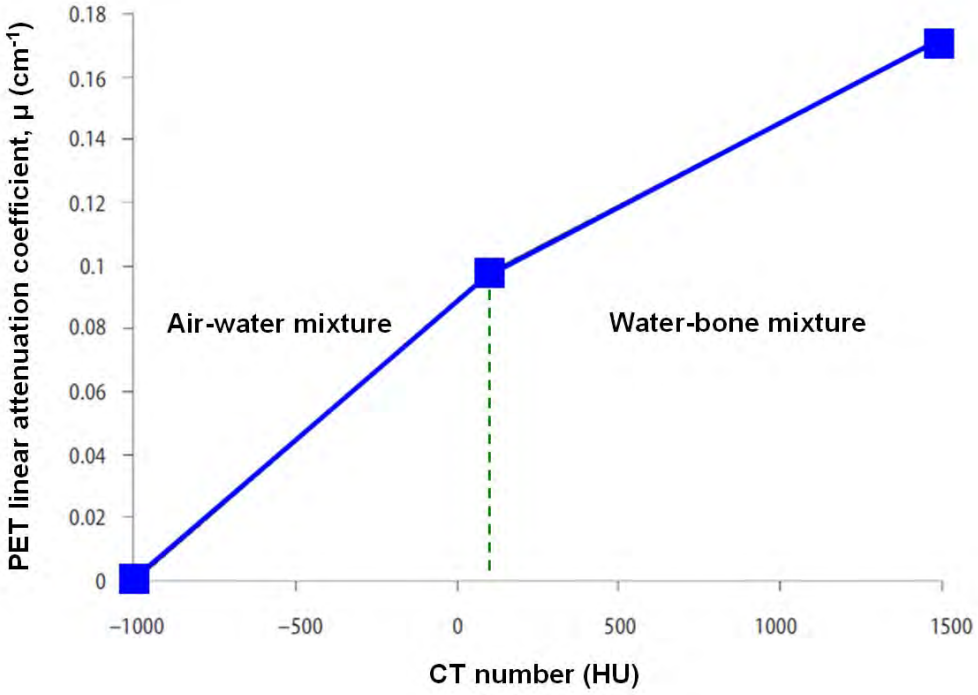

Figure 2.14: The simple bi-linear scaling algorithms that are typically used to convert the CT number (Hounsfield Unit; HU) to the linear attenuation value (μ) of 511 keV PET energy level. The graph shows the μ value as a function of the corresponding HU. An optimal threshold of about 100 HU (dashed green line) is applied for classifying all the biologic tissues of the CT images into two different compositions of either the air-water mixture or the water-bone mixture. Based on these scaling and conversion methods, the PET attenuation correction factors are calculated by using CT numbers [3].

2.4. Fluorodeoxyglucose (FDG)

Carbon, nitrogen, oxygen and hydrogen represent the fundamental elements of biological molecules. The first three elements have isotopes that decay by positron emission, however, hydrogen can generally be replaced with another similar element, known as Fluorine-18 (^{18}F) [28]. The routinely used positron emitters for PET and/or PET/CT imaging are listed in Table 2.3.

Table 2.3: Common positron emitters for PET and/or PET/CT imaging [32].

Radioisotope	Atomic number (protons)	Number of nucleons (protons + neutrons)	Approximate half-life (min)
Carbon-11	6	11	20
Nitrogen-13	7	13	10
Oxygen-15	8	15	2
Fluorine-18	9	18	110

Today, a number of positron-labelled radiopharmaceuticals are commercially available, and can either be applied in clinical or research studies. However, the most widely used one is ^{18}F-2-fluoro-2-deoxy-D-glucose, also known as Fluorodeoxyglucose (FDG). This radiopharmaceutical has been utilised for more than 90% of all PET oncological imaging [29], which mainly due to the longer half-life of ^{18}F compared to the others (refer to Table 2.3). Thus, FDG offers a capability to be transported to satellite PET or PET/CT imaging centres, especially for those without on-site cyclotron facility.

Fundamentally, FDG is an analogue of glucose, with a chemical formula of $C_6H_{11}FO_5$ [32]. However, the hydroxyl (OH) group at the Carbon-2 (C-2) position is missing and has been replaced by a Fluorine-18 (^{18}F) molecule [50] (refer to Fig. 2.15). Like glucose, FDG enters the living cell via glucose transporters which are located on the cell membrane. Once FDG has reached the cytoplasm of the cell, it undergoes the glycolysis process, and is phosphorylated to FDG-6-phosphate by the hexokinase enzyme. However, FDG-6-phosphate cannot be further metabolised by the glucose-6-phosphate isomerise enzyme, mainly due to the absence of an oxygen atom at the C-2 position. FDG-6-phosphate is also not a suitable substrate for the glucose-6-phosphatase

enzyme; an enzyme that is responsible for converting FDG-6-phosphate to FDG. As a consequence, FDG-6-phosphate is trapped in the cytoplasm [32, 50] (refer to Fig. 2.16).

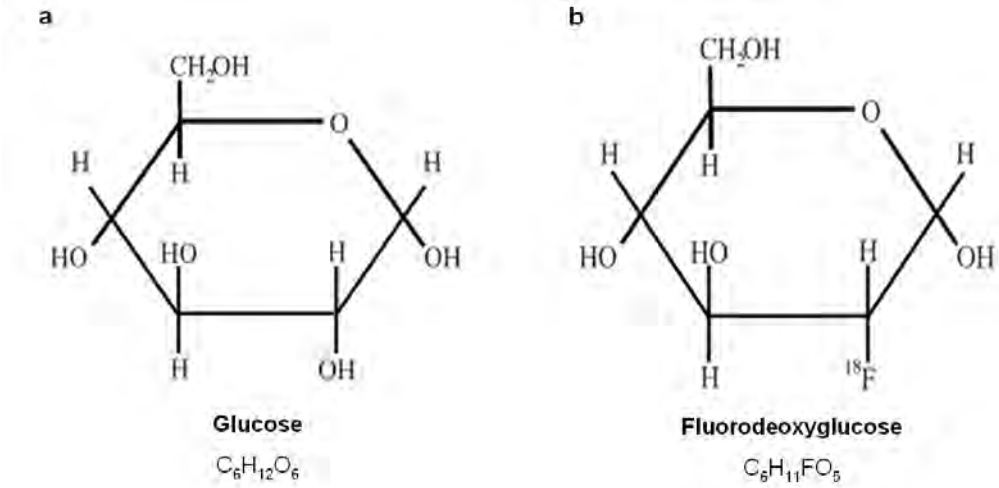

Figure 2.15: A comparison of the chemical structure of a) glucose ($C_6H_{12}O_6$) and b) Fluorodeoxyglucose; FDG ($C_6H_{11}FO_5$), in which the hydroxyl group (OH) at the C-2 position is being replaced by ^{18}F molecule [51].

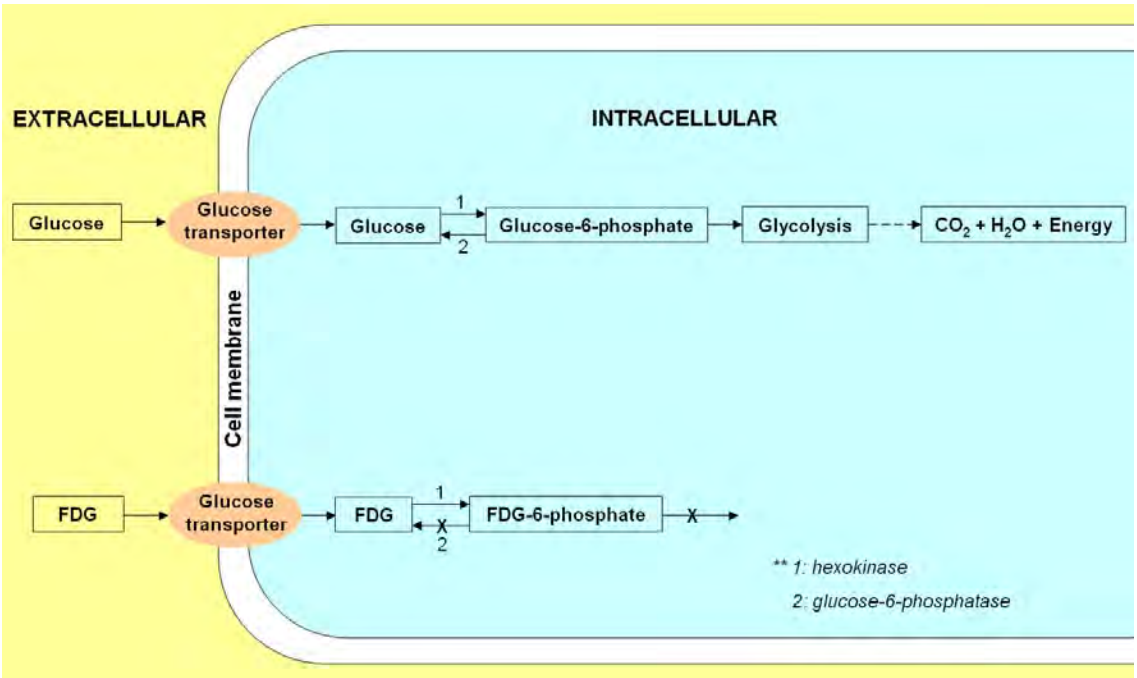

Figure 2.16: Schematic illustration for early metabolic pathway of glucose and FDG [32].

The radioactive Fluorine-18 (^{18}F) molecule will decay to its stable molecule, known as Oxygen-18 (^{18}O) [28] (Fig. 2.17). As in FDG-6-phosphate, ^{18}F atom at the C-2 position carries a negative charge; $^{18}F^-$. This unstable negative ion decays to a new stable negative ion of Oxygen-18 ($^{18}O^-$). Then, $^{18}O^-$ ion combines with a hydronium ion (H^+) from its aqueous environment, and creates a new substrate which is called glucose-6-phosphate labelled with a harmless non-radioactive "heavy oxygen" [52]. This new substrate can undergo a normal glycolysis process in the same way as the ordinary glucose, which finally produces non-radioactive end-products [52] (Fig. 2.18).

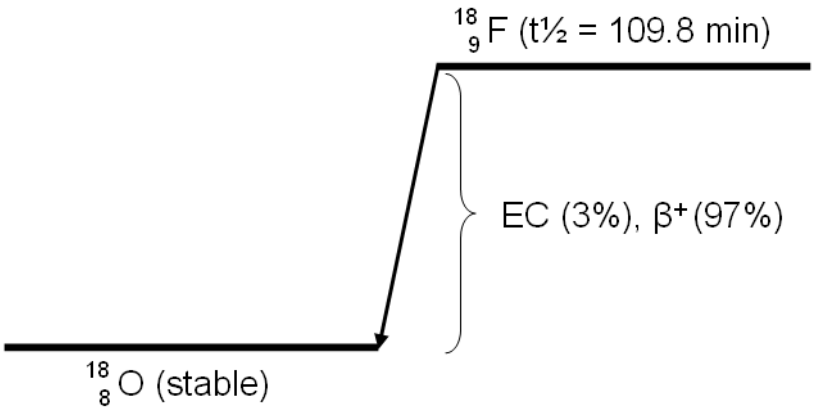

Figure 2.17: Decay scheme diagram for radioactive ^{18}F to its stable material; ^{18}O, which decays by both electron capture; EC, and positron emission; β^+ (t½; half-life).

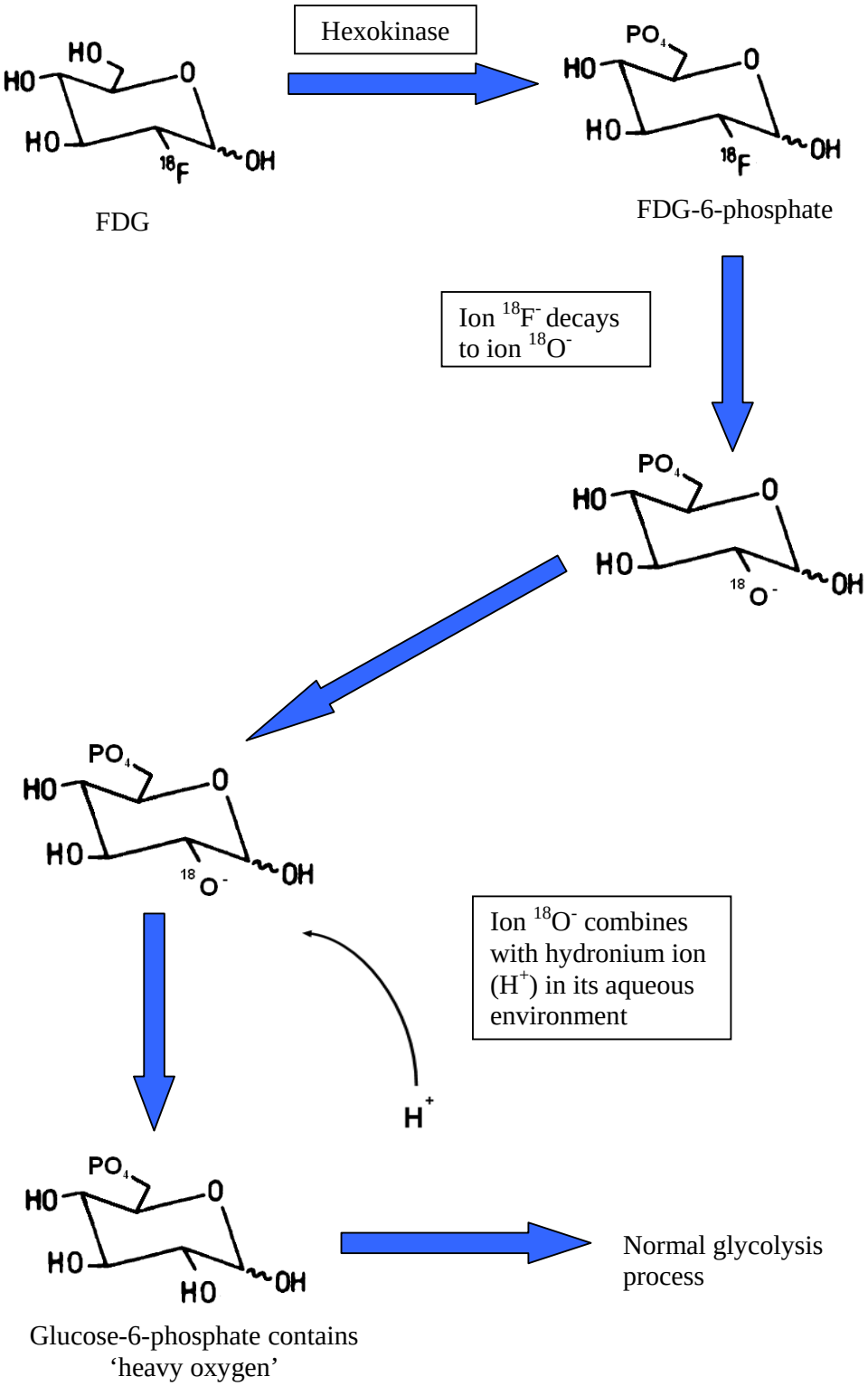

Figure 2.18: Schematic illustration for the biochemical pathway of FDG in the living cell.

2.5. Standardised Uptake Value (SUV)

Although visual assessment of PET and PET/CT fusion images is often sufficient for image analysis and interpretation, the quantitative image analysis using the standardised uptake value (SUV) is also commonly used to augment the finding by measuring the degree of FDG uptake on the area of the suspected lesion. SUV is a semiquantitative measurement that normalises the measured radioactivity concentration in a tissue to the body weight and total injected radioactivity [53], and a unitless ratio [32]; as in Equation 2.6.

$$SUV = \frac{Measured\ radioactivity\ concentration\ in\ a\ lesion\ (kBq/mL)}{Total\ injected\ radioactivity\ (kBq)\ /\ Body\ weight\ (g)} \quad (2.6)$$

The concentration of radioactivity is assumed to be uniformly distributed throughout the body [54]. Therefore, this value can be easily determined by marking the region of interest (ROI) at the desired area of the PET and PET/CT fusion images. SUV has also been known as an index of glucose metabolism which represents the amount of FDG uptake in a given ROI in relation to the average uptake throughout the body [55]. Indeed, this semiquantitative method is widely used to assess the metabolic activity in a lesion.

SUV value of more than 2.5 to 3.8 is frequently used as a cut-off value for differentiating between malignant and inflammatory/infectious lesions on PET and PET/CT fusion images [1-3]. This technique has been the preferred method for quantitative PET and PET/CT imaging as it is reproducible, practical and time-saving [56, 57]. Nevertheless, the clinical cut-off value for SUV based evaluation of PET and PET/CT fusion images is still a matter of debate, mainly due to the problems in defining

the normal values and threshold levels between the two main groups of lesions (malignant and inflammatory/infectious) [29]. In addition, several factors like the patient's serum glucose levels, insulin levels, the scanning time (time interval between FDG injection and image acquisition) and partial volume effects in PET imaging can significantly affect the accuracy of SUV [55, 58-61]. However, in the recent clinical study, it has been reported that the image analysis using SUV may result in more reliable diagnosis as compared to the visual assessment [62].

2.6. Common PET/CT image artifacts and the potential solutions

As mentioned earlier in section 2.3, PET/CT imaging system offers several advantages over a dedicated PET scanner. However, this integrated imaging modality still has some drawbacks especially in respect to the image artifacts. Improved knowledge and awareness of PET/CT image artifacts could play an important role towards producing more accurate image analysis and interpretation. This may in turn aid the nuclear medicine physicians and/or the nuclear medicine technologists in performing the scan in the best conditions possible, and thus, avoiding the repetition of the scan. PET/CT image artifacts mainly arise from the application of CT images for calculating the PET attenuation correction factors [42]. Accordingly, all these artifacts are categorised into four different groups, depending on their causes [42]: a) metallic implants, b) respiratory motion, c) contrast media, and d) truncation.

Metallic implants such as dental fillings, hip prosthetics and/or chemotherapy ports can generate streaking artifacts on CT images, which then results in the high PET attenuation coefficient values. This kind of artifacts will lead to an overestimation of the PET tracer uptake, and it may potentially cause false positive PET/CT findings. In order

to overcome this problem, an interpretation using non-attenuated PET images has been recommended [63, 64]. Furthermore, by asking the patient to remove all metallic objects before commencing the imaging scan, and documenting the location of nonremovable metallic objects, these approaches may help in identifying the source of the artifacts [42].

Respiratory motion artifact occurs due to the inconsistency of chest position during the PET and CT image acquisitions [42]. This misregistration artifact (also known as curvilinear cold area) is usually seen at the base of the lung [65]. This issue can be addressed sufficiently by reviewing the CT images for any anatomical abnormality, and a proper breathing instruction may also possibly reduce the occurrence of this image artifact [42].

Similar to the metallic implants, the application of contrast media (administered either through intravenous injection or oral) during the CT scan of PET/CT imaging can cause an artifact on PET images, in which it may result in false positive findings [66, 67]. However, instead of utilising the non-corrected PET images during the image interpretation, the proper patient's schedule can also help in reducing the occurrence of this artifact; by allowing the time gap (up to several days) particularly for those patients who have recently undergone the contrast-enhanced CT (CECT) scan [42].

For the truncation artifact, it is more frequently seen in large patients or when the scanning is performed with patient's arms down [68]. This artifact occurs due to the difference in the size of the field of view (FOV) between the CT and PET scanners: 50 cm vs. 70 cm [42, 68]. Truncation artifact may also cause an overestimation of the SUV value [68]. As a solution to this hitch, therefore patient needs to be carefully positioned at the centre of the PET/CT FOV with the arms at above of the head [42].

2.7. Tuberculosis

Apart from being routinely used in the imaging diagnosis of various malignancies, FDG PET/CT scan has also been found to be a valuable imaging technique for detecting many inflammation/infection diseases [4]. As highlighted in Chapter 1, the main focus of this thesis is to identify the potential role of FDG PET/CT imaging in the detection of a special type of tuberculosis infectious disease; extrapulmonary tuberculosis (EPTB). Thus, the current issues and practice pertaining to tuberculosis need to be addressed.

Tuberculosis (TB) remains one of the deadliest diseases in the world [69]. It is an airborne infectious disease, which caused by *Mycobacterium tuberculosis* infection. Even though the cause of TB was first identified by Robert Koch over than one century ago [70], it remains to be a major cause of morbidity and mortality, particularly in developing countries [18, 70]. In the most recent annual TB report published by World Health Organisation (WHO), Regional Office for the Western Pacific, there were an estimated about 3.5 million prevalent cases of TB in the Western Pacific Region (WPR), which consist of more than 1.9 million new TB cases [71]. In addition, the following four countries were respectively ranked from first to fourth for all incident cases: 1) China, 2) Philippines, 3) Vietnam, and 4) Cambodia. These four countries accounted for 93% of the total estimated incidence in the WPR. Indeed, the highest mortality rate was notified in Cambodia (89 cases per 100 000 population), while the lowest were in Australia and New Zealand (1 case per 100 0000 population) (refer to Fig. 2.19).

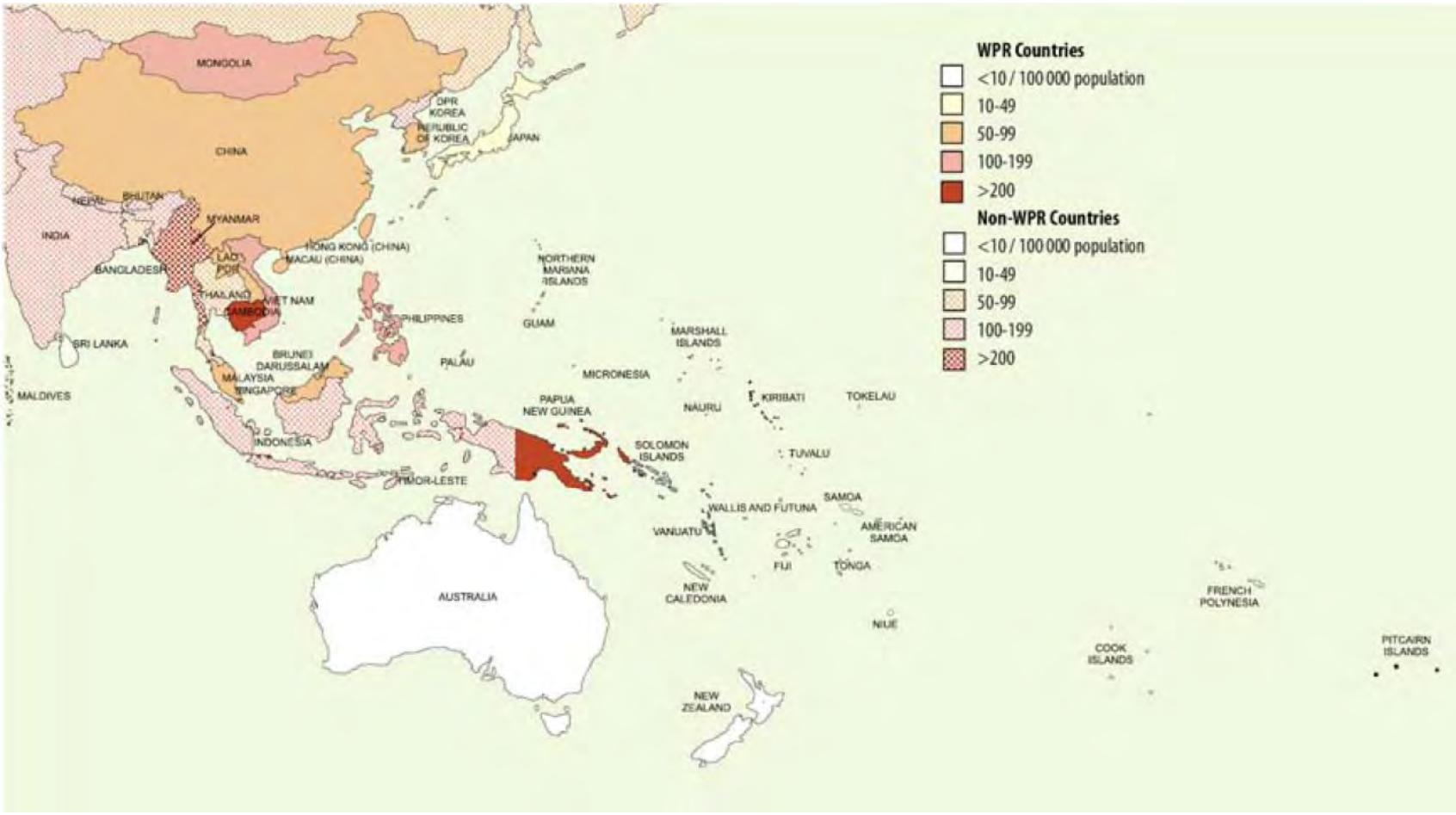

Figure 2.19: Case notification rates per 100 000 population, for all forms of TB cases in the countries and areas in the Western Pacific Region (WPR) and the neighbouring countries and areas [71].

2.7.1. Tuberculosis in Malaysia

TB also plays a major role in a developing country like Malaysia. It is an endemic disease [72] and can be considered as one of the most deadly infectious diseases in this country [73]; with a steady increasing pattern in the annual notified new TB cases [74]. As an intermediate TB burden country [75], in 2007, a total of 16 918 cases were notified with an estimated incidence rate per 100 000 population of about 103 [71]. The state with the highest disease burden was Sabah (3433 cases), followed by Selangor (2484 cases) and Sarawak (1705 cases), respectively [73]. In terms of gender, males outnumbered females with more than double in percentage (67.9% vs. 32.1%), and about 56.6% cases were in the patients with an age range of 25 – 54 years old [73].

TB is able to spread to any organ system in the body [12], thus it can be categorised into two different types, depending on the site of the lesion: (a) pulmonary, and (b) extrapulmonary; the term 'extra' describes the isolated occurrence of TB at the other body sites, excluding the lung. Extrapulmonary tuberculosis (EPTB) occurs in 5 – 20% of all TB cases [12, 76]. Generally, patients with EPTB are often presented with non-specific symptoms such as fever, anorexia, weight loss, malaise (discomfort) and fatigue, but these symptoms can also vary accordingly to the affected site [16].

In 2007, a total of 2107 new EPTB cases were recorded, which corresponded to about 13% from all notified TB cases [71] (refer to Fig. 2.20). The most common forms/sites of EPTB in Malaysian patients were reported to be the lymph nodes, bone and joint, and miliary TB [74]. In addition, according to the latest Malaysia's TB profile, the incidence of EPTB infectious disease has shown an increasing pattern [77]. Thus, this issue implies a significant importance for early detection and accurate diagnosis of EPTB.

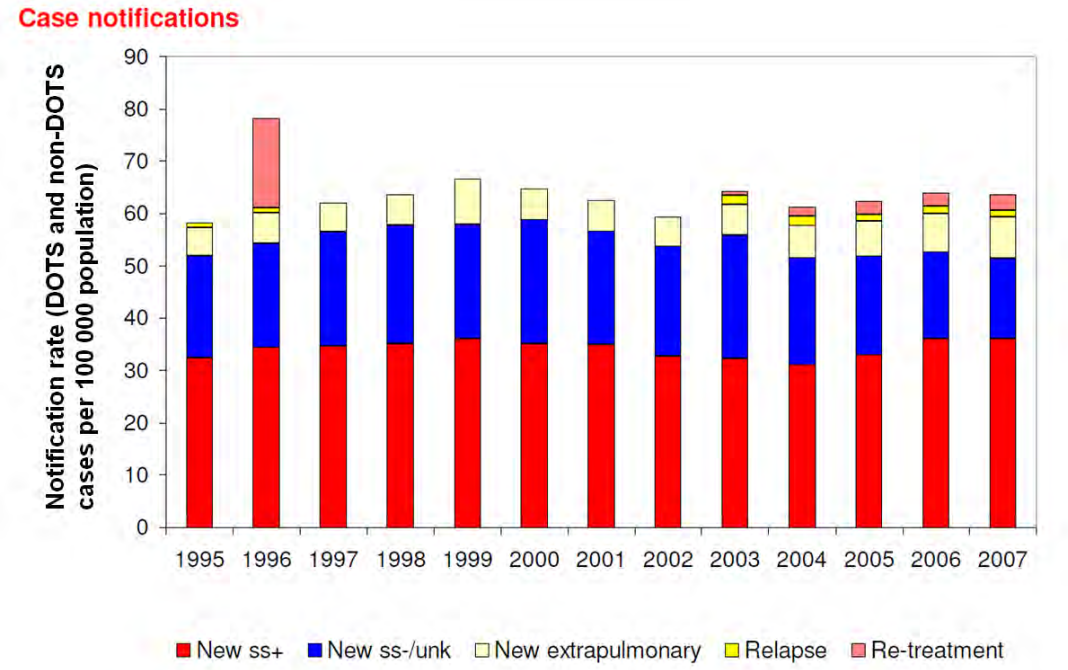

Figure 2.20: Tuberculosis profile for Malaysia. The notified cases were recorded from 1995 to 2007. *DOTS: Directly Observed Treatment Short-course, ss+: smear positive, ss-/unk: smear negative/unknown causes* [78].

2.7.2. Pathogenesis of tuberculosis in human

Mycobacterium tuberculosis (also known as tubercle bacillus) is an aerobic pathogen, and therefore it is more likely to become established in a tissue with high oxygen saturation such as the lung [10]. The tubercle bacilli (plural for tubercle bacillus) enter the human body via the respiratory route. The pathogenesis of TB in humans has been well documented and explained in the literature [10, 16, 79], and it can be divided into five stages [79] (refer to Fig 2.21 for the schematic illustration).

Stage 1 begins when the bacilli implant into the alveolus of the lung. As the first line of defence mechanism, the pulmonary alveolar macrophages will subsequently ingest and often destroy the bacilli through the phagocytosis process. However, the

bacilli that survive from the initial attack will multiply intracellularly until the macrophage ruptures; this is the beginning of *stage 2*. The dying macrophage will release the chemokines, which then attract other alveolar macrophages and monocytes/macrophages arriving from the bloodstream. The macrophages from the bloodstream are nonactivated and immature. Therefore, these macrophages can only ingest the bacilli without destroying them. The bacilli cannot harm the macrophages, and thus develop a symbiotic relationship with the macrophages. Over the time, the accumulation of macrophages and bacilli produce a microscopic tubercle.

Stage 3 is the cessation of the symbiotic stage of bacillary growth with subsequent tissue damage via Delayed Type Hypersensitivity (DTH). This mechanism kills the infected macrophages by damaging the blood vessels, and ends with the formation of a solid caseous centre. This eliminates the favourable intracellular environment for bacillary growth, because tubercle bacilli cannot multiply in solid caseum. Apart from DTH, there is also another process that acts synergistically in controlling the progression of the disease; it is known as Cell Mediated Immunity (CMI), which is responsible for the production of the activated macrophages.

Both CMI and DTH play an important role in *stage 4*. During this stage, the disease may become clinically apparent, and can be seen on the radiograph. If CMI is weak (*stage 4a*), the bacilli can escape from the edge of caseous centre and again multiply intracellularly in nonactivated macrophages, and as usual DTH will kill these infected cells. This results in the enlargement of the tubercle and its caseous centre. At this stage, the bacilli can be disseminated through the blood and lymphatic system, which then produce secondary lesions especially in the hilar lymph nodes, lungs, and other organs. On the other hand, if CMI is strongly developed (*stage 4b*), the escaping

bacilli are ingested and destroyed by highly activated macrophages, and finally ends with the stabilisation and regression of the lesions.

Consequent to *stage 4a*, *stage 5* begins when the solid caseum turns into liquid form; known as liquefied caseum. The bacilli may multiply extracellularly and reach tremendous numbers. The large numbers of bacilli are toxic to the tissues. It causes DTH to erode the nearby bronchial wall and forms a cavity. Then, bacilli in the liquefied caseum are discharged into the airways, and may spread to other parts of the lung and to the outside environment. These bacilli can also be contagious to members of the population.

In humans, it is believed that extrapulmonary dissemination of TB occurs at around two weeks after the initial infection [80]. The normal route for extrapulmonary dissemination of TB is first by the draining into the lymph nodes, then into the thoracic duct and followed by the blood stream [81]. However, it can also directly enter the blood system through the alveolar epithelial barrier or via the sites other than the lung; like the upper respiratory system (nasal cavity, pharynx and larynx) or the digestive system [81]. The following forms/types of EPTB are classified as severe; meningeal tuberculosis, military tuberculosis, pericardial tuberculosis, peritoneal tuberculosis, bilateral or extensive pleural effusion, spinal tuberculosis, intestinal tuberculosis, and genitourinary tuberculosis, whereas tuberculous lymphadenitis, bone tuberculosis (excluding spine), unilateral pleural effusion, peripheral joint tuberculosis, and skin tuberculosis are the less severe types of EPTB [82, 83].

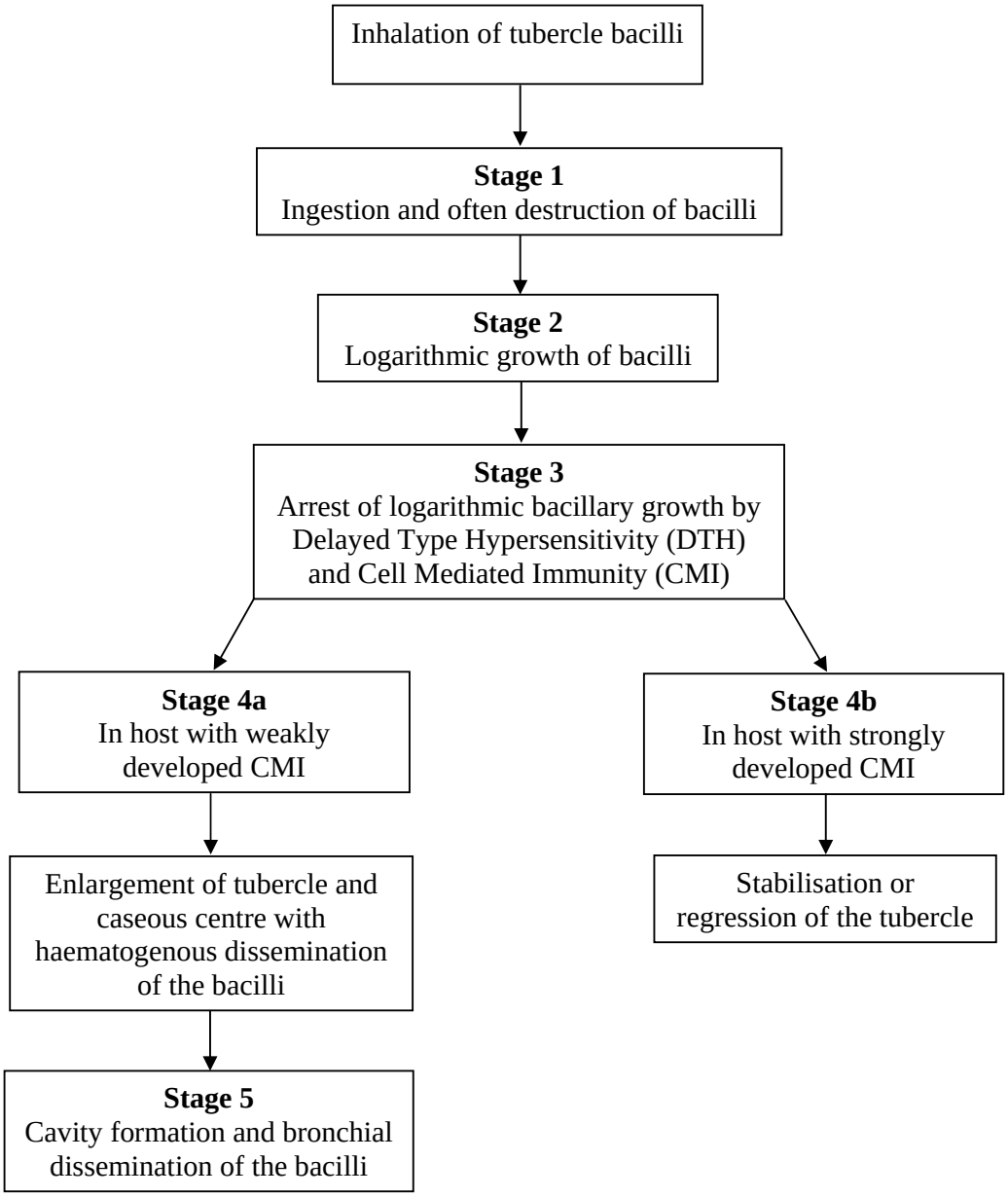

Figure 2.21: Schematic diagram for the pathogenesis of human tuberculosis [79].

2.7.3. Diagnosis of tuberculosis

Early identification and diagnosis are the main elements for effective control of TB [84]. The definitive diagnosis of TB is mainly based on the microscopic demonstration of Acid-Fast Bacilli (AFB) and culture isolation and identification of *Mycobacterium tuberculosis* in sputum or other clinical samples [84-86]. This involves a series of procedures that employ special reagents and techniques [69], but most of them suffer from either lacks of sensitivity and specificity [84, 85], or time consuming [69, 84, 85]. To develop clear understanding on the diagnosis process of TB, it can be divided into three major components: (1) clinical, (2) bacteriological, and (3) radiological.

2.7.3.1. Clinical diagnosis

The clinical diagnosis of TB is based on the clinical signs and symptoms. A person is suspected to have pulmonary TB, if he/she presents with either one or the combination of the following classical signs and symptoms [82]:

- Persistent of cough for more than two weeks
- Cough with sputum which occasionally contains blood; haemoptysis
- Low-grade fever
- Loss of weight and loss of appetite
- Difficulty in breathing; dyspnoea
- Night sweats
- Chest pain
- Hoarseness or loss of voice

These symptoms are however non-specific [86], and in fact, patients with active pulmonary infections may also be asymptomatic [18]. The haematological signs such as an elevated peripheral blood leukocyte count and a mild anaemia can also be correlated with TB [86]. On the other hand, the signs and symptoms for EPTB are also found to be non-specific [15] and vary according to the affected sites or tissues [16]. Therefore, in 2005, an effort in listing all signs and symptoms of EPTB was made by Golden and Vikram [87], as in Table 2.4.

Table 2.4: Clinical signs and symptoms of EPTB [87].

Signs and symptoms of EPTB
1. Ascites with lymphocyte predominance and negative bacterial cultures
2. Chronic lymphadenopathy (most common cervical node)
3. Cerebrospinal Fluid (CSF) lymphocytosis with elevated protein and low glucose
4. Differential diagnosis of Crohn's disease and amebiasis
5. Exudative pleural effusion with lymphocyte predominance and pleural thickening
6. Human Immunodeficiency Virus (HIV) infection
7. Monoarticular joint inflammation with negative bacterial cultures
8. Persistent sterile pyuria with or without haematuria
9. Tuberculosis-endemic country of origin
10. Unexplained pericardial effusion, constrictive pericarditis or pericardial calcification
11. Vertebral osteomyelitis involving the thoracic spine

2.7.3.2. Bacteriological investigations

Bacteriological or laboratory investigations for TB comprise many types of microscopic tests, and the most widely used and available method is the tuberculin skin test (also known as Mantoux test) [69]. It is based on the fact that infection with *Mycobacterium tuberculosis* produces a Delayed Type Hypersensitivity (DTH) reaction to certain

antigenic components of the organism that are contained in extracts of culture filtrates called ‘tuberculins’ [69]. This test is usually carried out by injecting 0.1 mL of the standard 5 tuberculin unit dose of purified protein derivative (5-TU PPD) into the dorsal surface of the forearm [69]. However in Malaysia, the standard dose for tuberculin skin test is only 2-TU [82]. The test is read 72 hours after injection, and the interpretation of the result is based on the diameter of induration, which can be divided into 3 categories:

1. Diameter of less than 10 mm (<10 mm) is considered to be a negative result, but this does not exclude a diagnosis of TB.
2. Diameter of 10 mm or more (≥10 mm) is classified as positive result.
3. Diameter of 15 mm or more (≥15 mm) may indicate recent infection.

In a patient who has a sputum-producing cough, the main diagnostic procedure consists of direct sputum smears for acid fast bacilli (AFB) [82, 86] and culture examination of three sputum specimens collected on different days [69, 82, 86]. The sputum smear is the easiest and quickest method, which provides the physician with a preliminary confirmation of TB [69]. There are two commonly used methods for AFB staining [69, 86]:

1. The carbolfuchsin method (include Ziehl-Neelson and Kinyoun methods), which will be used in combination with light microscope [86].
2. A fluorochrome procedure using auramine-rhodamine dye in combination with fluorescent microscope [86].

On the other hand, the culvitation of mycobacteria from the sputum and other clinical specimens requires a longer time; up to 8 weeks [69, 82], primarily because of

the slow growth rate of tubercle bacilli [18, 86]. As TB may occur in almost any site in the body (especially for EPTB and disseminated/ miliary TB cases); therefore many kinds of clinical specimens can be collected and sent for laboratory examinations like gastric aspirate, urine, cerebrospinal fluid, pleural fluid, peritoneal fluid, pericardial fluid, other biopsy specimens or resected tissue and cold abscess pus [12, 69]. Gastric aspiration may be necessary in particular for children and those patients who cannot produce sputum even though has been induced with aerosol inhalation [69]. Urine smears and culture examinations are usually negative, but it is mandatory in patients who are suspected with genitourinary tuberculosis [12].

When non-invasive techniques have not provided a definite diagnosis, invasive procedures such as percutaneous needle biopsy or aspiration, transbronchial biopsy, bone marrow biopsy, lung biopsy and liver biopsy should be conducted to procure tissue and/or other body fluids (including the pus aspirated from cold abscess) for culture investigation and histological evaluation [12, 69]. Automated culture system such as BACTEC (Becton Dickinson Microbiology Systems, Sparks, MD) represents a major improvement in the technology of mycobacterial identification [69, 86]. It allows the detection of *Mycobacterium tuberculosis* growth within 2 weeks [82, 86].

Polymerase Chain Reaction (PCR) is one of the nucleic acid amplification techniques, which aims for a rapid detection and identification of *Mycobacterium tuberculosis* from various clinical specimens, without the need for the culture examination [86, 88]. In fact, many studies show that PCR yields a higher sensitivity when compared to other laboratory examinations [85, 88, 89]. Consequently, PCR could be considered as an important microbiological test in the diagnosis of TB, particularly

for EPTB [12]. This test could also allow quick implementation of anti-tuberculous drugs treatment.

2.7.3.3. Radiological examinations

The radiological imaging for detecting TB usually consists of a multi-modality approach, from general radiographic to sectional and/or functional imaging modalities. Chest radiographs play a major role in the screening, diagnosis and monitoring the treatment response of patients with TB [18]. The pattern of disease on chest radiographs can be described either as primary TB or post-primary TB [18, 90]. Primary TB pattern represents the infection resulting from recent contact with *Mycobacterium tuberculosis*, whereas for post-primary TB pattern, it results from reactivation of a dormant focus within the lungs [90].

In primary TB, there are few signs that can clearly be seen on a chest radiograph such as pleural effusion (usually unilateral), parenchymal consodilation, and hilar or mediastinal lymphadenopathy [18, 90]. However, all of these imaging features are better depicted on CT images, which is more sensitive than chest radiograph [18, 90]. The parenchymal consodilation is most commonly dense and homogenous on CT images [18]. In addition, contrast-enhanced CT (CECT) images may demonstrate the enlarged lymph nodes with a typical central low attenuation (which represents caseous necrotic centre) and peripheral rim enhancement (which represents the vascular rim of the granulomatous inflammatory tissue) [18, 90, 91]. This pattern is strongly suggestive for TB [90].

For post-primary TB (also called as reactivation TB), the most common radiographic characteristic is focal or patchy heterogenous consodilation involving the

apical and/or posterior segments of the upper lobes, and/ or superior segment of the lower lobes [86]. Cavitation is the radiologic hallmark for the reactivated TB patients [18, 90]. Furthermore, the presence of endobronchial spread is also common in post-primary TB, and it appears as centrilobular small nodules with branching linear and nodular opacities (tree-in-bud sign) on CT images [92]. Both cavitation and tree-in-bud sign are the reliable indications for the active process of TB infection [18, 93]. The utilisation of PET scan can also help in detecting the tuberculous nodules [94, 95].

Similarly, for the imaging diagnosis of EPTB patients, the radiological investigations are mainly based on the sites of the involvement like lymph nodes, pleural cavity, abdomen, bone and joint, and central nervous system. All the imaging studies that relate to a particular EPTB infectious disease are highlighted and summarised in Table 2.5.

Table 2.5: Summary of the radiological examinations for several types of EPTB.

Types of EPTB	Radiological examinations
Tuberculous lymphadenitis	Chest radiograph [16, 87] and CECT [12]
Pleural tuberculosis	Chest radiograph [12, 16, 87] and chest CT scan [87]
Abdominal tuberculosis: a) gastrointestinal tuberculosis	Barium studies like small bowel barium meal and barium enema [96], and abdominal CT scan [87, 96]
b) peritoneal tuberculosis	Ultrasonography of the abdomen [16, 96] and abdominal CT scan [16]
c) genitourinary tuberculosis	Chest and abdomen radiographs [16], intravenous pyelography [12], percutaneous nephrogram [12] and abdominal CT scan [16, 87]
Bone and joint tuberculosis: a) spinal tuberculosis	Spine radiograph [16, 87], CT and MRI scans of the spine [12, 16, 87]
b) articular tuberculosis	Joint radiograph [87]
Central nervous system tuberculosis	CECT scan of the head [12, 16, 87] and gadolinium enhanced MRI scan of the brain [12]
Miliary tuberculosis	Chest radiograph [12, 87], chest CT scan [12, 87] and HRCT scan of the chest [12]
MRI; Magnetic Resonance Imaging, CECT; Contrast-enhanced Computed Tomography, HRCT; High Resolution Computed Tomography.	

2.7.3.4. Other diagnostic techniques

Few other diagnostic techniques are also clinically important, and they may help in the diagnosis of EPTB infectious disease such as echocardiography for pericardial tuberculosis [12] and colonoscopy for gastrointestinal tuberculosis [96]. In addition, recent study has found that optical imaging using fluorescent proteins can demonstrate the extrapulmonary spread of tuberculosis in a living animal [81], therefore it has been believed that this new technique could serve some potential benefits for human study in the near future.

2.7.4. Treatment of tuberculosis

TB can be completely curable through short-course chemotherapy. Directly observed treatment short-course (DOTS) is highly efficient and cost-effective, and it has been accepted as an international recommendation strategy for controlling TB infectious disease, regardless of either for PTB or EPTB [83]. According to the latest TB report from WHO, Malaysia had been reported to have a 100% DOTS coverage, and the overall treatment success rate for the WPR was about 92%, which was beyond the target of 85% [71]. Basically, the treatment of TB has five different aims, which are as the following [83]:

1. To cure the TB patient.
2. To prevent death form active TB or its late effects.
3. To prevent relapse of TB.
4. To decrease transmission of TB to others.
5. To prevent the development of acquired drug resistance.

Five drugs are considered as the essential first-line drugs for anti-tuberculous treatment: isoniazid (H), rifampicin (R), pyrazinamide (Z), streptomycin (S), and ethambutol (E) [86]. In Malaysia, the treatment for a new PTB/EPTB patient consists of a six months regimen , which can be divided into two different phases: (1) 2 months of intensive phase and (2) 4 months of continuation phase [74, 82]. During the intensive phase, patient will be prescribed with daily doses of S or E, H, R and Z, and followed by biweekly doses of H and R, or S, H and R for the continuation phase [15, 74, 82]. However, this continuation phase may be further extended particularly for severe forms of EPTB and immunocompromised patient. The patient management for the 6 months or 24 weeks period of the anti-tuberculous drugs treatment is summarised in Figure 2.22.

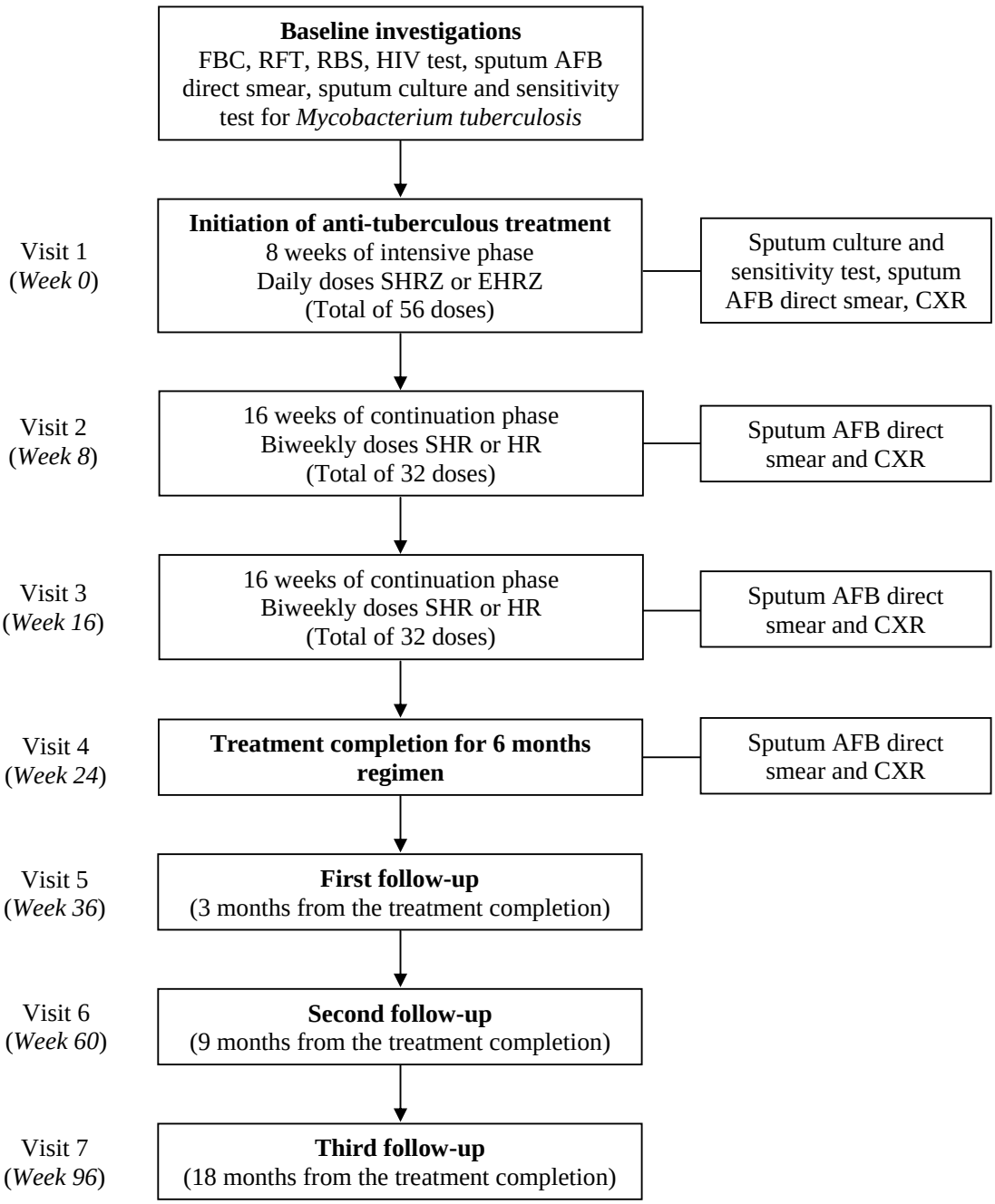

FBC; Full Blood Count, RFT; Renal Function Test, RBS; Random Blood Sugar, HIV; Human Immunodeficiency Virus, AFB; Acid-Fast Bacilli, S; streptomycin, H; isoniazid, R; rifampicin, Z; pyrazinamide (Z), E; ethambutol and CXR; chest x-ray.

Figure 2.22: Flow chart of 24 weeks or 6 months anti-tuberculous treatment in an adult patient [15, 82].

SECTION A

CLINICAL IMAGING

STUDY

This section A (Clinical imaging study) is divided into two parts:

1. Section A1: Background and the scanning methods.
2. Section A2: Results and discussion.

Each of these two parts is described in a separate chapter; Chapter 3 for section A1 and Chapter 4 for section A2, respectively.

CHAPTER 3

SECTION A1:

BACKGROUND AND THE SCANNING METHODS

This clinical trial is an important study of this research thesis. This chapter describes and details the FDG PET/CT scanning protocols of sixteen Malaysian patients, who were prospectively recruited for the trial. In addition, the retrospective data of FDG PET/CT imaging for twelve Italian patients who had a confirmed diagnosis of EPTB were acquired. The findings of these two datasets were analysed and compared. Overall, this chapter only covers the methodological aspects of all FDG PET/CT scans.

3.1. Background

As stated above, there are two datasets from two different patient populations involved in this clinical imaging study:

1. Prospective data of Malaysian patients.
2. Retrospective data of Italian patients.

For both populations, FDG PET/CT imaging was performed during the diagnosis procedure of the disease. First, details of the patient's preparation, scanning protocols of FDG PET/CT imaging and the image interpretation for Malaysian patients are explained and followed by those of Italian patients. However, due to *complicated circumstances*[*], only few Malaysian patients had undergone repeat FDG PET/CT scan with an interval of about six months from their initial diagnostic PET/CT scan. This repeated scan is termed as follow-up FDG PET/CT scan, and it will be further described in section 3.2.3.

[*] This phrase is mainly used to indicate that of all recruited Malaysian patients, some of them were categorised as defaulted and few patients refused to undergo repeat FDG PET/CT scan because of clinically well progressing with the given treatment. In addition, one patient died during the diagnosis process.

Numerous studies have demonstrated that the application of a special imaging technique known as dual time point imaging (DTPI) during both FDG PET and FDG PET/CT scans could enhance the differentiation between benign (including inflammatory and infectious) and malignant lesions [21-23, 97-105]. This DTPI technique means the image acquisitions are performed twice; initial and delayed scans, with a certain interval between the two scans. Furthermore, this technique was found to be useful for evaluating the activity status of a lesion in malignant and infectious diseases [106-112]. Based on these two advantages, it has been hypothesised that the use of DTPI technique during FDG PET/CT scan could increase the diagnostic values of this hybrid imaging modality in detecting and determining the lesions of the prospective Malaysian patients. The technical data primarily on the interval between each of the scans for all the referred studies are listed and summarised in Tables 3.1 and 3.2.

Aside from DTPI technique, the utilisation of an intravenous iodine-based contrast media during the CT scan of PET/CT imaging may offer some potential benefits, by providing more diagnostic information that is closely related with the enhancement of a lesion [113]. Indeed, CT (CECT) images have been found to increase the sensitivity and accuracy of detecting and characterising the lesions [114]. On the other hand, few reports state that when CECT data is used for calculating the PET attenuation correction factors, it will lead to the overestimated values [115-117], which then may cause false positive findings [66, 67]. However, the changes in the SUVs of PET and PET/CT fusion images were found to be clinically insignificant [5, 113, 118-122]. Therefore, this CECT scan has also been carried out during FDG PET/CT imaging of all recruited Malaysian patients.

Table 3.1: Chronological application of DTPI technique during FDG PET and FDG PET/CT scans in distinguishing malignant from benign lesions.

Author	Year	Initial scan acquisition (after injection of FDG)	Delayed scan acquisition (after injection of FDG)	Imaging modality
Hustinx, *et al.* [97]	1999	70 min (range, 47 – 112 min)	98 min (range, 77 – 142 min)	PET scanner
Nakamoto, *et al.* [98]	2000	60 min	120 min	PET scanner
Kubota, *et al.* [99]	2001	60 min	120 min	PET scanner
Zhuang, *et al.* [100]	2001	48 – 63 min	89 – 128 min	PET scanner
Matthies, *et al.* [101]	2002	69 min (range, 55 – 110 min)	122 min (range, 100 – 163 min)	PET scanner
Demura, *et al.* [102]	2003	60 min	180 min	PET scanner
Kumar, *et al.* [103]	2005	63 min	101 min	PET scanner
Xiu, *et al.* [104]	2007	58 min (range, 50 – 110 min)	114 min (range, 99 – 163 min)	PET scanner
Lan, *et al.* [23]	2008	45 – 55 min	150 – 180 min	PET/CT scanner
Alkhawaldeh, *et al.* [105]	2008	60 min	100 min (range, 90 – 110 min)	PET scanner
Suga, *et al.* [21]	2009	60 min (range, 56 – 65 min)	120 min (range, 110 – 131 min)	PET/CT scanner
Suga, *et al.* [22]	2009	60 min (range, 56 – 65 min)	120 min (range, 110 – 131 min)	PET/CT scanner

Table 3.2: Chronological application of DTPI technique during FDG PET and FDG PET/CT scans in assessing the activity status of a lesion.

Author	Year	Initial scan acquisition (after injection of FDG)	Delayed scan acquisition (after injection of FDG)	Imaging modality
Higashi, *et al.* [106]	2002	60 min	120 min	PET scanner
Nishiyama, *et al.* [107]	2006	62 min	146 min	PET scanner
Mavi, *et al.* [108]	2006	63 min (range, 46 – 112 min)	104 min (range, 81 – 156 min)	PET scanner
Kim, *et al.* [109]	2008	60 min (range, 53 – 71 min)	120 min (range, 109 – 131 min)	PET/CT scanner
Nishiyama, *et al.* [110]	2008	60 min	120 min	PET scanner
Zytoon, *et al.* [111]	2008	55 – 60 min	110 – 120 min	PET/CT scanner
Zytoon, *et al.* [112]	2009	55 – 60 min	100 – 120 min	PET/CT scanner

3.1.1. Malaysian patients

This prospective clinical trial was conducted from July 2008 to March 2009. A total of sixteen patients (nine men and seven women) who were highly suspected for extrapulmonary tuberculosis (EPTB) infection; based on the clinical signs of EPTB [87] or family history of TB and/or previously diagnosed with EPTB, were enrolled and evaluated (refer to Table 3.3). Their mean ± SD for age, height and weight were 35 ± 16 years (range 15 – 60 years), 161 ± 7 cm (range 148 – 173 cm) and 61 ± 13.8 kg (range 30.8 – 93.5 kg), respectively. All patients were from the teaching hospital of University Putra Malaysia, whom presented with a variety of non-specific clinical signs and symptoms like malaise (discomfort), low grade fever, lassitude (fatigue), weight loss and body ache. All of them underwent extensive clinical, radiological and histopathological investigations. However, none were on anti-tuberculosis drugs treatment at the time of FDG PET/CT scanning.

This research was approved by the ethics committee for human research at University Putra Malaysia and Ministry of Health Malaysia (Appendices 1 and 2). Details of the imaging protocol were explained by the physician in charge, and a written informed consent was obtained from all patients (Appendices 3 and 4).

As the gold standard of this study, the laboratory/microscopic findings (including the biopsy results) are required to attain a definitive diagnosis. If these findings are found to be inconclusive for TB, radiological and/or clinical assessment of the given treatment during the periodic follow-up visits could also play a major role in making the final diagnosis. The exclusion criteria are claustrophobia, severe obesity and linguistic/communication problems.

Table 3.3: Demographic data and clinical indications of all Malaysian patients.

Patient no.	Gender	Age	Weight (kg)	Height (cm)	Clinical indications
1	Female	26	93.5	159	Right neck and mediastinal nodes enlargement
2	Male	49	72	164	Backache
3	Female	22	60.5	148	Left submandibular lymphadenopathy
4	Male	53	58	172.5	Right hip pain
5	Female	31	56.4	160	Backache
6	Male	17	44	162	Anorexia
7	Male	28	60	158	Severe headache and poor general health condition
8	Female	19	55	154	History of tuberculous lymphadenitis and right anterior chest wall swelling
9	Female	24	30.8	153.5	Poor general health condition and anorexia
10	Female	29	77.8	161	Right neck pain and swollen, and low grade fever
11	Female	25	54	153	Left lateral neck swollen
12	Male	15	60.4	173	Heel pain and swollen with fluid collection
13	Male	51	68.4	164.5	Left knee joint pain
14	Male	59	60	170	Backache
15	Male	60	60	160	Severe backache
16	Male	55	65	163	Severe backache

3.1.2. Italian patients

The retrospective data of twelve confirmed EPTB patients, who underwent FDG PET/CT imaging between June 2007 and February 2008, were reviewed and evaluated (refer to Table 3.4). These data were from the Nuclear Medicine and PET/CT Centre of Ospedale Niguarda Ca' Granda, Milan, Italy and the Nuclear Medicine Department of Ospedale Santa Corona, Pietra Ligure, Italy. However, only FDG PET/CT imaging data were obtained for these patients, with no other details in their clinical information, mainly due to limited accessibility and a high patient privacy and confidentiality.

Table 3.4: Demographic data and date of the FDG PET/CT acquisition of Italian patients.

Patient no.	Gender	Age	Date of scanning
1	Male	74	June 7, 2007
2	Female	55	December 13, 2007
3	Female	39	February 20, 2008
4	Male	67	August 22, 2007
5	Female	59	July 31, 2007
6	Male	45	September 19, 2007
7	Female	54	January 16, 2008
8	Female	70	September 11, 2007
9	Male	76	August 29, 2007
10	Male	45	July 18, 2007
11	Female	80	July 25, 2007
12	Male	56	January 23, 2008

3.2. FDG PET/CT imaging

The image acquisition for FDG PET/CT scan usually includes the preparations of the patient, the scanning protocols and the image analysis and interpretation. Thus, in this section, each of these matters will be described in detail, particularly for Malaysian patients. However, for the twelve Italian patients, the information is only extracted from the FDG PET/CT imaging data that have been obtained during the image analysis and interpretation processes.

3.2.1. Malaysian patients

3.2.1.1. Patient preparation

All PET/CT examinations were conducted using the imaging facilities at two private hospitals: Prince Court Medical Centre, Kuala Lumpur, Malaysia and Beacon International Specialist Centre, Selangor, Malaysia.

Patients were required to be fasting overnight or at least 8h prior to the scanning day; however oral hydration with plain water was allowed. During the scanning day, the

blood glucose level was firstly checked and it should not exceed the normal range (>7.2 mmol/L; Table 3.5); as the high blood glucose level could affect the semiquantitative measurements of FDG PET and FDG PET/CT images [123]. Subsequently, patients were asked to change into a hospital gown in the preparation room and all their personal belongings were safely kept in a locker.

Based on patient's body weight, the amount of FDG radioactivity to be used was calculated and the preparation of FDG had been conducted in the hot lab (Fig. 3.1). Then, 1 L of negative oral CT contrast media (plain water) was given to those patients who were clinically fit, just before commencing the FDG injection (Fig. 3.2). The injected amount of FDG radioactivity for each patient was about 364 ± 97 mega Becquerel; MBq, (mean ± SD, ranging from 145 – 592 MBq; Table 3.5) which had been administered intravenously (Fig. 3.3). To maximise the injected amount of FDG, an infusion of 100 mL normal saline was applied immediately after the FDG injection. Patients were also administered intravenously with 20 mg of furosemide (Lasix); to accelerate renal excretion of FDG, and 20 mg of butylscopolamine (Buscopan); to reduce abdominal muscles spasm.

Subsequently, patients were asked to rest comfortably for about 55 ± 14 min (mean ± SD, ranging from 30 – 86 min; Table 3.5) in the preparation room. During this uptake period, patients were instructed to restrict their movements including talking; to minimise the potential of false positive FDG uptake in the muscles. Finally, just before entering the PET/CT scanning room, patients were asked to empty their bladder, as the scanning session may consume quite longer time and for maintaining their comfortability.

Figure 3.1: Preparation on the FDG is conducted in the hot lab, which has been equipped with the radioactivity meter. The amount of FDG radioactivity for the whole body PET/CT imaging is estimated based on patient's body weight.

Figure 3.2: A litre of plain water is given to act as negative oral contrast media during the preparation process. This method will help for better bowel distention during the image interpretation procedure [27, 124].

Figure 3.3: Intravenous injection of FDG is performed in the preparation room. Immediately after this injection, an infusion of using 100 mL normal saline is given for maximising the injected amount of FDG or minimising the amount of FDG left in the tube.

3.2.1.2. FDG PET/CT scanning protocols

In general, the scanning protocols of PET/CT imaging in this study are divided into two separate scans:

1. Whole body FDG PET/CT imaging
2. Dual time point imaging (DTPI) of FDG PET/CT scan

As mentioned in Chapter 1, there are no previous studies that have specifically utilised the DTPI technique during FDG PET/CT imaging of EPTB patients. In addition, the application of intravenous iodine-based contrast media on the CT component of FDG PET/CT scan for EPTB patients has not been well documented in the literature. Thus, almost all FDG PET/CT scans of this clinical imaging study were conducted using the DTPI technique and the intravenous injection of iodine-based contrast media.

3.2.1.2.1. Whole body FDG PET/CT scan

All FDG PET/CT scans were acquired using an integrated Biograph PET/CT system (Siemens Healthcare Solutions) which consists of lutetium oxyorthosilicate (LSO) crystal detectors (as of the Fig. 2.13 in Chapter 2). Patient was laid supine on the PET/CT table with both arms positioned above head. To acquire a precise anatomic correlation between PET and CT images, the scanning was performed with the arms in the same position for both PET and CT scans. For minimising technical errors and avoiding the occurrence of misregistration and truncation artifacts [42], the patient's body was carefully positioned using the guidance from longitudinal and horizontal laser beams. The patient was gently fixed to the scanning table by using two strapping belts

placed at the thigh and forearm regions. Immobilisation supports had also been given under patient's head and knee joint (Fig. 3.4).

The PET/CT imaging commenced with a standard CT topogram (110 kV); to define the scanning range (from base of skull to mid-thigh region). The scanning was performed in the cranio-caudal direction. The unenhanced CT scan (also called as low dose CT protocol) was first carried out using the following parameters: 30 mAs, 130 kV, 5 mm slice thickness, 4 mm collimation and 12 mm table feed per rotation. Then, an intravenous bolus injection of 100 mL iohexol (Omnipaque 350 mgI/mL, GE Healthcare) was administered to the patient as a contrast enhancing agent, and the contrast-enhanced CT (CECT) scan was immediately started using the same parameters as in unenhanced CT, but with higher tube current; 100 mAs (diagnostic dose CT protocol), for reducing the effects of the increased in tissue density due to the application of iodine contrast media [125] (Fig. 3.5). Upon completion of the CECT scan, straightaway, a whole body PET emission scan was performed using a three-dimensional (3-D) acquisition mode with the scanning time of 3 minutes per bed position; 6 to 10 bed positions were required depending on patient's height. All these image acquisitions took about 25 – 35 min to be completed.

3.2.1.2.2. Dual time point imaging of FDG PET/CT scan

After the acquisition of a whole body PET/CT scan, the patient was again asked to rest in the preparation room, in order to be made ready for the delayed PET/CT imaging (Fig. 3.6g). This special imaging technique is called dual time point imaging (DTPI) or known as double phase PET/CT. During this period of time, the initial whole body PET/CT images were reviewed and evaluated to confirm the limited regional coverage

(only for the regions where the lesions were detected) for the delayed scan, with 1 to 8 bed positions. Basically, this scanning method is similar to the previous two studies by Suga, *et al.* [21, 22], which it may result in reducing the radiation dose to the patient and increase the throughput capability of the scanner. A delayed PET/CT scan (Fig. 3.6h) was performed after about 136 ± 14 min (mean ± SD, ranging from 120 – 163 min; Table 3.5) from the FDG injection time, by utilising the same PET scanning parameters (3-D acquisition mode with the scanning time of 3 min per bed position) and low dose CT protocol as in the initial whole body PET/CT imaging. To avoid the occurrence of the image artifacts due to high concentration of contrast agent [67], therefore, no additional iodine-based contrast media was used during the CT scan of this delayed PET/CT imaging. In addition, the 2 hours delayed scanning time (from the FDG injection) was reported to be well tolerant among the fasted patients [22], and thus, it had been employed in this study.

During all the image acquisitions (initial whole body and delayed scans), patients were asked to breathe normally, or in other words no special breathing technique was applied in this study. The total scanning acquisition time for each of the patients was about an hour for both initial whole body and delayed scans. After completing these PET/CT scans, all patients had been served with light meal before they were sent back to the hospital.

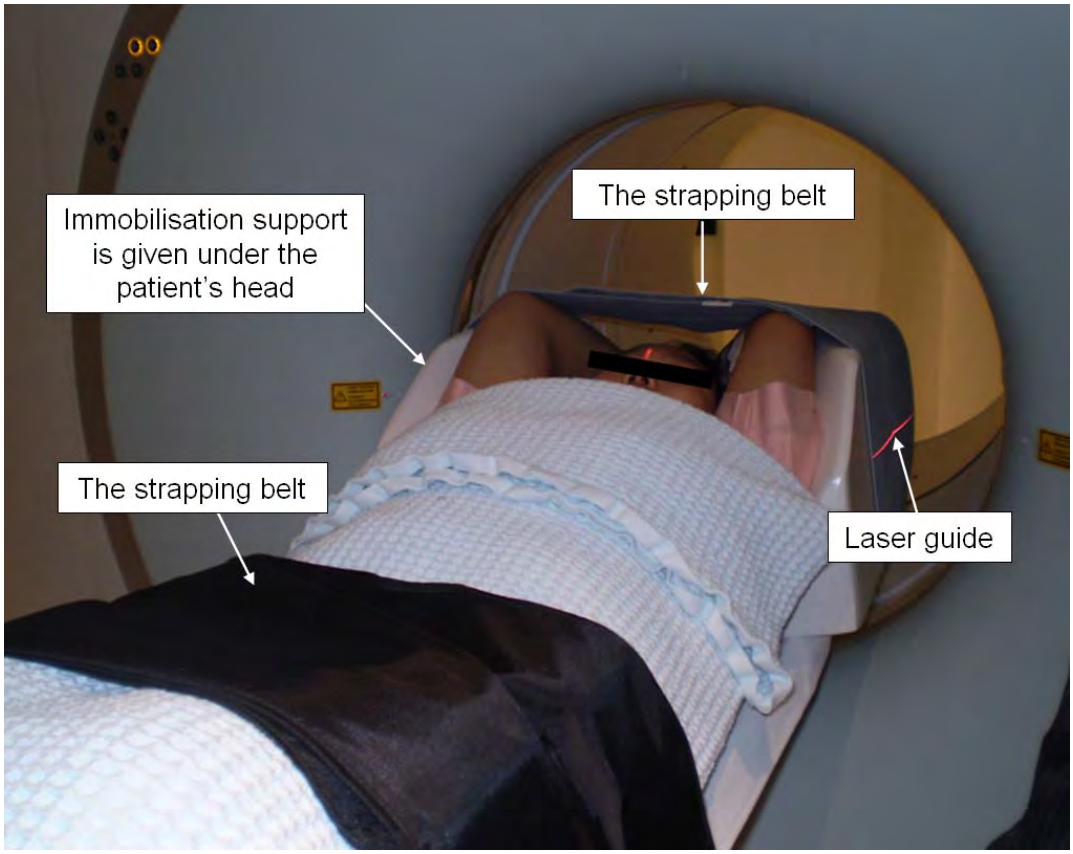

Figure 3.4: Position of the patient during the PET/CT image acquisitions with immobilisation supports under the head and knee joint. Both arms are positioned above the head and two strapping belts are used to minimise patient's movement. Note that two lasers are used for aiding the patient positioning.

Figure 3.5: Intravenous bolus injection of 100 mL iodine contrast media (Omnipaque 350) is given just before performing the contrast-enhanced CT (CECT) scan. This injection utilises the same route as for the FDG injection. After the injection the arm is repositioned at above of the head.

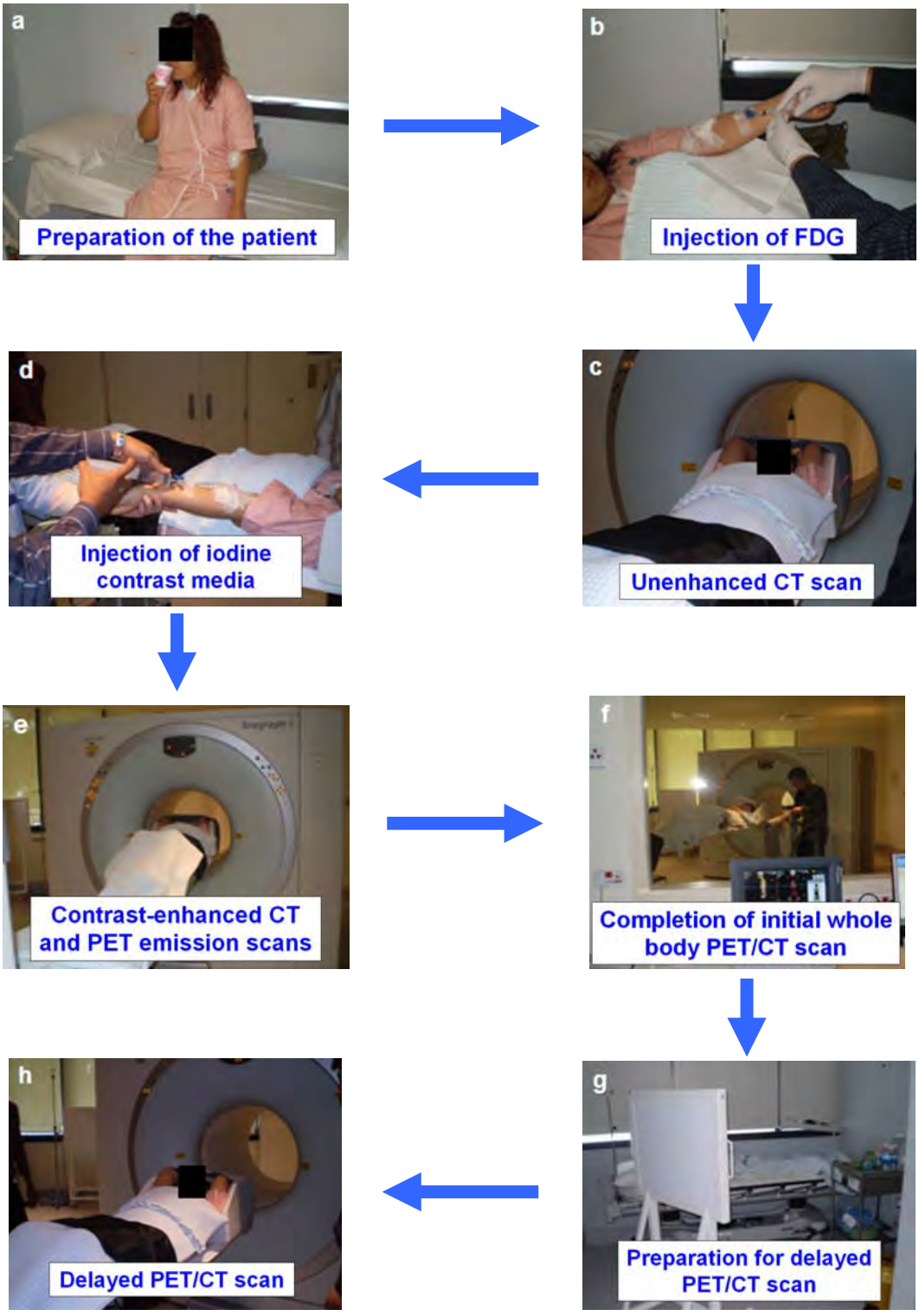

Figure 3.6: Schematic illustration for FDG PET/CT scans of Malaysian patients. (a – f) are the methods involved during the initial whole body PET/CT scan, whereas (g and h) are for the delayed PET/CT scan.

Table 3.5: The blood glucose level, the injected amount of FDG radioactivity and the scanning time of both PET/CT image acquisitions (initial whole body and delayed scans) for all sixteen Malaysian patients.

Patient no.	Blood glucose levels (mmol/L)	Injected FDG radioactivity (MBq)	Initial whole body scan; after the FDG injection time (min)	Delayed scan; after the FDG injection time (min)
1	7.0	592	30	138
2	4.0	419	41	126
3	4.8	277	57	120
4	5.3	322	73	132
5	7.0	337	58	128
6	4.7	145	75	131
7	6.4	382	61	–
8	4.6	361	55	120
9	5.1	383	42	158
10	7.1	500	64	141
11	4.3	368	46	121
12	4.7	375	49	152
13	4.4	346	86	163
14	1.4	272	46	133
15	3.8	354	51	–
16	5.3	383	47	–

MBq, megabecquerel; –, not done.

3.2.1.3. Image analysis and interpretation

For each of the scanning protocols, the image analysis and interpretation are slightly differed. Thus, this section is divided into two subsections:

1. Whole body FDG PET/CT imaging
2. DTPI of FDG PET/CT scan

3.2.1.3.1. Whole body FDG PET/CT scan

As usual, CT images are reconstructed in a 512 x 512 matrix, while PET images are in a matrix of 128 x 128 [42]. Thus, to fuse both of these images, the matrix of CT data need to be resized and matched PET data matrixes, which can either be done on the same

imaging acquisition system or using a different medical imaging workstation, depending on the manufacturer [42]. However, in this study, this process was made on the workstation. Attenuation-corrected PET images were reconstructed iteratively using a in standard protocol with an attenuation-weighted ordered subset expectation maximisation (OSEM) algorithm [126]. Both CT datasets (unenhanced CT and CECT) were utilised for attenuation correction of the whole body PET/CT images, creating two sets of PET/CT fusion images (PET/unenhanced CT and PET/CECT), based on the same set of PET emission data. All images were displayed in axial, coronal and sagittal planes along with maximum intensity projection (MIP) image. MIP image is a common 3-D image used for visualising FDG distribution throughout the body [32].

The image analyses were visually and semiquantitatively interpreted by an experienced radiologist. In the visual assessment of PET/CT images, the intensity of FDG uptake in the lesion was scored using a 4-point grading system: normal background uptake (grade 1), mild uptake as in liver or spleen (grade 2), higher uptake than liver or spleen (grade 3) and very high uptake with equal or more than brain/bladder uptake (grade 4). Grade 3 and/or 4 was considered to represent significantly high FDG uptake.

In the semiquantitative PET/CT image analysis, by utilising all the three imaging planes (axial, coronal and sagittal) of PET/CT fusion images, a volume of interest (VOI) with 3-D isocontours set at the 40% threshold line of the maximum standardised uptake value (SUV) [127, 128] was carefully drawn around the site of the suspected lesion that demonstrated a high FDG uptake. The maximum pixel value in the VOI was defined as maximum standardised uptake value (SUVmax), and it can be calculated by using the following equation [129-131]:

$$SUVmax = \frac{Maximum\ pixel\ value\ in\ VOI\ (\text{MBq/mL})}{[Injected\ radioactivity\ (\text{MBq})\ /\ Body\ weight\ (\text{g})]} \quad (3.1)$$

In this study, SUVmax value was employed mainly due to its higher reproducibility [132]. In addition, this semiquantitative value had been found to be less affected by the size and the location in the VOI during the image analysis procedure [32, 131]. A lesion was highly suspected and considered when it had exceeded the standard cut-off value of 2.5; SUVmax > 2.5 [133]. The SUVmax values of all detected lesions were recorded and labelled as $SUVmax1^{a}$ and/or $SUVmax1^{b}$ (the superscripts of 'a' and 'b' were respectively for PET/unenhanced CT and PET/CECT fusion images).

With regard to evaluating the effects of applying an intravenous iodine-based contrast media during the CT scan of FDG PET/CT imaging, a separate image analysis was performed. The changes in the Hounsfield unit; HU and the SUVmax values of four normal organs/tissues (heart, liver, spleen and urinary bladder) were measured. These organs/tissues were chosen based on the variations of the contrast media concentrations at the time of the CT image acquisition, and in fact, they were sited apart from the detected lesions. In order to quantify the maximum changes caused by the application intravenous iodine-based contrast media, the axial CT, fused PET/unenhanced CT and fused PET/CECT images of those four normal organs were analysed by manually identifying a single pixel that has the highest value in both HU and the SUVmax. For maintaining the consistency of the analysis, this single pixel was originally drawn on PET/CECT fusion images and then copied to PET/unenhanced CT fusion images. However, in some cases, the pixel was repositioned based on the anatomical structures, mainly to resolve the differences that had been caused by the movements of the patient.

3.2.1.3.2. Dual time point imaging of FDG PET/CT

The image analysis and interpretation of the delayed PET/CT scan were almost similar to the above section; initial whole body PET/CT imaging. For creating the PET/CT fusion images, as no CECT scan had been performed during this delayed imaging, therefore only unenhanced CT dataset was used. From these fusion images, the SUVmax values of the detected lesions were again measured by using the same VOI technique; as for the initial whole body images, and labelled as SUVmax2. As a result, the percentage difference between these two SUVmax values (%ΔSUVmax) was calculated based on the following equation [7, 21-23, 109, 111].

$$\%\Delta SUVmax = \frac{(SUVmax2 - SUVmax1)}{SUVmax1} \times 100\% \quad (3.2)$$

In the application of the above equation, both $SUVmax1^a$ and $SUVmax1^b$ values of the detected lesions were used. In addition, for comparing the imaging findings of the initial whole body and the delayed PET/CT scans, these two images were displayed simultaneously on the workstation.

3.2.2. Italian patients

3.2.2.1. Patient preparation

The preparation procedures in this group of patients were the same as for Malaysian patients, with a fasting period of at least 8h prior to the scanning day and normal blood glucose level. The injected amount of FDG radioactivity was based on patient's body weight and PET/CT image acquisitions commenced at about 1h after the injection (minimum resting time was no less than 45 min). However, as mentioned earlier

(section 3.1.2), more detailed information were not available due to limited accessibility and a high patient privacy and confidentiality.

3.2.2.2. FDG PET/CT scanning protocols

The scanning protocols for these twelve patients were mainly derived from the FDG PET/CT imaging data that had been visualised on the workstation. PET/CT scans were conducted by using the same imaging system as for Malaysian patients; Biograph PET/CT (Siemens Healthcare Solutions). Therefore, all images of both Malaysian and Italian patients are well-founded to be compared.

PET/CT scanning commenced with a standard CT topogram, covering the area from the base of the skull to the mid-thigh region. However, during this image acquisition procedure only low dose unenhanced CT scan (low dose CT protocol) was performed, by using the following parameters: 110 kV, 30 mAs and 5 mm slice thickness. Then, PET emission scan was conducted in a three-dimensional (3-D) acquisition mode at the scanning time of 5 min per bed position. Patient was positioned supine with both arms rested straight and placed close to the body.

3.2.2.3. Image analysis and interpretation

All PET/CT images were reconstructed on the workstation with the similar principles as in the initial whole body FDG PET/CT scan of Malaysian patients, but only the low dose unenhanced CT dataset was used for anatomical localisation and calculation of PET attenuation correction factors. Again, all images were displayed in axial, coronal and sagittal planes along with maximum intensity projection (MIP) image.

To avoid the occurrence of ambiguity and bias, this image analysis was visually and semiquantitatively interpreted by the same personnel using the same methods. As no delayed PET/CT scans had been performed, therefore, only the SUVmax values of the initial whole body images were measured and recorded (SUVmax1).

3.2.3. Follow-up FDG PET/CT scan

As specifically mentioned in section 3.1, the prospective data were from Malaysian patients. To assess the therapeutic responses for this group of patients, therefore, the follow-up PET/CT scan needs to be performed. However, only small number of patients had undergone this type of scanning, with an interval of about six months from their initial diagnostic PET/CT scan. Again, all PET/CT examinations were conducted at Prince Court Medical Centre, Kuala Lumpur, Malaysia and/or Beacon International Specialist Centre, Selangor, Malaysia.

This study was carried out from February 2009 to December 2009, and it consisted of six consecutive patients a male-to-female ratio of 1:1. The mean ± SD age, height and weight of these six patients were 33 ± 15 years, 161 ± 8 cm and 64 ± 19 kg, respectively. The patient preparation procedures were the same as described earlier, with the mean injected amount of FDG radioactivity was about 383 ± 136 MBq (ranging from 254 – 612 MBq). The whole body PET/CT imaging commenced at about 50 ± 17 min after the FDG injection with 6 – 7 bed positions, and followed by 1 – 3 bed positions for the delayed PET/CT scan at about 130 ± 14 min after the FDG injection time (refer to Table 3.6); by using the same scanning protocols as in the initial diagnostic PET/CT scan.

PET/CT fusion images were reconstructed with the same principles as described in the previous section, by utilising both unenhanced CT and CECT datasets for the initial whole body PET/CT images, while unenhanced delayed CT dataset was used for the delayed PET/CT images. Indeed, the image analysis and interpretation had also been performed by the same radiologist.

Table 3.6: The blood glucose level, the injected amount of FDG radioactivity and the scanning time of both PET/CT image acquisitions (initial whole body and delayed scans) for the first six Malaysian patients who underwent the follow-up FDG PET/CT scan. ***The patient number of this table is the same as in the Tables 3.3 and 3.5.***

Patient no.	Blood glucose levels (mmol/L)	Injected FDG radioactivity (MBq)	Initial whole body scan; after the FDG injection time (min)	Delayed scan; after the FDG injection time (min)
1	4.0	612	42	120
2	5.5	277	79	152
3	4.1	400	35	120
4	4.7	453	36	121
5	7.1	254	60	124
6	5.8	299	45	142
MBq, megabecquerel.				

Exclusively to the sixteen Malaysian patients, all of them underwent extensive laboratory/microscopic investigations. The sample of the tissue and/or aspirate was taken under the guided procedures of either using CT scan or ultrasound. The final diagnosis of all these patients was based on the laboratory findings and/or clinical/radiological assessments during their periodic follow-up visits.

3.3. Statistical analysis

The data extracted from the images obtained in these studies were expressed as mean ± standard deviation (SD). The difference in SUVmax values of all detected lesions from the initial whole body to the delayed FDG PET/CT scans was determined using a two-tailed paired samples t-test. This statistical test was also used to analyse the changes in SUVmax values caused by the application of an intravenous iodine-based contrast media during the CT scan of FDG PET/CT imaging. On the other hand, an independent samples t-test was carried out to determine the significance difference of two groups of patients like between Malaysian and Italian patients. All results were evaluated using a 5% error level and a difference was considered to be statistically significant when $P < 0.05$.

In order to assess the diagnostic quality or performance of all recorded and calculated data, the receiver operating characteristic (ROC) curve was used. An ROC curve is a plot of test sensitivity (plotted on the y axis) versus its false positive rate (FPR) or 1 − specificity (plotted on the x axis) [134, 135]. It is an effective method of evaluating the accuracy of a diagnostic test, and indeed, it has been widely used in radiology [135]. Sensitivity and specificity are defined as the number of true positive decisions divided by the number of actually positive cases and the number of true negative decisions divided by the number of actually negative cases, respectively [135]. One of the most popular measures of the ROC curve is an area under curve; it is a measure of the overall performance of a diagnostic test that can take on values between 0.0 and 1.0 [134, 135]. The closer an area under curve is to 1.0, the better the overall diagnostic performance of the test [135]. A test with an area under curve of 1.0 is considered as a perfectly accurate test [134, 135], and a practical lower limit for an area

under curve of a diagnostic test is 0.5 [135]. In addition, ROC curves can be used to compare the overall diagnostic performance of different tests by comparing their area under curve values [135]. From ROC curve, an optimum cut-off threshold value for all recorded and calculated data of this clinical imaging study could also be identified.

All the statistical analyses and ROC curves were performed using the Statistical Package for Social Sciences (SPSS) program for Windows version 18.0.

CHAPTER 4

SECTION A2:

RESULTS AND

DISCUSSION

This chapter presents the results obtained from the clinical imaging study and accompanied with the discussion. The major focus of this study is to develop an optimum FDG PET/CT scanning protocol for detecting the EPTB lesions.

4.1. Results

4.1.1. Malaysian patients

As mentioned in Chapter 3, all sixteen Malaysian patients underwent the initial whole body FDG PET/CT imaging, while DTPI technique was only performed in thirteen patients. Therefore, the results are classified according to the imaging procedure:

1. Whole body FDG PET/CT imaging
2. DTPI of FDG PET/CT scan

4.1.1.1. Whole body FDG PET/CT imaging

No adverse effects were noticed during and/or after the imaging acquisitions of all patients. However, only one patient had an underlying medical condition that contraindicated to the administration of iodine-based contrast media; patient 14 was previously diagnosed with end-stage renal failure. Thus, for this particular patient, the whole body FDG PET/CT scan was performed without utilising the iodine-based contrast media. The FDG PET/CT imaging findings; along with the SUVmax1 values ($SUVmax1^{a}$ and $SUVmax1^{b}$) of all detected lesions, the final diagnosis and the diagnostic method of all patients are listed in Table 4.1.

Of these sixteen patients, nine patients (five women and four men) were positively diagnosed with EPTB infectious disease, while the other seven patients were categorised as non-EPTB patients. The final diagnosis was mainly based on the

microscopic/histopathological findings of the sample sputum/aspirate/tissue (Fig. 4.1) and/or clinical/radiological assessment during the periodical follow up visits. Although there was no histological confirmation of *Mycobacterium tuberculosis* for the patients 2 and 5, due to increasing pattern of TB incidence in Malaysia and the high index of suspicion by the physicians, they were treated with anti-tuberculous (anti-TB) drugs. With no adverse reactions during the treatment period and significant progress in their general health conditions, therefore these two patients had been classified as EPTB patients. All EPTB patients were being prescribed with the standard regimen of anti-TB drugs treatment (2 months with daily doses of SHRZ or EHRZ, and biweekly doses of SHR or HR for the next 4 months). However, depending on the treatment responses (clinically, pathologically and/or radiologically), the physician would then decide either to continue or stop the treatment. Therefore, some of EPTB patients were under anti-tuberculous drugs for about 9 months, and even up to 12 months.

In contrast, all non-EPTB patients showed positive response after about a month or more with antibiotics treatment (excluding patient 12, who had surgical removal of the lesion, and patient 13, who had steroid therapy), which had been assessed during their periodical follow-up visits. Furthermore, only four patients (patients 11, 12, 13 and 15) were negatively diagnosed for EPTB infectious disease through histopathological investigations. Apparently, all FDG avid sites of patient 11 were caused by the physiological uptake of brown adipose tissues, rather than the infectious lesions. This interesting imaging finding is attached as an appendix for this thesis (Appendix 5), and it has also been recently cited by Son'kin and his colleagues in their review article about brown adipose tissues [136].

A total of 54 extrapulmonary lesions with avid FDG uptake were detected, in which 27 lesions were in EPTB patients and the remainder presented in non-EPTB patients. All of these detected lesions were in either grade 3 or 4 of the visual image analysis, and the SUVmax values of them were higher than the standard cut-off value of 2.5; SUVmax > 2.5. As shown in Table 4.1, entirely, there were no differences in the SUVmax values of all detected lesions from both PET/unenhanced CT and PET/CECT fusion images, which indicated that iodine-based contrast media could be used during the CT scan of FDG PET/CT imaging. The mean ± SD SUVmax values for EPTB and non-EPTB lesions were 7.0 ± 2.3 and 8.8 ± 4.6, respectively. There was an overlap on the distribution of these two mean values (Fig. 4.2 and 4.3) and the independent samples t-test resulted with an insignificant difference, $P = 0.07$. However, according to the receiver operating characteristic (ROC) curve analysis, when the SUVmax1 value of 5.7 was used as the cut-off point, the sensitivity and specificity were 51.9% and 40.7%, respectively (refer to Fig. 4.4). From a diagnostic imaging point of view, these values were quite low, and therefore, it can be concluded that the use of the SUVmax1 value alone was impractical for differentiating between EPTB and non-EPTB lesions.

For ethical reasons, it was impossible to perform biopsy and/or histological analysis on each lesion detected by means of this integrated imaging scan. Accordingly, the diagnostic quality (sensitivity, specificity and accuracy) of FDG PET/CT imaging in detecting the EPTB lesions could not be determined.

Figure 4.1: The aspiration of the pus collection from the right anterior chest wall region of patient 8 of the Malaysian patients, which has been performed under ultrasound guided and aseptic techniques.

Table 4.1: The FDG PET/CT imaging findings and the final diagnosis of all sixteen Malaysian patients.

Patient no.	Lesion site	SUVmax1[a]	SUVmax1[b]	Final diagnosis	Diagnostic method
EPTB					
1	1. Right base of the neck node	8.0	8.0	Tuberculous lymphadenitis	Aspiration biopsy
	2. Right parathyroid node	8.6	8.6		
	3. Right infraclavicular node	8.3	8.3		
	4. Right paratracheal	11.7	11.7		
2	T12 and L1 vertebral bodies	7.2	7.2	Tuberculous spondylitis	Anti-TB treatment response
3	Left submandibular node	9.7	9.7	Tuberculous lymphadenitis	Aspiration biopsy
4	Right hip joint	8.3	8.3	Tuberculous synovitis	Aspiration biopsy
5	1. L3-L4 intervetebral disc space	8.5	8.5	Tuberculous spondylitis	Anti-TB treatment response
	2. Left psoas muscle at level L4	6.7	6.7		
6	1. Right retrocrural node	6.0	6.0	Miliary tuberculosis	Tissue biopsy
	2. Right subhepatic node	3.5	3.5		
	3. Peripancreatic node	7.1	7.1		
7	1. Left psoas muscle	9.5	9.5	Miliary tuberculosis	AFB sputum test
	2. Left inguinal node	7.4	7.4		
	3. Left axillary node	7.5	7.5		
	4. Right paratracheal node	5.5	5.5		
	5. Right para-aortic node	9.5	9.5		
8	1. Right supraclavicular fossa	2.8	2.8	Tuberculous lymphadenitis	PCR
	2. Right anterior chest wall	5.8	5.8		
	3. Right subscapular soft tissue space	11.7	11.7		
9	1. Right crural node	4.3	4.3	Miliary tuberculosis	AFB sputum test
	2. Left diaphragmatic node	5.3	5.3		
	3. Right diaphragmatic node	3.4	3.4		
	4. Preaortic node	7.0	7.0		
	5. Left renal vein node	5.7	5.7		
	6. Left retrosternal node	4.8	4.8		
	7. Right carinal node	4.7	4.7		

(Continue on the next page)

Patient no.	Lesion site	SUVmax1[a]	SUVmax1[b]	Final diagnosis	Diagnostic method
Non-EPTB					
10	1. Right posterior triangle of neck (anterior)	3.5	3.5	Lymphadenitis	Antibiotics treatment response
	2. Right posterior triangle of neck (posterior)	3.8	3.8		
	3. Right paratracheal node	8.8	8.8		
11	1. Right supraclavicular brown fat	17.6	17.6	Lymphadenitis	Aspiration biopsy + antibiotics treatment response
	2. Left supraclavicular brown fat	18.9	18.9		
	3. Mediastinal brown fat	7.0	7.0		
	4. Right paravertebral brown fat	13.9	13.9		
	5. Left paravertebral brown fat	7.4	7.4		
	6. Right perirenal brown fat	10.4	10.4		
	7. Left perirenal brown fat	20.8	20.8		
12	Left calcaneum bone area	3.2	3.2	Brodie abscess	Tissue culture
13	1. Right posterior of 9th rib	9.6	9.6	Rheumatoid arthritis	Aspiration and tissue biopsies
	2. Right lateral of 10th rib	7.0	7.0		
	3. Right posterior of 11th rib	8.3	8.3		
	4. Tibial plateau of left knee joint	5.6	5.6		
14[*]	L5/S1 intervetebral disc space	4.6	–	Infective spondylitis	Antibiotic treatment response + MRI
15	1. Right head of humerus	8.0	8.0	Lung cancer with distant metastases	Aspiration biopsy + CT
	2. Right posterior clavicle node	4.9	4.9		
	3. Left posterior clavicle node	6.4	6.4		
	4. Left scapula area	5.1	5.1		
	5. Right adrenal gland	12.6	12.6		
	6. Left adrenal gland	7.5	7.5		
	7. T11 vertebral body	7.6	7.6		
	8. Right pubic bone area	12.2	12.2		
16	1. Left nasopharyngeal area	9.3	9.3	Infective spondylitis	Antibiotics treatment response
	2. T7 vertebral body	8.6	8.6		
	3. Left vastas muscle group	5.9	5.9		

EPTB, extrapulmonary tuberculosis; non-EPTB, non-extrapulmonary tuberculosis; T, thoracic vertebrae; L, lumbar vertebrae; S, sacral vertebrae; SUVmax1[a], maximum standardised uptake value from PET/unenhanced CT fusion image; SUVmax1[b], maximum standardised uptake value from PET/CECT fusion image; anti-TB, anti-tuberculous; PCR, Polimerase Chain Reaction; AFB, Acid Fast Bacilli; MRI, Magnetic Resonance Imaging; CT, Computed Tomography; –, not done.

[*] Patient who had been previously diagnosed with end-stage renal failure and no iodine-based contrast media was administered.

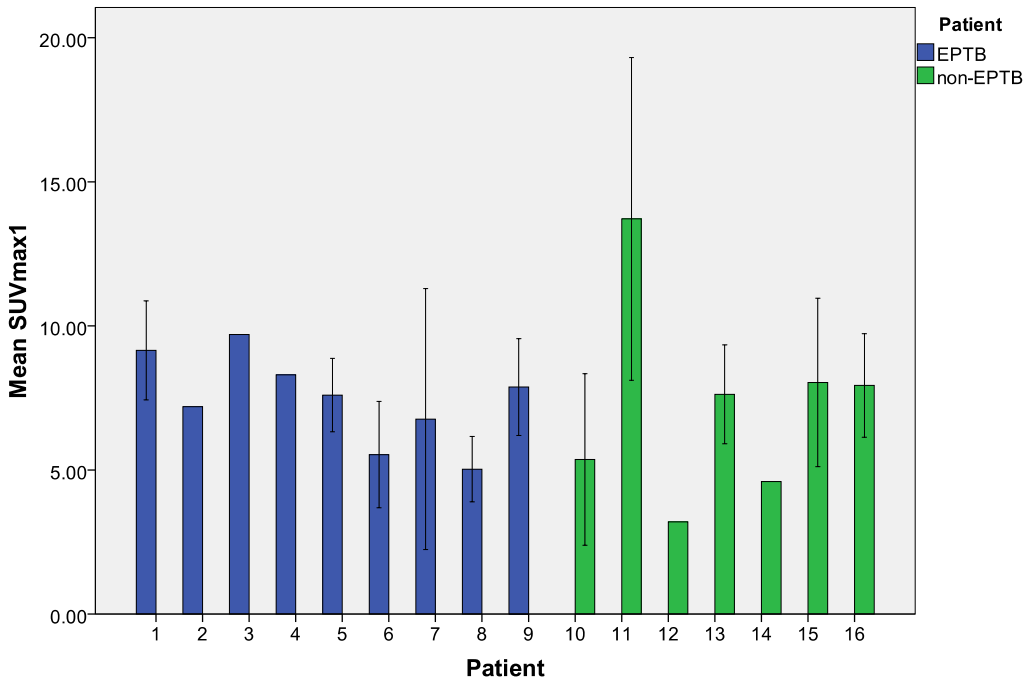

Figure 4.2: The mean SUVmax1 value for each of EPTB and non-EPTB patients. There is an overlapping distribution of this value between both EPTB and non-EPTB patients. ***Error bars represent ± standard deviation.***

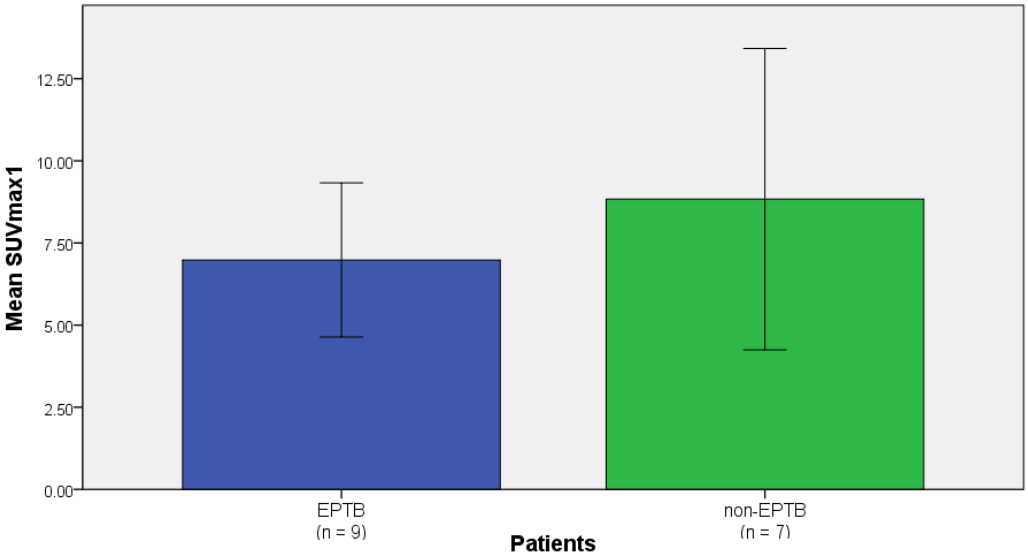

Figure 4.3: The mean SUVmax1 values of EPTB and non-EPTB lesions. There is no significant difference between these two mean values, where an independent samples t-test results with *P* = 0.07. ***Error bars represent ± standard deviation.***

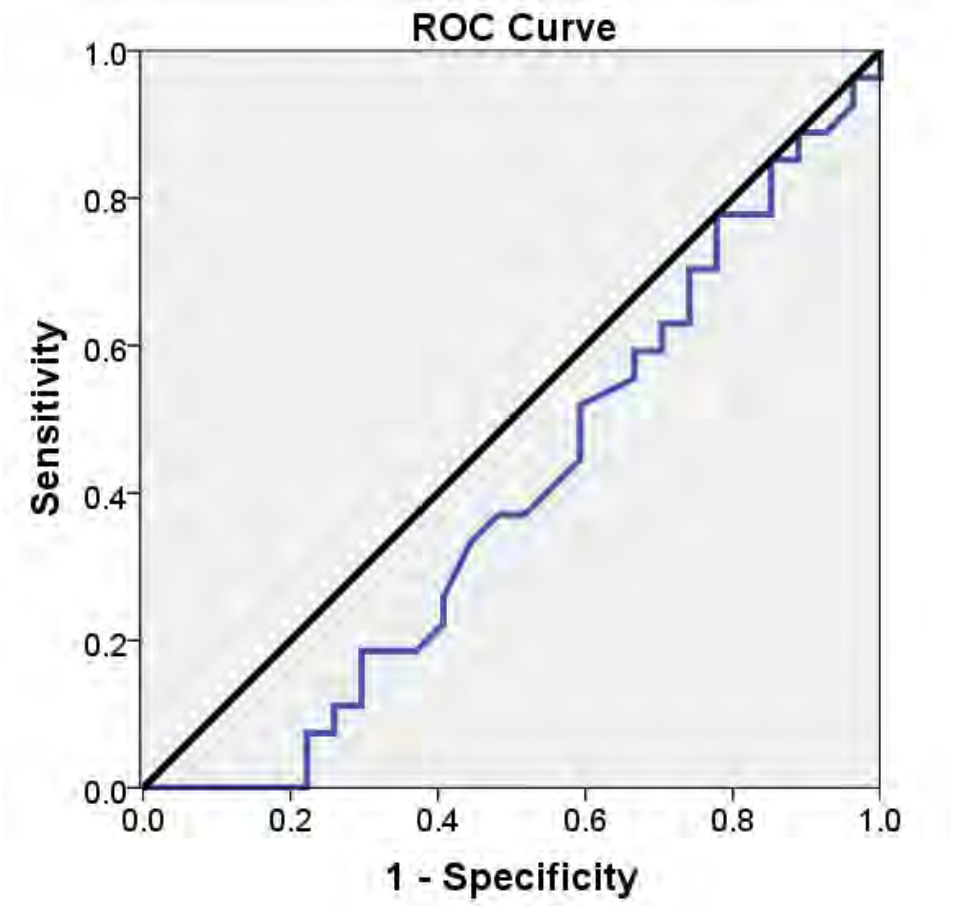

Figure 4.4: The receiver operating characteristic (ROC) curve on the diagnostic performance (sensitivity and specificity) of the SUVmax1 value in differentiating between EPTB and non-EPTB lesions. This analysis yields an area under curve of 0.398 (blue line). ***The black line represents the reference line of the ROC curve.***

4.1.1.1.1. The effects of using iodine-based contrast media on the SUVmax values of EPTB patients

The CT scans of the initial whole body FDG PET/CT imaging for all nine EPTB patients were conducted twice; with and without intravenous injection of iodine-based contrast media. Thus, to determine the effects of this contrast media on the SUVmax values of PET/CT fusion images, as previously highlighted in Chapter 3, a separate

analysis has been performed by measuring the changes in HU and SUVmax values of four normal organs (heart, liver, spleen and urinary bladder). The results are tabulated in Table 4.2.

All four normal organs showed a statistically significant increment in HU, except the urinary bladder (P = 0.54) (refer to Fig. 4.5). This result is not unexpected because an essential bladder enhancement can usually be seen on CT images when a 60-second scanning delay is used [137]. Nevertheless, in this study, the acquisition of CECT scan was commenced immediately after the intravenous injection of iodine-based contrast media.

On the contrary, all the changes in the SUVmax values of these four normal organs were found to have no statistical significance (P values > 0.05) (refer to Fig. 4.6 and 4.7). Combining these results with the findings from the changes in the SUVmax values of all EPTB lesions (Table 4.1), it suggests that iodine-based contrast media could potentially be applied during the CT scan of FDG PET/CT imaging in a group of EPTB patients, without producing any significant effects on the SUVmax values regardless of either in the lesion or the other normal organs.

Table 4.2: The differences in HU and SUVmax values of four normal organs, caused by an intravenous injection of iodine-based contrast media during the CT scan of FDG PET/CT imaging for nine confirmed EPTB patients. ***All data are expressed as mean ± SD.***

Organ	HU				SUVmax			
	without CM	with CM	*P* value	Remarks	without CM	with CM	*P* value	Remarks
Heart	42.44 ± 18.84	128.44 ± 22.96	< 0.05	S	1.79 ± 0.53	1.80 ± 0.53	0.60	NS
Liver	35.11 ± 18.37	98.78 ± 15.94	< 0.05	S	2.37 ± 0.70	2.37 ± 0.70	1.00	NS
Spleen	51.11 ± 25.14	96.89 ± 8.33	< 0.05	S	2.00 ± 0.60	2.00 ± 0.59	0.86	NS
Urinary bladder	11.89 ± 17.36	19.44 ± 30.41	0.54	NS	5.67 ± 3.22	5.66 ± 3.21	0.85	NS
HU, Hounsfield unit; SUVmax, maximum standardised uptake value; CM, iodine-based contrast media; S, significant; NS; not significant								

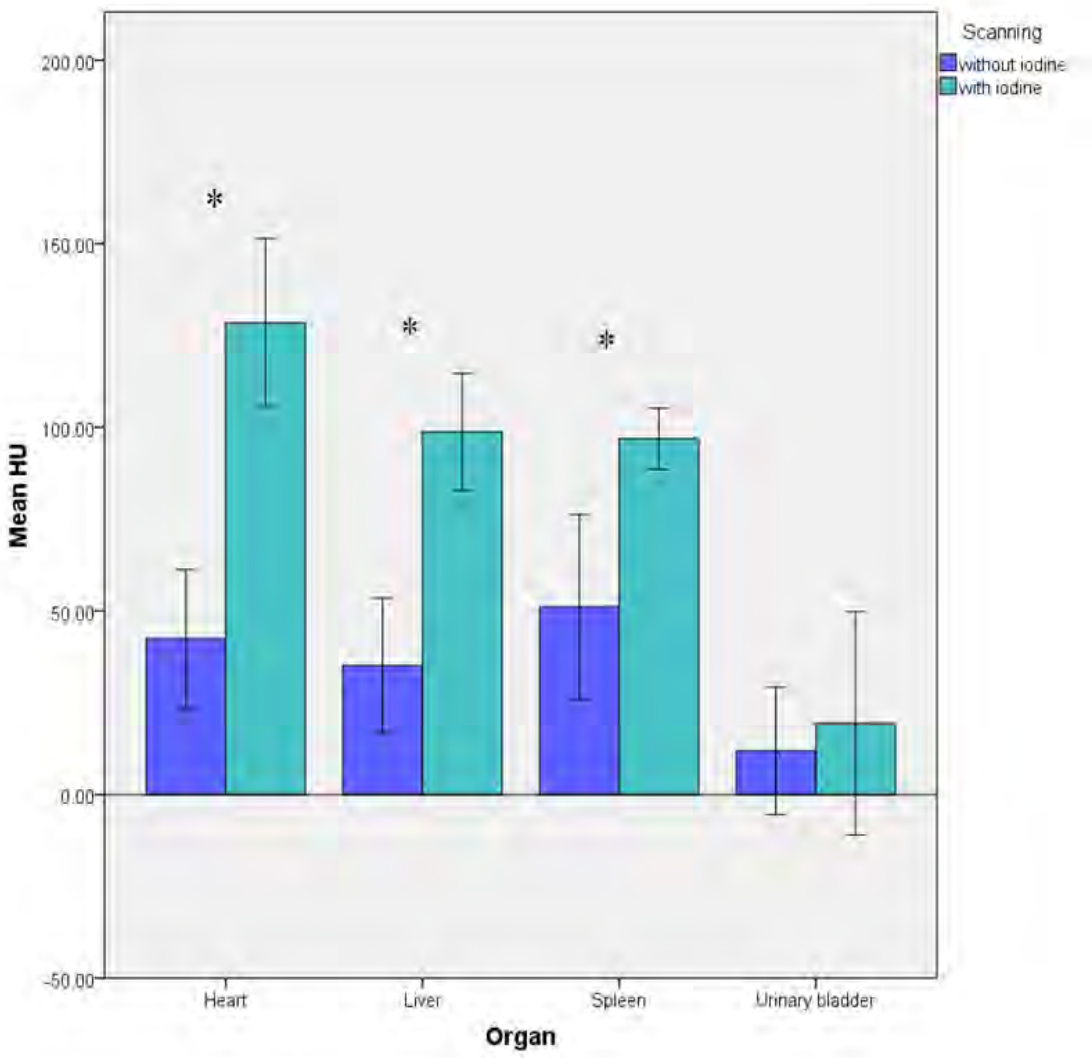

Figure 4.5: The mean HU values that have been obtained from the CT images of four normal organs (heart, liver, spleen and urinary bladder) before and after the intravenous injection of iodine-based contrast media. The two-tailed paired samples t-tests result with significant differences with *P* values of less than 0.05 (*) for all organs, except the urinary bladder (*P* = 0.54). *Error bars represent ± standard deviation.*

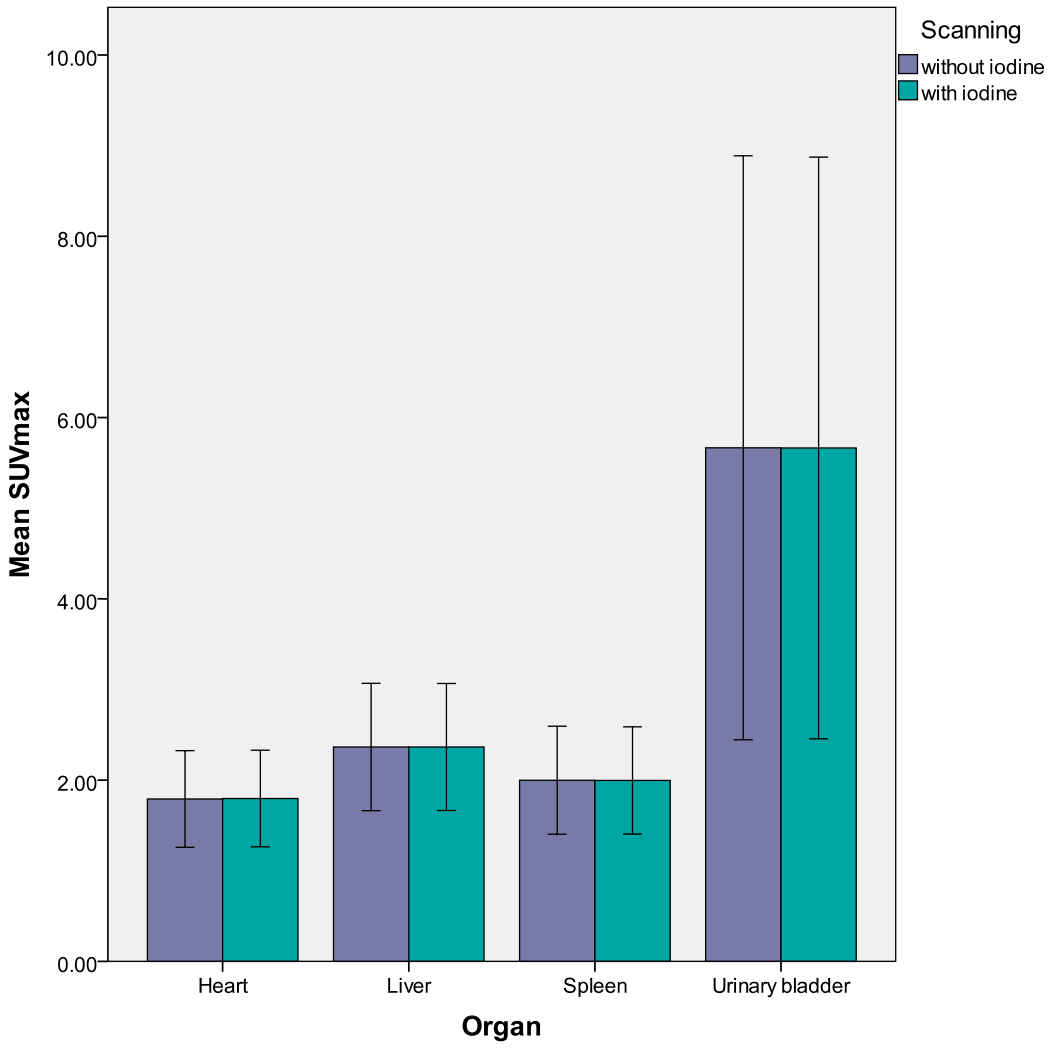

Figure 4.6: The mean SUVmax values that have been obtained from both PET/unenhanced CT and PET/CECT fusion images of four normal organs (heart, liver, spleen and urinary bladder). None of the changes in the SUVmax values of any of these organs are found to be statistically significant (*P* values > 0.05). *Error bars represent* ± *standard deviation.*

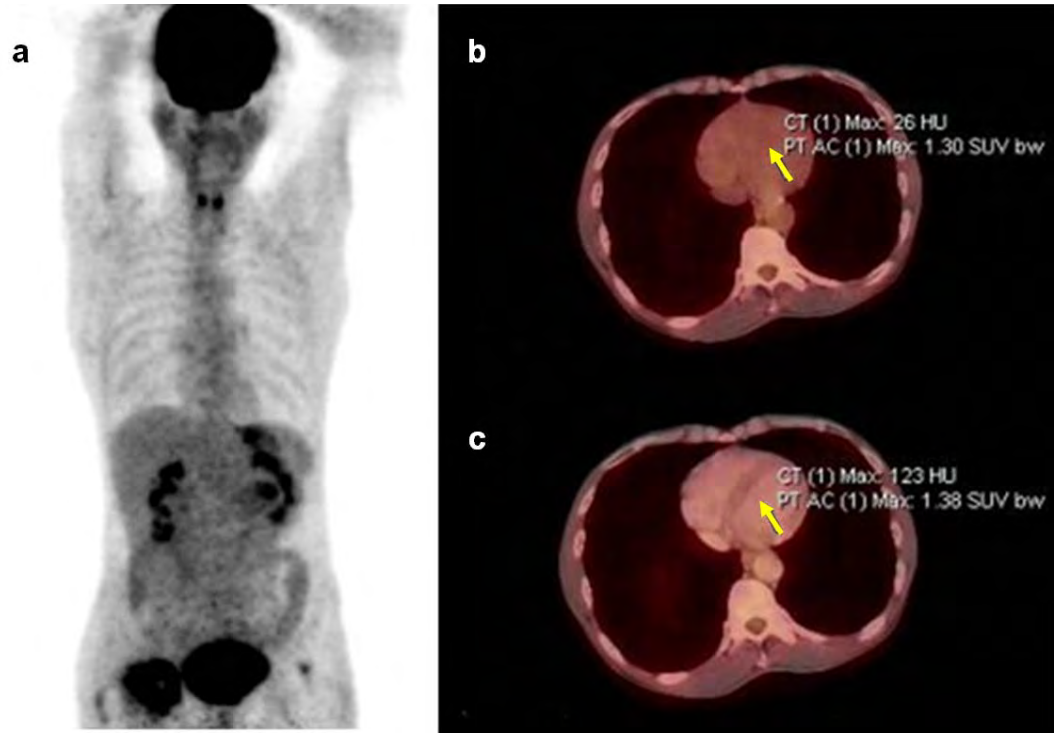

Figure 4.7: FDG PET/CT image acquisitions of patient 4 of the Malaysian patients. (a) Maximum intensity projection (MIP) image. (b) PET/unenhanced CT and (c) PET/CECT fusion images, which demonstrate the differences in HU and SUVmax values of his heart (yellow arrows). It has been clearly shown that the utilisation of iodine-based contrast media will cause enormous change in HU value (from 26 to 123), whereas the SUVmax value is increased minimally (from 1.30 to 1.38).

4.1.1.1.2. Diagnostic performance of FDG PET/CT imaging against the other conventional imaging modalities

As mentioned earlier, all sixteen Malaysian patients had undergone extensive clinical, radiological and histopathological investigations during their diagnosis process of the disease and the periodical follow-up visits. Thus, the diagnostic performance of FDG PET/CT imaging can be validated against the imaging findings of other conventional imaging modalities like general radiography, MRI and CT scans, and ultrasound. Any

suspicious sign of having tuberculous infection reported from these scanning (including FDG PET/CT imaging) was considered as a positive diagnostic imaging result. The microscopic/histopathological findings and the outcome of the treatment response (clinically and/or radiologically) during the follow-up visits are used as the baseline/standard, and all of these are summarised in Table 4.3.

Table 4.3: The diagnostic investigation results of all Malaysian patients.

Patient no.	PET/CT	CM	HPE or F/up
EPTB			
1	+	+	+
2	+	−	+
3	+	+	+
4	+	+	+
5	+	+	+
6	+	+	+
7	+	+	+
8	+	+	+
9	+	+	+
Non-EPTB			
10	+	−	−
11	−	+	−
12	−	−	−
13	−	−	−
14	+	+	−
15	−	−	−
16	+	+	−
CM, conventional imaging modalities; HPE, histopathological examination; F/up, follow-up; +, positive; −, negative.			

Table 4.4: The diagnostic performance of FDG PET/CT and other conventional imaging modalities in detecting the EPTB lesions of all sixteen Malaysian patients.

	Sensitivity	Specificity	Accuracy	PPV	NPV
PET/CT	100%	57.1%	81.3%	75%	100%
CM	88.9%	57.1%	75%	72.7%	80%
CM, conventional imaging modalities; PPV, positive predictive value; NPV, negative predictive value.					

The sensitivity, specificity, accuracy, positive and negative predictive values for PET/CT and other conventional imaging modalities are listed in Table 4.4. Based on these results, FDG PET/CT imaging has shown a relatively higher in its diagnostic performance as compared to the other conventional imaging modalities.

4.1.1.2. DTPI of FDG PET/CT scan

The DTPI of FDG PET/CT scans were only performed in thirteen patients, where other three patients were clinically unfit and presented with severe backache; patients 7, 15 and 16 (refer to Tables 3.3 and 3.5 in Chapter 3). Of these, only twelve patients underwent two CT examinations, which consisted of unenhanced CT and CECT scans during their FDG PET/CT imaging (exclude patient 14 who was previously diagnosed with end-stage renal failure, refer to Table 4.1). However, for this analysis, only 11 patients were included (patient 11 was excluded due to the fact that all her detected FDG areas were caused by the physiological brown fats uptakes, refer to Appendix 5). All the SUVmax values (SUVmax1; initial whole body scan, and SUVmax2; delayed scan) for each of the detected lesions are tabulated in Table 4.5.

A total of 30 extrapulmonary lesions with avid FDG uptake were detected. All lesions showed the SUVmax values of higher than standard cut-off value of 2.5; SUVmax > 2.5, during both image acquisitions (excluding only one lesion of patient 8). The mean ± SD values for SUVmax1 and SUVmax2 of the 22 EPTB lesions were 6.8 ± 2.5 and 7.9 ± 3.2, respectively. There was a significant difference between these two time points (P = 0.001) (refer to Fig. 4.8). This result indicated that there was a significant increment on SUVmax values between the two time points within the studied EPTB lesions. The mean %ΔSUVmax of the EPTB lesions was about 16%, with

the highest value of about 40% had been recorded at the right infraclavicular node of patient 1 (Fig. 4.9).

In comparison, for the eight non-EPTB lesions, the mean ± SD values of SUVmax1 and SUVmax2 were 6.2 ± 2.6 and 6.5 ± 2.8, respectively. There was a significant difference between these two time points (P = 0.044) (refer to Fig. 4.8). However, the pattern of SUVmax change in these non-EPTB lesions was less apparent than those of EPTB lesions, in which the mean %ΔSUVmax value was only about 4% (Fig. 4.10).

When comparing the mean of %ΔSUVmax values from both types of lesions (EPTB vs. non-EPTB), there was an insignificant difference statistically (P = 0.06) (refer to Fig. 4.11). This result indicated that the %ΔSUVmax value was insufficient to be used for differentiating between EPTB and non-EPTB lesions. However, according to the ROC curves analyses (Fig. 4.12), when the SUVmax1 value of 5.7 was used as the cut-off value, the sensitivity and specificity were 68.2% and 50%. When the SUVmax2 value of 5.9 was used as the cut-off value, the sensitivity and specificity were 72.7% and 50%. When %ΔSUVmax value of 7.6 was used as the cut-off value, the sensitivity and specificity were 77.3% and 75%. Based on these results, %ΔSUVmax value demonstrated the highest diagnostic performance as compared with the other two values; SUVmax1 and SUVmax2.

Table 4.5: The SUVmax values for each of the detected lesions from DTPI of FDG PET/CT imaging in the eleven of Malaysian patients. ***Note that the patient number is the same as in Table 4.1.***

Patient no.	Lesion site	SUVmax1	SUVmax2	%ΔSUVmax
EPTB				
1	1. Right base of the neck node	8.0	10.4	30.0
	2. Right parathyroid node	8.6	11.8	37.2
	3. Right infraclavicular node	8.3	11.6	39.8
	4. Right paratracheal	11.7	15.7	34.2
2	T12 and L1 vertebral bodies	7.2	9.5	31.9
3	Left submandibular node	9.7	11.2	15.5
4	Right Hip	8.3	8.9	7.2
5	1. L3-L4 intervetebral disc space	8.5	10.7	25.9
	2. Left psoas muscle at level L4	6.7	8.1	20.9
6	1. Right retrocrural node	6.0	6.0	0.0
	2. Right subhepatic node	3.5	4.3	22.9
	3. Peripancreatic node	7.1	8.1	14.1
8	1. Right supraclavicular fossa	2.8	2.3	-17.9
	2. Right anterior chest wall	5.8	6.8	17.2
	3. Right subscapular soft tissue space	11.7	8.8	-24.8
9	1. Right crural node	4.3	4.8	11.6
	2. Left diaphragmatic node	5.3	6.2	17.0
	3. Right diaphragmatic node	3.4	4.0	17.6
	4. Preaortic node	7.0	7.1	1.4
	5. Left renal vein node	5.7	6.7	17.5
	6. Left retrosternal node	4.8	5.3	10.4
	7. Right carinal node	4.7	5.7	21.3
Non-EPTB				
10	1. Right posterior triangle of neck (anterior)	3.5	4.0	14.3
	2. Right posterior triangle of neck (posterior)	3.8	4.0	5.3
	3. Right paratracheal node	8.8	9.5	8.0
12	Left calcaneum bone	3.2	2.9	-9.4
13	1. Right posterior of 9th rib	9.6	10.3	7.3
	2. Right lateral of 10^{th} rib	7.0	7.4	5.7
	3. Right posterior of 11th rib	8.3	8.3	0.0
	4. Tibial plateau of left knee joint	5.6	5.8	3.6

EPTB, extra-pulmonary tuberculosis; non-EPTB, non-extra-pulmonary tuberculosis; T, thoracic vertebrae; L, lumbar vertebrae; SUVmax1, maximum standardised uptake values at early imaging; SUVmax2, maximum standardised uptake values at delayed imaging; %ΔSUVmax, percentage difference of SUVmax values.

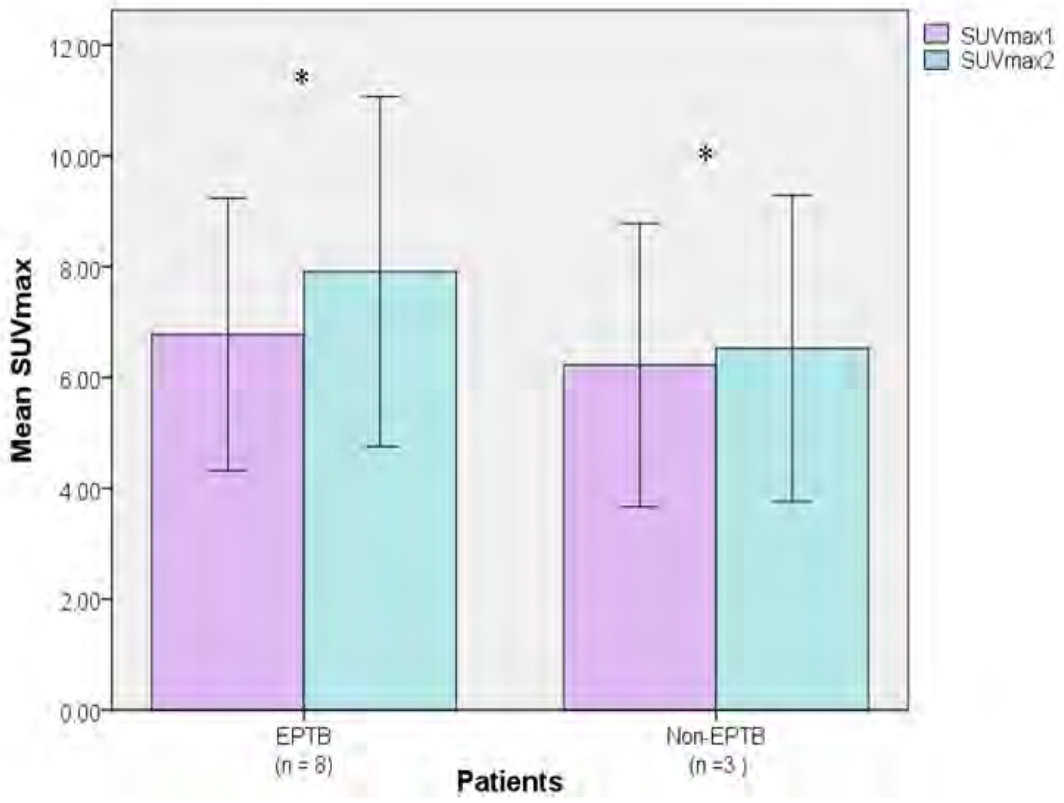

Figure 4.8: The mean differences in the SUVmax values of EPTB and non-EPTB Malaysian patients, obtained from PET/CT fusion images of 22 EPTB and 8 non-EPTB lesions during the image acquisition of using DTPI technique. The two-tailed paired samples t-tests result with significant differences with *P* values of less than 0.05 (*) for both groups of patients. However, the changing pattern in non-EPTB patients is smaller in amplitude than of EPTB patients. *Error bars represent ± standard deviation.*

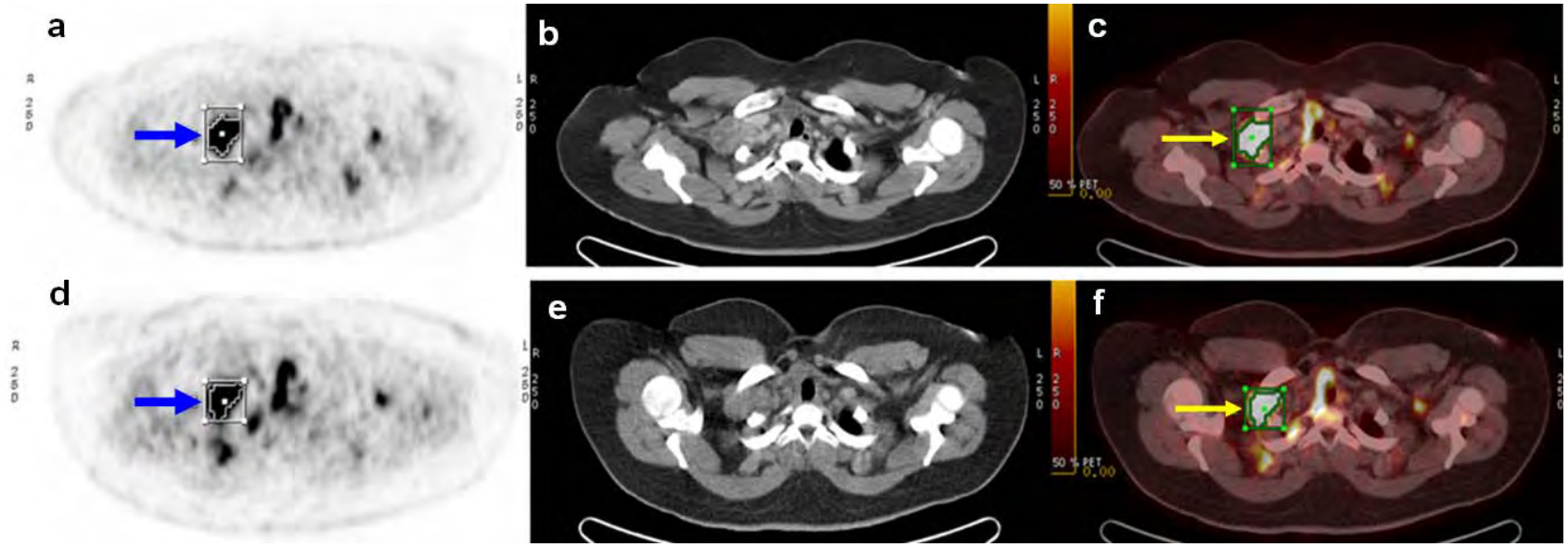

Figure 4.9: FDG PET/CECT image acquisitions of patient 1 of Malaysian patients showing an avid FDG activity at her right infraclavicular lymph node (blue arrows). (a) PET image of early scan. (b) Contrast-enhanced CT (CECT) image of early scan with peripheral enhancement of the right infraclavicular node. (c) PET/CECT fusion image which demonstrated a volume of interest (VOI) at the right infraclavicular node; SUVmax value was 8.3 (yellow arrow). (d) Delayed PET image at almost the same level as in (a). (e) Delayed CT image at almost the same level as in (b). (f) PET/CT fusion image showed higher SUVmax value; 11.6 (yellow arrow). The percentage difference between these two SUVmax values (%ΔSUVmax) was about 40%.

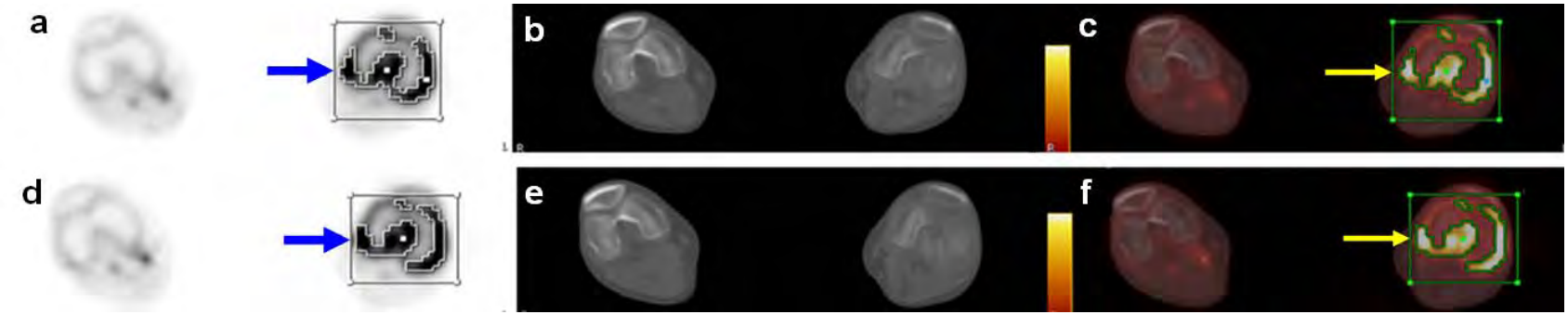

Figure 4.10: FDG PET/CECT image acquisitions of patient 11 of Malaysian patients showing an avid FDG activity at the tibial plateau of his left knee joint (blue arrows). (a) PET image of early scan. (b) Contrast-enhanced CT (CECT) image using bone window setting of early scan. (c) PET/CECT fusion image which demonstrated a volume of interest (VOI) at the left tibial plateau; SUVmax value was 5.6 (yellow arrow). (d) Delayed PET image at almost the same level as in (a). (e) Delayed CT image also using bone window setting at almost the same level as in (b). (f) PET/CT fusion image showed higher SUVmax value; 5.8 (yellow arrow). The percentage difference between these two SUVmax values (%ΔSUVmax) was only about 4%.

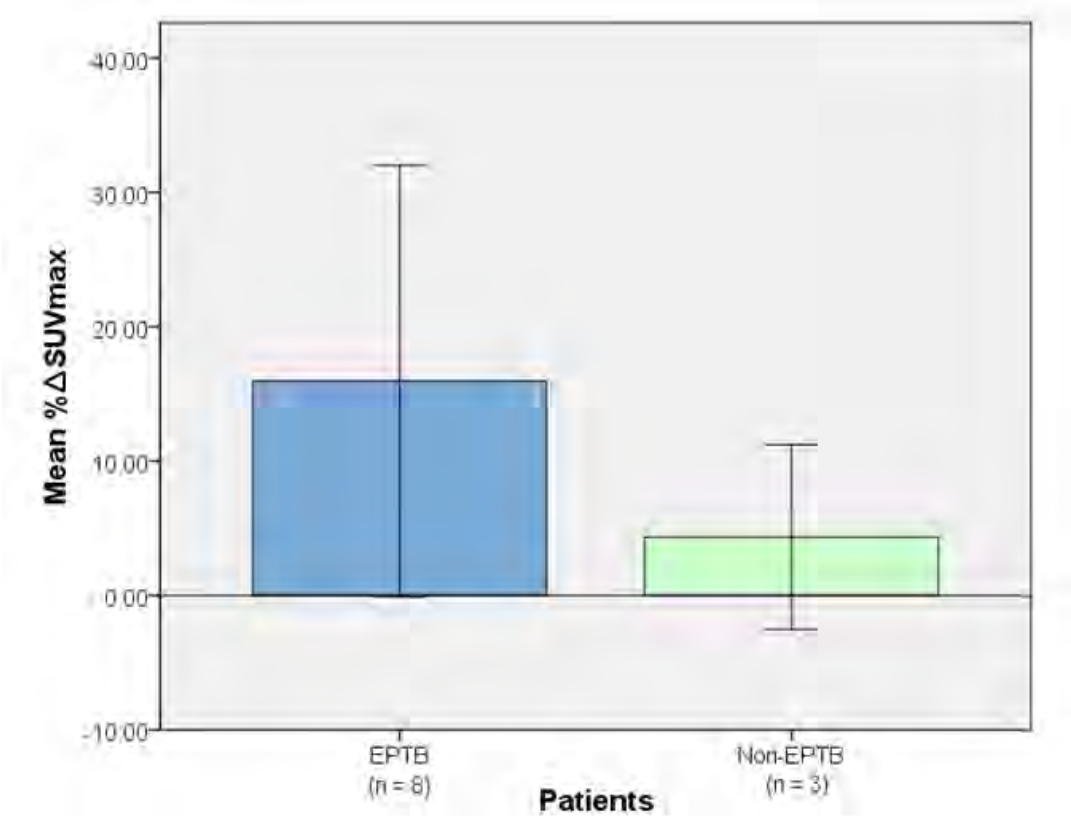

Figure 4.11: The mean difference in %ΔSUVmax value of EPTB and non-EPTB patients. An independent samples t-test shows no significant difference with *P* = 0.06. *Error bars represent* ± *standard deviation.*

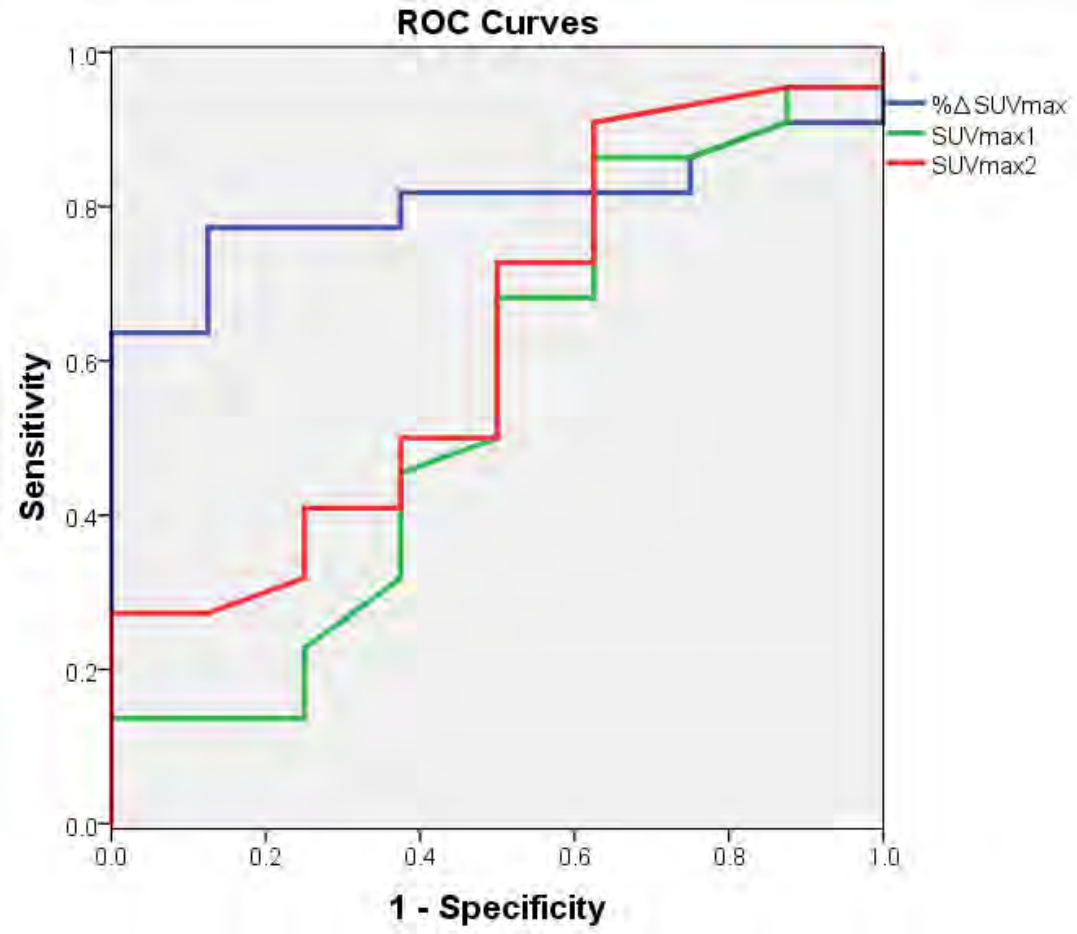

Figure 4.12: The receiver operating characteristic (ROC) curves that compare the diagnostic performance (sensitivity and specificity) of the SUVmax1, SUVmax2 and %ΔSUVmax values in differentiating between EPTB and non-EPTB lesions. This analysis yields that the use of %ΔSUVmax value (blue line) is superior to the other two values, with an area under curve of 0.804.

4.1.2. Italian patients

A total of 19 extrapulmonary lesions with avid FDG uptake were detected, in these twelve confirmed EPTB patients (as listed in Table 4.6). Again, all the detected lesions were in either grade 3 or 4 of the PET/CT visual analysis, with SUVmax > 2.5. The mean ± SD of the SUVmax1 value for these EPTB lesions was 7.8 ± 4.0.

Table 4.6: The SUVmax1 values of all detected EPTB lesions from the twelve Italian patients.

Patient no.	Lesion site	SUVmax1
1	1. Posterolateral aspect left rib, at the level of T4	13.4
	2. Right pretracheal node, at the level of T4 vertebral body	6.7
	3. Right peribroncheal node	8.6
2	L2-L3 intervertebral disc	9.8
3	1. Right 8th intercostal muscle	7.8
	2. Left sternum	9.3
	3. Left prevertebral area space of lower cervical and thoracic spines	8.8
4	Left hip joint	6.7
5	Left knee joint	5.0
6	Left shoulder joint	4.7
7	1. L4-L5 intervertebral disc	7.2
	2. Mediastinal node	5.3
	3. Right hilar node	5.8
8	Right hip joint	4.9
9	L3-L4 intervertebral disc	10.0
10	Right hip joint	3.1
11	Right knee joint	20.8
12	1. T10 -T11 intervertebral disc	4.8
	2. Right carinal	5.0
T, thoracic vertebrae; L, lumbar vertebrae; SUVmax, maximum standardised uptake value.		

4.1.2.1. Comparison between the SUVmax values of EPTB lesions in Malaysian and Italian patients

When comparing between the mean SUVmax1 values of EPTB lesions in both Malaysian and Italian patients, an independent samples t-test revealed an insignificant statistical difference with a *P* value equal to 0.404 (refer to in Fig. 4.13). This indicates

that an infectious lesion like EPTB could have a high FDG uptake, which then results in a high SUVmax value. Thus, FDG PET/CT scan is proven to be an important diagnostic imaging procedure in depicting EPTB lesions.

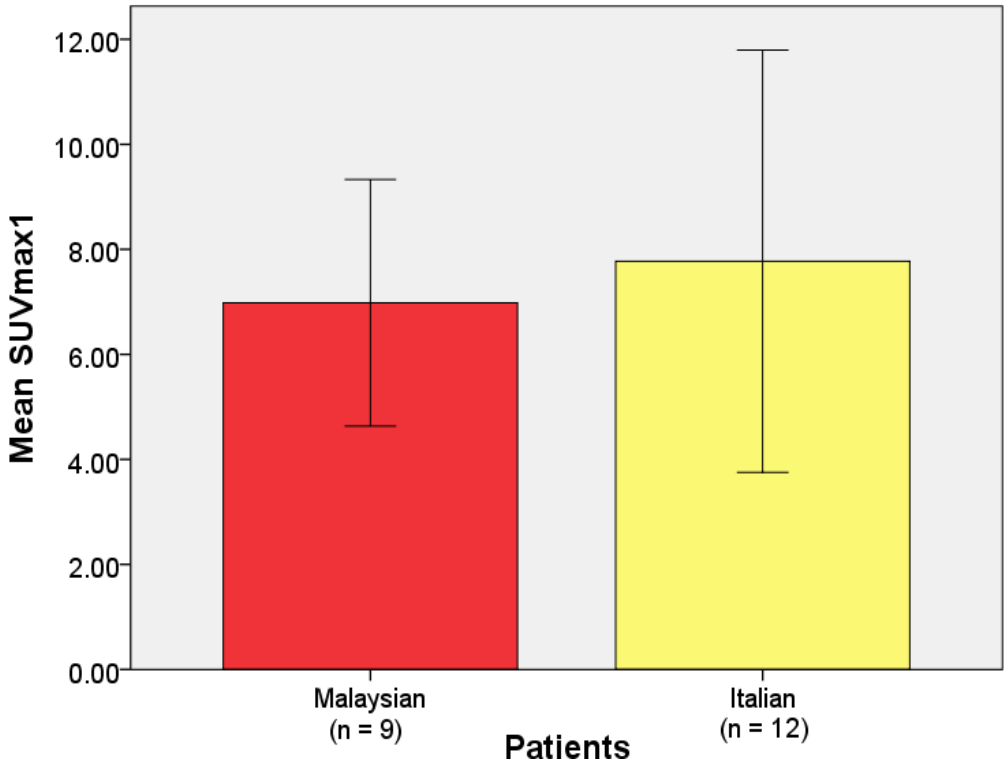

Figure 4.13: Bar charts show the mean SUVmax1 values of EPTB lesions in both Malaysian and Italian patients. There is no significant difference between these two mean values, as the independent samples t-test results with *P* = 0.404. *Error bars represent* ± *standard deviation.*

4.1.3. Follow-up FDG PET/CT scan

All six patients were treated with anti-tuberculous drugs for at least six months prior to the follow-up scanning acquisition. From the follow-up FDG PET/CT images, twelve EPTB lesions were re-evaluated and reviewed (refer to Table 4.7). Of that, eight lesions were found to have no more FDG uptake, which then had been classified as complete remission and positive treatment response (Fig. 4.14 and 4.15). On the contrary, the other four lesions still demonstrated a significantly high FDG uptake (SUVmax > 2.5), and categorised as the active EPTB lesions.

4.1.3.1. Comparison between the SUVmax values of EPTB lesions in the follow-up and initial diagnostic FDG PET/CT scans

When comparing the SUVmax values of the detected EPTB lesions during the follow-up scan with the initial PET/CT fusion images of the diagnostic process, the four EPTB lesions exhibited a substantial reduction in their SUVmax values. However, these lesions had demonstrated an increasing pattern in the SUVmax values of the delayed PET/CT fusion images (Fig. 4.16 and 4.17). This imaging characteristic was assumed to be a sign of an active lesion with a partial treatment response, and therefore the anti-tuberculous treatment of these particular patients was continued for another three months, or in some patients up to six months. These findings show that FDG PET/CT imaging can be considered as a valuable imaging modality for detecting and monitoring the treatment response of EPTB patients. Furthermore, DTPI may offer some helps to the physician in assessing the activity status of EPTB lesion, which then will facilitate the treatment management of the patient.

Table 4.7: Comparison between the initial diagnostic and follow-up FDG PET/CT findings of the first six Malaysian EPTB patients.

Patient no.	Lesion site	Initial diagnostic PET/CT			Follow-up PET/CT		
		SUVmax1	SUVmax2	%ΔSUVmax	SUVmax1	SUVmax2	%ΔSUVmax
1	1. Right base of the neck	8.0	10.4	30.0	Complete remission		
	2. Right parathyroid	8.6	11.8	37.2	Complete remission		
	3. Right infraclavicular	8.3	11.6	39.8	4.3	6.7	55.8
	4. Right paratracheal	11.7	15.7	34.2	5.3	8.1	52.8
2	T12 and L1 vertebral bodies	7.2	9.5	31.9	7.0	9.0	28.6
3	Left submandibular node	9.7	11.2	15.5	Complete remission		
4	Right hip joint	8.3	8.9	7.2	4.1	4.7	14.6
5	1. L3-L4 intervetebral disc space	8.5	10.7	25.9	Complete remission		
	2. Left psoas muscle at level L4	6.7	8.1	20.9	Complete remission		
6	1. Right retrocrural node	6.0	6.0	0.0	Complete remission		
	2. Right subhepatic node	3.5	4.3	22.9	Complete remission		
	3. Peripancreatic node	7.1	8.1	14.1	Complete remission		

T, thoracic vertebrae; L, lumbar vertebrae; SUVmax1, maximum standardised uptake values at early imaging; SUVmax2, maximum standardised uptake values at delayed imaging; %ΔSUVmax, percentage difference of SUVmax values.

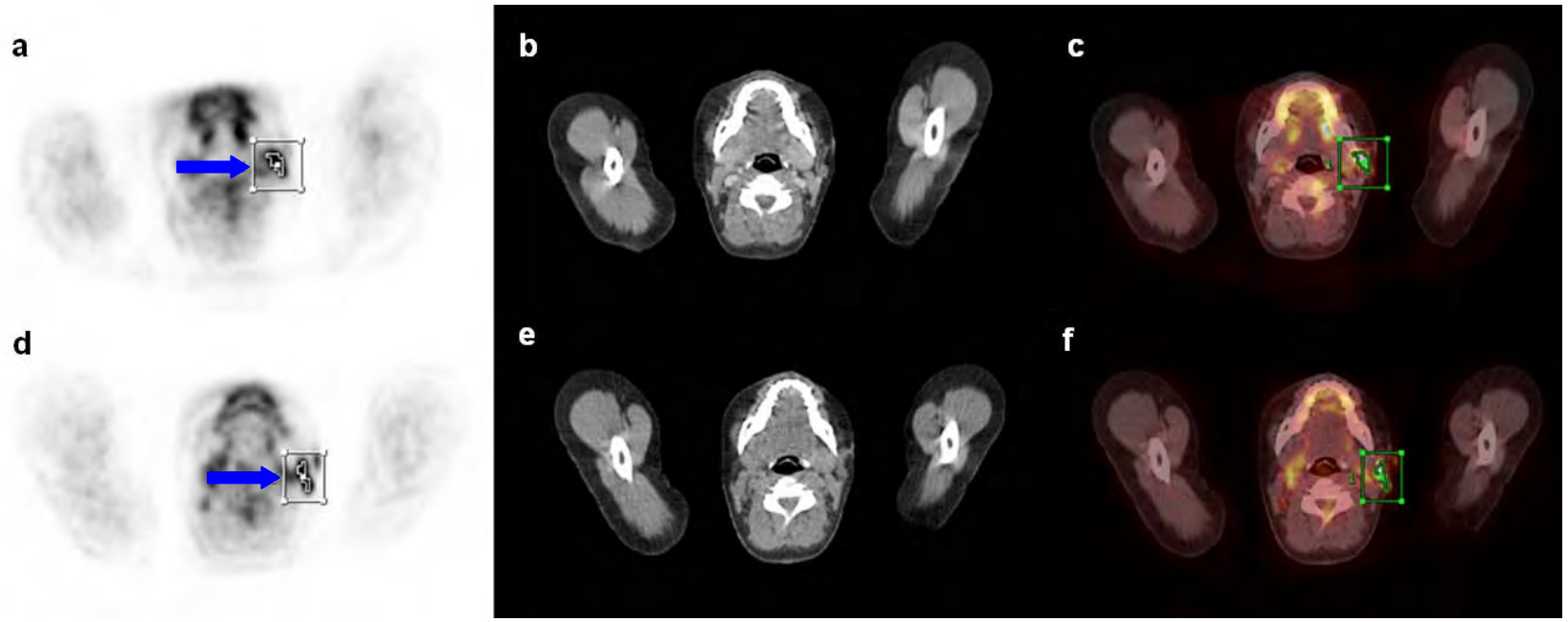

Figure 4.14: PET/CT images during the diagnosis process of patient 3 of Malaysian patients show an avid FDG activity at her left submandibular lymph node (blue arrows). (a) Axial PET image of early scan. (b) Axial Contrast-enhanced CT (CECT) image of early scan. (c) Axial PET/CECT fusion image which demonstrated a volume of interest (VOI) at the left submandibular lymph node with 9.7 in SUVmax value. (d) Axial delayed PET image at almost the same level as in (a). (e) Axial delayed CT image at almost the same level as in (b). (f) Axial PET/CT fusion image showed higher SUVmax value; 11.2. The percentage difference between these two SUVmax values (%ΔSUVmax) was about 16%.

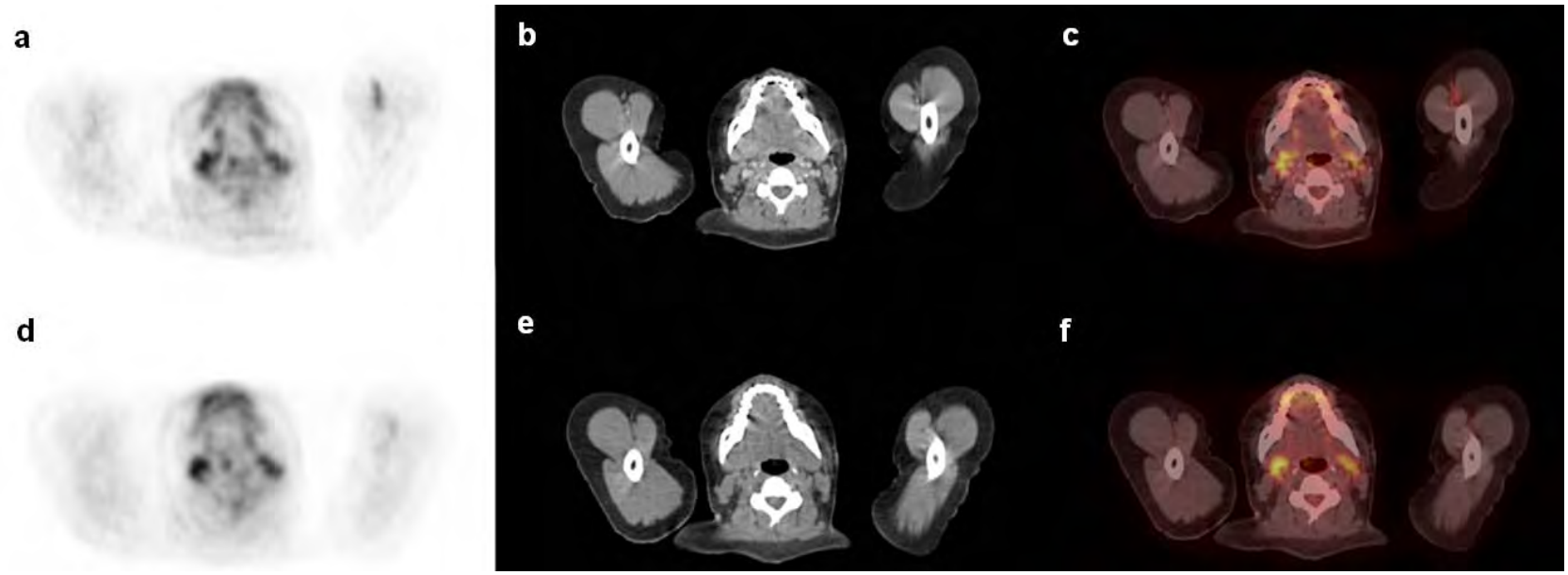

Figure 4.15: Follow-up PET/CT images of patient 3 of Malaysian patients at almost the same level as in Fig. 4.14, show no more avid FDG activity at her left submandibular lymph node. (a) Axial PET image of early scan. (b) Axial Contrast-enhanced CT (CECT) image of early scan. (c) Axial PET/CECT fusion image. (d) Axial delayed PET image at almost the same level as in (a). (e) Axial delayed CT image at almost the same level as in (b). (f) Axial PET/CT fusion image at almost the same level as in (c). These findings have been classified as complete remission of the disease. Note that the bilateral symmetrical FDG avid areas are found to be caused by the physiological brown fats uptakes.

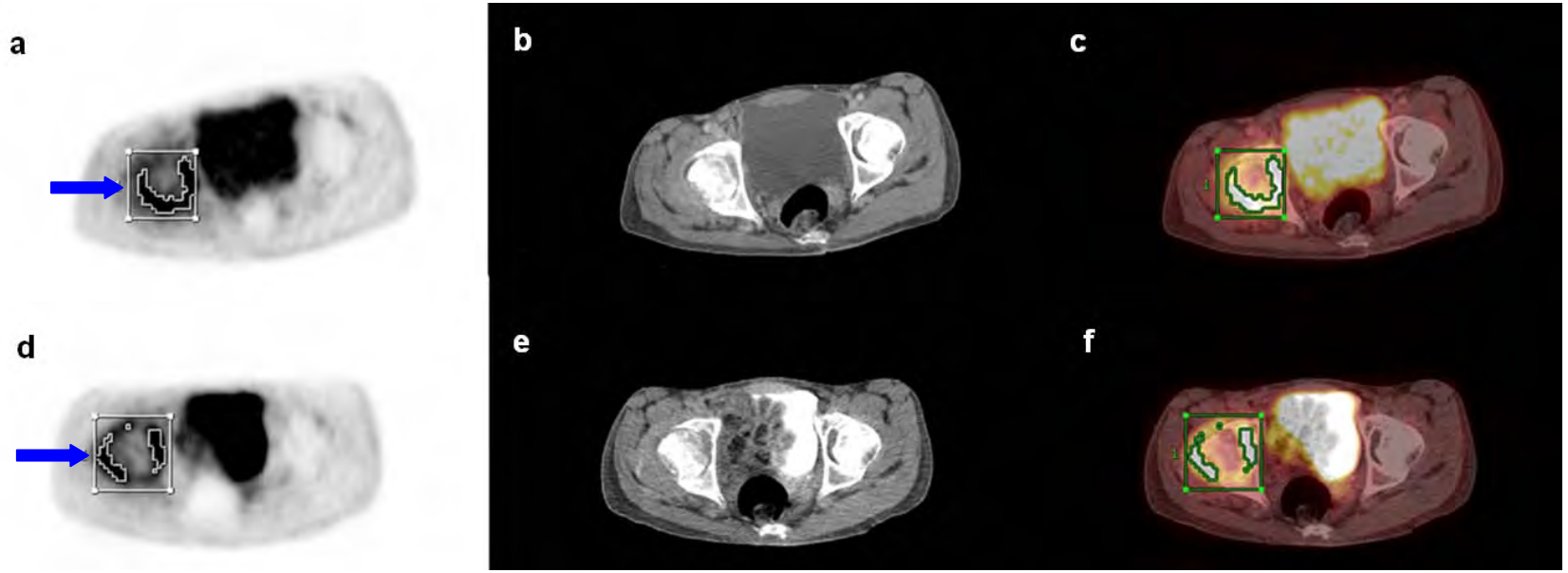

Figure 4.16: PET/CT images during the diagnosis process of patient 4 of Malaysian patients show an avid FDG activity at his right hip joint (blue arrows). (a) Axial PET image of early scan. (b) Axial Contrast-enhanced CT (CECT) image of early scan. (c) Axial PET/CECT fusion image which demonstrated a volume of interest (VOI) at the right hip joint with SUVmax value of 8.3. (d) Axial delayed PET image at almost the same level as in (a). (e) Axial delayed CT image at almost the same level as in (b). (f) Axial PET/CT fusion image showed higher SUVmax value; 8.9. The percentage difference between these two SUVmax values (%ΔSUVmax) was about 7%.

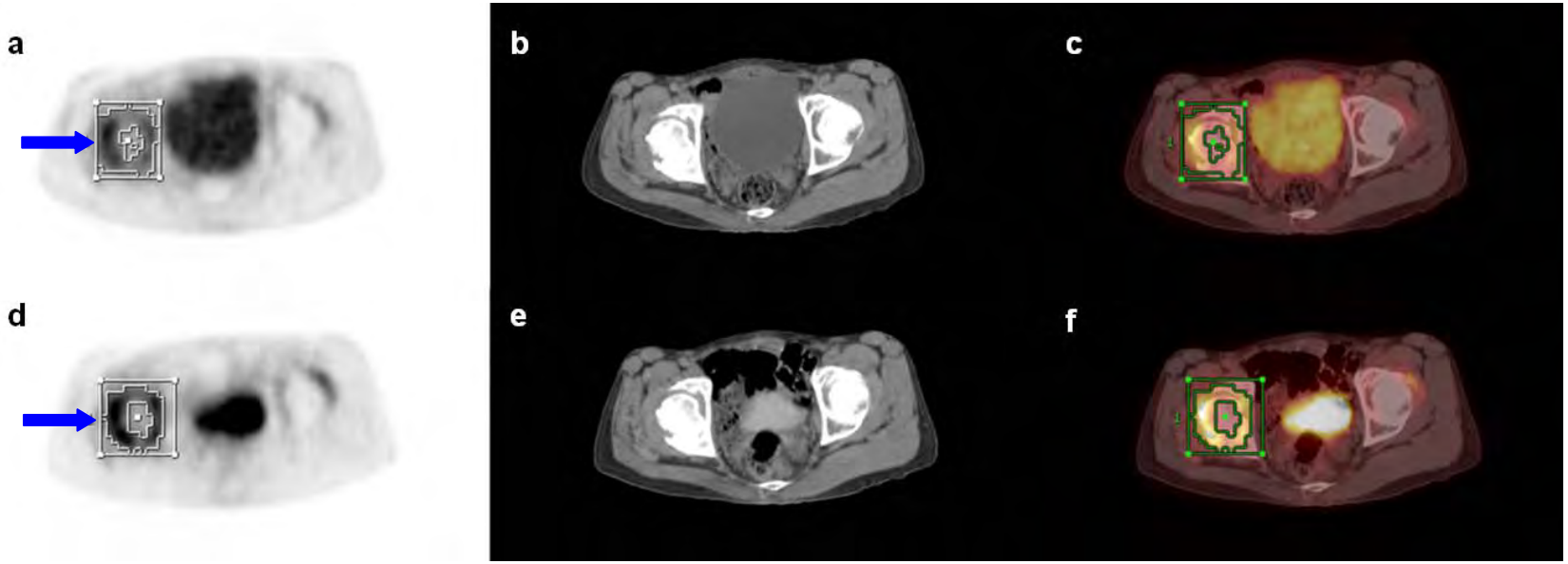

Figure 4.17: Follow-up PET/CT images of patient 4 of Malaysian patients show less avidity of FDG uptake at his right hip joint (blue arrows), as compared with the previous images in Fig. 4.16. (a) Axial PET image of early scan. (b) Axial Contrast-enhanced CT (CECT) image of early scan. (c) Axial PET/CECT fusion image with SUVmax value of 4.1 at the right hip joint. (d) Axial delayed PET image at almost the same level as in (a). (e) Axial delayed CT image at almost the same level as in (b). (f) Axial PET/CT fusion image showed higher SUVmax value; 4.7. The percentage difference between these two SUVmax values (%ΔSUVmax) was about 15%, which corresponds to an active lesion. However, this less avidity of FDG uptake of the lesion is classified as a partial treatment response.

4.2. Discussion

All the detected EPTB lesions of both Malaysian and Italian patients were found to have high accumulation of FDG. In addition, the application of iodine-based contrast media during the CT scan of FDG PET/CT imaging in the nine Malaysian EPTB patients demonstrated no significant changes in the SUVmax values of the lesions and the four normal organs. However, DTPI of FDG PE/CT scan seemed to be insufficient imaging technique for differentiating between EPTB and non-EPTB lesions. Reasons behind all of these findings are discussed in the following sections.

4.2.1. FDG uptake in EPTB lesions

In order to assess the feasibility of FDG PET/CT imaging in detecting EPTB lesions, it is essential to have a clear understanding of the mechanism that causes a high FDG uptake in this type of lesion. Pathophysiologically, EPTB emerges from the evolution process of primary TB infection [15]; in which the normal route for extrapulmonary spread of TB initially starts with the transportation of tubercle bacilli into the lymphatic system and followed by the dissemination of these bacilli into the blood circulation system [81]. Thus, the accumulating mechanism for FDG in EPTB lesions is strongly believed to be the same as in pulmonary TB (PTB) lesions.

Mycobacterium tuberculosis commonly enters the human body via the respiratory tract. As the first defence mechanism to stop the intrusion, the alveolar macrophages will phagocytose this pathogen [10]. This process explains the major role of macrophages in combating TB infection. Other inflammatory cells such as lymphocytes and neutrophils are also responsible for overcoming this infection [10]. Indeed, at an active stage, all these inflammatory cells will have high glucose metabolic

activity [6]. Therefore, the high accumulation of FDG at the sites of active tuberculous lesions is not a surprising finding, and it can be clearly seen in PET and/or PET/CT fusion images.

An earlier study by Ichiya *et al.* [138] found that positron emission tomography (PET) could be used in detecting infectious lesions such as PTB. However, there is still scarce data on the use of FDG PET/CT imaging during the diagnostic procedure of EPTB infectious disease. Only a few recent studies have found that EPTB lesion could have an FDG avid area in PET/CT images [7, 19, 62, 139, 140]. Similarly, in this study, all the detected EPTB lesions (from both populations; Malaysia and Italy) exhibit high SUVmax values; ranging from 2.8 to 20.8. Thus, based on the findings of this clinical imaging study, FDG PET/CT scan has been proven to offer valuable diagnostic information in depicting EPTB lesions.

On the other hand, when comparing the mean SUVmax1 values of EPTB and non-EPTB lesions among all sixteen Malaysian patients, it showed an insignificant statistical difference (7.0 ± 2.4 vs. 8.8 ± 4.6, $P = 0.07$), with a substantial overlapping in the SUVmax1 values of these two groups of lesions. Based on these results, it is strongly suggested that the SUVmax1 value alone cannot clearly differentiate between EPTB and other infectious lesions, although FDG PET/CT imaging can reliably depict EPTB lesions. Therefore, in the standard clinical practice, to establish the final/definite diagnosis of a disease, the semiquantitative analysis of PET/CT fusion images still needs to be augmented with other radiological and/or pathological findings. In addition, it has been recommended that extra caution and attention should be taken when interpreting FDG PET/CT images, especially if TB is considered as epidemic/endemic disease in a particular region or state [123, 132].

4.2.2. Effects of iodine contrast media on SUVmax values of PET/CT images

The utilisation of iodine-based contrast media during CT scan of PET/CT imaging is still considered as a controversial issue [115]. Few studies recommend that unenhanced CT scan is sufficient to be used during the PET/CT imaging acquisitions [141, 142], whereas others advocate that the PET/contrast-enhanced CT (PET/CECT) imaging is the real "one-stop-shop" examination, which offers more accurate diagnosis of various diseases [25, 121, 143]. The advocates argue that PET/CECT scan could result in a change of patient's clinical management, which may then avoid any unnecessary therapy [144, 145]. Besides, it has been reported that there is no pharmacologic interaction between iodine contrast media and FDG, as the injections are conducted with an hour interval between them [113]. Therefore, in this study, FDG PET/CECT scans were carried out during the initial whole body imaging of all Malaysian patients (except for patient 14 who was previously diagnosed with end-stage renal failure).

The PET/CT image analysis using the standardised uptake values (SUVs) was reported to provide more reliable diagnostic information than that of the visual assessment [62]. However, there are several factors that could affect the reproducibility of these SUVs, which mostly depends on the scanning protocols like time of imaging (after FDG injection), type of reconstruction algorithms, type of attenuation maps, size of the region of interest, changes in uptake by organs other than the pathologic lesion, and methods of analysis (SUVmax and SUVmean) [146]. As a consequence, in standard clinical practice, the SUVs technique of PET/CT image analysis is compared and augmented with the findings of the other conventional imaging modalities in order to establish the imaging diagnosis of a disease.

The application of iodine-based contrast media in CT component of PET/CT imaging could be problematic due to incorrect mapping of the PET attenuation correction factors that have been generated from the CECT image dataset [122]. During the calculation of the PET attenuation correction factors, the conversion algorithm may not be able to distinguish between the bony structures and the highly enhanced soft tissues, and this will lead to an overestimated value of the correction factors [115-117]. However, this effect has been found to be clinically insignificant because it does not change the diagnostic interpretation of a disease [113, 118, 119, 122].

All the above data have been acquired from various types of cancer patients. To date, no study has attempted to address this issue in inflammations/infections, more specifically in EPTB infectious disease. Thus, in this study, the differences in SUVmax values of five different tissues (including the lesions) from the nine Malaysian EPTB patients were quantified. Interestingly, the results showed that none of the changes in any of these tissues were found to be statistically significant (all *P* values were higher than 0.05). Based on these findings, it is accepted that iodine-based contrast media can safely be applied in FDG PET/CT imaging of EPTB patients, without producing any significant effects on the SUVmax values regardless of either in the lesions or the normal organs.

4.2.3. Dual time point imaging (DTPI) of FDG PET/CT scan in EPTB patients

Currently, there is no consensus on the optimal scanning protocols of FDG PET/CT imaging that can be employed for accurately differentiating between inflammatory/infectious and malignant lesions [5]. An earlier animal model study by Yamada *et al.* [6] found that the FDG uptake of an inflammatory/infectious tissue

reached its peak in about 60 min after the time of injection, but then it gradually decreased with time. On the contrary, malignant lesions have been shown to keep increasing the FDG uptake for up to several hours after the injection time [98]. Based on this unique imaging characteristic of these two different pathologies, numerous studies have postulated that DTPI technique is a better and more reliable imaging method for differentiating multiple types of lesions on FDG PET/CT imaging [7, 21-23, 62, 109].

The usefulness of DTPI technique in distinguishing between benign and malignant lesions in the thoracic region had been previously investigated in few studies [102, 104, 123, 132]. All these studies highlighted that the SUVmax value of active pulmonary tuberculosis (PTB) lesion could have an increment of up to 46% on the delayed PET/CT images, as compared with the initial images. Based on these findings, it shows that active PTB lesion has a similar imaging feature as in the malignant lesion. Therefore, DTPI technique of FDG PET/CT scan could not be effectively applied for differentiating benign from malignant lesions, particularly for the tuberculosis endemic/epidemic countries [123, 132].

On the other hand, a recent study has been conducted by Sathekge *et al.* [7] with the utilisation of DTPI technique during FDG PET/CT scans in a group of sixteen confirmed tuberculosis patients. As expected, their entire EPTB lesions show increasing pattern in the SUVmax values of the delayed FDG PET/CT images, with the highest mean percentage change of about 45% has been recorded in the SUVmax values of the bone involvement cases. These findings are in good agreement with the results of this clinical imaging study, where the SUVmax values of all detected EPTB lesions also increase during the delayed PET/CT imaging (exclude the two lesions of patient 8; a

relapsed EPTB patient, and one lesion of patient 6). However, when comparing the mean percentage change in the SUVmax values of our EPTB and non-EPTB lesions, it shows a statistically insignificant difference. This result indicates that DTPI technique is not a practical imaging method in distinguishing between EPTB and non-EPTB lesions on FDG PET/CT scan. Furthermore, it may conclude that the initial whole body PET/CT scan is a sufficient imaging procedure for differentiating EPTB from other infectious diseases.

The findings on the utilisation of DTPI technique during FDG PET/CT scans in the eleven of Malaysian patients have been documented and accepted for publication in Journal of Medical Imaging and Radiation Oncology; JMIRO.

4.2.4. FDG PET/CT imaging in assessing therapeutic responses of EPTB patients

Apart from detecting EPTB lesions, FDG PET/CT scan has been recently found to be a useful imaging tool for monitoring the therapeutic responses in EPTB patients [139]. Correspondingly, it is in accordance with the findings of this clinical imaging study. Out of the six Malaysian EPTB patients who underwent the follow-up FDG PET/CT scan (after completing the standard 6 months anti-TB treatment), complete remission signs with undetectable FDG uptake were clearly demonstrated in all EPTB lesions of the three patients. These imaging findings were classified as a positive treatment response, and for this reason, their anti-TB drugs treatment had been stopped.

In contrast, the other three patients were categorised as partially responded to anti-TB treatment, where a substantial decline in the SUVmax values was detected in all their EPTB lesions. But, these lesions had also exhibited increasing patterns on the

delayed PET/CT images, which could be classified as a sign of an active lesion with partial treatment response. Based on these results, it is highly recommended that FDG PET/CT imaging should be applied in evaluating and monitoring responses to anti-TB treatment in patients with EPTB. In addition, the %ΔSUVmax value can potentially be used as a clinical imaging indicator for determining the activity status of EPTB lesion, in which this method may offer some benefits to the physician in choosing and deciding the correct treatment management for EPTB patients. However, this study warrants to be conducted in larger cohort of EPTB patients.

4.2.5. Technical factors that can improve the quality of FDG PET/CT images

As mentioned earlier, all FDG PET/CT image acquisitions of the sixteen Malaysian patients were conducted under the normal breathing phase (no information regarding this issue was obtained from the retrospective Italian data). Respiratory motion is known to be one of the most common causes for the misregistration artifact, which occurs mainly due to the inconsistency in position of the chest between both PET and CT acquisitions [42]. This kind of artifact has clearly been seen on the thoracic region of three patients (patients 8, 10 and 11; refer to Fig. 4.18). However, this misregistration artifact does not cause any problems in interpreting PET/CT fusion images, and in fact, this issue can be resolved effectively by reviewing the CT images for any sign of anatomical abnormalities [42]. Based on this observation, it has been believed that the normal breathing technique is acceptable to be used during PET/CT imaging.

In this clinical imaging study, all sixteen Malaysian patients placed both arms at above of the head (please refer to Fig. 4.7), but it was not the case for those twelve Italian patients (Fig. 4.19). Nevertheless, during the follow-up PET/CT scans, only one

of the six Malaysian patients (patient 2) was not capable of positioning both arms at above of his head; due to back pain, consequently the scanning was performed whilst his arms were placed by the side. Based on his body size, this patient was not categorised as a large patient, and therefore no truncation artifact was detected at the edge of CT Field of View (FOV) [68]. However, some fuzzy streaking lines were noticed at the area beyond his hands, which could have been caused by the humerus bones of the upper limbs, as shown in Fig. 4.20. From this finding, it is strongly suggested that whenever possible the whole body PET/CT imaging should be conducted with both arms placed over the head [146]. This method is optimal for preventing the occurrence of the truncation artifact, in addition to generating clearer PET/CT fusion images [42].

Metallic implants can cause streaking artifacts on PET/CT fusion images [63, 147]. These artifacts were found in two of the Italian patients, who had metallic prosthetic implants at the lower lumbar region (patient 7) and right hip joint (patient 8). As recommended, the image should be interpreted using non-attenuated PET images [63, 64], however, in this study, the images of these two patients were analysed by applying the bone window setting CT images (window width: 2000, and window level: 350), and then fused with PET images (Fig. 4.21). Based on our experience, this technique minimises the amount of streaking artifacts, making it helpful for better interpreting and analysing PET/CT fusion images.

The utilisation of an intravenous iodine-based contrast media during the CT scan of PET/CT imaging has been reported to cause an artifact on PET images [67]. However, as mentioned earlier, it was not the case in this clinical imaging study. No statistically and clinically significant effects were demonstrated on the SUVmax values

of either the lesion or the normal organs, even though an intravenous injection of iodine-based contrast media had been applied during the CT scan of FDG PET/CT imaging in a group of nine EPTB patients.

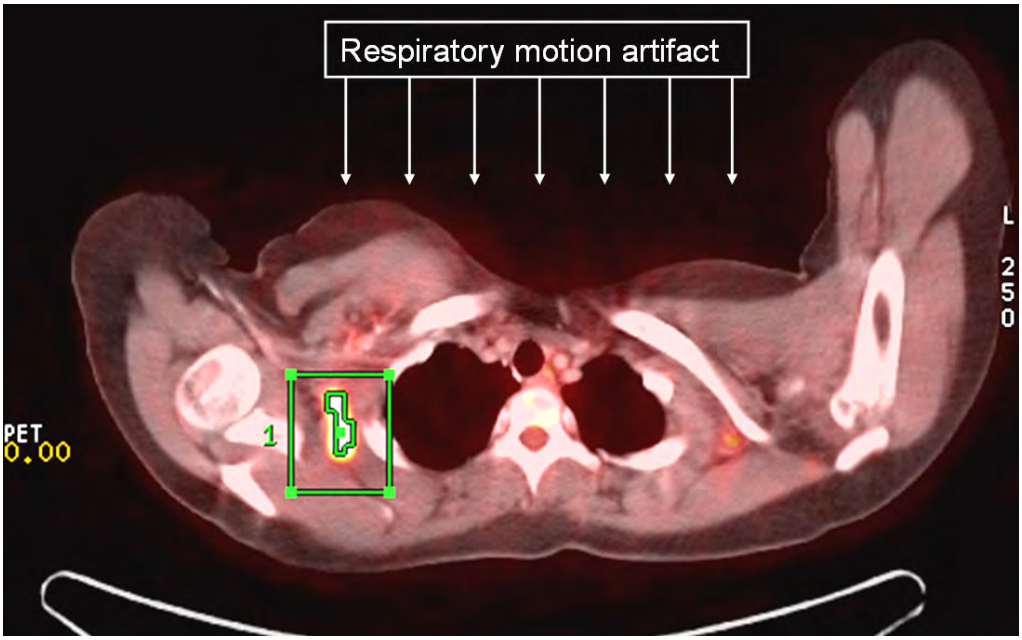

Figure 4.18: PET/CECT fusion image of patient 8 of Malaysian patients shows the respiratory motion artefact, which can be seen as the fuzzy reddishness outline particularly at her anterior thoracic region. The green box represents a volume of interest (VOI) at the right subscapular soft tissue space with SUVmax value of 11.7.

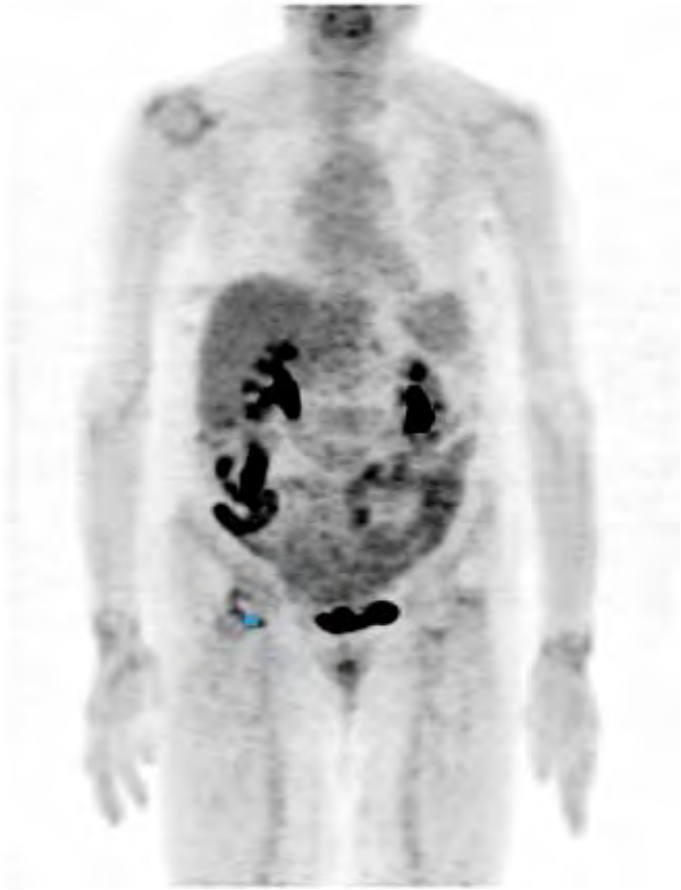

Figure 4.19: Anterior Maximum Intensity Projection (MIP) image from one of Italian patients (patient 8) shows both hands position (by the sides) during her PET/CT imaging. Small blue box demonstrates an avid FDG activity at her right hip joint with SUVmax value of 4.9.

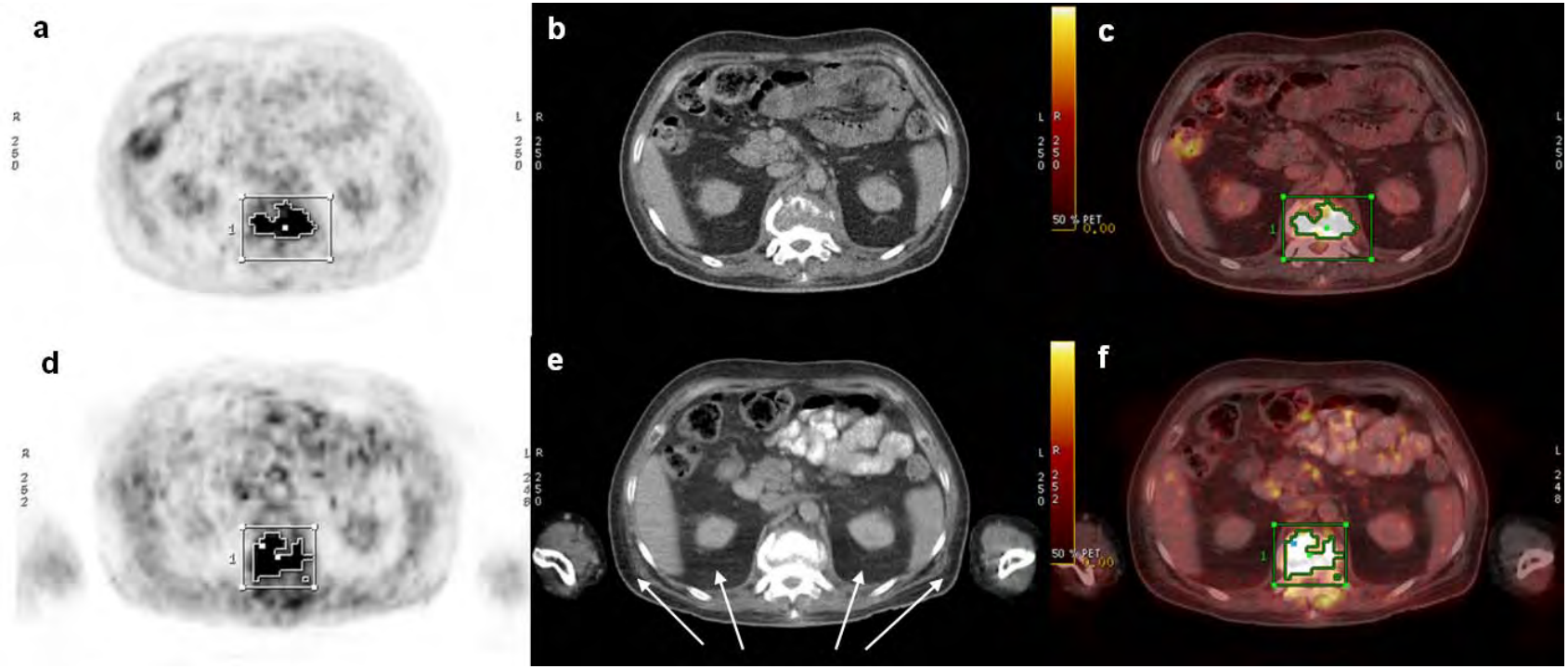

Figure 4.20: The axial PET (a & d), Contrast-enhanced CT (b & e) and fused PET/CECT (c & f) images from patient 2 of Malaysian patients. The upper row (a-c) images represent the PET/CT images during the initial diagnostic scan, whilst the lower row (d-f) images are during the follow-up scan. The white thin arrows demonstrate the fuzzy streaking lines, which occurs due to the humerus bones of the upper limbs. However, this patient is not large enough to produce truncation artifact at the rim region of CT Field of View (FOV).

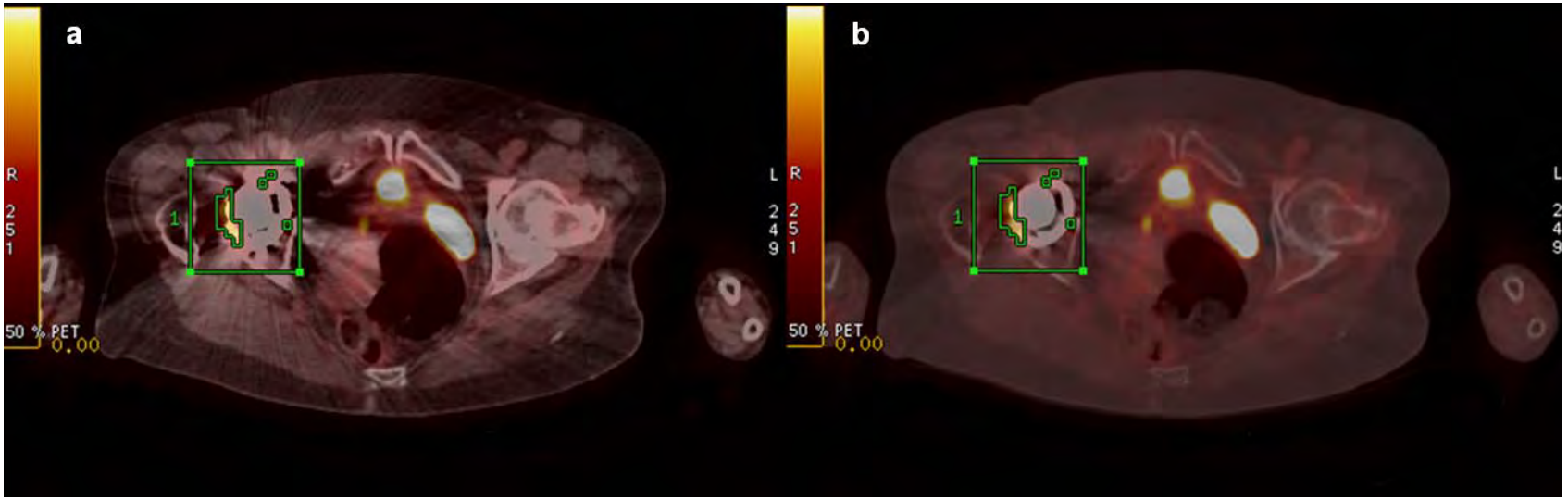

Figure 4.21: Axial PET/CT fusion images from patient 8 of Italian patients show streaking artifact, which has been caused by metallic hip prosthetic implant at her right hip joint. (a) PET/CT fusion image at an abdomen window CT setting; width: 400 and level: 40, demonstrates a remarkable streaking artifact. (b) Less streaking artifact is seen when the PET image has been fused with bone window setting of CT image; width: 2000 and level: 350. The SUVmax values of both VOIs from these two images are same; 4.9.

Overall, here are the findings of this clinical imaging study:

1. All detected EPTB lesions from both Malaysian and Italian patients have shown high FDG uptakes, with the SUVmax values ranging from 2.8 to 20.8. These lesions can clearly be depicted on FDG PET/CT fusion images. Thus, it has been proven that FDG PET/CT scan is an important imaging procedure for detecting EPTB lesions. Furthermore, in the detection of EPTB lesions, FDG PET/CT imaging has demonstrated a relatively higher in its diagnostic performance as compared with the other conventional imaging modalities.
2. The application of intravenous iodine-based contrast media does not cause any statistically and clinically significant differences in the SUVmax values of either in EPTB lesions or the normal organs. Therefore, an intravenous injection of iodine-based contrast media can safely be applied during the CT scanning of FDG PET/CT imaging of EPTB patients.
3. Dual time point imaging (DTPI) technique of FDG PET/CT scan seems to be an impractical imaging method for differentiating between EPTB and non-EPTB lesions. As a result, the initial whole body FDG PET/CT imaging is a valuable scanning procedure in distinguishing EPTB from other infectious diseases.
4. FDG PET/CT imaging provides more diagnostic information in terms of evaluating and monitoring the therapeutic responses of EPTB patients, which may help the physician for the treatment management of EPTB patient.
5. To prevent the occurrence of truncation artifact on PET/CT fusion images, the scanning should be performed with both arms are placed at above of the head. In addition, the normal breathing is an adequate method for the image acquisitions of PET/CT imaging.

SECTION B

PHANTOM STUDY

CHAPTER 5

The results displayed in the previous chapter clearly indicate that the utilisation of an intravenous iodine contrast media during the CT scan of FDG PET/CT imaging will not significantly affect the SUVmax values of the five different tissues (heart, liver spleen, urinary bladder and lesion) in a group of nine confirmed EPTB patients. Thus, to further prove this clinical finding, an experimental phantom study was executed. This chapter briefly describes the issues regarding the application of iodine contrast media in FDG PET/CT scan. The experimental set up and results of the application of iodine contrast media during the CT scan of FDG PET/CT imaging and their effects on the SUVs (SUVmax and SUVmean) of PET/CT fusion images are then presented and discussed.

5.1. Introduction

In PET/CT imaging, the CT data is commonly used for two main purposes: 1) calculate the attenuation correction factors of the PET emission data, and 2) provide an accurate anatomical localisation of the lesions. As the PET attenuation correction factors can be derived from the CT data, hence, the PET transmission scan of using an external radiation source may no longer be necessary [43]. Routinely, the conversion of CT data (expressed in Hounsfield Units; HU) into the PET attenuation correction factors employs a simple bi-linear transform method [2, 4, 5], however this method is only well established for unenhanced CT scan [43, 49, 122]. Therefore, the CT scanning of PET/CT imaging is generally acquired without the utilisation of any contrast enhancing agents [121].

In contrast, when the CECT data is used for calculating the PET attenuation correction factors, it could cause the image artifacts on PET/CT fusion images (appear as FDG avid areas) [67, 148]. These artifacts occur due to an overlapping between the

HU values of the contrast enhanced soft tissues and the bones in CECT images, and accordingly, the standard conversion algorithm cannot distinguish these two structures [122]. This will lead to an overestimate on the PET attenuation correction factors [115-117]; because the attenuation value of iodine falls off more rapidly with increasing energy (mostly caused by the photoelectric effect) as compared with the attenuation values of tissues having less density than iodine [118]. The fundamental explanation of these image artifacts is well addressed in the literature [49, 122, 149, 150].

This study attempted to determine if any correction was required when iodine contrast media had been employed during FDG PET/CT imaging. The changes in the SUVs caused by the administration of iodine contrast media were measured, using a phantom designed to simulate as closely possible as in the actual patient scanning conditions. For this reason, an anthropomorphic phantom had been utilised in this study, and it was specifically designed to simulate a case of spinal tuberculosis at the lower abdomen region. The phantom allowed insertion of three dried human spinal vertebrae; to simulate the spine, and a tube of containing FDG solution could be positioned in the foramen; to simulate a spinal lesion. To the best of our knowledge, no phantom study has been previously reported to determine the effects caused by the application of non-ionic iodine contrast media on the SUVs in this clinically important geometry. Therefore, the aim of this study was to address a gap in the literature by quantifying the differences on the SUVs of the PET/CT images under the conditions above.

5.2. Materials and methods

5.2.1. PET/CT imaging acquisition

All the imaging acquisitions of this study were performed on a Philips Gemini Dual PET/CT system at the Nuclear Medicine Department of The Alfred Hospital, Melbourne, Australia. This integrated imaging system consists of an Allegro 3-D PET scanner with gadolinium oxyorthosilicate (GSO) crystal detectors, and an Mx8000 EXP Dual-Slice CT scanner. The image acquisition commenced with a low-dose CT scout view (120 kVp), to set the scan lengths of the CT and PET scans, followed by a CT scan (140 kVp, 30 mAs, slice thickness of 5 mm, pitch factor of 1.0 and gantry rotation speed of 1.0 s), and finally the PET emission scan. The scanning parameters of the PET emission were: 3-D acquisition mode; slice image matrix of 144 x 144 pixels, axial Field of View (FOV) 18 cm, acquisition time 3 min per FOV, and slice thickness 4 mm with 5 mm reconstruction thickness to match the CT images.

5.2.2. FDG PET/CT scans of the phantom

All FDG PET/CT scans were conducted using an anthropomorphic phantom, comprising an ovoid plexiglass cylinder with such size and thickness as to replicate a standard man's chest wall. These phantom scans are divided into four different phases:

1. *Phase 1*: Simulation of an enhanced liver.
2. *Phase 2*: PET/CT imaging of the simulated liver.
3. *Phase 3*: PET/CT imaging of the simulated liver and bony lesion.
4. *Phase 4*: PET/CT imaging of the simulated liver, bony lesion and blood vessels.

As stated above, across all the phases of this phantom study, liver has been chosen as the organ of interest. It is because of three main reasons:

1. Liver is the second largest organ in human body.
2. Liver shows an elevation in CT numbers (HU) on CECT images.
3. Liver has a moderate physiological uptake of FDG on PET images.

5.2.2.1. *Phase 1:* Simulation of an enhanced liver

The uptake of iodine contrast media in the liver is dependent upon the delay from injection to scanning, but based on our clinical experience and the data published by Halls [151], the optimum HU for a normal liver due to iodine contrast media uptake in a CECT scan should be more than 100. In this study, a one litre normal saline bag was used to simulate a normal liver (labelled as saline bag 2). Prior to the PET/CT scanning procedure, iodine contrast media (Omnipaque 300 mgI/mL, GE Healthcare) was injected into saline bag 2 (at 5mL intervals). The CT scans were performed until saline bag 2 had an average maximum HU (HUmax) of greater than 100, to simulate the HU values of iodine contrast enhancement in a normal liver. For stabilisation purposes, four extra saline bags were inserted into the phantom along with saline bag 2, as depicted in Fig. 5.1. To eliminate the possibility of machine dependent artifacts influencing the results, the CT scans were conducted using the PET/CT system. These CT scans were also repeated three times to establish reproducibility of the results.

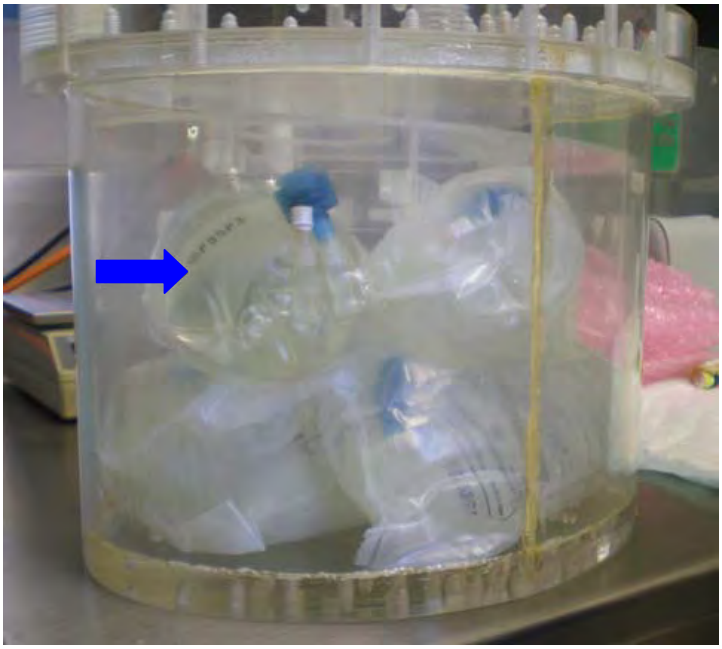

Figure 5.1: The set-up for the anthropomorphic phantom, which has been filled with saline bag 2 and four additional saline bags. The blue arrow shows saline bag 2 which has been injected with 15mL of iodine contrast media, so that the CT number of the bag is over 100 HU and it can be used to simulate iodine contrast enhancement in a normal liver.

5.2.2.2. *Phase 2:* PET/CT imaging of the simulated liver

Two saline bags (saline bag 1; without iodine contrast media, and saline bag 2; with iodine contrast media) were employed during this phase. The saline bags were injected with 9.3 MBq radioactivity of FDG each. For the first scan of this phase, saline bag 1 and four extra saline bags were inserted into the phantom to simulate clinically appropriate scatter conditions for PET/CT imaging. PET/CT2a was then acquired with saline bag 1 in the phantom. For the second scan, saline bag 1 was replaced by saline bag 2. PET/CT2b was then acquired with saline bag 2 in the phantom. The set up of the phantom for imaging is shown in Fig. 5.2.

Figure 5.2: The set-up of the phase 2 phantom imaging study. The phantom is first imaged with saline bag 1 in place to obtain PET/CT2a (saline bag 1 contains radioactive FDG but no iodine contrast media). Then, the phantom is re-imaged with saline bag 2; replacing saline bag 1, to obtain PET/CT2b (saline bag 2 contains the same radioactivity of FDG as in saline bag 1, but also contains the typical clinically observed iodine contrast uptake for a normal liver).

5.2.2.3. *Phase 3:* PET/CT imaging of the simulated liver and spinal lesion

In this phase, a simulation of bony structures was introduced into the anthropomorphic phantom; therefore three dried human spinal vertebrae were used. One test tube (designated tube 1) of volume 10 mL and inner diameter 1 cm containing FDG (1.3 MBq) was inserted into the vertebral foramen of the vertebrae (Fig. 5.3). Saline bags 1 and 2 were re-used for this phase, but with two weeks interval from the phase 2 imaging (to assure that the radioactivity is totally decayed). For this phase both bags were injected with 9.5 MBq radioactivity of FDG. To minimise the impact of minor

variations in phantom geometry on the results, PET/CT imaging was repeated four times, with the following compositions (refer Table 5.1): (a) PET/CT3a imaging of saline bag 1 only, (b) PET/CT3b imaging of saline bag 2 only, (c) PET/CT3c imaging of saline bag 1 and tube 1, and (d) PET/CT3d imaging of saline bag 2 and tube 1.

Figure 5.3: The blue arrow indicates tube 1, showing the positioning into which it has been placed within the vertebral foramen to simulate an FDG avid spinal lesion. This setting is only a gross approximation to spinal tuberculosis. Spinal TB typically grows within the vertebral body and not within the spinal cord [87].

Table 5.1: PET/CT scans of phase 3 phantom study.

PET/CT scanning of phase 3	Simulated situation	Inserted structures
a) PET/CT3a	liver with FDG uptake but without iodine contrast uptake	saline bag 1 only
b) PET/CT3b	liver with FDG and iodine contrast uptake	saline bag 2 only
c) PET/CT3c	liver with FDG uptake but without iodine contrast uptake, and spinal lesion FDG uptake	saline bag 1 and tube 1
d) PET/CT3d	liver with FDG and iodine uptake, and spinal lesion FDG uptake	saline bag 2 and tube 1

5.2.2.4. *Phase 4:* PET/CT imaging of the simulated liver, spinal lesion and blood vessels

In the lower abdomen region, the closest structures to the vertebral columns which are expected to show CECT enhancement are the abdominal aorta and inferior vena cava. To simulate this, another two test tubes were introduced (designated as tube 2 and 3), tube 3 having a higher concentration than tube 2 (19.0 mg/mL vs. 6.0 mg/mL). In this phase, again, two weeks interval from the previous phase was applied. The modular components of the plexiglass phantom for phase 4 were then: saline bag 1 with no iodine contrast and 9.3 MBq of FDG, saline bag 2 with sufficient iodine contrast to increase its CT number by 100 HU and also with 9.3 MBq of FDG, tube 1 with 1.7 MBq of FDG, tube 2 stuck to the side of the vertebrae when deployed, and tube 3 also stuck to the side of vertebrae when deployed (tube 2 and 3 were not deployed at the same time, Fig. 5.4). Six separate PET/CT imaging sessions were conducted in phase 4, with the following phantom compositions (refer Table 5.2): (a) PET/CT4a imaging of the phantom with saline bag 1 and test tube 1, to simulate imaging spinal tuberculosis with liver FDG uptake in the absence of iodine; (b) PET/CT4b imaging of saline bag 2 and tube 1, to simulate imaging spinal tuberculosis with a liver with iodine contrast and FDG uptake; (c) PET/CT4c imaging of saline bag 1, tube 1 and tube 2, to simulate imaging spinal tuberculosis in proximity to blood vessels with a low contrast uptake and a liver with FDG uptake but no contrast uptake; (d) PET/CT4d imaging of saline bag 2 and tube 1 and tube 2, to simulate imaging spinal tuberculosis in proximity to a blood vessel with a low contrast uptake and a liver with FDG uptake and contrast uptake; (e) PET/CT4e imaging of saline bag 1, tube 1 and tube 3, to simulate imaging spinal tuberculosis in proximity to a blood vessel with high contrast uptake and a liver

with FDG uptake and no contrast uptake; (f) PET/CT4f imaging of saline bag 2, tube 1 and tube 3, to simulate imaging spinal tuberculosis in proximity to a blood vessel with high contrast uptake and a liver with FDG uptake and contrast uptake (Fig. 5.4).

Table 5.2: PET/CT scans of phase 4 phantom study.

PET/CT scanning of phase 4	Simulated situation	Inserted structures
a) PET/CT4a	liver with FDG uptake but without iodine contrast uptake, and spine lesion FDG uptake	saline bag 1 and tube 1
b) PET/CT4b	liver with FDG and iodine uptake, and spine lesion FDG uptake	saline bag 2 and tube 1
c) PET/CT4c	liver with FDG uptake but without iodine contrast uptake, spinal lesion FDG uptake and low blood vessel enhancement	saline bag 1, tubes 1 and 2
d) PET/CT4d	liver with FDG and iodine uptake, spinal lesion FDG uptake and low blood vessel enhancement	saline bag 2, tubes 1 and 2
e) PET/CT4e	liver with FDG uptake but without iodine contrast uptake, spinal lesion FDG uptake and high blood vessel enhancement	saline bag 1, tubes 1 and 3
f) PET/CT4f	liver with FDG and iodine uptake, spinal lesion FDG uptake and high blood vessel enhancement	saline bag 2, tubes 1 and 3

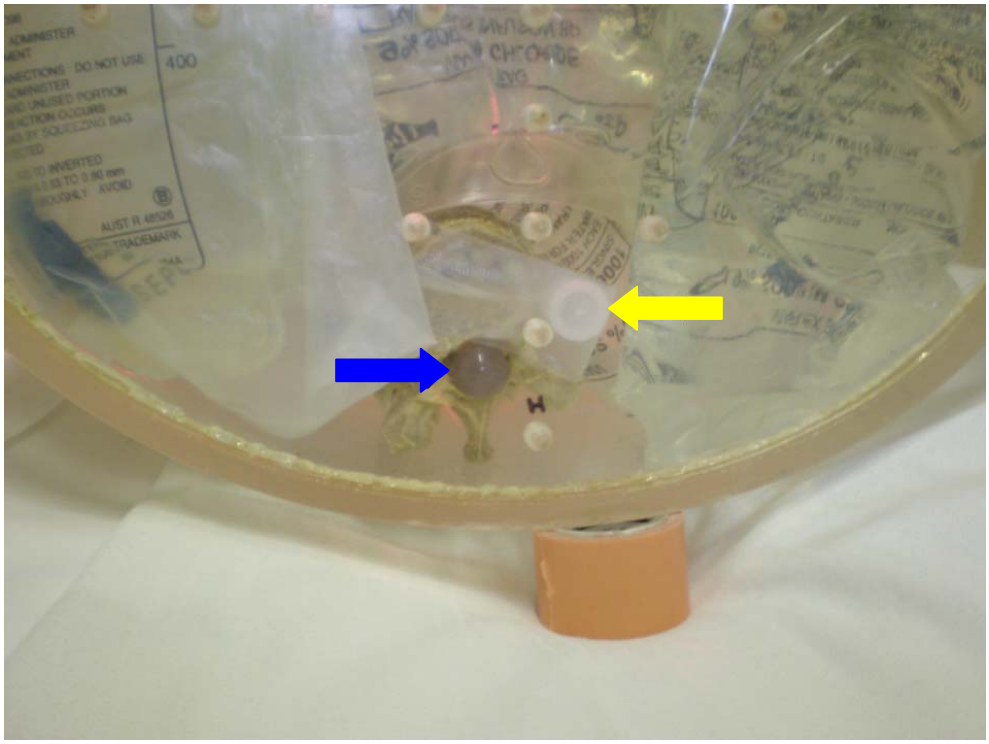

Figure 5.4: The set-up for PET/CT imaging of the phase 4 case (f). The blue arrow shows the position of tube 1 in the vertebral foramen, containing 1.7 MBq of FDG to simulate spinal tuberculosis. The yellow arrow shows the position of tube 3 stuck to the side of dried vertebrae, containing a higher concentration of iodine contrast media (19.0 mg/mL) to simulate the effect of a blood vessel with high contrast uptake. Saline bag 2 (not discernable) is also present to simulate a liver with FDG and iodine contrast uptakes.

5.2.3. Image analysis

As a standard practice of the department, all PET emission images were reconstructed using the 3-D row-action maximum-likelihood algorithm (RAMLA) and the CT dataset was used to calculate the PET attenuation correction factors. All co-registered images were reviewed on the same imaging acquisition computer system in axial, coronal and sagittal planes along with the maximum intensity projection (MIP) images; a common 3-D image used for visualising FDG distribution throughout the body [32]. The CT

images were reviewed in the soft tissue window setting (width: 350, level: 35) for general image interpretation. To measure HUmax for tube 2 and tube 3, the highest pixel values were determined by direct inspection by the operator of the axial images displayed on the CT console.

In order to obtain the SUVs as in a real patient, these values were relative to a nominal clinical injected dose of radioactivity for a 70 kg adult (370 MBq). For each of the structures (saline bags 1 and 2, and test tube 1), the SUVs were quantified by carefully drawing a 2-dimensional (2-D) region of interest (ROI) on the single slice of the attenuation corrected PET/CT fusion images; that gave the highest SUVmax and SUVmean values, using an automatic isocontour technique set at the 70% threshold line of the maximum pixel value (Fig. 5.5c). These ROIs were segmented by an experienced nuclear medicine technologist. The maximum (SUVmax) and mean (SUVmean) values were recorded.

Owing to a very small sample size, thus, the statistical analyses using the non-parametric tests seemed to be more appropriate [152]. The Wilcoxon Signed Rank Test (alternative to the parametric paired samples t-test) was used to determine the difference in SUVs in phase 3 of the phantom study, while for phase 4, the analysis was performed using the non-parametric Friedman Test (alternative to the parametric one-way repeated measures ANOVA). *P* values of less than 0.05 were considered to be statistically significant. The absolute difference in SUVmax and SUVmean values (ΔSUVmax and ΔSUVmean) of each structure was also calculated. These statistical analyses were carried out using the SPSS program for Windows version 18.0.

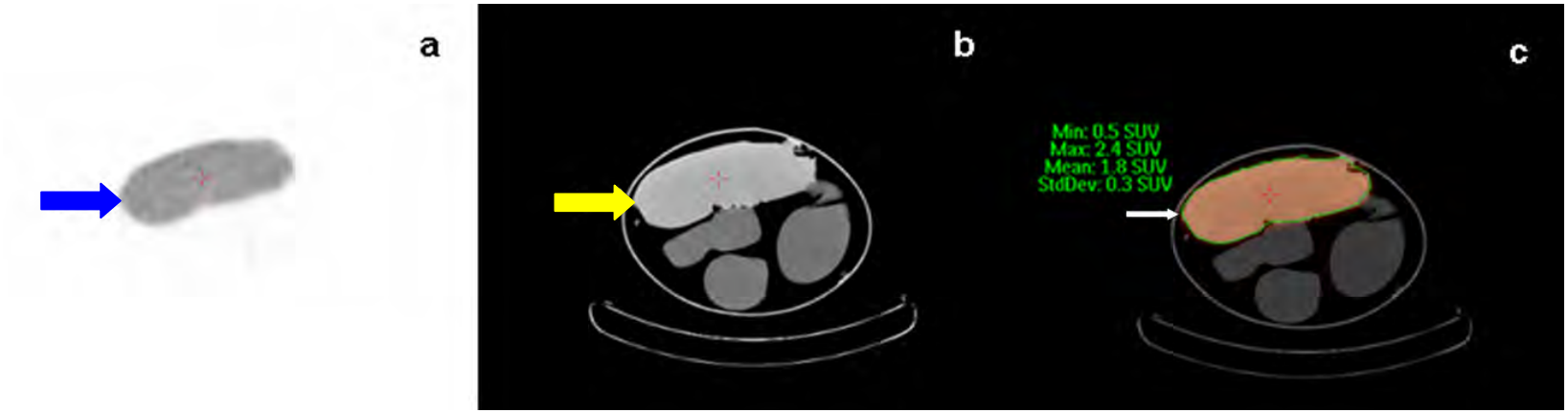

Figure 5.5: An example of the image analysis on axial PET/CT fusion image. (a) PET image without attenuation correction shows the moderate activity of saline bag 2 (blue arrow). (b) CT image shows the contrast-enhancement of saline bag 2 with the average HUmax of 105 (yellow arrow). (c) Attenuation corrected PET/CT image shows the ROI of saline bag 2 with SUVmax and SUVmean values of 2.4 and 1.8, respectively (white arrow).

5.3. Results

Overall, the range of SUVs for saline bags 1 and 2 generated in this study was 1.5 – 2.5. In *phase 1* of the phantom study, the average HUmax values for saline bag 1 and 2 were about 15 and 105, respectively. Saline bag 2 yielded the average HUmax of 105 after the injection of 15mL of iodine contrast media (approximately 4.5 mg/mL in concentration). For *phase 2*, the highest absolute difference in SUVmax value (ΔSUVmax) between saline bag 1 and 2 in the PET/CT images of phase 2 was +0.2 (the range for the SUVmax values of both saline bags was 2.1 – 2.3), whereas the highest ΔSUVmean was equal to zero; the SUVmean value of 2.0 was detected in all imaging planes.

The statistical analyses of the results for *phase 3* are summarised in Table 5.3. The highest ΔSUVmax from saline bags 1 and 2, and tube 1 were -0.2, -0.2 and +0.9, respectively (the ranges were found to be 2.1 – 2.4 for both saline bags, and 9.1 – 12.5 for tube 1). Furthermore, saline bag 2 and tube 1 demonstrated a lesser difference in the highest ΔSUVmean of about -0.4 and +0.6 (the SUVmean values were ranging from 1.5 to 1.9 for saline bag 2, and from 2.4 to 4.5 for tube 1), while saline bag 1 showed a similar value to the ΔSUVmax (-0.2; range of 1.6 – 1.8). However, across all simulations, no statistically significant difference in SUVmax and SUVmean of any structure was observed ($P > 0.05$).

The details analyses of the results for *phase 4* are summarised in Table 5.4. With the separate insertion of other tubes (tubes 2 and 3), the highest ΔSUVmax for saline bags 1 and 2 were +0.2 and +0.1, respectively (the range for the SUVmax values of both saline bags was 2.0 – 2.3). These two structures exhibited an increase and unchanged in the ΔSUVmean: +0.1 for saline bag 1 (it showed the SUVmean value of 1.6) and zero

for saline bag 2 (the SUVmean value of 1.6 was detected in all imaging planes). However, the highest absolute difference in tube 1 remained at the same value (+1.5), for both SUVmax (range from 18.4 – 22.7) and SUVmean (range from 3.6 – 7.3). Again, all these changes were found to be statistically insignificant ($P > 0.05$).

Table 5.3: The results of the statistical analyses of *phase 3* PET/CT imaging.

Structure	Mean ± SD SUVmax[a] (SUVmean[a])	Mean ± SD SUVmax[b] (SUVmean[b])	Mean ± SD SUVmax[c] (SUVmean[c])	Mean ± SD SUVmax[d] (SUVmean[d])	Highest ΔSUVmax (ΔSUVmean)	Wilcoxon test SUVmax (SUVmean)
Saline bag 1	2.33 ± 0.06 (1.80 ± 0.00)	-	2.17 ± 0.06 (1.63 ± 0.06)	-	-0.2 (-0.2)	NS (NS)
Saline bag 2	-	2.37 ± 0.06 (1.83 ± 0.06)	-	2.37 ± 0.15 (1.70 ± 0.17)	-0.2 (-0.4)	NS (NS)
Tube 1	-	-	11.13 ± 1.78 (3.53 ± 1.00)	11.63 ± 1.42 (3.80 ± 0.75)	0.9 (0.6)	NS (NS)

All data in parentheses are for the SUVmean. SD, standard deviation; [a], PET/CT3a; [b], PET/CT3b; [c], PET/CT3c; [d], PET/CT3d; SUVmax, Maximum Standardised Uptake Value; ΔSUVmax, the absolute difference in SUVmax value; SUVmean, Mean Standardised Uptake Value; ΔSUVmean, the absolute difference in SUVmean value; NS, not significant.

Table 5.4: The results of the statistical analyses of *phase 4* PET/CT imaging.

Structure	Mean ± SD SUVmax[a] (SUVmean[a])	Mean ± SD SUVmax[b] (SUVmean[b])	Mean ± SD SUVmax[c] (SUVmean[c])	Mean ± SD SUVmax[d] (SUVmean[d])	Mean ± SD SUVmax[e] (SUVmean[e])	Mean ± SD SUVmax[f] (SUVmean[f])	Highest ΔSUVmax (ΔSUVmean)	Friedman test SUVmax (SUVmean)
Saline bag 1	2.20 ± 0.10 (1.53 ± 0.06)	-	2.10 ± 0.00 (1.57 ± 0.06)	-	2.13 ± 0.15 (1.53 ± 0.06)	-	0.2 (0.1)	NS (NS)
Saline bag 2	-	2.17 ± 0.06 (1.60 ± 0.00)	-	2.07 ± 0.06 (1.60 ± 0.00)	-	2.10 ± 0.00 (1.60 ± 0.00)	0.1 (0.0)	NS (NS)
Tube 1	22.43 ± 0.50 (5.73 ± 1.15)	22.43 ± 0.64 (5.70 ± 0.85)	22.20 ± 1.00 (6.00 ± 1.47)	20.33 ± 1.78 (5.27 ± 1.61)	21.10 ± 1.67 (5.40 ± 1.15)	20.97 ± 1.43 (5.24 ± 1.52)	1.5 (1.5)	NS (NS)
Tube 2 (150 HU)	N	N	Y	Y	N	N		
Tube 3 (475 HU)	N	N	N	N	Y	Y		

All data in parentheses are for the SUVmean. SD, standard deviation; [a], PET/CT4a; [b], PET/CT4b; [c], PET/CT4c; [d], PET/CT4d; [e], PET/CT4e; [f], PET/CT4f; SUVmax, Maximum Standardised Uptake Value; ΔSUVmax, the absolute difference in SUVmax value; SUVmean, Mean Standardised Uptake Value; ΔSUVmean, the absolute difference in SUVmean value; NS, not significant; N, not inserted; Y; inserted.

5.4. Discussion

Across all phases of this phantom study, the range of SUVs in saline bags 1 and 2 were found to be within the clinically reported values for the normal liver; 1.49 – 4.89 [153]. The semiquantitative analysis of PET/CT images using the SUVs is reported to provide more reliable diagnosis than that of the visual assessment [62]. However, the reproducibility of the SUVs is dependent on the scanning protocols such dose uptake time, type of reconstruction algorithms, choice of attenuation maps, size of the region of interest, changes in uptake by organs other than the tumour, and methods of analysis (SUVmax and SUVmean) [146]. Therefore, in order to establish the final diagnosis of a disease, the PET/CT findings are still being compared along with the other radiological and/or pathological results.

In the initial part of this phantom study (*phase 2*), the differences in the SUVs of the normal liver caused by the use of iodine contrast media during PET/CT image acquisition were investigated. The percentage difference in the SUVmax values of this study (approximately 10%) is very close to that reported in a previous clinical finding by Yau *et al.* [113]. In the latter part of this study (*phases 3 and 4*), the experimental works were mainly focused on the simulation of a spinal tuberculosis case. Spinal tuberculosis was considered as one of the most common forms of extrapulmonary tuberculosis (EPTB) in Malaysia [74]. Thus, the set-up of this phantom study is strongly believed to provide a clinical benefit particularly for detecting the lesion of EPTB infectious disease.

This phantom study aimed to quantify the changes in SUVs (SUVmax and SUVmean) after the introduction of iodine contrast media during PET/CT imaging. Based on the results of this study, the highest percentage difference in SUVmax and

SUVmean values were about 10% and 26%, respectively. These values are in agreement with the previous phantom and patient based findings [113, 118, 119, 122, 154], which have concluded that the changes in both SUVmax and SUVmean values are not clinically significant although iodine contrast media has been utilised during the PET/CT imaging acquisitions. Indeed, two other clinical studies have demonstrated even greater percentage difference in SUVmax value of up to 27%, but this amount is still categorised as clinically insignificant [121, 149]. Furthermore, no pharmacologic interaction has been found between iodine contrast media and FDG, as both of them are usually administered with an interval of about an hour [113]. Therefore, based on the results of this phantom study and our recently published patients' data [155], PET/CECT scan is suitable to be applied as a routine imaging procedure, which can offer an excellent imaging diagnosis for an infectious disease like EPTB.

Even though the results of this anthropomorphic phantom study are sufficient to support the conclusion on clinical significance, there is still room for further optimisation of the measurement technique in future research. In this study, for example, dried human vertebrae with lower in density than encountered *in vivo* were used. Hence, by substituting these bones with other compact bones such as the mid-shaft of the femur, the inevitable loss of bone density could be compensated, which then may result in better simulation of a spinal tuberculosis case.

5.5. Conclusion

This phantom study has shown that the application of iodine-based contrast media during PET/CT imaging will not cause any statistically or clinically significant differences in the measurements of SUVmax and SUVmean values for an experimental set-up that mimics spinal tuberculosis at the lower abdomen region. Therefore, it has been recommended that iodine-based contrast media can safely be used during the CT scan of PET/CT imaging (excluding the patients with contraindications to iodine-based contrast media), without affecting the diagnostic accuracy of this integrated imaging modality. In addition, a complete intrinsic co-registration of diagnostic morphological and functional data can be obtained from this PET/CECT scanning procedure.

SECTION C

DOSIMETRIC STUDY

CHAPTER 6

Based on the results of the clinical imaging study (as in Chapter 4), FDG PET/CT scan is proven to be a valuable imaging tool for detecting and localising EPTB lesions. This is the chief outcome of this research, which clearly demonstrates that FDG PET/CT imaging can be utilised during the diagnosis procedure of EPTB patients. By adding this ionising radiation based imaging modality, an obvious question which is related to the extra radiation dose received by a patient needs to be addressed. To fully solve this issue, a comprehensive dosimetric investigation and validation is required, in order to accurately measure the radiation dose delivered by both CT and PET scans. However, this thesis is mainly about introducing a new imaging modality in the diagnosis of EPTB infectious disease. Therefore, only a limited work was conducted for estimating the amount of radiation dose arising from FDG PET/CT scan.

6.1. A theoretical and historical overview of PET/CT dosimetry

Theoretically, the absorbed radiation dose to a patient who undergoes PET/CT imaging consists of two different types of exposures; internal exposure from the PET scan and external irradiation from the CT scan [2, 156]. The absorbed radiation doses to the different body organs and tissues in CT and PET scans are not uniform throughout the body [36], and however, these very different patterns of the doses can be compared through the calculations of the effective dose [36, 157]. In fact, the International Commission on Radiological Protection (ICRP) has recommended that the effective dose can be used to calculate the whole body dose of the non-uniform irradiation [158]. In addition, it has been found that the effective dose is a valuable measurement for comparing and optimising between different techniques of the radiological examinations, such as in general radiography, CT and nuclear medicine [159, 160]. For

FDG PET/CT imaging, the effective dose is the sum of the effective doses arising from all the scanning components, in which the common scanning protocols consist of [156]:

- a CT topogram (also known as scout view) for defining the area of scanning,
- a low-dose CT scan,
- a FDG PET emission scan and
- a diagnostic CT scan.

Effective dose is a single derived parameter, which aims to reflect the relative risk from the exposure to ionising radiation [161]. This quantity does not only account for the different organ doses, but also for the varying radiation susceptibilities of the organs and tissues within the body region that has been exposed to ionising radiation [156]. Effective dose (E) is calculated as the product of the dose equivalent calculated and its appropriate tissue weighting factor [162], as described in Equation 6.1:

$$E = W_T \cdot H_T \tag{6.1}$$

where is W_T the weighting factor for tissue (or organ) T, and is H_T the calculated dose equivalent for tissue T (in milisieverts: mSv). The effective dose is expressed in SI unit of sieverts (Sv).

Tissue weighting factors (W_T) represent the relative radiation sensitivity of each type of body tissue as determined from population averages over age and sex, and these values are derived from the atomic bomb survivors cohort [159, 160]. These weighting factors were initially defined by the ICRP in their publication no. 26 (ICRP 26), back in year 1977 [163], then were updated in ICRP 60 (1990) [164] and the most recent were

with ICRP 103 (2007) [165], as listed in Table 6.1. These revisions projected the advances in knowledge about radiation sensitivity of various organs and tissues [161]. The variations between the tissue weighting factors of these three reports are ranging from -83% to +140%, depends on the calculated tissue, and therefore, the calculation of effective doses may differ substantially depending on which ICRP publication is used [161].

Table 6.1: Tissue weighting factors (W_T) from ICRP Publications 26, 60 and 103 [161].

Tissue or organ (W_T)	Publication		
	ICRP 26	**ICRP 60**	**ICRP 103**
Gonads	0.25	0.20	0.08
Red bone marrow	0.12	0.12	0.12
Lung	0.12	0.12	0.12
Colon		0.12	0.12
Stomach		0.12	0.12
Breast	0.15	0.05	0.12
Bladder		0.05	0.04
Liver		0.05	0.04
Esophagus		0.05	0.04
Thyroid	0.03	0.05	0.04
Skin		0.01	0.01
Bone surface	0.03	0.01	0.01
Brain			0.01
Salivary glands			0.01
Remainder organs	0.30	0.05	0.12
Total; $\sum W_T$	1.00	1.00	1.00

For each of the scanning components (PET and CT), the methods of estimating the absorbed radiation dose and/or the effective dose are different, and this will be explained further in the next few sections of this chapter.

6.1.1. PET radiation dose

In nuclear medicine, the radiopharmaceutical that has been administered through either oral (absorption from the gastrointestinal tract) or intravenous injection, is non-uniformly distributed within the body [36], and its chemical structure will determine the organs in which the radiopharmaceutical is concentrated and excreted [36, 157]. Therefore, it is not an easy task to accurately measure the amount of radiation dose delivered by the radiopharmaceutical that has been distributed over a large area/volume. In fact, several factors could affect the calculation of the absorbed radiation dose from a nuclear medicine procedure such as the radiopharmaceutical used, the administered radioactivity, and the age and body weight of the patient [157]. In addition, for each organ/tissue, the absorbed radiation dose is determined by the administered radioactivity and the amount of radiopharmaceutical in the organ/tissue and nearby organs and/or tissues integrated over time [157].

6.1.1.1. ICRP publications

Since 1988, the Task Group of the ICRP had calculated the organ absorbed doses and effective doses of an adult, 15-, 10-, 5- and 1-year-old children, from a number of radioactive substances that were commonly used in nuclear medicine; ICRP 53 [166]. These data were then revised in ICRP 80 (1998) [167], and the most recent in ICRP 106 (2008) [168]. Considering the fact that FDG is the most frequently used radiopharmaceutical in the clinical PET and/or PET/CT imaging, and all the scanning procedures of this research work have been conducted on adult patients, therefore the description of this section will only be focussing on the estimation of FDG PET dose for an adult patient.

The dose coefficient values of various organs and the effective dose coefficient value for FDG (adult only) from three different ICRP publications (ICRP 53, ICRP 80 and ICRP 106) are tabulated in Table 6.2. The absorbed radiation dose in organ or tissue T from FDG PET scan (D_T); in miligrays (mGy), can be calculated according to Equation 6.2 [158, 169]:

$$D_T = A \cdot \Gamma_T^{FDG} \tag{6.2}$$

where *A* is the administered radioactivity of FDG (in mega Becquerel: MBq) and Γ_T^{FDG} is the absorbed dose coefficient value for organ or tissue T (in mGy per MBq) that can be obtained from either one of the three ICRP publications; ICRP 53, ICRP 80 and ICRP 106. On the other hand, the effective dose (*E*); in mSv, resulting from an intravenous administration of the A radioactivity of FDG (in MBq) can be estimated using the following equation [169]:

$$\begin{aligned} E &= \sum_T W_T \cdot D_T \\ &= A \cdot \sum_T W_T \cdot \Gamma_T^{FDG} \\ &= A \cdot \Gamma_E^{FDG} \end{aligned} \tag{6.3}$$

where the total tissue weighting factors ($\sum W_T$) is equal to 1, as given in ICRP 26, 60 and 103 (refer to Table 6.1), and Γ_E^{FDG} is the effective dose coefficient value for FDG which

has been expressed in mSv per MBq, and provided by ICRP 53 [166], 80 [167] and 106 [168] (refer to Table 6.2).

Table 6.2: The dose coefficient values of various organs and the effective dose coefficient value for FDG from ICRP Publications 53 [166], 80 [167] and 106 [168] (adult data only).

Organ	Absorbed dose per unit activity administered, Γ_T^{FDG} (mGy/MBq)		
	ICRP 53	ICRP 80	ICRP 106
Adrenals	0.0140	0.0120	0.0120
Bladder	0.1700	0.1600	0.1300
Bone surfaces	0.0100	0.0110	0.0110
Brain	0.0260	0.0280	0.0380
Breasts	0.0110	0.0086	0.0088
Gallbladder		0.0120	0.0130
Stomach	0.0120	0.0110	0.0110
Small intestine	0.0130	0.0130	0.0120
Colon		0.0130	0.0130
Upper large intestine	0.0130	0.0120	0.0120
Lower large intestine	0.0160	0.0150	0.0140
Heart	0.0650	0.0620	0.0670
Kidneys	0.0210	0.0210	0.0170
Liver	0.0120	0.0110	0.0210
Lungs	0.0110	0.0100	0.0200
Muscles		0.0110	0.0100
Esophagus		0.0110	0.0120
Ovaries	0.0150	0.0150	0.0140
Pancreas	0.0120	0.0120	0.0130
Red marrow	0.0110	0.0110	0.0110
Skin		0.0080	0.0078
Spleen	0.0120	0.0110	0.0110
Testes	0.0120	0.0120	0.0110
Thymus		0.0110	0.0120
Thyroid	0.0097	0.0100	0.0100
Uterus	0.0200	0.0210	0.0180
Remaining organs	0.0110	0.0110	0.0120
Effective dose coefficient, Γ_E^{FDG} (mSv/MBq)	0.0270	0.0190	0.0190

It is important to note that there are some variations in the organs absorbed dose coefficient values and the effective dose coefficient value of the three ICRP

publications. For instance, the absorbed dose coefficient values for gallbladder, colon, muscles, esophagus, skin and thymus were first listed as primary organs in ICRP 80. Furthermore, these coefficient values have changed over the time. As an example, the absorbed dose coefficient values of urinary bladder and lower large intestine decrease in each subsequent publication (ICRP 106), whereas for brain, the value is increased in all three ICRP publications. Besides, for breasts, heart, liver and lungs, the absorbed dose coefficient values have decreased in ICRP 80, but then increase in ICRP 106. However, only for red marrow, the absorbed dose coefficient value remains unchanged through all the publications. For the effective dose coefficient value, it is higher in ICRP 53 as compared to those of ICRP 80 and ICRP 106. As a consequence for all these changes, the estimation of the organ absorbed dose and the effective dose for the exact same PET scan can differ substantially depending on which ICRP publication is used.

6.1.2. CT radiation dose

Three different scanning protocols are commonly employed for the CT component of PET/CT imaging [36]:

1. Diagnostic CT scan.
2. CT scan for co-registration and localisation.
3. CT for calculating the attenuation correction map.

Each of these scanning protocols can differently affect the total effective dose of the PET/CT imaging [36].

When PET/CT imaging is conducted with the whole body diagnostic CT protocol, the CT component will be the major contributor for the total absorbed

radiation dose [170]. The term ‘diagnostic’ means that the scan is usually carried out with the utilisation of intravenous and/or oral contrast media [27], also referred as contrast-enhanced CT (CECT) scan. In fact, this type of scanning technique requires higher tube current (mA) value in order to compensate for an increase in the tissue density, and therefore will result in the elevation of the absorbed radiation dose. However, when the CT is acquired on the basis of co-registration and localisation, the tube current can be reduced to about 35% from the tube current of diagnostic CT scan [36]. Furthermore, if the CT scan is only needed for measuring the attenuation correction map, the exposure factors (tube current and kVp) can be further decreased, which may then produce an effective dose as minimum as 3% of the effective dose from the diagnostic CT scan [36].

6.1.2.1. Computed Tomography Dose Index (CTDI), Dose Length Product (DLP) and the effective dose

One of the most common and useful dosimetric quantities in CT scan is the computed tomography dose index (CTDI). This quantity is defined as the integral of the dose profile for a single-slice along a line parallel to the axis of rotation divided by the nominal slice thickness [171, 172], and it is measured from 14 contiguous sections [173].

$$CTDI = \frac{1}{T}\int_{-7T}^{7T} D(z)dz \tag{6.4}$$

T represents the nominal slice thickness and $D(z)$ is the dose distribution along a line parallel to the z-axis. This CTDI includes the radiation scattered into the neighbouring

volume of the slice [171]. To overcome the limitations of CTDI that related with the measurement from 14 contiguous sections, a more convenient radiation dose index was established by using a fixed integration interval of 100 mm for any thickness of *T* [171, 173]. This newer radiation dose index was termed as $CTDI_{100}$ (refer to Equation 6.5), and it can directly be measured using a pencil ionisation chamber with an active length of 100 mm [171, 173, 174].

$$CTDI_{100} = \frac{1}{T}\int_{-50mm}^{50mm} D(z)dz \tag{6.5}$$

In order to incorporate the absorption characteristics of a patient, CTDI is commonly measured on the acrylic cylindrical phantoms of having either 16 or 32 cm diameter to simulate the exposure of the head or body region [171, 173, 175]. These phantoms have holes (one at the centre and four at the peripheral) that allow for the insertion of the ionisation chamber with an active length of 100 mm [171, 174, 176]. With the assumption that dose in a CTDI phantom decreases in radial direction from surface to centre, the average CTDI in an irradiated slice from a single exposure can be calculated by using the weighted CTDI ($CTDI_w$) [171, 174]; in mGy to air [174]:

$$CTDI_w = \tfrac{1}{3} CTDI_{100,c} + \tfrac{2}{3} CTDI_{100,p} \tag{6.6}$$

where $CTDI_{100,c}$ represents the measured CTDI at the central position and $CTDI_{100,p}$ is the average CTDI measured from four different periphery locations (east, west, south and north parts).

With the advent technology in CT scanner, it has lead to the introduction of another CTDI, which is referred as volume CTDI ($CTDI_{vol}$). This $CTDI_{vol}$ is an index that quantifies the intensity of radiation beam being produced by the CT scanner [177], and has been incident onto the patient [175]. This value represents the average absorbed radiation dose in the x, y, and z directions for a specific scanning protocol [178], and it is expressed in terms of air kerma, in mGy unit [177]. In helical/spiral CT, it can be defined as the weighted CTDI ($CTDI_w$) divided by the pitch [178, 179], (Equation 6.7).

$$CTDI_{vol} = CTDI_w / pitch \tag{6.7}$$

Pitch is equal to the table increment distance per x-ray tube rotation divided by the nominal beam width at the isocentre of the CT scanner [179].

On the other hand, to obtain a dose quantity that describes the radiation exposure for a full scan or a complete examination, another dose descriptor known as the dose length product (DLP) has been introduced [171]. DLP is defined as the product of the $CTDI_{vol}$ and the irradiated scan length (in cm) [161, 180], and expressed in mGy · cm unit (refer to Equation 6.8). It can be used to quantify the total amount of radiation received by a patient from a given CT examination [181].

$$DLP = CTDI_{vol} \cdot scan\ length \tag{6.8}$$

Both CTDI and DLP are the recommended dosimetric quantities that describe the CT dose and practice [171]. Indeed, these two values can directly be obtained from

the display screen of the operator console in the current commercial CT imaging system [156, 169, 182]. However, both of these values are actually meant to serve as an index of radiation dose due to the CT exposure only, and cannot be used as an accurate estimation of the radiation dose acquired by an individual patient [173]. Therefore, the radiation risk for a patient who has undergone CT examination can be estimated from the effective dose (*E*) [171].

For CT scan, the effective dose (*E*) can be calculated either by utilising the value of DLP or $CTDI_{vol}$. According to the previous study by Christner *et al.* [161], and ICRP 102 [178], the effective dose (*E*) is calculated based on the DLP value of a CT scan, as the following Equation 6.9:

$$E = k \cdot DLP \tag{6.9}$$

where *k* coefficient is an empirical weighting factor, which is a function of the anatomical region scanned (expressed in $mSv \cdot mGy^{-1} \cdot cm^{-1}$ unit). This value can be obtained directly from ICRP 102 (2007) [178], as tabulated in table below.

Table 6.3: The *k* coefficient values for adult and paediatric patients of various ages for various anatomical scanning regions [178].

Anatomical region	*k* coefficient ($mSv \cdot mGy^{-1} \cdot cm^{-1}$)				
	0-year-old	1-year-old	5-year-old	10-year-old	Adult
Head	0.0110	0.0067	0.0040	0.0032	0.0021
Neck	0.0170	0.0120	0.0110	0.0079	0.0059
Head and neck	0.0130	0.0085	0.0057	0.0042	0.0031
Chest	0.0390	0.0260	0.0180	0.0130	0.0140
Abdomen and pelvis	0.0490	0.0300	0.0200	0.0150	0.0150
Chest, abdomen and pelvis (trunk)	0.0440	0.0280	0.0190	0.0140	0.0150

Although DLP of the CT scan can be used to estimate the effective dose (*E*), a recent study has found that this method could end with an underestimated dose value, as compared with the effective doses derived from the organs/tissues weighting factors of ICRP 60 and ICRP 103 (E_{60} and E_{103}; the subscripts 60 and 103 represent the ICRP publication used) [161]. Based on this, it gives more constructive and academic reasons why in this study $CTDI_{vol}$ should be applied for estimating the effective dose (*E*), rather than using the DLP. In addition, a previous study by Brix, G. and his co-workers have established the dose coefficient value that relates $CTDI_{vol}$ with the CT effective dose (Γ_E^{CT}), approximately 1.47 mSv/mGy [169]. This coefficient has been developed from the mean value of the measured absorbed doses from thirteen organs, which could represent the coefficient value of a whole body CT scan that extends from the thyroid to symphysis pubis [2, 156]. Therefore, the CT effective dose (*E*) can be estimated using the following [2, 156]:

$$E = \Gamma_E^{CT} \cdot CTDI_{vol} \tag{6.10}$$

The absorbed radiation dose received by a patient from the CT examination is determined by various factors such as the inherent characteristics of the CT scanner, the size of the patient, the anatomical region scanned, and the scanning protocol and technique used [181]. To be more specific, for the last influence factor, it can be classified further into few scanning parameters like tube current-time product (miliampere-seconds: mAs), x-ray beam energy (peak kilovoltage: kVp), slice thickness, object thickness or attenuation, and pitch [173]. Among all these, mAs is the most important factor that corresponds to the number of x-ray photons in the defined

exposure time [181], and it has linear relation with the CT radiation dose [157, 181]. Therefore, for a given CT scanner, when all other scanning parameters are exclusively held constant, halving the mAs means halving the radiation dose [157, 181]. In addition, few recommendations have been documented in ICRP 87, for reducing the radiation dose to the patient during CT scan that can be applied by the user and the manufacturer [181], as listed in the Table 6.4.

Table 6.4: The recommendations for patient dose reduction during CT scan [181].

Measures for the CT user	Measures for the CT manufacturer
▪ Checking the indication and limiting the scanned volume	▪ Increasing the pre-filtration of the radiation spectrum
▪ Adapting the scanning parameters to the patient cross-section	▪ Attenuation-dependent tube current modulation
▪ Pronounced reduction of mAs values for children	▪ Low-dose scanning protocols for children and special indications
▪ Use of spiral CT with pitch factors > 1 and calculation of overlapping images instead of acquiring overlapping single scans	▪ Automatic exposure control (AEC) for conventional CT and spiral CT
▪ Adequate selection of image reconstruction parameters	▪ Noise-reducing image reconstruction procedures
▪ Use of z-filtering with multi-slice CT systems	▪ Further development of algorithm for z-filtering and adaptive filtering

6.2. FDG PET/CT dose estimation of Malaysian patients

Of the Malaysian cohort, the dosimetric data of PET/CT scans were only acquired for twelve patients. This sample size was somewhat reduced due to the fact that our clinical imaging study was conducted by using the PET/CT facilities from the two private hospitals; Prince Court Medical Centre and Beacon International Specialist Centre, and later, all images were reviewed and evaluated on the workstation at our institution (Nuclear Imaging Centre, University Putra Malaysia). Although dual time point imaging (DTPI) technique had been successfully employed in thirteen Malaysian

patients, $CTDI_{vol}$ of the delayed CT scans were only obtained for eight patients. All these dosimetric data are tabulated in Table 6.5.

Table 6.5: The dosimetric data and administered radioactivity of FDG for all sixteen Malaysian patients.

Patient no.	CTDIvol (mGy)			FDG radioactivity (MBq)
	Unenhanced CT	CECT	Delayed CT	
1	3.05	10.18	3.14	592
2	2.42	2.42	2.42	419
3	2.08	6.40	2.20	277
4	1.61	5.26	1.23	322
5	5.40	5.40	n/a	337
6	5.40	5.40	n/a	145
7	n/a	n/a	–	382
8	1.91	6.70	2.29	361
9	n/a	n/a	n/a	383
10	2.42	8.61	2.63	500
11	1.99	6.70	1.65	368
12	1.74	5.68	0.98	375
13	n/a	n/a	n/a	346
14	n/a	–	n/a	272
15	1.65	5.68	–	354
16	1.87	6.28	–	383
CTDIvol, volume CT Dose Index; CECT, contrast-enhanced CT; n/a, not available; –, not done.				

Owing to slight variations in the scanning parameters (patients 2, 5 and 6) and some missing data (patients 7, 9, 13 , 14, 15 and 16), the estimation of the effective dose from CT, PET and PET/CT scans could only be calculated for the other seven patients. In these dose estimations, the effective dose coefficient value for CT (Γ_E^{CT}) has been computed from the original data of the previous study by Brix *et al.* [169] together with slight modification on their data; by multiplying their organ-specific CT absorbed dose coefficient (Γ_E^{CT}) with the most recent tissue weighting factor published in the ICRP 103 [165]. This goes the same for the effective dose coefficient value of FDG (Γ_E^{FDG}),

as it is acquired using the data from several studies [158, 169, 183], and again some modifications have been applied on these published data, through the utilisation of the tissue weighting factor from the ICRP 103 [165] and the organ absorbed dose coefficient of FDG from the ICRP 106 [168]. (All the modifications and calculations of the PET and CT effective doses are presented in Appendices 6 and 7). Based on this limited set of data, the statistical analyses were performed using the SPSS program for Windows version 18.0. All results were evaluated using a 5% error level and a difference was considered to be statistically significant when $P < 0.05$.

6.2.1. Calculation results and analyses

The means and standard deviations (SD) of all scans are presented in Table 6.6. In order to test for any differences among the four stand-alone imaging scans (unenhanced CT, CECT, delayed CT and PET), a one-way repeated measures ANOVA with the post-hoc Bonferroni test were performed on the mean effective doses of each scan. The multivariate approach to the analysis of within-subjects data was used. A significant difference was found among the four stand-alone imaging conditions (Wilks' Lambda (Λ) = 0.024, F (3, 4) = 54.047, P = 0.001, η^2 = 0.976). Post-hoc testing was carried out using pairwise comparisons of estimated marginal means with Bonferroni adjusted α levels. Significant differences at $P < 0.05$ were found for all six possible pairwise comparisons, except for the pair between unenhanced CT and delayed CT scans (refer to Fig. 6.1). There was no significant difference between the mean effective doses of the unenhanced CT and the delayed CT scans (P = 1.00).

Table 6.6: The effective doses of the stand-alone and the integrating PET/CT scans for the seven Malaysian patients.

Patient no.	Effective dose (mSv)					
	Stand-alone scan				Integrating PET/CT scan	
	Unenhanced CT (A)	CECT (B)	Delayed CT (C)	PET (D)	A + B + D	A + B + C + D
1	4.41	14.71	4.54	10.48	29.60	34.14
3	3.01	9.25	3.18	4.90	17.16	20.34
4	2.33	7.60	1.78	5.70	15.63	17.41
8	2.76	9.68	3.31	6.39	18.83	22.14
10	3.50	12.44	3.80	8.85	24.79	28.59
11	2.88	9.68	2.38	6.51	19.07	21.46
12	2.51	8.21	1.42	6.64	17.36	18.78
Mean	3.06	10.22	2.92	7.07	20.35	23.27
± SD	0.70	2.50	1.12	1.93	5.01	5.97

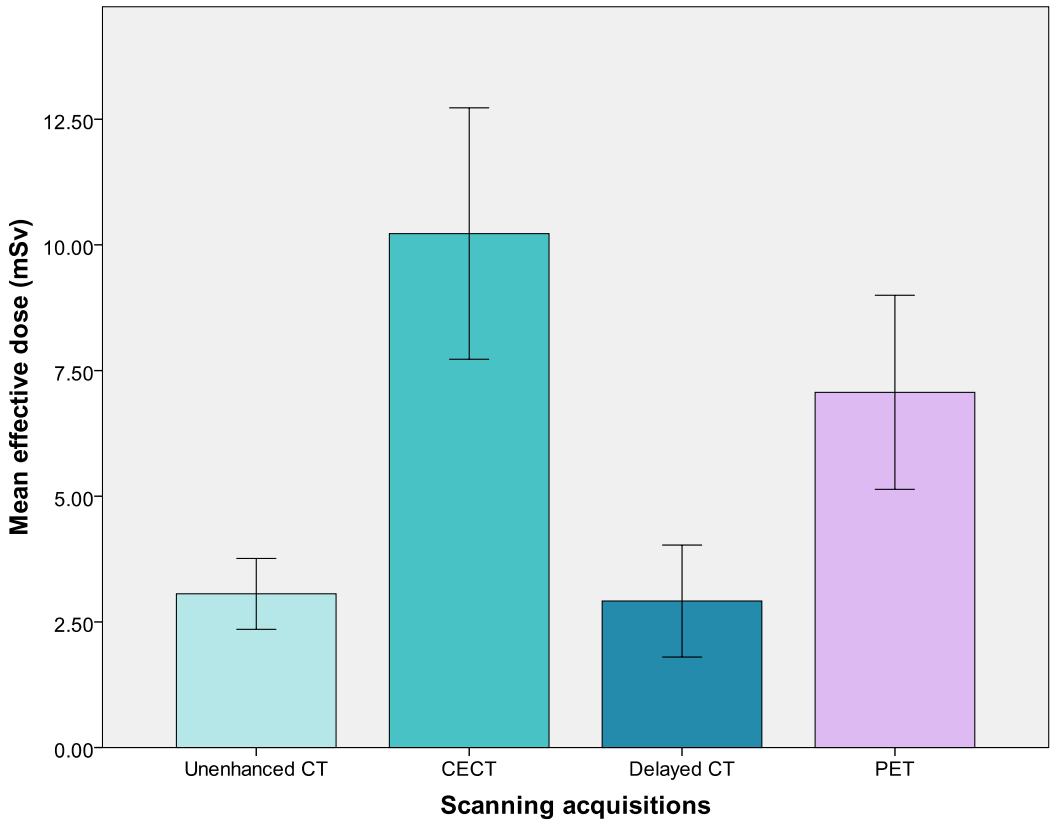

Figure 6.1: The mean differences in the effective doses of unenhanced CT, CECT, delayed CT and PET scans for the seven Malaysian patients. One-way repeated measures ANOVA results with a significant difference among the four stand-alone imaging conditions (Wilks' Lambda (Λ) = 0.024, *F* (3, 4) = 54.047, *P* = 0.001, η^2 = 0.976). In addition, post-host Bonferroni test has shown significant differences at *P* < 0.05 for all six possible pairwise comparisons, except for the pair between unenhanced CT and delayed CT scans (*P* = 1.00). *Error bars represent* ± *standard deviation.*

For the effective doses of the two integrated PET/CT scans (PET, unenhanced CT and CECT, and PET, unenhanced CT, CECT and delayed CT), a paired samples *t*-test was used. There was a highly statistically significant difference between the means effective doses of both integrated scans ($P < 0.001$) (refer to Fig. 6.2). This result indicated that there was a significant increment on the effective dose when the delayed CT scan was conducted during the DTPI technique of FDG PET/CT scan. The mean additional effective dose that had been attributed from the delayed CT scan was approximately 2.91 ± 1.12 mSv.

In comparison, when PET is integrated with CECT scan only (B + D), the effective dose will be substantially reduced by more than one seventh of the total PET, unenhanced CT and CECT effective dose (17.29 ± 4.34 mSv vs. 20.35 ± 5.01 mSv). However, the combination of PET with unenhanced CT scans (A + D) may result in enormous dose reduction towards the total effective dose, which is approximately half of that from PET, unenhanced CT and CECT scans (10.12 ± 2.56 mSv vs. 20.35 ± 5.01 mSv). Therefore, it has been strongly believed that both scanning methods (PET/unenhanced CT and PET/CECT) could potentially offer some benefits especially when radiation dose is the major concern.

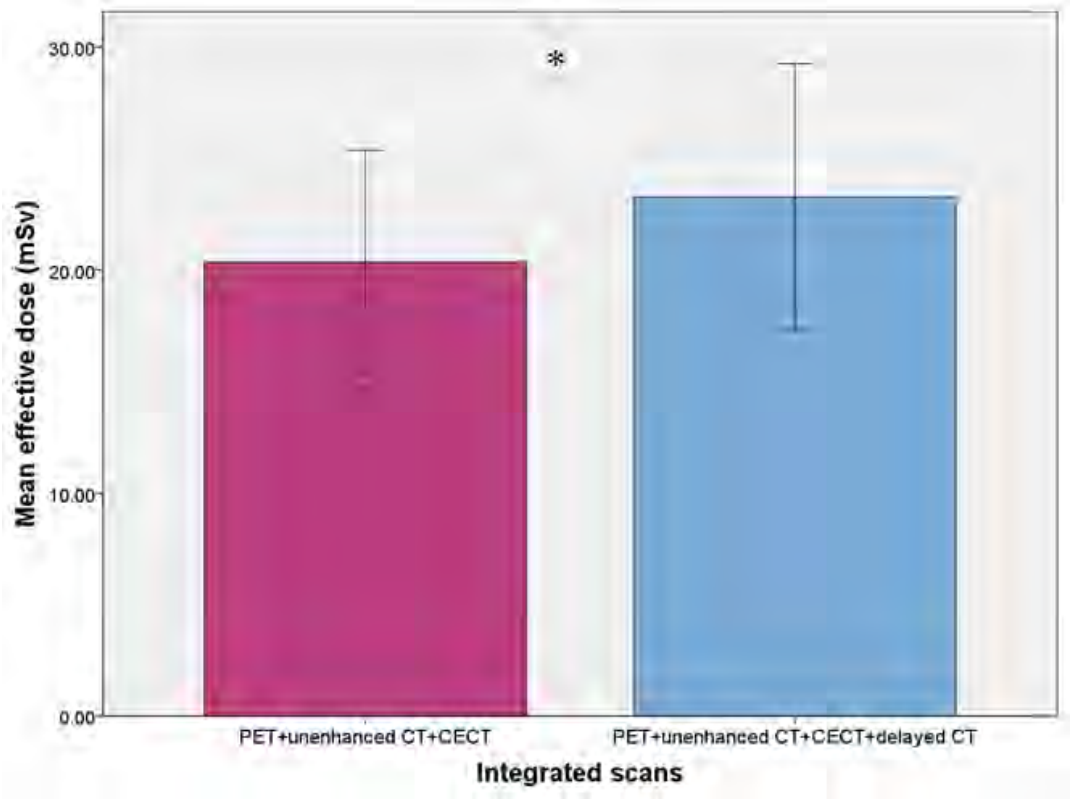

Figure 6.2: The mean difference in the effective doses of the two integrated scanning acquisitions (PET + unenhanced CT + CECT and PET + unenhanced CT + CECT + delayed CT) for the seven Malaysian patients. A two-tailed paired samples t-test results with a high significant difference with *P* value of less than 0.001 (*). *Error bars represent* ± *standard deviation.*

6.2.2. Discussion

Our results demonstrate that CT examinations are the major contributor towards the total effective dose of PET/CT imaging, which corresponds to approximately 65%. However, when a delayed CT scan is performed, the attributed percentage is then increased to as high as 76% of the total effective dose: PET + unenhanced CT + CECT + delayed CT. This finding is in concordance with a recent retrospective study by Chawla, S. C. and her colleagues [184]. Furthermore, they have specifically mentioned that the diagnostic CT scan with the utilisation of intravenous contrast media is a standard of practice for the PET/CT imaging at their institution, which is the same as in the clinical trial of this research. Indeed, their PET/CT imaging system (Biograph PET/CT, Siemens Healthcare Solutions) and the CT scanning parameters (especially the mAs, kVp and scanning coverage area) are also similar to this study, and thus, the data are comparable. In another study, Huang *et al.* [158] reported a range of the whole body PET/CT effective dose was from 13.45 mSv to 32.18 mSv, depending on the CT protocol used and the gender of the patient. Correspondingly, up to 81% of the total PET/CT effective dose were attributable to the CT doses [158].

In this study, the injected amount of FDG radioactivity was derived from patient's body weight. For all sixteen Malaysian patients, the injected radioactivity was about 6.11 MBq/kg (refer to Table 6.5). This amount is larger than the value used in a recent PET/CT dosimetric study by Khamwan *et al.* [183], although the physical characteristics (body weight and height) of these patients are generally about the same with the patients from its neighbouring country (Thailand). Therefore, it is expected that all PET scans of this study could result in the higher effective doses. However, when comparing the total PET/CT effective dose of each patient with those of Thai patients, it

has shown a very good agreement (exclude patient 1, as she has received the largest amount of injected radioactivity of FDG; 592 MBq, because of a high body weight, approximately 94 kg), even if two CT examinations (unenhanced CT and CECT) are performed during the image acquisitions. This is mainly due to the utilisation of lower mAs value (30 mAs for unenhanced CT and 100 mAs for CECT) during all the CT scans of this study; mAs is one of the main parameters that controls the CT radiation dose [181].

The mean PET/CT effective dose of this limited number of Malaysian patients is also in accordance with the findings of two previous studies [169, 184]. Although by performing the delayed CT scan has resulted with a significant increment in the total PET/CT effective dose, the mean effective dose of this special scanning protocol is still within their reported effective dose range; about 25 mSv. Indeed, it is relatively less than the mean effective dose from the protocol C of the Huang's study [158]; 31.91 and 32.18 mSv for female and male patients, respectively. Therefore, it has been believed that the addition radiation dose caused by the delayed CT scan is not a major issue, and this DTPI technique can perhaps be applied as a standard protocol, especially if it helps in enhancing the diagnostic accuracy of PET/CT imaging.

In order to better estimate the effective dose of PET scan, the calculation should be computed using a specialised software called OLINDA [185]. This software has been developed by a research group from the Vanderbilt University, Tennessee, and it is commonly used to estimate the internal radiation dose from the administration of radionuclide in nuclear medicine. In contrast, for the CT effective dose, several softwares are currently available in the market such as ImPACT, CT Dose, CT-Expo and ImpactDose. Owing to no access of such softwares, therefore, the PET/CT effective

dose of this study was only derived from the calculation methods by utilising the available dosimetric descriptors; $CTDI_{vol}$ and administered radioactivity of FDG.

6.2.3. Conclusion

The mean effective dose arising from FDG PET/CT scans in the seven Malaysian patients of this study is in accordance with the previously reported values (less than 25 mSv), even though DTPI technique has been utilised during the imaging acquisitions. CT scans are found to be the major contributor for the total PET/CT effective dose, and therefore, if some modifications have been carried out on the CT scanning parameters, this approach may extensively reduce the total PET/CT effective dose.

6.3. The dosimetric experiments to partially validate the clinical data

As mentioned earlier, this dosimetric study also consists of multiple experimental *attempts*[‡] for quantifying the amount of the radiation dose arising from FDG PET/CT scan. In order to clearly describe all steps and procedures used in conducting of these experiments, this section is divided into two different categories:

1. FDG PET/CT irradiation
2. Constructing and plotting the dose response curves

[‡] The term *attempt* is used to indicate that a full dosimetric study for an accurate measurement of the radiation dose delivered by FDG PET/CT to an organ or the whole body is not done in this thesis. To do that, a comprehensive dosimetric investigation and validation is required, which is beyond the aims of this thesis.

6.3.1. FDG PET/CT irradiation

In this study, an anthropomorphic phantom (the same as in Chapter 5) was used. A small piece of XRCT and XRQA gafchromic films was sticked onto the outer surface of the phantom, for measuring the radiation dose delivered by the CT component of PET/CT imaging (refer to Fig. 6.3). These two types of films are the most sensitive radiochromic films that currently available in the market, which can detect the absorbed radiation dose as low as 0.1 mGy [186]. Furthermore, a syringe that contained an amount of FDG radioactivity (1 GBq) was tapped inside the phantom, and three dosimeters (XRCT and XRQA films, and *PRESAGE*[§]) were deployed as close as possible to the syringe. Then, a CT scan was performed by using the same exposure parameters as for the low-dose CT of FDG PET/CT imaging (140 kVp, 30 mAs, slice thickness of 5 mm, pitch factor of 1.0 and gantry rotation speed of 1.0 s) on Philips Gemini Dual PET/CT system. Immediately after completing the CT scan, those two outer films (XRCT and XRQA) were removed, but the remaining three dosimeters (inside the phantom) were kept the same for the next 24 hours. All these irradiations were conducted at the Nuclear Medicine Department of The Alfred Hospital, Melbourne, Australia.

[§] PRESAGE is a dosimeter made of polyurethane matrix, which is suitable for 3-D dosimetry. In this study, PRESAGE was bought from Heuris Pharma LLC, Skillman, New Jersey, USA.

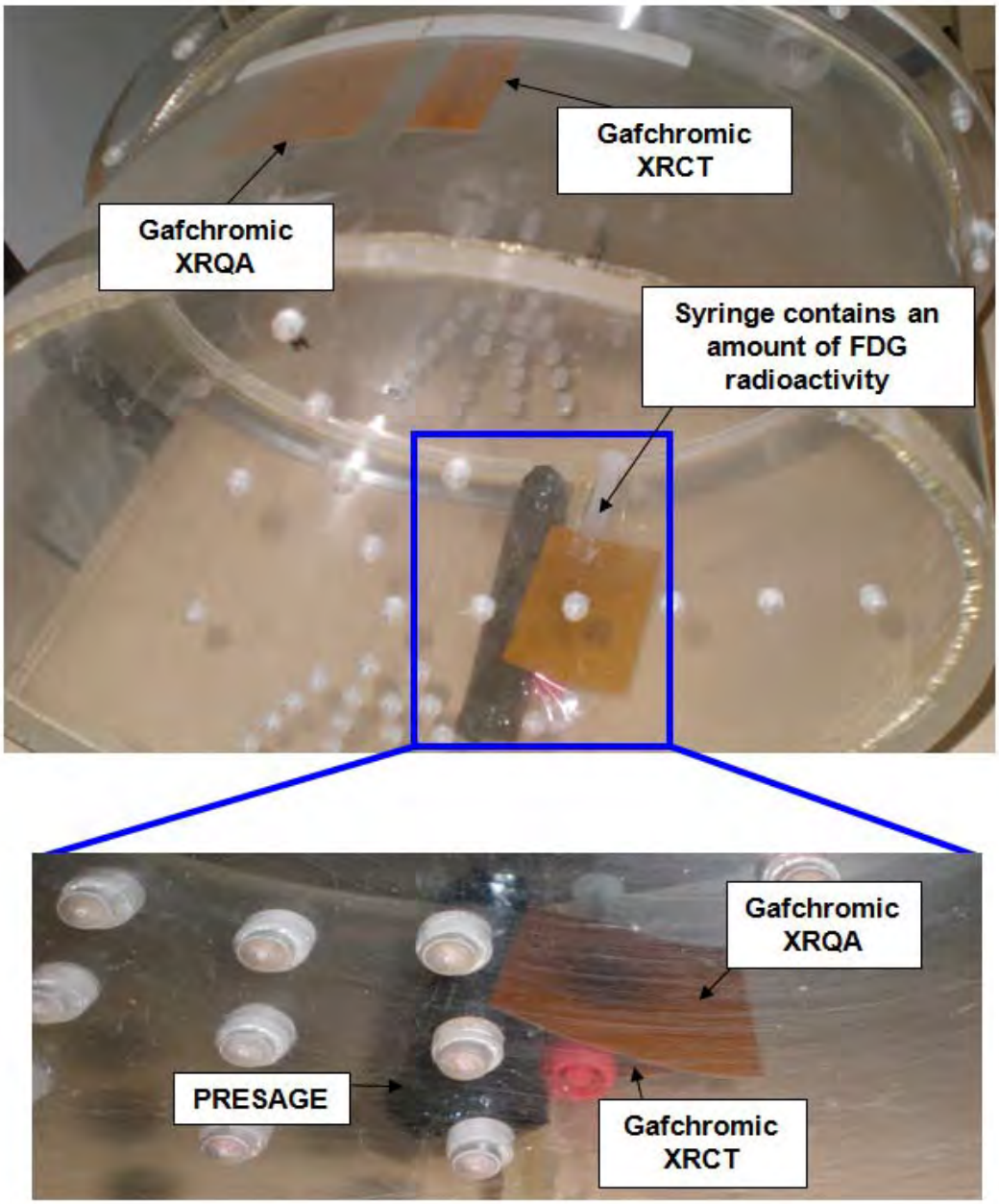

Figure 6.3: The set-up for FDG PET/CT irradiation of the anthropomorphic phantom, where three dosimetry methods (Gafchromic XRCT and XRQA films, and PRESAGE) have been utilised.

6.3.2. The dose response curves

PET/CT imaging system consists of two dedicated scanners that operate with two different types of energies; polychromatic x-ray at mean photon energy of 70 keV and monochromatic gamma radiation with 511 keV energy level [3, 187]. Thus, the dose response curve for each of these electromagnetic waves (x-ray and gamma radiation) needs to be constructed and plotted separately. The description on the methods used for constructing and plotting the dose response curves of x-ray will be first presented and then followed by those for gamma radiation.

6.3.2.1. The x-ray dose response curves

With the aim of covering a wide range of energy, this section can be divided into two, according to the method of irradiations:

1. Irradiations with CT machine at an energy range of 80 – 140 kVp.
2. Irradiations with a superficial x-ray radiotherapy (SXRT) machine at 150 kVp energy level.

6.3.2.1.1. CT irradiations

Both gafchromic XRQA and XRCT films are suitable to be used for CT dose assessment, as stated in the literature [186, 188-190]. Because of this reason, these two films were selected in this study. In order to obtain a free-in-air condition, the films were tapped at the end of PET/CT table, in which the table was then raised to its isocentric level. The long axis of both films was placed perpendicular to the CT x-ray beam (refer to Fig. 6.4). A total of sixteen irradiations with different exposure factors (as listed in Table 6.7) were carried out by using only the CT component of the same

PET/CT imaging system (Philips Gemini Dual). Then, $CTDI_{vol}$ of each irradiation was recorded accordingly.

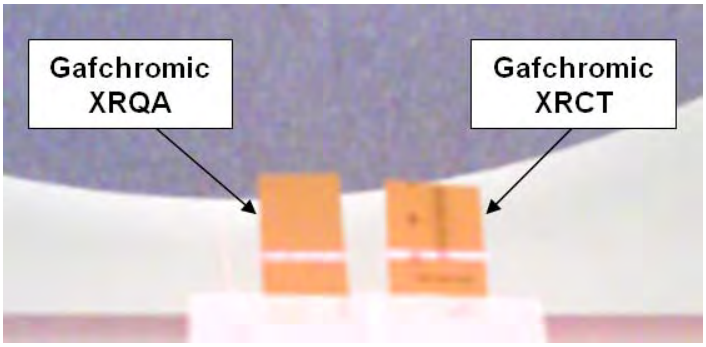

Figure 6.4: The set-up for CT irradiation of gafchromic XRCT and XRQA films with the CT scanner of PET/CT imaging system.

Table 6.7: The exposure factors (kVp and mAs) of all sixteen CT irradiations that have been carried out for constructing and plotting the dose response curves of gafchromic XRCT and XRQA films at various CT energies (80 kVp – 140 kVp).

Irradiation	**1**	**2**	**3**	**4**	**5**	**6**	**7**	**8**	**9**	**10**	**11**	**12**	**13**	**14**	**15**	**16**
kVp	80	80	80	80	100	100	100	100	120	120	120	120	140	140	140	140
mAs	170	340	600	760	170	340	600	760	170	340	600	760	170	340	600	760

6.3.2.1.2. SXRT irradiations

This dosimetric experiment was performed after completing the analyses of all films from CT irradiations. Based on the results obtained (which will be described later), only gafchromic XRCT film was used. The irradiations of XRCT films using SXRT machine (Therapax 3 Series, Pantak Inc., Branford, CT, U.S.A.) were carried out at William Buckland Radiotherapy Centre (The Alfred Hospital, Melbourne, Australia). This SXRT machine has a dose rate of about 1.00 Gy/min. In this study, all XRCT film pieces were irradiated to the various low radiation doses (0.5, 1.0, 5.0 and 20.0 mGy)

with 150 kVp (1.0 mm Cu HVL) x-ray energy using a 15 cm diameter collimator at 87 cm distance between the x-ray tube and the films (refer to Fig. 6.5). These dose values were believed to produce an adequate degree of film blackening for the tested x-ray beam energy, and in fact, the highest dose of 20.0 mGy was within the range for the mean calculated whole body FDG PET/CT effective dose of the seven Malaysian patients (refer to Table 6.6); there is no difference between the absorbed dose and the effective dose for gamma and x rays (1 mGy ≈ 1 mSv) [191].

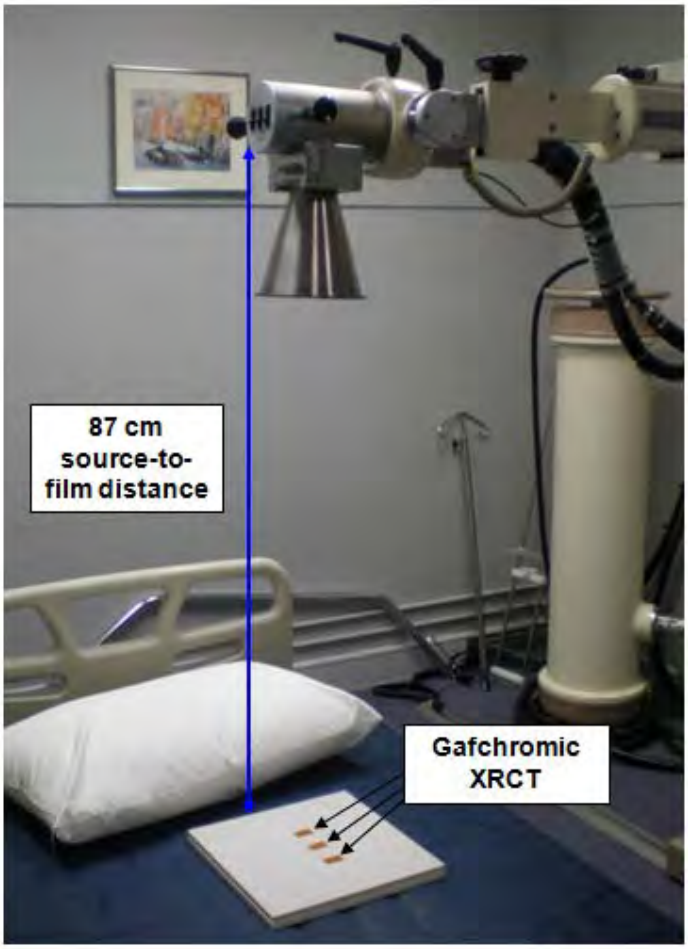

Figure 6.5: The set-up for gafchromic XRCT films irradiations with the SXRT machine, where the source to film distance is kept at approximately 87 cm. All irradiations are performed at 150 kVp x-ray energy with a 15 cm diameter collimator.

6.3.2.2. The gamma radiation dose response curves

In developing the dose response curves of gamma radiation, again, only XRCT type of film was utilised. The films were exposed to two different sources of gamma radiation:

1. Technetium-99m (Tc-99m).
2. Flourine-18 (F-18).

6.3.2.2.1. Technetium-99m irradiations

For the irradiations with Tc-99m radioisotope (gamma ray energy of about 140.5 keV), a cylinder container with peripheral rods was used (refer to Fig. 6.6). A syringe which contained 15 GBq radioactivity of Tc-99m was inserted and placed at the centre of the container. Then, three pieces of XRCT films were stuck onto the three peripheral rods, where the distance of the films to the radiation source was about 5 cm. The amount of absorbed radiation dose was measured by using a compact ionisation chamber (CC13, Wellhöfer) that had been connected to a multichannel dosimeter. The distance between this ionisation chamber and the radiation source was also kept at approximately 5 cm. The films were irradiated for 30, 60 and 90 min, and the count charge of each irradiation was recorded. In addition, to accurately quantify the absorbed radiation dose, the level of background radiation was measured for all three irradiated time. By this, the net absorbed dose of all irradiations could be calculated.

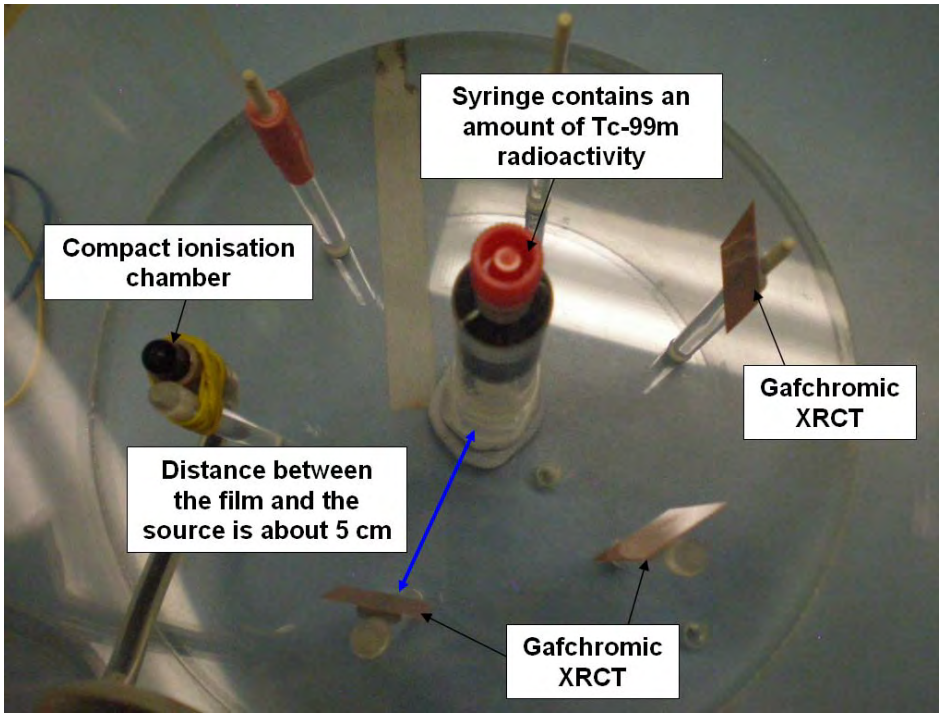

Figure 6.6: The set-up for gafchromic XRCT films irradiations with Technetium-99m; Tc-99m (gamma energy of 140.5 keV). The irradiations have been performed for 30, 60 and 90 min.

6.3.2.2.2. Flourine-18 irradiations

By utilising the same methods as in Tc-99m irradiations, XRCT films had also been exposed to a higher gamma energy of 511 keV produced by F-18. However, for this experiment, only 1.9 GBq radioactivity of F-18 was used (refer to Fig. 6.7). The variation between the measured radioactivity of the two isotopes used was due to a couple of different factors, most importantly the very large difference in their half-lives. The F-18 which was produced off-site and delivered very early in the morning has a half life of 109 minutes. The Tc-99m on the other hand was milked from a generator on-site just prior to being used and has a much longer half -life of 6 hours. In addition, all the experiments were performed after the completion of the daily clinical works, by

which the initial activity of the delivered F-18 had decayed significantly. Both of these are acknowledged to be the limiting factors of this dosimetric study.

For radiation protection and safety reasons, both Tc-99m and F-18 irradiations were conducted in the brachytherapy room at William Buckland Radiotherapy Centre, The Alfred Hospital, Australia.

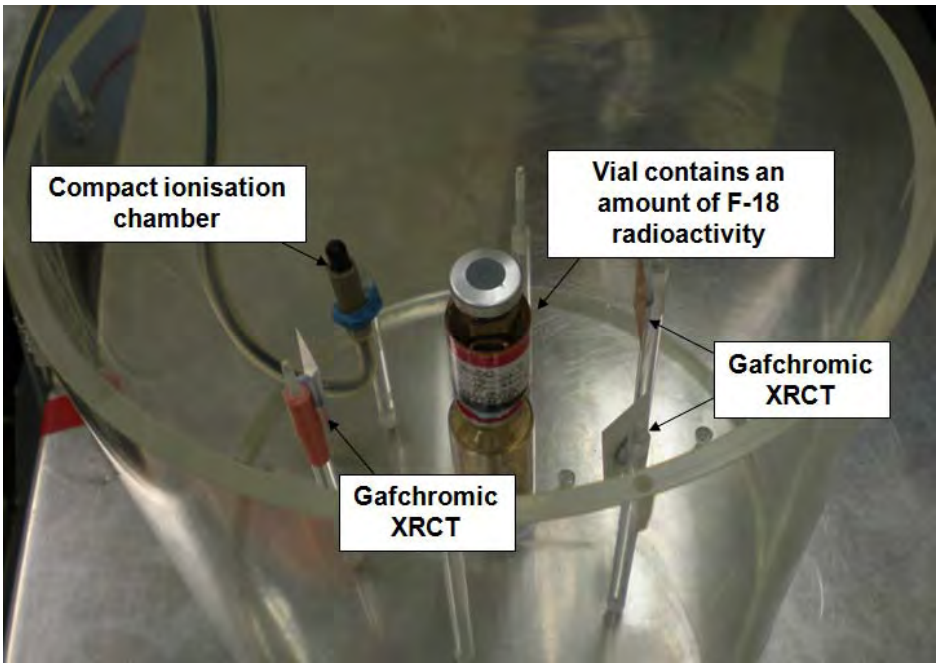

Figure 6.7: The set-up for gafchromic XRCT films irradiations with Flourine-18; F-18, solution (gamma energy of 511 keV). The irradiations have been performed for 30, 60 and 90 min.

6.3.3. The dosimetric results and analyses

All gafchromic XRCT and XRQA films were scanned using an Epson Perfection V700 photo flatbed scanner (Seiko Epson Corporation, Nagano, Japan) at least 24 hours after the irradiations; to minimise the effects from post irradiation colouration [192, 193],

with 24-bit colour red, green, blue (RGB) mode in reflective format without any filters and image enhancement options. The images of 600 dpi resolution were saved as uncompressed tagged image file (tif) format, which then were analysed using ImageJ software (version 1.37) with RGB split and red colour 33.3% technique. The red channel values were selected for the image analyses of this study because the main absorption peak of these films (after the irradiation) had been found to be at 636 nm, which was the same as in the red region of the visible light spectrum [189, 194]. By subtracting the mean gray value of an unirradiated film with those of the irradiated films, the net gray values for all the exposed films were obtained. From these data, the dose response curve of the gafchromic films from each irradiation was then plotted.

6.3.3.1. FDG PET/CT irradiation

In quantifying the amount of radiation dose delivered by the CT component of PET/CT imaging, both gafchromic XRCT and XRQA films had demonstrated slight colour changes with the mean net gray values of 12.04 and 8.16, respectively (refer to Fig. 6.8). On the other hand, with 24 hours irradiation to 1 GBq radioactivity of F-18, an obvious colour change was detected on these two XRCT and XRQA films, in which the mean net gray values were approximately 156 and 155 (refer to Fig. 6.9). These results clearly indicate that both XRCT and XRQA films are suitable to be applied for dose measurement in CT and FDG PET/CT scans.

In contrast, no radiochromic colour change was observed on PRESAGE. This finding was not unexpected because PRESAGE was commonly used in measuring a high radiation dose (of the order of 1 Gy or more), particularly for radiotherapy [195-197].

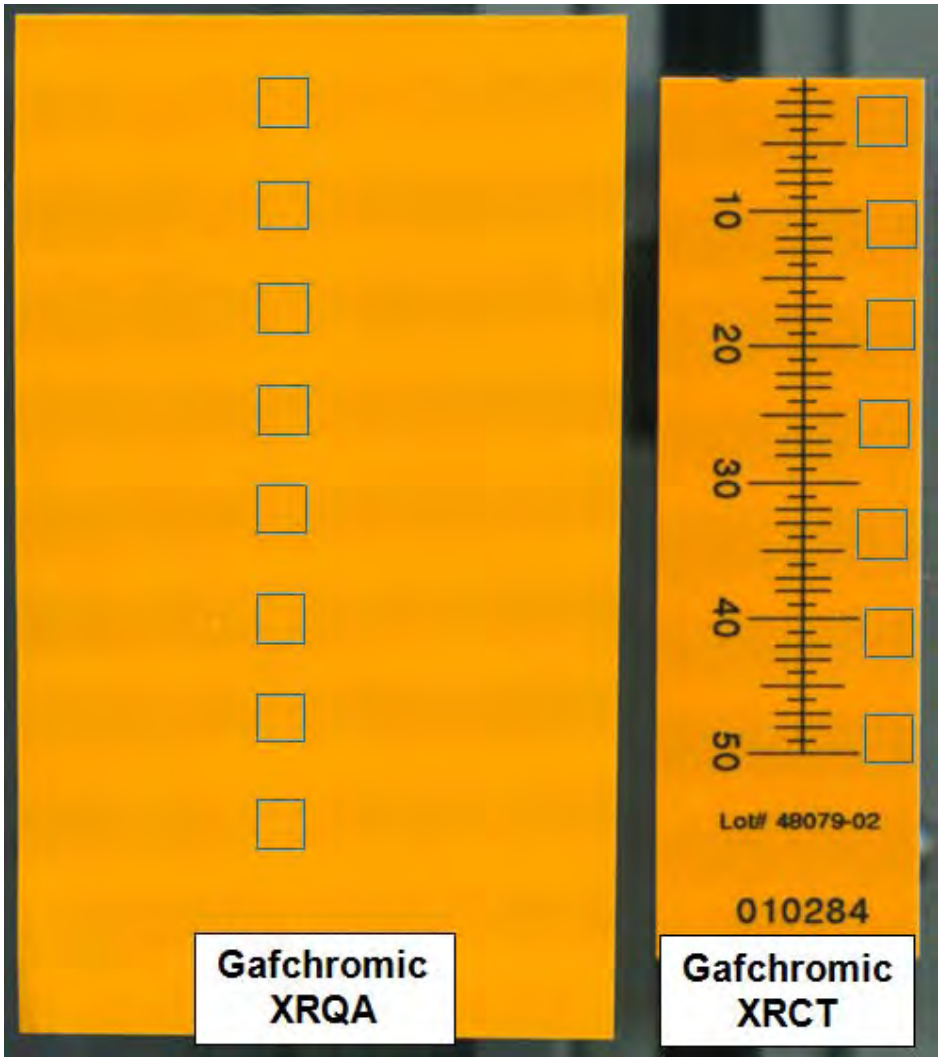

Figure 6.8: Gafchromic XRQA and XRCT films at 24 hours after irradiation to the CT component of PET/CT imaging. The mean net gray values of both films are 8.16 and 12.04, respectively. ***The blue boxes represent the area of determining the gray value from the irradiated CT slices. For an accurate measurement of the absorbed dose on XRCT film, the position of all boxes is kept away from the black metric scale, as it could affect the gray value reading.***

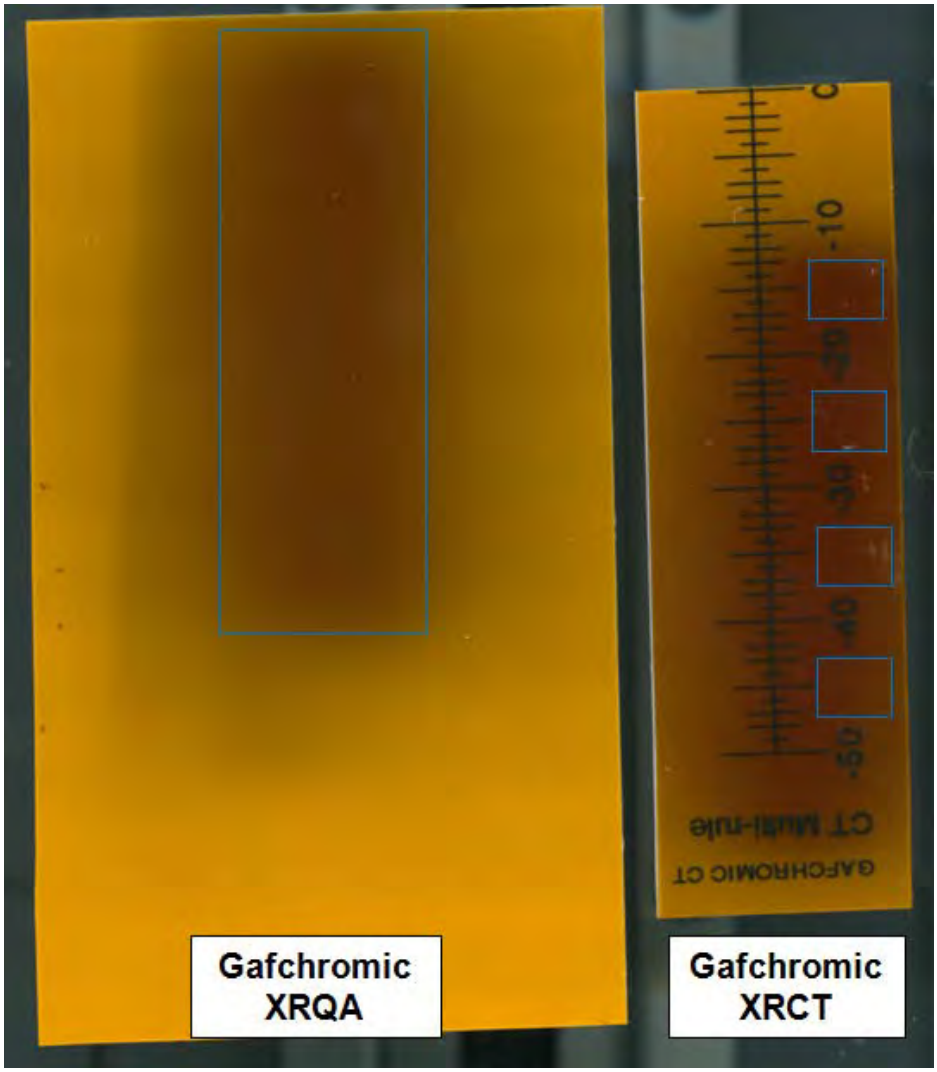

Figure 6.9: Gafchromic XRQA and XRCT films at 24 hours after irradiation to 1 GBq radioactivity of FDG and the CT component of PET/CT imaging. The mean net gray values of both films are 155.18 and 159.93, respectively. ***The blue boxes represent the area of determining the gray value from the irradiated films. For an accurate measurement of the absorbed dose on XRCT film, the position of all boxes is kept away from the black metric scale, as it could affect the gray value reading.***

6.3.3.2. The dose response curves

6.3.3.2.1. The x-ray dose response curves

All the exposed gafchromic XRCT and XRQA films of the sixteen CT irradiations are shown in Figures 6.10 and 6.11. In addition, the $CTDI_{vol}$ of all CT irradiations are listed in Table 6.8. Based on these data, the dose response curves for both XRCT and XRQA films were plotted against the recorded $CTDI_{vol}$ of each energy level. Interestingly, across all the tested energy levels (80 – 140 kVp), gafchromic XRCT film had demonstrated a slightly higher in the sensitivity for detecting the absorbed radiation dose than those of XRQA film (refer to Fig. 6.12). Therefore, for the subsequent irradiations (SXRT, Tc-99m and F-18), only XRCT film was used.

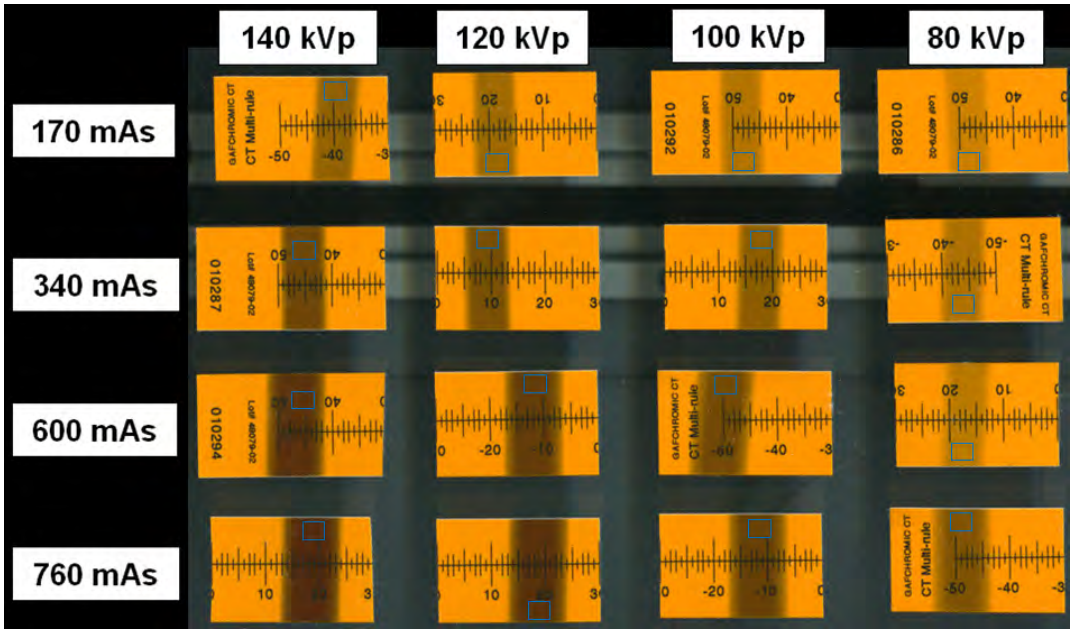

Figure 6.10: Gafchromic XRCT films at 24 hours after CT irradiations with various exposure factors (kVp and mAs). ***The blue boxes represent the area of determining the gray value from the irradiated CT slices.***

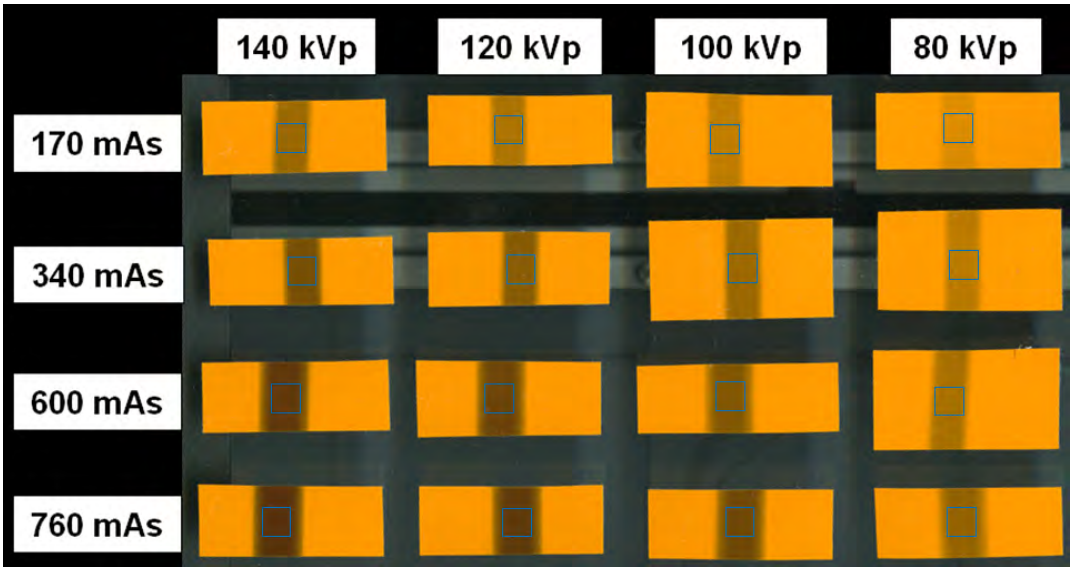

Figure 6.11: Gafchromic XRQA films at 24 hours after CT irradiations with various exposure factors (kVp and mAs). ***The blue boxes represent the area of determining the gray value from the irradiated CT slices.***

Table 6.8: The $CTDI_{vol}$ of all sixteen CT irradiations.

Irradiation	$CTDI_{vol}$ (mGy)
1	6.68
2	13.36
3	23.57
4	33.19
5	12.60
6	25.21
7	49.44
8	62.62
9	20.51
10	41.02
11	80.44
12	101.89
13	29.21
14	58.42
15	114.56
16	145.11

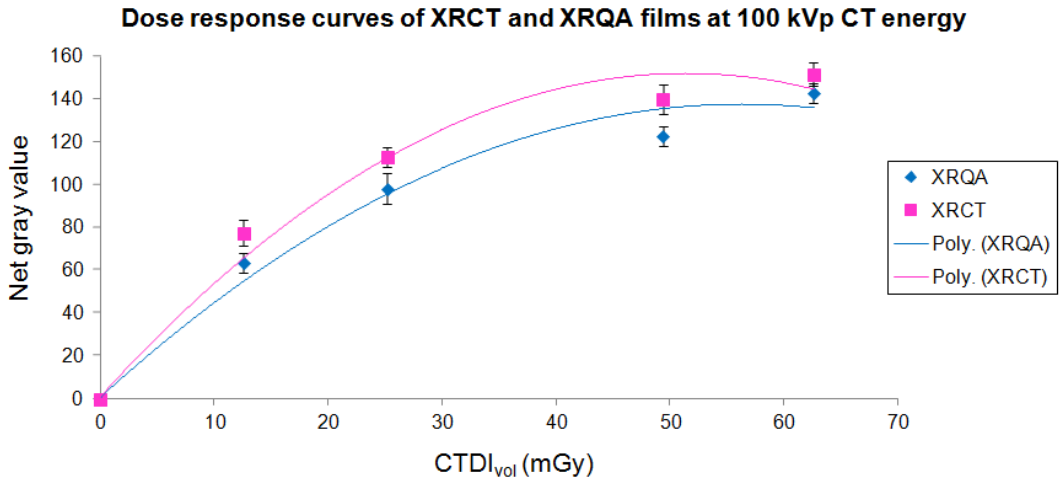

Figure 6.12: Dose response curves of gafchromic XRCT and XRQA films at 100 kVp CT energy. Both curves fit with second order polynomial trend lines. This result shows that XRCT film has a slightly higher sensitivity in detecting the absorbed radiation dose than XRQA film. *Error bars represent* ± *standard deviation*.

For the irradiations with SXRT machine, a noticeable colour change can be seen after the films were exposed to 20.0 mGy dose (Fig. 6.13). The dose response curve of this dosimetric experiment was again well fitted with second order polynomial trend line (Fig. 6.14).

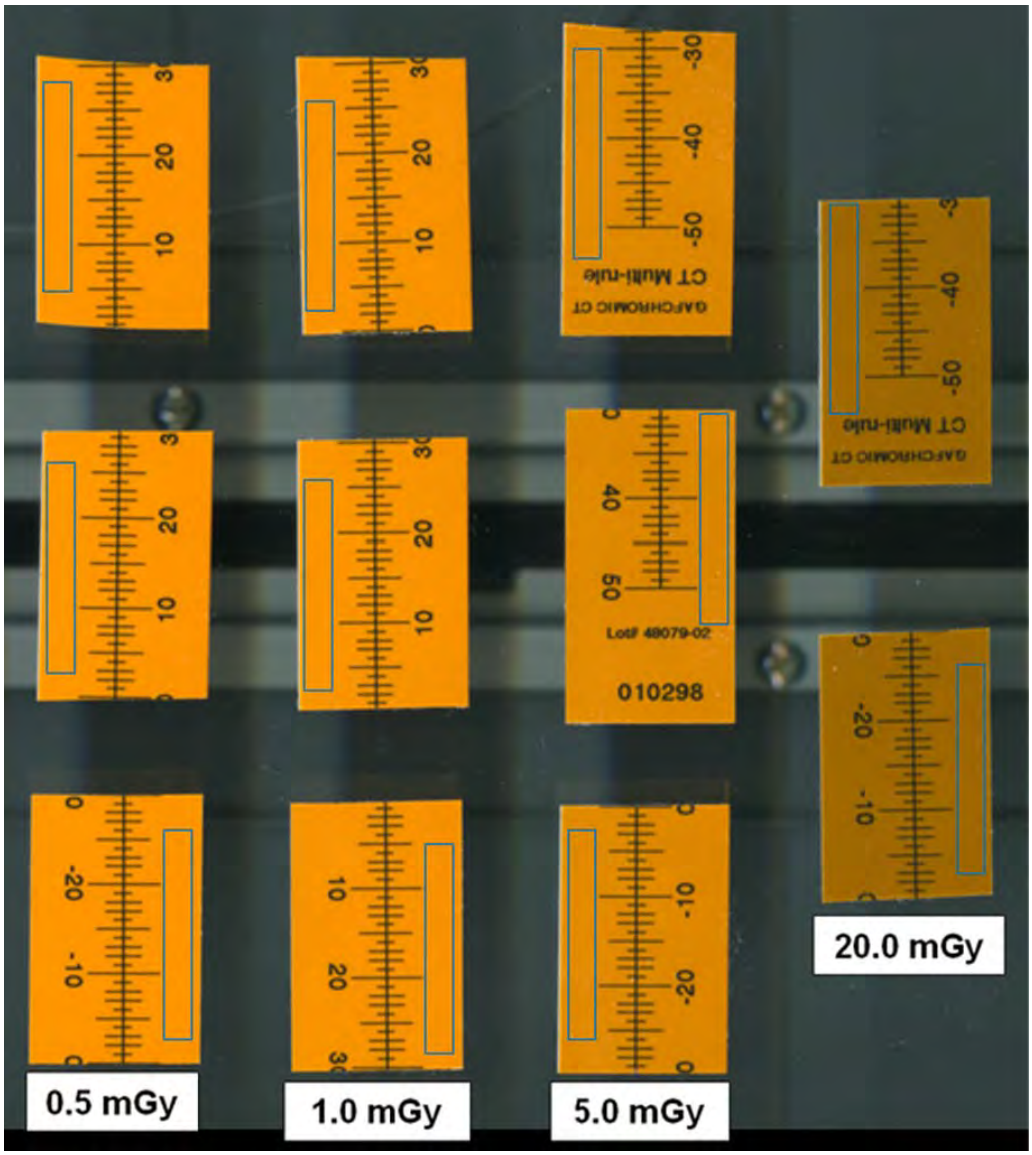

Figure 6.13: Gafchromic XRCT films at 24 hours after the irradiations with SXRT machine at 150 kVp energy level. A noticeable colour change can be seen at 20.0 mGy dose. ***The blue boxes represent the area of determining the gray value from the irradiated films.***

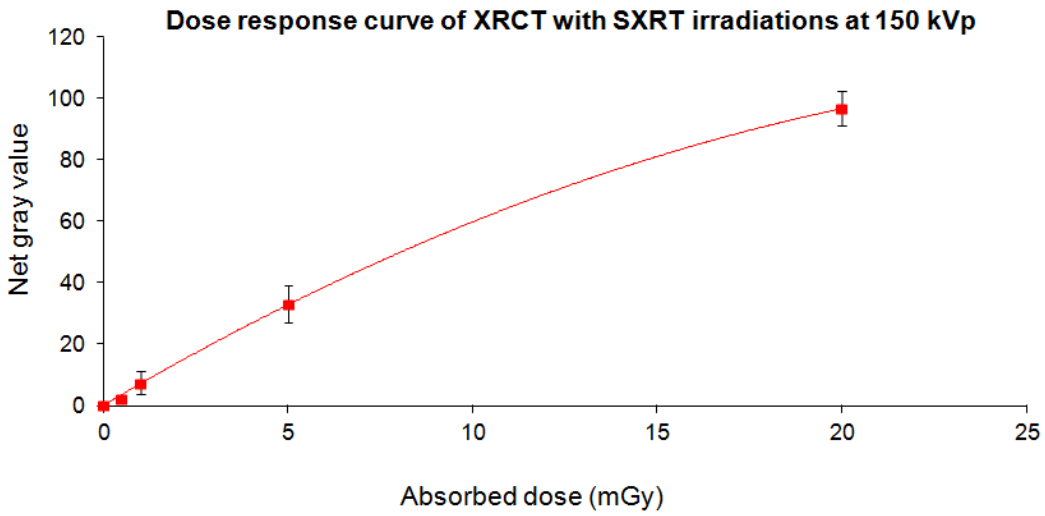

Figure 6.14: The dose response curve of XRCT film with the irradiations of SXRT machine at 150 kVp energy level. The curve fits with second order polynomial trend line. ***Error bars represent ± standard deviation*****.**

6.3.3.2.2. The gamma radiation dose response curves

XRCT film was changed in its colour at 60 min irradiation time to 15 GBq radioactivity of Tc-99m (Fig. 6.15). On the contrary, none of these films displayed visible colour changes after the exposures to 1.9 GBq radioactivity of F-18, even with 90 min irradiation time (Fig. 6.16). This was due to a vast variation in the radioactivity of both isotopes. However, the dose response curves of the two different irradiations (Tc-99m and F-18) were well fitted with second order polynomial trend lines (Fig. 6.17 and 6.18). These results may indicate that gafchromic XRCT is an appropriate type of radiochromic film for being utilised in estimating the radiation doses arising from different gamma energy levels, but, the dose response curve of each energy needs to be obtained [190].

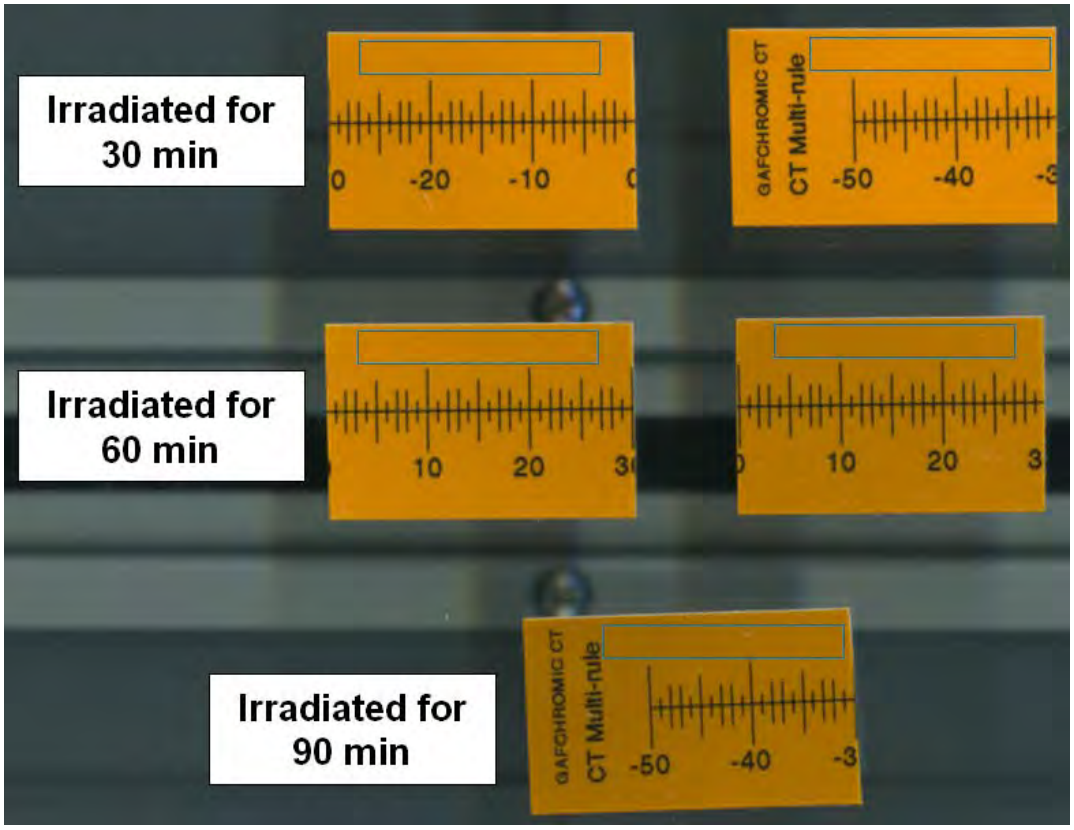

Figure 6.15: Gafchromic XRCT films at 24 hours after the irradiations with 15 GBq radioactivity of Tc-99m (140.5 keV). A noticeable colour change can be seen at 60 min irradiation time. ***The blue boxes represent the area of determining the gray value from the irradiated films.***

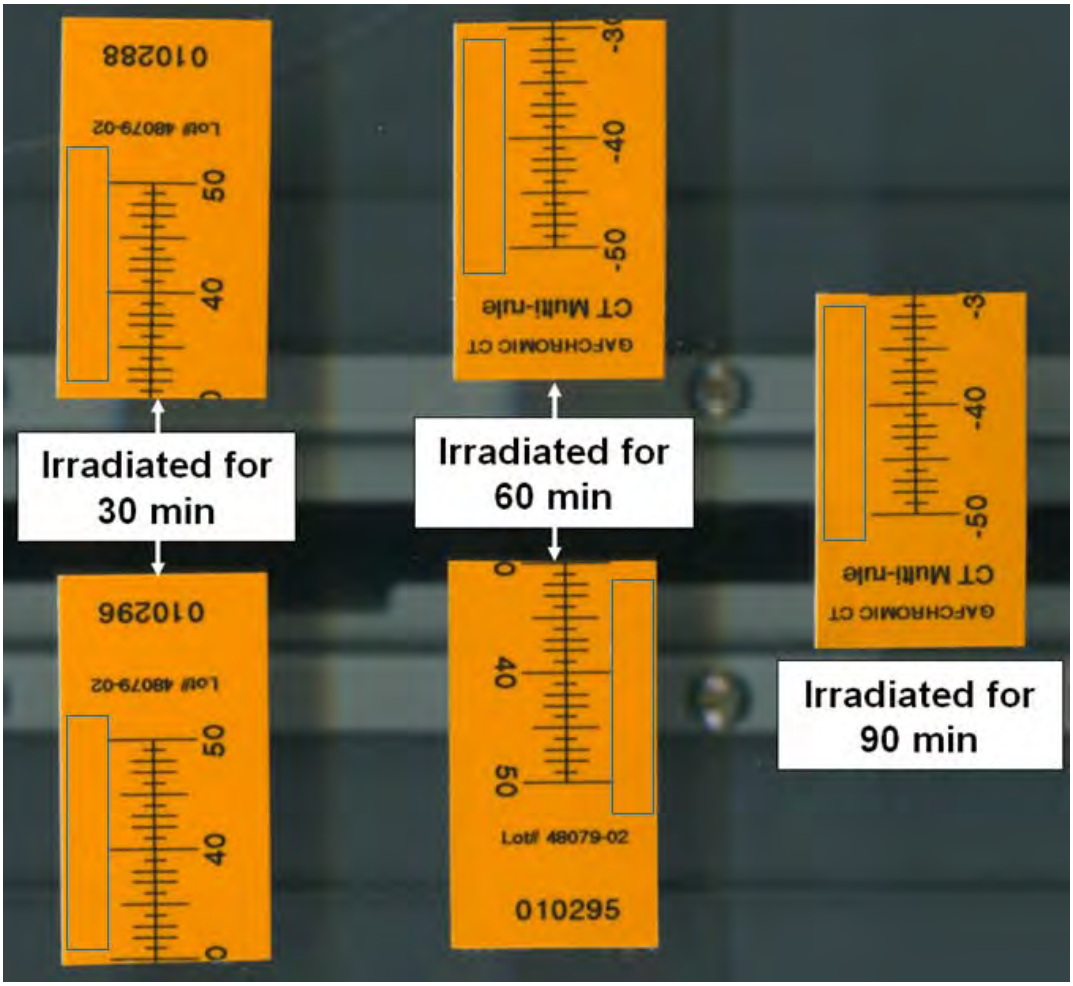

Figure 6.16: Gafchromic XRCT films at 24 hours after the irradiations with 1.9 GBq radioactivity of FDG (511 keV). Of these three different irradiation times, none of the films are found to have a visible colour change. ***The blue boxes represent the area of determining the gray value from the irradiated films.***

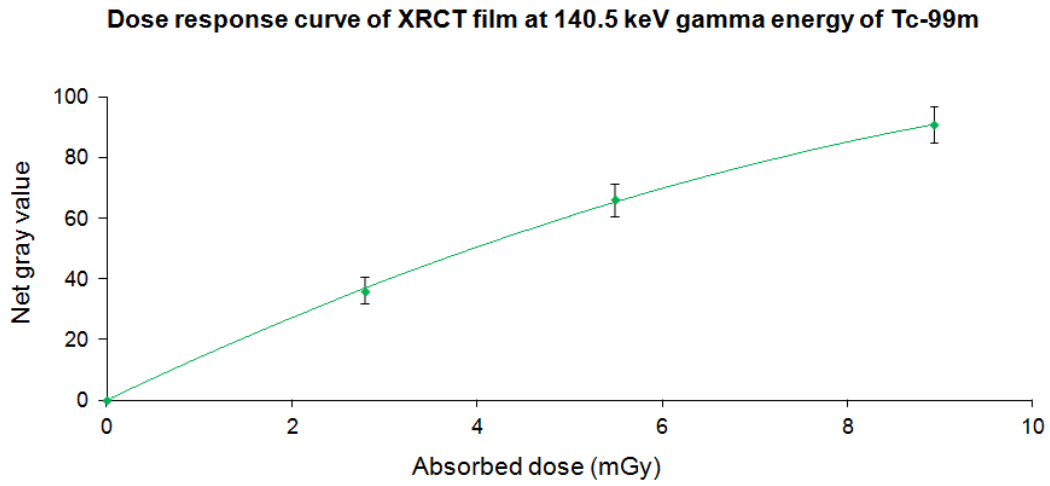

Figure 6.17: The dose response curve of XRCT film at Tc-99m gamma energy level (140.5 keV). The curve fits with second order polynomial trend line. *Error bars represent* ± *standard deviation*.

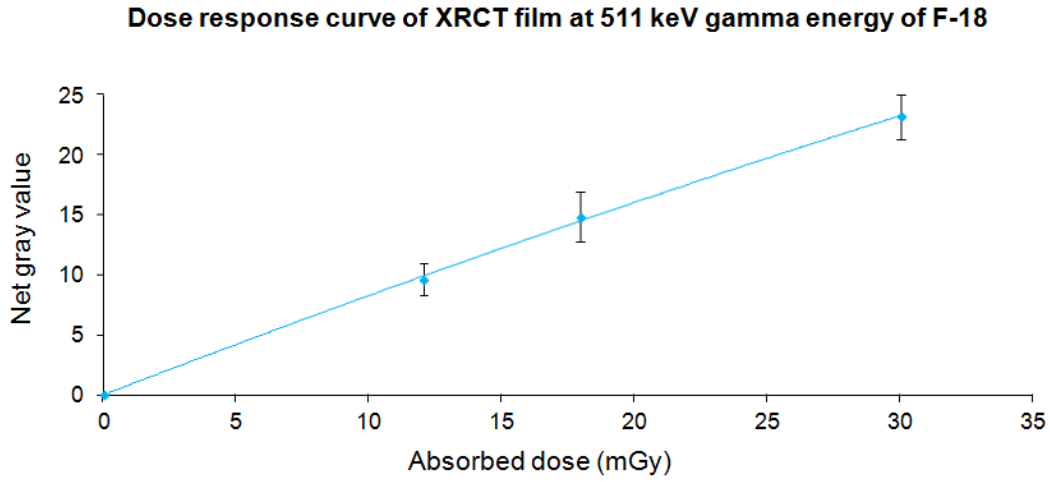

Figure 6.18: The dose response curve of XRCT film at F-18 gamma energy the level (511 keV). The curve fits with second order polynomial trend line. *Error bars represent* ± *standard deviation*.

6.3.4. Discussion

Gafchromic XRCT and XRQA films are commonly and routinely utilised in the dose assessments of CT scan and diagnostic radiology [186, 194]. Indeed, both of these films consist of the same active and radiation-sensitive materials [194]. However, the results from CT irradiations of this dosimetric study showed, across the tested energy range (80 – 140 kVp), XRCT film was slightly more sensitive in recording and detecting the absorbed radiation dose as compared with XRQA film. Thus, in constructing the dose response curves of the later irradiations (SXRT and gamma radiation), only XRCT film was used.

In the irradiations with SXRT machine, the absorbed radiation doses were ranging from 0.5 mGy to 20.0 mGy. Although these values seem to be quite minimal, the manufacturer has stated that gafchromic XRCT film can be used to measure the absorbed dose as low as 0.1 mGy [186]. Thus, XRCT film is capable to detect the lower absorbed radiation doses of these dosimetric experiments. On the other hand, when comparing the dose response curves of Tc-99m with F-18 (both radiopharmaceuticals emit gamma radiation), at the higher energy levels, more doses were required to produce an equivalent degree of film blackening. This finding is in accordance with the previous study by Butson *et al.* [186], even though all their XRCT films have been irradiated with an x-ray beam. Therefore, it is clear that gafchromic XRCT film is sensitive and suitable to be applied for quantifying the low absorbed radiation dose that has been delivered either by x or gamma ray.

6.3.5. Conclusion

Although accurate dose quantification for the whole body FDG PET/CT imaging has not been achieved throughout these experimental attempts, the results show that gafchromic XRCT film could potentially be used for measuring the absorbed radiation dose of FDG PET/CT scan. Therefore, the findings of this preliminary study have opened a new window for two-dimensional (2-D) dose measurement in FDG PET/CT imaging, particularly by using the radiologic type of gafchromic film.

6.4. Recommendations for reducing the FDG PET/CT radiation dose

Several studies have recommended few techniques or strategies in managing the PET/CT radiation dose to the patient [36, 156, 157, 183, 184, 187]. These techniques are classified according to the scanning component; FDG PET and CT scans.

6.4.1. FDG PET scan

Radiation dose to patients, whom have been intravenously administered with FDG, is directly proportional to the injected radioactivity [156, 187]. Thus, by reducing the amount of injected radioactivity of FDG, the radiation dose can effectively be reduced. In addition, some studies have proposed a lower FDG administered radioactivity of 5.2 MBq/kg, particularly when performing PET/CT imaging to a pediatric patient [36, 198-200]. In this case, if a lower FDG administered radioactivity (5.2 MBq/kg) is used during the clinical trial of this research, the PET effective dose of each patient could be further reduced up to 15%.

On the other hand, to compensate with the lower administered radioactivity of FDG and obtain a good quality PET emission image (with adequate count density), the imaging time per bed position may need to be increased [36, 156, 187]. Correspondingly, Gelfrand, M. J. [36] has reported that imaging time of 5 min per bed position is sufficient to be applied during PET/CT scan. However, when the per bed position imaging time is increased, it means that a longer total scanning time is required to perform a complete whole body PET/CT scan [156, 187]. This can result in patient discomfort, which then may cause a motion-induced misregistration artifact in the corresponding PET and/or CT images [156, 187]. Therefore, there should be a balance between the amount of administered radioactivity of FDG and the selected imaging time per bed position.

Another technique that can be employed for reducing the radiation dose from PET scan is by conducting the PET image acquisition in three-dimensional (3-D) mode [36, 157]. This 3-D acquisition mode enhances the sensitivity of the PET scanner as compared with 2-D mode [36, 157]. For this reason, PET emission scans of all patients from both populations (Malaysia and Italy) were carried out using 3-D acquisition mode, as described in the Chapter 3.

Apart from all of the above techniques, frequent voiding during uptake phase and after the scan is also a very effective measure to reduce the radiation dose in PET imaging [156, 187]. It can be achieved either by a good oral hydration or the administration of a diuretic drug like furosemide [146] (this method has been applied in all sixteen Malaysian patients during their preparation time, as mentioned in the Chapter 3). The rational for this approach is mainly based on fact that FDG is finally

accumulated in the urinary bladder, and this can be a major source of internal exposure to the bladder itself as well as to its neighbouring organs [169].

6.4.2. CT scan

As highlighted in section 6.3 of this chapter, there are three different scanning protocols that are commonly conducted during the CT scan of PET/CT imaging: diagnostic contrast-enhanced CT, co-registration and anatomical localisation CT, and CT for the attenuation correction mapping only. Each of these protocols results with a significant variation in the total PET/CT effective dose [36]. Thus, by properly knowing the main purpose of the CT scan before commencing PET/CT imaging, it could be very beneficial to the patient in terms of reducing the radiation dose. This fact augments the need for fully trained radiation technologist, which could facilitate him/her to choose the best approach to be employed during the scanning [178, 181].

Tube current modulation (generally known as Automatic Exposure Control; AEC) technique is one of the most effective methods for managing the radiation dose of the CT scan [201, 202]. This technique can considerably reduce the radiation dose to the patient in multi detector CT (MDCT) scan, without affecting the image quality [202]. However, it should be noted that the tube current modulation technique was not applied in the entire CT examinations of PET/CT imaging for both Malaysian and Italian patients (as mentioned in Chapter 3). Furthermore, the CT scanning parameters like mA, time per rotation, mAs, kVp, pitch value and slice thickness can significantly affect the CT effective dose [157]. The relationship between each of these parameters with the CT effective dose has been concisely addressed in the previous study by Gelfand, M. J. and Lemen, L. C. [157]. Nevertheless, out of all the parameters, mA and mAs are the

key elements [181], in which it is widely accepted that by decreasing these two values the CT radiation dose can be substantially reduced [184], as both of them have linear relation to the CT absorbed radiation dose [157].

The mAs reduction technique was exclusively applied during the CT scans of the three Malaysian patients; patients 2, 5 and 6 (as highlighted in section 6.4.1). For patient 2, the mAs value of 30 had been used during both of his CT scans (unenhanced CT and CECT), while 50 mAs was employed for patients 5 and 6. Based on the CT images of these three patients, 50 mAs was found to be sufficient for CECT scan; this lower mAs value produces the same diagnostic image quality with good organ enhancement as in 100 mAs (as shown in Fig. 6.19d). By halving the mAs value, the CT radiation dose has also been reduced by half, which is highly beneficial for the patient especially in regards to pediatric patients. However, if the mAs value was further reduced to 30 (as in patient 2), the image quality of the CECT images had been degradated significantly, due to the greater noise content [157] (Fig. 6.19f). Therefore, based on these findings, it could be suggested that 30 mAs is suitable to be used during the low dose CT protocol or unenhanced CT scan (as in the case of CT for anatomical localisation and co-registration images). In addition, if CT scan is performed for the diagnostic purposes (CECT), the selection of 50 mAs is seemed to be a better approach rather than using the higher mAs value.

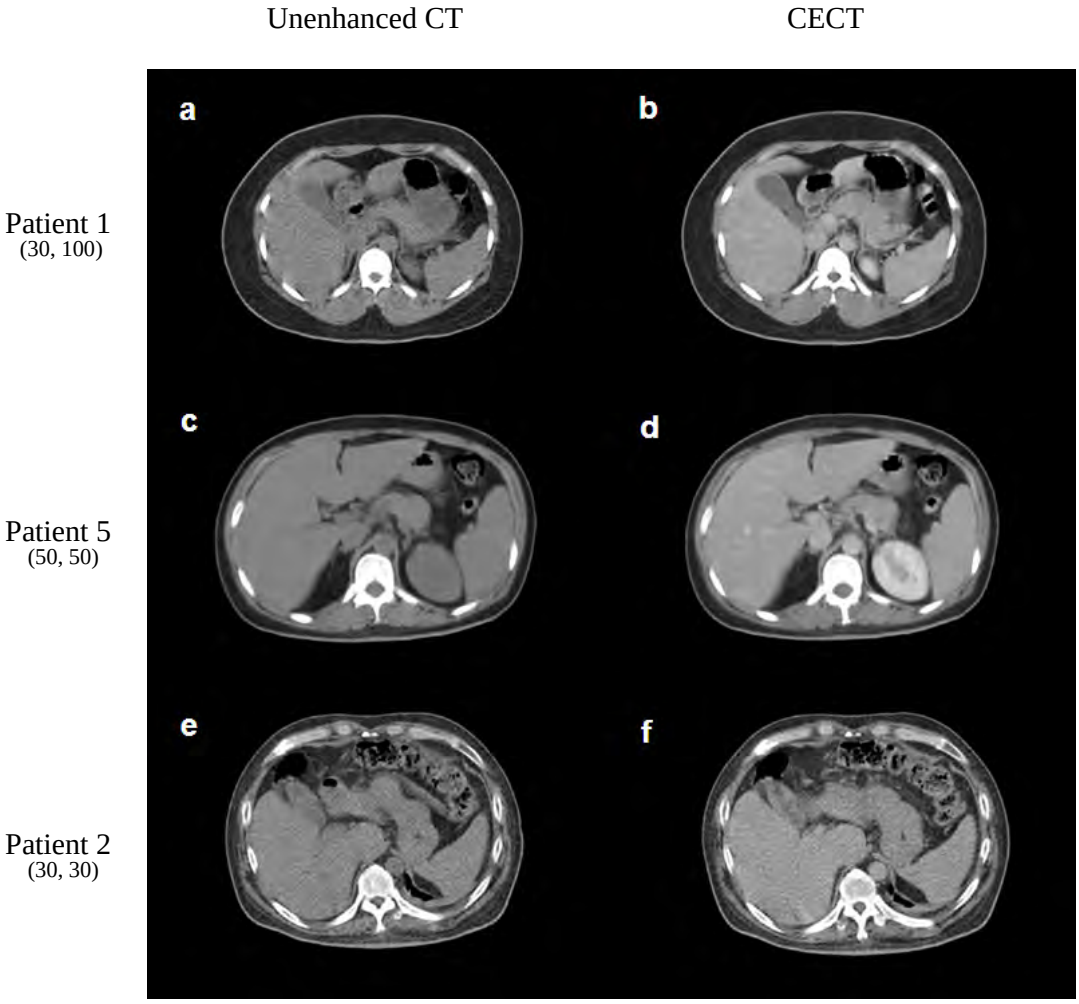

Note: The numbers in parentheses represent the mAs values that have been used during the unenhanced CT and CECT scans, respectively.

Figure 6.19: Example of the unenhanced CT (a, c & e) and CECT (b, d & f) images from patients 1, 5 and 2 of the Malaysian patients. The mAs value of 30 seems more appropriate to be used during unenhanced CT, as compared to 50 mAs (a & e vs. c). In CECT scans, although the mAs has been reduced by half (from 100 to 50 mAs), there is no different in the image quality of both images (b & d), where the later image can still demonstrate a good organs enhancement (d). However, if the mAs is further reduced to 30, the image quality has been extensively decreased; by less evident of organs enhancement and greater noise content (f).

CHAPTER 7

CONCLUSIONS

AND

FUTURE DIRECTIONS

This research has encompassed three distinct studies; starting with the clinical trial, followed by a phantom study and the dosimetric study. Based on all findings of this research work, the following conclusions have been reached. These in turn have also given rise to possible future research directions.

7.1. Conclusions

'FDG PET/CT imaging can clearly detect EPTB lesion'

This research thesis comprises novel and original work based on innovative scanning techniques of using an integrated PET/CT imaging system in detecting EPTB lesions. The major findings of this thesis are:

- All the detected EPTB lesions from both populations of the patients (Malaysia and Italy) in this study can clearly be depicted on the FDG PET/CT fusion images, with the high SUVmax1 values; ranging from 2.8 to 20.8. However, the utilisation of SUVmax1 value (from initial whole body FDG PET/CT scan) alone seems to be an impractical for the image analysis method in differentiating between EPTB and non-EPTB lesions. Thus, in standard clinical practice, the FDG PET/CT imaging finding still needs to be compared with the results of the other radiological examinations.

- Iodine-based contrast media can safely be applied during FDG PET/CT imaging of EPTB patient, in which it will not significantly and clinically affect the

SUVmax values of the fused images. This patients' finding has also been augmented with the results of the anthropomorphic phantom study, where no statistical differences are found on the SUVmax and SUVmean values of the simulated tissues (liver, blood vessels and spinal lesion).

- DTPI technique of FDG PET/CT scan may not be an effective scanning procedure for distinguishing EPTB from other infectious lesions. However, based on the results of follow-up FDG PET/CT scan in the six Malaysian EPTB patients, this technique could help the physician for determining the activity status of EPTB lesion. This interesting imaging finding warrants further investigation in larger cohort of patients who have completed the six months anti-TB treatment.

- The mean effective dose arising from FDG PET/CT scans of this study is in accordance with the previously reported values (< 25 mSv), even though DTPI technique has been performed during the imaging acquisitions. In addition, 50 mAs value could be an optimal tube current-time product for FDG PET/CT imaging when contrast-enhanced CT (CECT) scan is required. By using this mAs value, the amount of CT radiation dose can be reduced by half as compared with the higher value (100 mAs), and at the same time maintains the same diagnostic CT image quality.

- From dose assessment perspective, gafchromic XRCT film has a potential to be applied for quantifying the absorbed radiation dose arising from FDG PET/CT

imaging in two-dimensional (2-D). However, more comprehensive experiments need to be conducted in order to solve the uncertainties of utilising a 2-D dose measurement for estimating the whole body radiation dose. This issue is opened for future studies in the radiation dose measurement of FDG PET/CT imaging.

In conclusion, this research has shown that a comprehensive assessment of EPTB infectious disease might be obtained by supplementing the anatomical manifestations of the lesions seen on CT images with the functional characteristics provided by the PET images, which results in a multi-dimensional multi-modality evaluation. The findings of this thesis could offer a significant change in the diagnostic algorithm of EPTB infection, in which it appears that, the improvement in detecting and determining the extension of EPTB lesions has been achieved. These observations, taken together, provide the beginnings of a suitable body of evidence upon which a physician can make a clinical decision on whether the use of FDG PET/CT imaging is indicated for the detection of EPTB lesions.

7.2. Future directions

Two studies that could possibly be performed in order to complement and verify the results of this research include:

1. A prospective study of using a dynamic scanning protocol during FDG PET/CT imaging of EPTB patients. The result of this study would give a detailed assessment and better understanding on the FDG accumulating process of EPTB lesion.

2. The application of other radiopharmaceutical, such as FDG-labelled white blood cells (FDG-WBC) for detecting EPTB lesions. FDG-WBC has been previously reported to have a high sensitivity and specificity in the detection of infectious lesion. Thus, by conducting this study, it could enhance the capability and feasibility of using PET/CT imaging in identifying and localising EPTB lesions. This study may also provide an alternative radiotracer for the imaging diagnosis of EPTB infectious disease.

APPENDICES

Appendix 1: Human Ethics Approval from University Putra Malaysia (UPM)

Appendix 2: Human Ethics Approval from Ministry of Health Malaysia

Appendix 3: Patient's Information Sheet

Appendix 4: Informed Consent Form

Appendix 5: Brown Fat Case Report

Appendix 6: Estimating the PET Effective Dose

Appendix 7: Estimating the CT Effective Dose

Appendix 8: Published papers

Appendix 1

UNIVERSITI PUTRA MALAYSIA
FAKULTI PERUBATAN DAN SAINS KESIHATAN
FACULTY OF MEDICINE AND HEALTH SCIENCES

(Translated Version From Bahasa Malayu)

Our Ref : UPM/FPSK/PADS/T7-MJKEtikaPer/F01(LECT_Aug01)
Dated : 23 Oktober 2007

To Whom It May Concern

Sir/Madam,

RESEARCH PROJECT :

EVALUATION OF FUSION INTEGRATED IMAGING TECHNIQUE 18F FDG PET CT IN EXTRAPULMONARY MYCOBACTERIUM TUBERCULOSIS INFECTION

RESERACHER : ASSOCIATTE PROF DR ABDUL JALIL NORDIN

The Ethical Committee for Medical Research , Faculty of Medicine and Health Sciences has decided that there is no ethical issues against the above mentioned research proposal .

Thank you

'With Knowledge We Serve'

Yours sincerely,

PROFESSOR DR AZHAR MD ZAIN

Chairman
Ethical Committee for Medical Research
Faculty of Medicine and Health Sciences
University Putra Malaysia

Fakulti Perubatan dan Sains Kesihatan, Universiti Putra Malaysia, 43400 UPM Serdang, Selangor Darul Ehsan.
: 603-89466000, 89468519, 89468482 : 603-89426957 http://www.medic.upm.edu.my
Fakulti Perubatan dan Sains Kesihatan, Kampus Klinikal HKL, Jalan Masjid, 50586 Kuala Lumpur.

Appendix 2

PEJABAT TIMBALAN KETUA PENGARAH KESIHATAN
OFFICE OF THE DEPUTY DIRECTOR-GENERAL OF HEALTH
(PENYELIDIKAN & SOKONGAN TEKNIKAL)
(RESEARCH & TECHNICAL SUPPORT)
KEMENTERIAN KESIHATAN MALAYSIA
MINISTRY OF HEALTH MALAYSIA
Aras 12, Blok E7, Parsel E, Presint 1
Level 12, Block E7, Parcel E, Precinct 1
Pusat Pentadbiran Kerajaan Persekutuan
Federal Government Administrative Centre
62590 PUTRAJAYA

Tel : 03 88832543
Faks : 03 88895184

MEDICAL RESEARCH & ETHICS COMMITTEE
MINISTRY OF HEALTH MALAYSIA
c/o Institute for Health Management
Jalan Rumah Sakit, Bangsar
59000 Kuala Lumpur

Ruj. Kami :(6)dlm.KKM/NIHSEC/08/0804/P07-195
Tarikh : 5 Mac 2008

Project Title :
Evaluation of Fusion Integrated Imaging Technique 18F FDG PET CT In Extrapulmonary Mycobacterium Tuberculosis Infection.

Principal Investigator : Assoc Prof Dr Abdul Jalil Nordin
Nuclear Medicine Specialist
Head, Radionuclide Imaging Unit
Faculty of Medicine & Health Sciences
University Putra Malaysia

Documents received and reviewed with reference to the above study:

1. Borang JTP/KKM/1-2
2. Research Proposal
3. Patient Information Sheet and Informed Consent Form - English and Malay
4. Letter of Undertaking from UPM – indeminity and patient insurance
5. Curriculum Vitae of Principal Investigator and co-investigators.

The Medical Research & Ethics Committee, Ministry of Health Malaysia operates in accordance to the International Conference of Harmonization Good Clinical Practice Guidelines.

Comments (if any):

Project Sites: Hospital Serdang / Hospital Putrajaya

Decision by Medical Research & Ethics Committee:
(√) Approved
( ) Conditionally Approved
( ) Disapproved

Date of Approval : 5 March 2008

Shahnaz

DR SHAHNAZ MURAD
For Chairman
Medical Research & Ethics Committee
Ministry of Health Malaysia

Subject Information Sheet

You are being selected to participate in this research project on **'18F FDG PET CT evaluation in mycobacterium tuberculosis extra pulmonary infection'**

Purpose
The purpose of this research project is to document all findings of EXTRAPULMONARY Mycobacterium Tuberculosis infection, using 18F-FDG PET-CT modality.

Procedures involve
Within these research activities, you will be subjected to PET CT examination with 18F FDG injection. There will be two occasions where this examination takes part. The first examination takes place during 'early check point' for the purpose of diagnosis. This will be followed by a prolonged period of treatment using Direct Observation Treatment Scheme DOTS for over an interval of 6 months. After completion of treatment with antituberculous drugs, you will have to undergo another round of PET CT examination to observe the treatment responsiveness and to observe any residual changes.

Your responsibilities
Your responsibility is to cooperate with our team of doctors.

You are required to be fasting for at least 6 hours prior to all above mentioned procedures.

During the imaging procedure, we require your full cooperation to ensure good optimum quality of images to be produced.

The experiment

The experimental part of this research activity is to look at the pattern of activity of 18^F FDG uptake in the tuberculous infective lesion that you have on PET CT imaging modality.

a.What is Positron Emission Tomography?

Positron emission tomography, also called PET imaging or a PET scan, is a diagnostic examination that involves the acquisition of physiologic images based on the detection of radiation from the emission of positrons. Positrons are tiny particles emitted from a radioactive substance administered to the patient. The subsequent images of the human body developed with this technique are used to evaluate a variety of diseases.

b.How should I prepare for the procedure?

PET is usually done on an outpatient basis. Your doctor will give you detailed instructions on how to prepare for your examination. You should wear comfortable, loose-fitting clothes. You should not eat for four hours before the scan. You will be encouraged to drink water. Your doctor will instruct you regarding the use of medications before the test.

How does the procedure work?

Before the examination begins, a radioactive substance is produced in a machine called a cyclotron and attached, or tagged, to a natural body compound, most commonly glucose, but sometimes water or ammonia. Once this substance is administered to the patient, the radioactivity localizes in the appropriate areas of the body and is detected by the PET scanner.

Different colors or degrees of brightness on a PET image represent different levels of tissue or organ function. For example, because healthy tissue uses glucose for energy, it accumulates some of the tagged glucose, which will show up on the PET images. However, cancerous tissue, which uses more glucose than normal tissue, will accumulate more of the substance and appear brighter than normal tissue on the PET images.

To begin the procedure, your permission will be asked to draw 5 mls of blood to look at your glucose level to ensure you are at 'true fasting' state. Your physical statistics and body weight will be measured to derive your lean body mass in order to calculate the dosage of 18F -FDG which will be in the form of normal saline. A small amount of radioactive glucose is then injected into your bloodstream.

There is no danger to you from this injection. Glucose (also known as sugar) is a common substance every cell in your body needs in order to function. Radioactive glucose must pass multiple quality control measures before it is used for any patient injection.

The radiation exposure associated with PET is similar to that associated with a conventional CT scan.

After the injection, you will wait approximately an hour, while the injection material is distributed throughout your body.

Then, you will be asked to lie on a table that passes slowly through the scanner. The scanner resembles a CT scanner, but has a much larger opening. Some people fall asleep during the scan. Before the imaging procedure, you will be asking to empty your bladder. During imaging procedures, you are required to lie still on the table couch and breathe quietly. The whole procedure will last about 40 to 50 minutes.

Upon completion of the image acquisition, you will be informed by the radiographer in-charge.

When a disease strikes, the biochemistry of your tissues and cells are changed. In cancer, for example, cells begin to grow at a much faster rate, feeding on sugars like glucose. PET works by using a small amount of a tracer drug chemically attached to glucose or other compounds. You are injected with the tracer. It travels through your body emitting signals and eventually collects in the organs targeted for examination. If an area in an organ is cancerous or infected, the signals will be stronger than in the surrounding tissue. A scanner records these signals and transforms them into pictures of chemistry and function.

How will I feel afterwards?

You should feel fine. There are no side-effects from the injected tracer.

Is PET Safe?

The risks associated with a PET scan are minimal. Most studies are conducted with an injection made up of radioactive glucose (sugar). The radiation exposure associated with PET is similar to a conventional whole-body diagnostic CT scan.
In terms of comparison the risk of radiation exposure is 400 times chest radiograph which is equal to 8 mSv with a lifetime cancer mortality risk estimation of 4.0×10^{-4}.
However, the information gathered from this study will be invaluably beneficial to you and others. Therefore the advantages in carrying out this examination definitely outweigh the risk.

What are the benefits vs. risks?
Because PET allows study of body function, it can help physicians detect alterations in biochemical processes that suggest disease before changes in anatomy are apparent with other imaging tests, such as CT or MRI.

The expected benefits from PET CT imaging as compared to other routine conventional method of imaging in your illness will be higher detection rate of infective foci. Therefore follow up can be done more accurately following anti tuberculous drug treatment by prolonging the course of the treatment. This will make the treatment more effective and precise in terms of duration.

Current practice using conventional method of imaging often failed in holding up the course of infection effectively as the organism involved managed to ‘hide’ in the ‘normal looking tissues’ during follow up study.
Thus, it will make treatment to this illness ineffective. This may result in further complication and complicates further by disability.

PET CT imaging procedure has been performed world wide and has been recently established in Malaysia even though the technology has been around for the past 5-8 years in the modern western and far eastern countries. So far, there has been no reported trial related injury during the procedure.

Because the radioactivity is very short-lived, your radiation exposure is low. The substance amount is so small that it does not affect the normal processes of the body.

The radioactive substance may expose radiation to the fetus in patients who are pregnant or the infants of women who are breast-feeding. The risk to the fetus or infant should be considered in relation to the potential information gain from the result of the PET examination. If you are pregnant, you should inform the PET imaging staff before the examination is performed.

What happens after my scan?

After your scan, you will get up from the scanner bed and check out with the receptionist. You will be notified when your results will be available.

a.Are there potential side effects to a PET scan?

No, there are no side effects to having a PET scan performed. The only pain involved is the needle prick when you receive the radiopharmaceutical injection and it doesn't differ from any other type of injection you might receive in its "pain quotient."

b.When will I get my results?

You will ordinarily receive your results within 24 hours of your PET scan.

Are there alternatives to PET?

Yes and no. There are examinations that you can have performed. CT and MRI, for example, both examine the anatomical (physical) structure. Therefore, they can be useful in determining the size and location of a tumor; however, neither of them can determine the tumor's viability, whereas PET can determine whether a tumor is still active.

Why is PET not well known? Why have I never heard of PET before?

While PET has been around for years, it has only been in the last few years that PET has moved from the research realm to the diagnostic/clinical sphere. In Malaysia this is the latest modern advanced technology available in aiding the clinician to diagnosed disease.

How many PET studies are performed per year?

In the Western community (Europe and US), approximately 350,000 PET scans will be performed in 2002. The numbers of scans are increasing dramatically, now that PET is no longer only for research purposes. It is estimated that within the next five years in excess of 2,000,000 PET scans will be performed per year.

Do I have to pay?

You are very fortunate to have this opportunity to be examined using a very sophisticated equipment from the latest invention in diagnostic imaging in medicine. Unfortunately, this examination is very expensive. The cost of the examination is RM 7 000 per patient but the sponsor will bear the expenses.

Though non obligatory, we would be grateful if you are kind enough to contribute at any amount voluntarily to reduce the cost of this examination. The money will be 'recycled' in recruiting other potential subjects for similar investigation.

Your return trip with appropriate transport to the PET CT Centre in Wijaya International Medical Centre / Subang Jaya Medical Centre or Putrajaya Hospital will be provided.

Do I have to take part?
Your involvement in this research activity is on a voluntary basis. If you decide to withdraw, be kind enough to inform us in due consideration. You will not be panelized for your decision.

Confidentiality
The authority from Faculty of Medicine UPM and the Ministry of Health Malaysia will be granted direct access to your original medical records for verification of these research activities. However, your confidentiality will not be violated. Your records will be kept safe and will never be available for the public. Your identity will be hidden in all published data including oral and poster presentation or during scientific writing.

Whom to contact?
The following consultants are available if you need further clarification in relation to this study:

1. Professor Madya Dr Abdul Jalil Nordin
Radionuclide Imaging Unit
Faculty Medicine, UPM
Tel: 012 3042842

2. Dr Noraini Abdul Rahim
Consultant Radiologist
Diagnostic Imaging Department
Serdang Hospital
Tel: 012 2801847

Alternative Centres for PET CT examination
Under the following circumstances, this research activity may be withhold or postponed:

1. Inavailability of 18F FDG in case of cyclotron or its component breaks down
2. Break down of PET CT machine
3. Shut down of the Centre

The activity may also take place at other centres with PET CT facilities like Subang Jaya Medical Centre and Putrajaya Hospital or Prince Court Hospital depending on the availability of substance for injection and the machine.

Upon resuming our research activity we will inform you in due time.

Duration of research activities

You are expected to be involved in this research activity for at least 6-8 months from the date of confirming your diagnosis till completion of antibiotic treatment for 6 months or 12 months.
Along this period, you are expected to undergo PET CT examination twice i.e. at the beginning of infection and upon completion of your treatment. We anticipate approximately not less than 27 patients to be participating in this activity.

Universiti Putra Malaysia
Nuclear Imaging Unit, Faculty Medicine & Health Sciences , University Putra Malaysia, Serdang 43400, Malaysia

INFORMED CONSENT FORM

TITLE
"Evaluation of Fusion Integrated Imaging Technique 18F FDG PET CT in Extrapulmonary Tuberculosis Infection"

PROTOCOL IDENTIFIER:

SPONSOR:
University Putra Malaysia

PRINCIPAL INVESTIGATOR:
Professor Madya Dr Abdul Jalil Nordin

INSTITUTION ADDRESS:
Radionuclide Imaging Unit, Faculty Of Medicine and Health Sciences, University Putra Malaysia, Serdang 43400

THE NATURE AND PURPOSE OF THE STUDY
You have been invited to take part in a research study with an investigational procedure called Positron Emission Tomography Computed Tomography (PET CT) for the potential diagnosis of Extrapulmonary Tuberculous Infection. This *PET CT device* is manufactured by either SIEMENS or General Electric (GE).
The purpose of this study is to assess the effectiveness and accuracy of PET CT device compared to conventional imaging devices Computed Tomography (CT) Scan or Magnetic Resonance Imaging (MRI) in the diagnosis and treatment of extrapulmonary Tuberculous infection

STUDY DESCRIPTION
If you decide to participate in this study, you will be one of 60 subjects. The maximum length of time of your participation in this study will be 8 months apart. If necessary, however, the study may be stopped or you may be withdrawn from the study at any time.
You will be subjected to PET CT examination with 18^{F} FDG injection. There will be two occasions where this examination takes part. The first examination takes place during 'early check point' for the purpose of diagnosis. After completion of treatment with antituberculous drugs, you will have to undergo another round of PET CT examination to observe the treatment responsiveness and to observed any residual changes on PET CT .

While participating in the study, you are requested to give your full cooperation to the attending doctor. You understand that as a subject on a research study, you have certain responsibilities.

Your study doctor will schedule your visit to another institution with PET CT facility for you to undergo this investigation . The site will be within Klang Valley and your doctor will arrange the return transportation for you. PET is usually done on an outpatient basis. Your doctor will give you detailed instructions on how to prepare for your examination. You should wear comfortable, loose-fitting clothes. You should not eat for four hours before the scan. You will be encouraged to drink water. Your doctor will instruct you regarding the use of medications before the test. Before the examination begins, a radioactive substance is produced in a machine called a cyclotron and attached, or tagged, to a natural body compound, glucose. Once this substance is administered to you, the radioactivity localizes in the appropriate areas of the body and is detected by the PET scanner.

To begin the procedure, your permission will be asked to draw 5 mls of blood to look at your glucose level to ensure your are at 'true fasting' state. Your physical statistics and body weight will be measured to derived your lean body mass in order to calculate the dosage of 18F -FDG which will be in the form of normal saline . A small amount of radioactive glucose is then injected into your bloodstream.

Then, you will be asked to lie on a table that passes slowly through the scanner. The scanner resembles a CT scanner, but has a much larger opening. Some people fall asleep during the scan. Before the imaging procedure, you will be ask to empty your bladder. During imaging procedures, you are required to lie still on the table couch and breath quietly. The whole procedure will last about 40 to 50 minutes.

Upon completion of the image acquisition, you will be informed by the radiographer in-charge. After your scan, you will get up from the scanner bed and check out with the receptionist. You will be notified when your results will be available.

RISKS OF STUDY PARTICIPATION

Experience with the use of this device for investigation in clinical research to date has shown that there are no side effects to having a PET scan performed. The only pain involved is the needle prick when you receive the radiopharmaceutical injection and it doesn't differ from any other type of injection you might receive.

The risks associated with a PET scan are minimal. Most studies are conducted with an injection made up of radioactive glucose (sugar). The radiation exposure associated with PET is similar to a conventional whole-body diagnostic CT scan.

In terms of comparison the risk of radiation exposure is 400 times chest radiograph which is equal to 8 mSv with a lifetime cancer mortality risk estimation of 4.0×10^{-4} . However, the informations gathered from this study will be invaluably beneficial to you and others. Therefore the advantages in carrying out this examination definitely outweigh the risk.

POSSIBLE BENEFITS OF STUDY PARTICIPATION

The main goal of this research study is to learn more about the value of PETCT in the management of extrapulmonary tuberculous infection. Because PET allows study of body function, it can help physicians detect alterations in biochemical processes that suggest disease before changes in anatomy are apparent with other imaging tests, such as CT or MRI.

The expected benefits from PET CT imaging as compared to other routine conventional method of imaging in your illness will be higher detection rate of infective foci. Therefore follow up can be done more accurately following anti tuberculous drug treatment by prolonging the course of the treatment. This will make the treatment more effective and precise in terms of duration.

Current practice using conventional method of imaging often failed in holding up the course of infection effectively as the organism involved managed to 'hide' in the 'normal looking tissues' during follow up study.
Thus will make treatment to this illness ineffective. This may result in further complication and complicates further by disability.

OTHER AVAILABLE METHODS

There are examinations that you can have performed. CT and MRI, for example, both examine the anatomical (physical) structure. Therefore, they can be useful in determining the size and location of a tumor; however, neither of them can determine the tumor's viability, whereas PET can determine whether a tumor is still active.

TREATMENT FOR STUDY-RELATED INJURY

Eventhough the risks associated with a PET scan are minimal, every effort to prevent any injury that could result from this trial will be taken by the study doctor.
If you suffer any physical injury as a result of participation in this study, or believe you have sustained a research-related injury, you should contact . Prof Madya Dr Abdul Jalil Nordin, at 012 3042842 and immediate medical therapy will be made available to you at your study hospital. No compensation is available; any injury as a result of your participation will be evaluated and treated in keeping with the benefits or care to which you are entitled.

WITHDRAWAL FROM STUDY

Your involvement in this research activity is on a voluntary basis . If you decide to withdraw, be kind enough to inform us in due consideration. You will not be panelized for your decision.

TO OBTAIN FURTHER INFORMATION

If during the course of this study, you or your relatives have any questions about the study please contact your study doctor :

Professor Madya Dr Abdul Jalil Nordin at Radionuclide Imaging Unit Faculty Medicine UPM, SERDANG and/or Dr. Noraini Abdul Rahim at Diagnostic Imaging Department ,Serdang Hospital, SERDANG

If you experience any side-effects or medical problems now or during the study, please also contact the above doctors.

VOLUNTARY PARTICIPATION

You understand that participation in this study is voluntary and that if you decide not to participate, you will experience no penalty or loss of benefits to which you would otherwise be entitled outside of this study. If you decide to participate, you may change your mind about being in the study, and may stop at any time. You understand that you must inform the doctor of this decision immediately. You understand that such a decision on your part will not influence the availability of future medical care or other benefits to which you are otherwise entitled outside of this study. You understand that follow-up final visit evaluations may be requested if you decide to withdraw from this study.

You understand that you or your legally acceptable representative will be informed in a timely manner of any new information that may affect your willingness to continue participation in this study.

You will not receive any compensation for your participation in the trial. However, reimbursement on payment for transport to and from clinic for the visits scheduled in the study will be paid.

CONFIDENTIALITY

The authority from Faculty of Medicine UPM and the Ministry of Health Malaysia will be granted direct access to your original medical records for verification of this research activities . However, your confidentiality will not be violated. Your records will be kept safe and will never be available for the public. Your identity will be hidden in all published datas including oral and poster presentation or during scientific writing .

READ AND FULLY UNDERSTOOD

CERTIFICATION BY INVESTIGATOR

I, being the supervising study doctor, confirm that I have fully explained the nature, purpose and reasonably foreseeable risks of taking part in this study to the patient/parent or legal representative. He/she has read and kept a copy of the Patient Information sheet and signed Consent Form. He/she has freely agreed to participate in the trial.

Signature of investigator
Date

Name of investigator

CONSENT BY SUBJECT

I have read and understood the Patient Information Sheet about this research and have been given the chance to ask any questions. I understand and accept the answers that have been given.

I confirm that I have been given enough time to think about and have freely agreed to take part in this research and know that I can at any time, ask for more information from the doctor and cease to participate in the research without this affecting my usual medical care in any way.

I also understand that should I decide to stop taking part in this study, I do not need to give any reason why, except if it is due to the effects of the investigation . In this case I must report the details to the doctor.

Finally, I agree to participate in the research and to closely follow the instructions I am given. I have received a copy of the patient information sheet and consent form.

Study Participant's Signature
Date

Study Participant's Name
IC No:

Legally Authorized Representative's Signature (If applicable)
Date

Legally Authorized Representative's Name

IC No

CERTIFICATION BY IMPARTIAL WITNESS

Witness's Signature (If applicable)
Date

Witness's Name

IC No :

Case Report Singapore Med J 2010; 51(2) : e37

Brown fat uptake of ^{18}F-FDG on dual time point PET/CT imaging

Hairil Rashmizal A R, Noraini A R, Rossetti C, Abdul Jalil N

ABSTRACT

The aim of this report was to assess the changes in the ^{18}F-fluorodeoxyglucose (^{18}F-FDG) uptake of brown fats on integrated positron emission tomography/computed tomography (PET/CT) imaging. The patient presented with an enlargement of the neck lymph nodes, and was suspicious for tuberculous lymphadenitis. A whole body PET/CT imaging was performed, followed by a delayed imaging of the neck and thoracic regions. A visually increased ^{18}F-FDG uptake was taken as a positive finding. A semi-quantitative evaluation was performed using a maximum standardised uptake value (SUVmax) with a cut-off value above 2.5. There were a number of ^{18}F-FDG avid activity areas seen at the supraclavicular, mediastinal, paravertebral and perirenal regions. These are in keeping with the physiological ^{18}F-FDG uptake in brown fat. The differences in SUVmax between the two scans ranged from −20 percent to +20 percent. Based on our observation, dual time point imaging may not be a reliable method for assessing the ^{18}F-FDG uptake of brown fat.

Keywords: brown fat, dual time point imaging, ^{18}F-FDG, PET/CT

Singapore Med J 2010;51(2):e37-e39

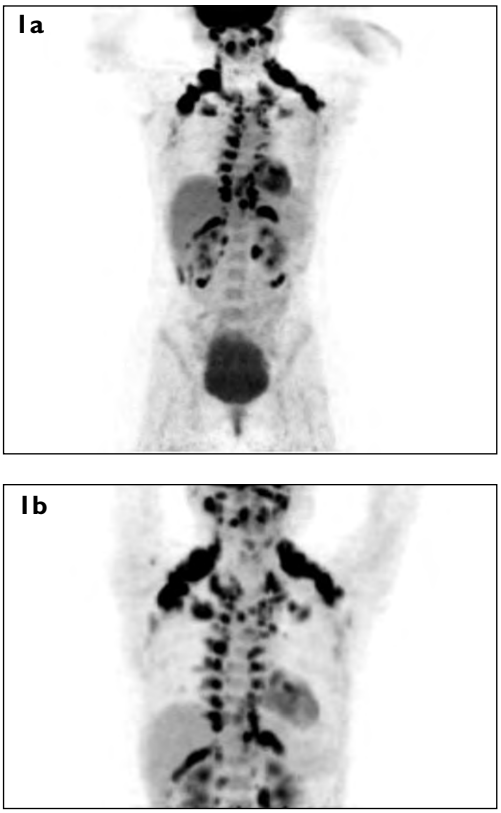

Fig. 1 (a) Multi-imaging planar (MIP) image shows the initial whole body PET/CT imaging. (b) MIP of the second PET/CT imaging (limited from the base of the skull to the upper abdominal region and covering the whole liver) shows the distribution of high 18F-FDG uptake of brown fats.

INTRODUCTION

In the last two decades, it was believed that the uptake of ^{18}F-fluorodeoxyglucose (^{18}F-FDG) in the neck and shoulder regions was caused by muscle uptake. However, this issue was resolved after the introduction of fusion physiological and morphological imaging modalities, namely positron emission tomography/computed tomography (PET/CT), which clearly showed that the uptake was of brown fat.[1-4]

Human adipose tissue can be divided into two types, white fat and brown fat. White fat mainly serves to protect the body parts, while the main function of brown fat is heat generation. Brown fat has a high density of mitochondria in the fat cells and is rich in vascularisation. These features are responsible for the brownish colour of brown fat. Brown fat can be named according to its location: supraclavicular, mediastinal, paravertebral and perirenal. Supraclavicular fat can extend from the neck inferiorly to the shoulders, and sometimes, to the axillae. Mediastinal fat exists in small pockets that are linked with all the structures of the mediastinum. Paravertebral brown fat runs parallel to the thoracic vertebrae on either side of the spinal column and extends into the intercostal spaces. Perirenal fat tends to be concentrated on the top of the kidneys at the location of the adrenal glands.

The biological mechanism for the accumulation of ^{18}F-FDG uptake in brown fat is well established.[1,5] Previous studies have mainly focused on supraclavicular brown fat,[1,2,6,7] whereas the other areas of brown fat have been under-reported. It is important for physicians to recognise these normal variants of ^{18}F-FDG uptake

Discipline of Medical Radiations, School of Medical Sciences, Bundoora West Campus, Royal Melbourne Institute of Technology University, Bundoora, Victoria 3083, Australia

Hairil Rashmizal AR, BSc
Postgraduate student

Diagnostic Imaging Department, Serdang Hospital, Kajang 43000, Malaysia

Noraini AR, MD
Radiologist

Nuclear Medicine and PET/CT Centre, Ospedale Niguarda Ca' Granda, Piazza Ospedale Maggiore 3, Milan 20126, Italy

Rossetti C, MD
Director and Associate Professor

Faculty of Medicine and Health Sciences, University Putra Malaysia, Serdang 43400, Malaysia

Abdul Jalil N, MD
Associate Professor and Head of Nuclear Imaging Unit

Correspondence to:
Dr Abdul Jalil Nordin
Tel: (60) 3 8947 2775
Fax: (60) 3 8947 2775
Email: drimaging@yahoo.com

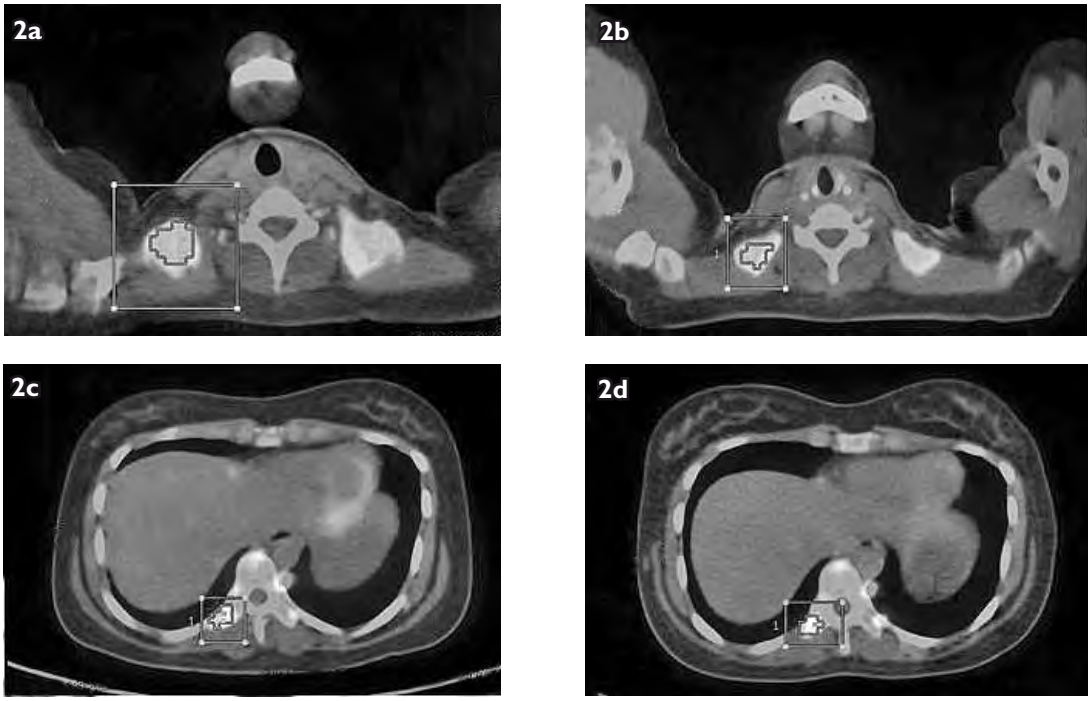

Fig. 2 Image acquisitions of ^{18}F-FDG PET/CT show (a & b) an increase in the SUVmax values of the right supraclavicular brown fat from 17.6 on the initial scan to 20.1 on the delayed scan and (c & d) a decrease in the SUVmax values of the right paravertebral brown fat from 13.9 to 11.7.

in brown fat, so that they are not misinterpreted as a significant pathologic state. To the authors' knowledge, dual time point imaging (DTPI) using ^{18}F-FDG PET/CT on brown fat, especially for the mediastinal and perirenal areas, has not been previously described.

CASE REPORT

A 25-year-old Malay woman presented with a history of left lateral neck swelling for several weeks. There were no general symptoms of tuberculosis (TB) infection such as cough, low grade fever, night sweat or loss of weight. The patient had a family history of TB infection, and her sister had been diagnosed with pulmonary tuberculosis (PTB) infection seven months ago. The patient was screened for TB infection through blood investigation, sputum test and acid fast bacilli, but the results were negative. The aspiration of the swollen neck lymph node suggested a reactive node. The patient underwent a whole body PET/CT examination to assess the extension of the lesion.

A DTPI approach was applied during the scanning session. All imaging studies were performed on a dual-modality PET/CT system (Biograph 6, Siemens Medical Solutions Inc, Hoffman Estates, IL, USA). PET/CT imaging was started 46 minutes after an intravenous injection of 368.3 MBq of ^{18}F-FDG. The total acquisition time for the initial whole body PET/CT was about 25 minutes. Using the same parameters, a delayed PET/CT imaging was obtained about 121 minutes after the ^{18}F-FDG injection (time interval between the first and second imaging was about 75 minutes), and it was limited to the neck, thorax and upper abdomen regions, covering the whole liver (Fig. 1).

In this case, a semi-quantitative evaluation method using the maximum standardised uptake value (SUVmax) was applied to evaluate the imaging findings. Inconsistencies in measurement were observed in the SUVmax values of the brown fat at different locations between the initial and delayed images. The initial SUVmax1 measured along the right and left supraclavicular, mediastinal, right and left paravertebral as well as the right and left perirenal were 17.6, 18.9, 7.0, 13.9, 7.4, 10.4 and 20.8, respectively. In the delayed imaging, the SUVmax2 of the mediastinal, right paravertebral and left perirenal declined to 5.6, 11.7 and 18.5, respectively, whereas the rest showed an increment (Fig. 2). The differences in SUVmax between the two readings, expressed as Δ%SUVmax, ranged from approximately –20% to +20% (Table I).

DISCUSSION

Brown fat can lead to false positive interpretations for PET imaging. The aim of this report is to demonstrate the imaging characteristics of brown fat on ^{18}F-FDG PET/CT, as described by several other studies.[1-4,6,8] It is well known that brown fat mainly functions in non-shivering

Table I. The SUVmax and Δ%SUVmax values of the different areas of brown fat.

Area of brown fat	SUVmax 1[a]	SUVmax 2[b]	Δ%SUVmax[c]
Right supraclavicular	17.60	20.10	14.20
Left supraclavicular	18.90	22.70	20.11
Mediastinal	7.00	5.60	−20.00
Right paravertebral	13.90	11.70	−15.83
Left paravertebral	7.40	7.80	5.41
Right perirenal	10.40	11.20	7.69
Left perirenal	20.80	18.50	−11.06

SUVmax: maximum standardised uptake value
[a] Maximum SUV derived from first PET/CT imaging acquisition.
[b] Maximum SUV derived from second PET/CT imaging acquisition.
[c] The percentage differences in maximum SUV.

thermogenesis by stimulating the sympathetic nerve system, which can cause a significant increase of glucose uptake in brown fat.[9] The amount of glucose uptake in brown fat has been shown to be closely correlated with gender,[9,10] age,[9] cold exposure[2] and medications.[10,11]

The ^{18}F-FDG SUVs in our patient were in the range of those reported by Yeung et al[3] and Hadi et al.[8] The four main areas of brown fat appearance on the ^{18}F-FDG PET/CT were highlighted and the SUVmax changes during DTPI protocol were observed. In our case, there were remarkable reductions in the SUVmax values between the two time points (Δ%SUVmax), which can be seen clearly in the brown fat located at the mediastinal, paravertebral and perirenal areas, while the rests of the values showed a 5%–20% increment. No specific pattern was observed in the changes from either side of the body.

The inconsistent uptake of ^{18}F-FDG on DTPI protocol in our patient is similar to that in previous reports,[7,12] except that in our patient, premedications, such as muscle relaxants, were not prescribed prior to the examination, unlike in the other studies.[7,10] The patient's comfort was ensured by providing a warm blanket and maintaining a pleasant room temperature. In view of the heavy patient workflow in the department, we selected a two-hour interval for our second time point of imaging, as recommended in previous studies.[13,14]

In conclusion, based on our limited observation and in view of the inconsistent SUV changes in brown fat glucose uptake with time, DTPI protocol may not be a useful method for improving the diagnostic value of ^{18}F-FDG PET/CT examination at this point. In order to have a constructive understanding of the ^{18}F-FDG uptake of brown fat in DTPI imaging, further investigations with a larger group of patients are warranted.

REFERENCES

1. Hany TF, Gharehpapagh E, Kamel EM, et al. Brown adipose tissue: a factor to consider in symmetrical tracer uptake in the neck and upper chest region. Eur J Nucl Med Mol Imaging 2002; 29:1393-8.
2. Cohade C, Mourtzikos KA, Wahl RL. "USA-Fat": prevalence is related to ambient outdoor temperature-evaluation with 18F-FDG PET/CT. J Nucl Med 2003; 44:1267-70.
3. Yeung HWD, Grewal RK, Gonen M, Schoder H, Larson SM. Patterns of 18F-FDG uptake in adipose tissue and muscle: a potential source of false-positives for PET. J Nucl Med 2003; 44:1789-96.
4. Truong MT, Erasmus JJ, Munden RF, et al. Focal FDG uptake in mediastinal brown fat mimicking malignancy: a potential pitfall resolved on PET/CT. AJR Am J Roentgenol 2004; 183:1127-32.
5. Weber WA. Brown adipose tissue and nuclear medicine imaging. J Nucl Med 2004; 45:1101-3.
6. Cohade C, Osman M, Pannu HK, Wahl RL. Uptake in supraclavicular area fat ("USA-Fat"): description on 18F-FDG PET/CT. J Nucl Med 2003; 44:170-6.
7. Döbert N, Menzel C, Hamscho N, et al. Atypical thoracic and supraclavicular FDG-uptake in patients with Hodgkin's and non-Hodgkin's lymphoma. Q J Nucl Med Mol Imaging 2004; 48:33-8.
8. Hadi M, Chen CC, Whatley M, Pacak K, Carrasquillo JA. Brown fat imaging with (18)F-6-fluorodopamine PET/CT, (18)F-FDG PET/CT, and (123)I-MIBG SPECT: a study of patients being evaluated for pheochromocytoma. J Nucl Med 2007; 48:1077-83.
9. Evans KD, Tulloss TA, Hall N. 18FDG uptake in brown fat: potential for false positives. Radiol Technol 2007; 78:361-6.
10. Tatsumi M, Engles JM, Ishimori T, et al. Intense (18)F-FDG uptake in brown fat can be reduced pharmacologically. J Nucl Med 2004; 45:1189-93.
11. Söderlund V, Larsson SA, Jacobsson H. Reduction of FDG uptake in brown adipose tissue in clinical patients by a single dose of propranolol. Eur J Nucl Med Mol Imaging 2007; 34:1018-22.
12. Alkhawaldeh K, Alavi A. Quantitative assessment of FDG uptake in brown fat using standardized uptake value and dual-time-point scanning. Clin Nucl Med 2008; 33:663-7.
13. Nakamoto Y, Higashi T, Sakahara H, et al. Delayed (18)F-fluoro-2-deoxy-D-glucose positron emission tomography scan for differentiation between malignant and benign lesions in the pancreas. Cancer 2000; 89:2547-54.
14. Kim IJ, Lee JS, Kim SJ, et al. Double-phase 18F-FDG PET–CT for determination of pulmonary tuberculoma activity. Eur J Nucl Med Mol Imaging 2008; 35:808-14.

APPENDIX 6

Estimating the PET effective dose of the seven Malaysian patients

This appendix describes the calculations that have been performed in order to figure out the whole body effective dose coefficient of FDG (Γ_E^{FDG}) for the PET component of PET/CT imaging. For this, some modifications on the data of the several studies [158, 169, 183] are carried out by utilising the tissue weighting factor (W_T) of the ICRP 60 [164] and 103 [165], and the organ absorbed dose coefficient of FDG (Γ_T^{FDG}) of the ICRP 80 [167] and 106 [168]. In total, there are four modifications, in which three are based on the data from Brix *et al.* [169] and one from the data of Huang *et al.* [158].

In the study conducted by Brix, G. and his co-workers, they calculated their whole body effective dose coefficient for FDG (Γ_E^{FDG}) from the data of the 13 organs or tissues [169]. The weighting factors for these organs were taken from the ICRP 60 [164], and these values were then multiplied by the organ absorbed dose coefficient for FDG of the ICRP 80 [167]. For modification 1, the tissue weighting factors remained the same as in Brix's study, but the organ absorbed dose coefficient of FDG (Γ_T^{FDG}) was taken from the ICRP 106 [168]. In modifications 2 and 3, the tissue weighting factors of the ICRP 103 [165] were used, however the organs absorbed dose coefficient (Γ_T^{FDG}) was based on the data of the ICRP 80 [167]; modification 2, and the ICRP 106 [168] for modification 3.

The whole body effective dose coefficient of FDG (Γ_E^{FDG}) in the Huang's study was developed based on the data of the 23 organs, with the utilisation of the tissue weighting factors (W_T) from the ICRP 103 [165] and the organs absorbed dose coefficient of FDG (Γ_T^{FDG}) values from the ICRP 80 [167]. However, in modification 4

of this study, the organ absorbed dose coefficient of FDG (Γ_T^{FDG}) have been changed with those from the ICRP 106 [168]. In addition, a recent study on Thai cancer patients has proposed the whole body effective dose coefficient for FDG (Γ_E^{FDG}) of about 14.08 μSv/MBq [183], which is the lowest in value as compared to others (please refer to Table A6.1). Therefore, in this research, by including the effective dose coefficient value for FDG (Γ_E^{FDG}) from the ICRP 106 [168], a total of 8 coefficient values have been generated. All these values are then multiplied with the injected amount of FDG radioactivity for the seven Malaysian patients. Based on these results, the mean effective dose of each patient is calculated, as listed in Table A6.2.

Table A6.1: The list of seven whole body effective dose coefficient values for FDG (Γ_E^{FDG}) that have been used in the calculations of this study.

Organ	Organ or tissue effective dose coefficient for FDG, $W_T \cdot \Gamma_T^{FDG}$ (μSv/MBq)						
	Brix *et al.* [169]	Modification 1	Modification 2	Modification 3	Huang *et al.* [158]	Modification 4	Khamwan *et al.* [183]
Gonads	2.70	2.50	1.08	1.00	1.08	1.00	0.92
Lungs	1.20	2.40	1.20	2.40	1.20	2.40	0.56
Stomach	1.32	1.32	1.32	1.32	1.32	1.32	1.39
Colon	1.56	1.56	1.56	1.56	1.56	1.56	1.26
Red bone marrow	1.32	1.32	1.32	1.32	1.32	1.32	2.17
Esophagus	0.55	0.60	0.44	0.48	0.44	0.48	–
Thyroid	0.50	0.50	0.40	0.40	0.40	0.40	0.42
Liver	0.55	1.05	0.44	0.84	0.44	0.84	1.19
Bladder	8.00	6.50	6.40	5.20	6.40	5.20	2.55
Breasts	0.34	0.44	1.03	1.06	1.03	1.06	0.88
Bone surfaces	0.11	0.11	0.11	0.11	0.11	0.11	0.21
Skin	0.08	0.08	0.08	0.08	0.08	0.08	0.01
Brain	–	–	–	–	0.28	0.38	–
Thymus	–	–	–	–	0.14	0.16	–
Spleen	–	–	–	–	0.14	0.14	0.89
Adrenal glands	–	–	–	–	0.16	0.16	–
Pancreas	–	–	–	–	0.16	0.17	–
Kidneys	–	–	–	–	0.27	0.22	1.64
Large intestine	–	–	–	–	0.18	0.17	–
Small intestine	–	–	–	–	0.17	0.16	–
Uterus	–	–	–	–	0.27	0.23	–
Muscles	–	–	–	–	0.14	0.13	–
Heart	–	–	–	–	0.81	0.87	–
Remaining organs	0.55	0.60	1.32	1.44	–	–	–
Whole body effective dose coefficient, Γ_E^{FDG} (μSv/MBq)	19.00	19.00	16.70	17.20	18.10	18.55	14.08

Table A6.2: The calculations for the mean value of the whole body PET effective dose of our patients.

		Effective dose coefficient for FDG, Γ_E^{FDG} (mSv/MBq)								
		Γ_E^1	Γ_E^2	Γ_E^3	Γ_E^4	Γ_E^5	Γ_E^6	Γ_E^7	Γ_E^8	
		0.01900	0.01900	0.01900	0.01670	0.01720	0.01810	0.01855	0.01408	
Patient no.	Injected radioactivity of FDG, A (MBq)	Effective dose (mSv)								Mean
		$A \cdot \Gamma_E^1$	$A \cdot \Gamma_E^2$	$A \cdot \Gamma_E^3$	$A \cdot \Gamma_E^4$	$A \cdot \Gamma_E^5$	$A \cdot \Gamma_E^6$	$A \cdot \Gamma_E^7$	$A \cdot \Gamma_E^8$	
1	592	11.25	11.25	11.25	9.89	10.18	10.72	10.98	8.34	10.48
3	277	5.26	5.26	5.26	4.63	4.76	5.01	5.14	3.90	4.90
4	322	6.12	6.12	6.12	5.38	5.54	5.83	5.97	4.53	5.70
8	361	6.86	6.86	6.86	6.03	6.21	6.53	6.70	5.08	6.39
10	500	9.50	9.50	9.50	8.35	8.60	9.05	9.28	7.04	8.85
11	368	6.99	6.99	6.99	6.15	6.33	6.66	6.83	5.18	6.51
12	375	7.13	7.13	7.13	6.26	6.45	6.79	6.96	5.28	6.64

Γ_E^1, effective dose coefficient from ICRP 106 [168]; [168]; Γ_E^2, effective dose coefficient from Brix *et al.* [169]; Γ_E^3, effective dose coefficient from our modification 1; Γ_E^4, effective dose coefficient from our modification 2; Γ_E^5, effective dose coefficient from our modification 3; Γ_E^6, effective dose coefficient from Huang *et al.* [158]; Γ_E^7, effective dose coefficient from our modification 4; Γ_E^8, effective dose coefficient from Khamwan *et al.* [183].

APPENDIX 7

Estimating the CT effective dose of the seven Malaysian patients

This appendix describes the calculations for the organ or tissue effective dose coefficient of the whole body CT scan (Γ_E^{CT}). For this research, the data are adapted from the previous study by Brix, *et al.* [169], with a slight modification of using the most recent tissue weighting factor (W_T) from the ICRP 103 [165].

In Brix's study, the whole body CT effective dose coefficient that related with $CTDI_{vol}$ (Γ_E^{CT}) was derived by multiplying the measured absorbed dose from the 13 organs with their weighting factors (W_T) of the ICRP 60 [164]. However, for the modification of this study, the tissue weighting factors (W_T) from the ICRP 103 [165] were utilised. Therefore, a total of two different whole body CT effective dose coefficient values (Γ_E^{CT}) (refer to Table A7.1) have been generated for this research. To estimate the whole body CT effective dose of the seven Malaysian patients, these two coefficient values are multiplied with the $CTDI_{vol}$ of each scanning protocols. Based on this, the mean CT effective dose of each patient is calculated, as listed in Table A7.2.

Table A7.1: The two whole body CT effective dose coefficient values (Γ_E) that have been used in the calculations of this study.

Organ	Organ or tissue CT effective dose coefficient, $W_T \cdot \Gamma_T^{CT}$ (mSv/mGy)	
	Brix, et al [169]	Modification 1
Gonads	0.28	0.113
Lungs	0.174	0.174
Stomach	0.174	0.174
Colon	0.184	0.184
Red bone marrow	0.153	0.154
Esophagus	0.072	0.057
Thyroid	0.123	0.096
Liver	0.079	0.063
Bladder	0.069	0.055
Breasts	0.072	0.173
Bone surfaces	0.009	0.009
Skin	0.007	0.007
Remaining organs	0.069	0.164
Whole body CT effective dose coefficient, Γ_E^{CT} (mSv/mGy)	1.47	1.42

Table A7.2: The calculations for the mean value of the CT effective dose of all the scanning protocols in our patients.

			Effective dose coefficient for whole body CT, Γ_E^{CT} (mSv/mGy)		
			Γ_E^1	Γ_E^2	
			1.47	1.42	
Patient no.	Scan	$CTDI_{vol}$ (mGy)	Effective dose (mSv)		Mean
			$CTDI_{vol} \cdot \Gamma_E^1$	$CTDI_{vol} \cdot \Gamma_E^2$	
1	Unenhanced CT	3.05	4.48	4.33	4.41
	CECT	10.18	14.96	14.46	14.71
	Delayed CT	3.14	4.62	4.46	4.54
3	Unenhanced CT	2.08	3.06	2.95	3.01
	CECT	6.40	9.41	9.09	9.25
	Delayed CT	2.20	3.23	3.12	3.18
4	Unenhanced CT	1.61	2.37	2.29	2.33
	CECT	5.26	7.73	7.47	7.60
	Delayed CT	1.23	1.81	1.75	1.78
8	Unenhanced CT	1.91	2.81	2.71	2.76
	CECT	6.70	9.85	9.51	9.68
	Delayed CT	2.29	3.37	3.25	3.31
10	Unenhanced CT	2.42	3.56	3.44	3.50
	CECT	8.61	12.66	12.23	12.44
	Delayed CT	2.63	3.87	3.73	3.80
11	Unenhanced CT	1.99	2.93	2.83	2.88
	CECT	6.70	9.85	9.51	9.68
	Delayed CT	1.65	2.43	2.34	2.38
12	Unenhanced CT	1.74	2.56	2.47	2.51
	CECT	5.68	8.35	8.07	8.21
	Delayed CT	0.98	1.44	1.39	1.42

Γ_E^1, CT effective coefficient from Brix *et al.* [169]; Γ_E^2, CT effective dose coefficient from our modification 1.

Appendix 8

Journal articles

1. Abdul Razak HR, Nordin AJ, Ackerly T, Van Every B, Martin R and Geso M. Quantifying the effects of iodine contrast media on standardised uptake values of FDG PET/CT images: an anthropomorphic phantom study. Accepted for publication in Australasian Physical & Engineering Sciences in Medicine (APESM) journal on 6th of July, 2011.
2. Hairil Rashmizal AR, Geso M, Noraini AR and Abdul Jalil N. The imaging characteristics of extrapulmonary tuberculous lesions on dual time point imaging (DTPI) of FDG PET/CT. Accepted for publication in Journal of Medical Imaging and Radiation Oncology (JMIRO) on 10th of March, 2011.
3. Hairil Rashmizal AR, Geso M, Noraini AR and Abdul Jalil N. The effect of integrating contrast enhanced CT in FDG PET/CT imaging of Extrapulmonary Tuberculosis patients: preliminary data. ANZ Nuclear Medicine. 2010;41(4):19-23.
4. HR Abdul Razak, N Abdul Rahim and AJ Nordin. Dual time point imaging of FDG PET/CT in a tuberculous spondylodiscitis. Biomed Imaging Interv J. 2010;6(2):e18.
5. Hairil Rashmizal AR, Noraini AR, C Rossetti and Abdul Jalil N. Case report: Brown fat uptake of ^{18}F-FDG on dual time point PET/CT imaging. Singapore Med J. 2010;51(2):e37-e39.

Oral presentations

1. Hairil Rashmizal AR, Abdul Jalil N, Deb P and Geso M. The utilisation of PET/CT modality in detecting the extrapulmonary tuberculosis (EPTB) lesions and the effects of iodine contrast media during the image acquisitions, at Engineering and

Physical Sciences in Medicine & the Australian Biomedical Engineering Conference 2010 (EPSM-ABEC 2010), from 5-9th of December 2010, in Melbourne, Australia.

2. N Abdul Jalil, AR Hairil Rashmizal, AR Noraini and C Rossetti. Iodinated contrast media does not cause an overestimation of maximum standardised uptake values (SUVmax) in extrapulmonary tuberculosis patients, at 29th International Symposium on Radioactive Isotopes in Clinical Medicine and Research, from 16-19th of January 2010, in Bad Hofgastein, Austria.

Poster presentations

1. Hairil Rashmizal AR, Geso M, Noraini AR and Abdul Jalil N. FDG PET/CT for detecting and monitoring treatment response of Extrapulmonary Tuberculosis patients: a preliminary Malaysian data, at 3rd Asia Pacific Region Conference of the International Union Against Tuberculosis and Lung Disease (IUATLD), from 8-11th July 2011, in Hong Kong, PR China.
2. Hairil Rashmizal AR, Geso M, Noraini AR and Abdul Jalil N. Diagnostic value of dual time point imaging of ^{18}FDG PET/CT for the detection of extrapulmonary tuberculous lesions, at 2010 World Molecular Imaging Congress (WMIC), from 8-11th September 2010, in Kyoto, Japan.
3. Hairil Rashmizal AR, Noraini AR, Suriani MS, C Rossetti and Abdul Jalil N. Brown Fat Uptake of ^{18}F-FDG on Dual Time Point Imaging PET/CT: a Case Report, at 18th Annual Scientific Meeting of the Singapore Radiological Society, from 26-29th March 2009, in Singapore.

REFERENCES

1. Ben-Haim, S., Ell, P., *^{18}F-FDG PET and PET/CT in the Evaluation of Cancer Treatment Response.* J Nucl Med, 2009. 50(1): p. 88-99.
2. Townsend, D.W., *Positron Emission Tomography/Computed Tomography.* Semin Nucl Med, 2008. 38(3): p. 152-166.
3. Townsend, D.W., *Basic Science of PET and PET/CT*, in *Positron Emission Tomography: Clinical Practice*, P.E. Valk, et al., Editors. 2006, Springer: London. p. 1-16.
4. Glaudemans, A., Signore, A., *FDG-PET/CT in infections: the imaging method of choice?* Eur J Nucl Med Mol Imaging, 2010. 37(10): p. 1986-1991.
5. Zhuang, H., Alavi, A., *Evolving Role of FDG-PET Imaging in the Management of Patients with Suspected Infection and Inflammatory Disorders*, in *Positron Emission Tomography: Clinical Practice*, P.E. Valk, et al., Editors. 2006, Springer: London. p. 303-316.
6. Yamada, S., Kubota, K., Kubota, R., Ido, T., Tamahashi, N., *High Accumulation of Fluorine-18-Fluorodeoxyglucose in Turpentine-Induced Inflammatory Tissue.* J Nucl Med, 1995. 36(7): p. 1301-1306.
7. Sathekge, M., Maes, A., Kgomo, M., Stoltz, A., Pottel, H., Van de Wiele, C., *Impact of FDG PET on the management of TBC treatment: a pilot study.* Nuklearmedizin, 2010. 49(1): p. 35-40.
8. Nordin, A.J., Rashmizal, H., Abdul Rahim, N., Rossetti, C., *Potential false positive active extra pulmonary tuberculosis lesions on FDG PET/CT imaging in malignancy.* Dicle Med J, 2010. 37(1): p. 42-47.
9. Rosenbaum, S., Lind, T., Antoch, G., Bockisch, A., *False-Positive FDG PET Uptake−the Role of PET/CT.* Eur Radiol, 2006. 16(5): p. 1054-1065.
10. Raja, A., *Immunology of tuberculosis.* Indian J Med Res, 2004. 120(4): p. 213-232.
11. Kubota, R., Yamada, S., Kubota, K., Ishiwata, K., Tamahashi, N., Ido, T., *Intratumoral Distribution of Fluorine-18-Fluorodeoxyglucose In Vivo: High Accumulation in Macrophages and Granulation Tissues Studied by Microautoradiography.* J Nucl Med, 1992. 33(11): p. 1972-1980.

12. Sharma, S.K., Mohan, A., *Extrapulmonary tuberculosis.* Indian J Med Res, 2004. 120: p. 316-353.
13. Fanning, A., *Tuberculosis: 6. Extrapulmonary disease.* CMAJ, 1999. 160(11): p. 1597-1603.
14. Kamal, M.S.M., Ahasan, H.N., Ahmed, S., Ayaz, K., Mahbub, M.S., Khan, M.A.I., Gupta, R.D., Alam, M.B., Miah, M.T., *Isolation and Identification of Mycobacterium from Extrapulmonary Specimen at NTRL, NIDCH.* J Medicine, 2010. 11: p. 128-130.
15. Malaysian Thoracic Society, *Guidelines on Management of Tuberculosis.* 1996 [cited on 9th January 2008];
Available from: http://www.mts.org.my/resources/Guidelines_TB.html#top.
16. Rockwood, R.R., *Extrapulmonary TB: What You Need to Know.* Nurse Practitioner, 2007. 32(8): p. 44-49.
17. Arora, V.K., Gupta, R., *Trends of extra-pulmonary tuberculosis under revised national tuberculosis control programme: a study from South Delhi.* Indian J Tuberc, 2006. 53: p. 77- 83.
18. Jeong, Y.J., Lee, K.S., *Pulmonary Tuberculosis: Up-to-Date Imaging and Management.* Am J Roentgenol, 2008. 191(3): p. 834-844.
19. Hofmeyr, A., Eddie Lau, W.F., Slavin, M.A., *Mycobacterium tuberculosis infection in patients with cancer, the role of 18-fluorodeoxyglucose positron emission tomography for diagnosis and monitoring treatment response.* Tuberculosis, 2007. 87(5): p. 459-463.
20. Sathekge, M., Maes, A., Kgomo, M., Pottel, H., Stolz, A., Van De Wiele, C., *FDG uptake in lymph-nodes of HIV+ and tuberculosis patients: implications for cancer staging.* Q J Nucl Med Mol Imaging, 2010. 54(8): p. 698-703.
21. Suga, K., Kawakami, Y., Hiyama, A., Sugi, K., Okabe, K., Matsumoto, T., Ueda, K., Tanaka, N., Matsunaga, N., *Dual-time point 18F-FDG PET/CT scan for differentiation between 18F-FDG-avid non-small cell lung cancer and benign lesions.* Ann Nucl Med, 2009. 23(5): p. 427-435.

22. Suga, K., Kawakami, Y., Hiyama, A., Sugi, K., Okabe, K., Matsumoto, T., Ueda, K., Tanaka, N., Matsunaga, N., *Differential diagnosis between 18F-FDG-avid metastatic lymph nodes in non-small cell lung cancer and benign nodes on dual-time point PET/CT scan.* Ann Nucl Med, 2009. 23(6): p. 523-531.
23. Lan, X.L., Zhang, Y.X., Wu, Z.J., Jia, Q., Wei, H., Gao, Z.R., *The value of dual time point 18F-FDG PET imaging for the differentiation between malignant and benign lesions.* Clin Radiol, 2008. 63(7): p. 756-764.
24. Kitajima, K., Murakami, K., Yamasaki, E., Domeki, Y., Kaji, Y., Morita, S., Suganuma, N., Sugimura, K., *Performance of integrated FDG-PET/contrast-enhanced CT in the diagnosis of recurrent uterine cancer: comparison with PET and enhanced CT.* Eur J Nucl Med Mol Imaging, 2009. 36(3): p. 362-372.
25. Kitajima, K., Murakami, K., Yamasaki, E., Domeki, Y., Tsubaki, M., Sunagawa, M., Kaji, Y., Suganuma, N., Sugimura, K., *Performance of integrated FDG PET/contrast-enhanced CT in the diagnosis of recurrent colorectal cancer: Comparison with integrated FDG PET/non-contrast-enhanced CT and enhanced CT.* Eur J Nucl Med Mol Imaging, 2009. 36(9): p. 1388-1396.
26. Kitajima, K., Murakami, K., Yamasaki, E., Kaji, Y., Fukasawa, I., Inaba, N., Sugimura, K., *Diagnostic accuracy of integrated FDG-PET/contrast-enhanced CT in staging ovarian cancer: comparison with enhanced CT.* Eur J Nucl Med Mol Imaging, 2008. 35(10): p. 1912-1920.
27. Antoch, G., Freudenberg, L.S., Stattaus, J., Jentzen, W., Mueller, S.P., Debatin, J.F., Bockisch, A., *Whole-Body Positron Emission Tomography-CT: Optimized CT Using Oral and IV Contrast Materials.* Am J Roentgenol, 2002. 179(6): p. 1555-1560.
28. Cherry, S.R., Phelps, M.E., *Positron Emission Tomography: Methods and Instrumentation*, in *Diagnostic Nuclear Medicine*, M.P. Sandler, et al., Editors. 2003, Lippincott Williams & Wilkins Philadelphia. p. 61-84.
29. Lonsdale, M.N., Beyer, T., *Dual-modality PET/CT instrumentation--Today and tomorrow.* Eur J Radiol, 2010. 73(3): p. 452-460.
30. Bailey, D.L., Karp, J.S., Surti, S., *Physics and Instrumentation in PET*, in *Positron Emission Tomography: Basic Sciences*, Bailey, D.L., Townsend, D. W., Valk, P. E., Maisey, M. N., Editors. 2005, Springer: London. p. 13-39.

31. Sharp, P.F., Welch, A., *Positron Emission Tomography*, in *Practical Nuclear Medicine*, Sharp, P.F., Gemmell, H.G., Murray, A.D., Editors. 2005, Springer: London. p. 35-48.
32. Workman, R.B.J., Coleman, R.E., *Fundamentals of PET and PET/CT Imaging*, in *PET/CT: Essentials for Clinical Practice*, Workman, R.B.J., Coleman, R.E., Editors. 2006, Springer: New York. p. 1-22.
33. Kinahan, P.E., Hasegawa, B.H., Beyer, T., *X-ray-based attenuation correction for positron emission tomography/computed tomography scanners.* Semin Nucl Med, 2003. 33(3): p. 166-179.
34. Halpern, B.S., Dahlbom, M., Quon, A., Schiepers, C., Waldherr, C., Silverman, D.H., Ratib, O., Czernin, J., *Impact of Patient Weight and Emission Scan Duration on PET/CT Image Quality and Lesion Detectability.* J Nucl Med, 2004. 45(5): p. 797-801.
35. International Atomic Energy Agency, IAEA, *A Guide to Clinical PET in oncology: Improving Clinical Management of Cancer Patients*. 2008, IAEA: Vienna.
36. Gelfand, M.J., *Dosimetry of FDG PET/CT and other molecular imaging applications in pediatric patients.* Pediatr Radiol, 2009. 39(Suppl 1): p. S46-S56.
37. Ulzheimer, S., Flohr, T., *Multislice CT: Current Technology and Future Developments*, in *Multislice CT*, Baert, A.L., Knauth, M., Sartor, K., Editors. 2009, Springer: Berlin. p. 3-23.
38. Hsieh, J., *Helical or Spiral CT*, in *Computed tomography: principles, design, artifacts and recent advances*. 2009, SPIE and John Wiley & Sons: Washington. p. 327-373.
39. Townsend, D., Beyer, T., *Anato-Molecular Imaging: Combining Structure and Function*, in *Positron Emission Tomography*. 2005. p. 179-202.
40. Pelizzari, C.A., Chen, G.T.Y., Spelbring, D.R., Weichselbaum, R.R., Chen, C. T., *Accurate Three-Dimensional Registration of CT, PET, and/or MR Images of the Brain.* J Comput Assist Tomogr, 1989. 13(1): p. 20-26.

41. Wahl, R.L., Quint, L.E., Cieslak, R.D., Aisen, A.M., Koeppe, R.A., Meyer, C.R., *"Anatometabolic" Tumor Imaging: Fusion of FDG PET with CT or MRI to Localize Foci of Increased Activity.* J Nucl Med, 1993. 34(7): p. 1190-1197.
42. Sureshbabu, W., Mawlawi, O., *PET/CT Imaging Artifacts.* J Nucl Med Technol, 2005. 33(3): p. 156-61.
43. Burger, C., Goerres, G., Schoenes, S., Buck, A., Lonn, A., Schulthess, G.V., *PET attenuation coefficients from CT images: experimental evaluation of the transformation of CT into PET 511-keV attenuation coefficients.* Eur J Nucl Med Mol Imaging, 2002. 29(7): p. 922-927.
44. Khurshid, K., McGough, R.J., Berger, K., *Automated cardiac motion compensation in PET/CT for accurate reconstruction of PET myocardial perfusion images.* Phys Med Biol, 2008. 53: p. 5705-5718.
45. Beyer, T., Townsend, D.W., Brun, T., Kinahan, P.E., Charron, M., Roddy, R., Jerin, J., Young, J., Byars, L., Nutt, R., *A Combined PET/CT Scanner for Clinical Oncology.* J Nucl Med, 2000. 41(8): p. 1369-1379.
46. Poeppel, T.D., Krause, B.J., Heusner, T.A., Boy, C., Bockisch, A., Antoch, G., *PET/CT for the staging and follow-up of patients with malignancies.* Eur J Radiol, 2009. 70(3): p. 382-392.
47. Groves, A., Speechly-Dick, M.-E., Dickson, J., Kayani, I., Endozo, R., Blanchard, P., Shastry, M., Prvulovich, E., Waddington, W., Ben-Haim, S., Bomanji, J., McEwan, J., Ell, P., *Cardiac ^{82}rubidium PET/CT: initial European experience.* Eur J Nucl Med Mol Imaging, 2007. 34(12): p. 1965-1972.
48. Humm, J., Rosenfeld, A., Guerra, A., *From PET detectors to PET scanners.* Eur J Nucl Med Mol Imaging, 2003. 30(11): p. 1574-1597.
49. Kinahan, P.E., Townsend, D.W., Beyer, T., Sashin, D, *Attenuation correction for a combined 3D PET/CT scanner*. Med Phys, 1998. 25(10): p. 2046-2053.
50. Mustafa, S., Alavi, A., Elgazzar, A.H., *Basis of 18F-FDG Positron Emission Tomography Imaging,* in *The Pathophysiologic Basis of Nuclear Medicine*. 2006. p. 50-66.
51. Hamacher, K., Coenen, H.H., Stocklin, G., *Efficient Stereospecific Synthesis of No-Carrier-Added 2-[18F]-Fluoro-2-Deoxy-D-Glucose Using Aminopolyether Supported Nucleophilic Substitution.* J Nucl Med, 1986. 27(2): p. 235-238.

52. Rioja, J., Rodríguez-Fraile, M., Lima-Favaretto, R., Rincón-Mayans, A., Peñuelas-Sánchez, I., Zudaire-Bergera, J.J., Parra, R.O., *Role of positron emission tomography in urological oncology.* BJU International, 2010. 106(11): p. 1578-1593.

53. Keyes, J.W., Jr., *SUV: Standard Uptake or Silly Useless Value?* J Nucl Med, 1995. 36(10): p. 1836-1839.

54. Schiepers, C., Hoh, C., *FDG-PET Imaging in Oncology*, in *Diagnostic Nuclear Medicine*, Schiepers C., Baert, A.L., Sartor, K., Editors. 2006, Springer: Berlin. p. 185-204.

55. Hickeson, M., Yun, M., Matthies, A., Zhuang, H., Adam, L.-E., Lacorte, L., Abass, A., *Use of a corrected standardized uptake value based on the lesion size on CT permits accurate characterization of lung nodules on FDG-PET.* Eur J Nucl Med Mol Imaging, 2002. 29(12): p. 1639-1647.

56. An, Y.-S., Sun, J., Park, K., Hwang, S., Park, K., Sheen, S., Lee, S., Lee, K., Yoon, J.-K., *Diagnostic Performance of 18F-FDG PET/CT for Lymph Node Staging in Patients with Operable Non-small-cell Lung Cancer and Inflammatory Lung Disease.* Lung, 2008. 186(5): p. 327-336.

57. Hashimoto, Y., Tsujikawa, T., Kondo, C., Maki, M., Momose, M., Nagai, A., Ohnuki, T., Nishikawa, T., Kusakabe, K., *Accuracy of PET for Diagnosis of Solid Pulmonary Lesions with 18F-FDG Uptake Below the Standardized Uptake Value of 2.5.* J Nucl Med, 2006. 47(3): p. 426-431.

58. Langen, K.J., Braun, U., Kops, E. R., Herzog, H., Kuwert, T., Nebeling, B., Feinendegen, L.E., *The Influence of Plasma Glucose Levels on Fluorine-18-Fluorodeoxyglucose Uptake in Bronchial Carcinomas.* J Nucl Med, 1993. 34(3): p. 355-359.

59. Lindholm, P., Minn, H., Leskinen-Kallio, S., Bergman, J., Ruotsalainen, U., Joensuu, H., *Influence of the Blood Glucose Concentration on FDG Uptake in Cancer-A PET Study.* J Nucl Med, 1993. 34(1): p. 1-6.

60. Boerner, A.R., Weckesser, M., Herzog, H., Schmitz, T., Audretsch, W., Nitz, U., Bender, H.G., Mueller-Gaertner, H.W., *Optimal scan time for fluorine-18 fluorodeoxyglucose positron emission tomography in breast cancer.* Eur J Nucl Med, 1999. 26(3): p. 226-230.

61. Hamberg, L.M., Hunter, G.J., Alpert, N.M., Choi, N.C., Babich, J.W., Fischman, A.J., *The Dose Uptake Ratio as an Index of Glucose Metabolism: Useful Parameter or Oversimplification?* J Nucl Med, 1994. 35(8): p. 1308-1312.

62. Lee, I.S., Lee, J.S., Kim, S.-J., Jun, S., Suh, K.T., *Flourine-18-Flourodeoxyglucose Positron Emission Tomography/Computed Tomography Imaging in Pyogenic and Tuberculosis Spondylitis: Preliminary Study.* J Comput Assist Tomogr, 2009. 33(4): p. 587-592.

63. Kamel, E.M., Burger, C., Buck, A., von Schulthess, G.K., Goerres, G, *Impact of metallic dental implants on CT-based attenuation correction in a combined PET/CT scanner.* Eur Radiol, 2003. 13(4): p. 724-728.

64. Goerres, G.W., Hany, T.F., Kamel, E.M., von Schulthess, G.K., Buck, A., *Head and neck imaging with PET and PET/CT: artefacts from dental metallic implants.* Eur J Nucl Med Mol Imaging, 2002. 29(3): p. 367-370.

65. Osman, M.M., Cohade, C., Nakamoto, Y., Wahl, R.L., *Respiratory motion artifacts on PET emission images obtained using CT attenuation correction on PET-CT.* Eur J Nucl Med Mol Imaging, 2003. 30(4): p. 603-606.

66. Cohade, C., Osman, M., Nakamoto, Y., Marshall, L.T., Links, J.M., Fishman, E.K., Wahl, R.L., *Initial Experience with Oral Contrast in PET/CT: Phantom and Clinical Studies.* J Nucl Med, 2003. 44(3): p. 412-416.

67. Antoch, G., Freudenberg, L.S., Egelhof, T., Stattaus, J., Jentzen, W., Debatin, J.F., Bockisch, A., *Focal Tracer Uptake: A Potential Artifact in Contrast-Enhanced Dual-Modality PET/CT Scans.* J Nucl Med, 2002. 43(10): p. 1339-1342.

68. Mawlawi, O., Erasmus, J.J., Pan, T., Cody, D.D., Campbell, R., Lonn, A.H., Kohlmyer, S., Macapinlac, H.A., Podoloff, D.A., *Truncation Artifact on PET/CT: Impact on Measurements of Activity Concentration and Assessment of a Correction Algorithm.* Am J Roentgenol, 2006. 186(5): p. 1458-1467.

69. Dunlap, N.E., Bass, J., Fujiwara, P., Hopewell, P., Horsburgh, C.R., Salfinger, M., Simone, P.M., *Diagnostic Standards and Classification of Tuberculosis in Adults and Children* . Am J Respir Crit Care Med, 2000. 161(4): p. 1376-1395.

70. Tufariello, J.M., Chan, J., Flynn, J.L., *Latent tuberculosis: mechanisms of host and bacillus that contribute to persistent infection.* Lancet Infect Dis, 2003. 3(9): p. 578-590.
71. World Health Organisation, WHO, *Tuberculosis Control in the Western Pacific Region,* in *2009 Report*. 2009.
72. Rasit, A.H., Ibrahim, S.F., Wong, C.C., *The Role of Polymerase Chain Reaction (PCR) in Diagnosis of Spine Tuberculosis after Pre-operative Anti-tuberculosis Treatment.* Malaysian Orthopaedic Journal, 2011. 5(1): p. 8-12.
73. Malaysian Association for the Prevention of Tuberculosis, MAPTB, *Still Fighting the TB Scourge*, Venugopalan, B., Editor. 2009, Ministry of Health Malaysia: Kuala Lumpur.
74. Iyawoo, K., *Tuberculosis in Malaysia: problems and prospect of treatment and control.* Tuberculosis, 2004. 84(1-2): p. 4-7.
75. World Health Organisation, WHO, *Regional Strategic Plan to Stop TB in the Western Pacific*, Western Pacific Region Office, Editor. 2000: Manila.
76. Smith, I., *Mycobacterium tuberculosis Pathogenesis and Molecular Determinants of Virulence.* Clin Microbiol Rev, 2003. 16(3): p. 463-496.
77. World Health Organisation, WHO, *Malaysia Tuberculosis Profile*. 2011 [cited on 5th January 2011]; Available from: www.who.int/tb/data.
78. World Health Organisation, WHO, *Malaysia Tuberculosis Profile: Surveillance and Epidemiology*. 2010 [cited on 28th May 2010]; Available from: www.who.int/tb/data.
79. Dannenberg, A.M., *Stages in the Pathogenesis of Human and Rabbit Tuberculosis,* in *Pathogenesis of Human Pulmonary Tuberculosis: Insights from the Rabbit Model*. 2006, American Society for Microbiolgy Press: Washington. p. 22-33.
80. Balasubramanian, V., Wiegeshaus, E.H., Taylor, B.T., Smith, D.W.., *Pathogenesis of tuberculosis: pathway to apical localization.* Tuberc Lung Dis, 1994. 75(3): p. 168-178.
81. Kong, Y., Subbian, S., Cirillo, S.L.G., Cirillo, J.D., *Application of optical imaging to study of extrapulmonary spread by tuberculosis.* Tuberculosis, 2009. 89(Supplement 1): p. S15-S17.

82. Malaysia Ministry of Health and Academy of Medicine of Malaysia, *Practice Guidelines for the Control and Management of Tuberculosis*. 2002: Kuala Lumpur.
83. World Health Organisation, WHO, *Treatment of Tuberculosis: Guidelines for National Programmes*. 2003: Geneva.
84. Tiwari, V., Jain, A., Verma, R.K., *Application of enzyme amplified mycobacterial DNA detection in the diagnosis of pulmonary & extra-pulmonary tuberculosis.* Indian J Med Res, 2003. 118(12): p. 224-228.
85. Negi, S.S., Anand, R., Basir, S.F., Pasha, S.T., Gupta, S., Khare, S., Lal, S., *Protein antigen b (Pab) based PCR test in diagnosis of pulmonary & extra-pulmonary tuberculosis.* Indian J Med Res, 2006. 124: p. 81.
86. Leung, A.N., *Pulmonary Tuberculosis: The Essentials.* Radiology, 1999. 210(2): p. 307-322.
87. Golden, M.P., Vikram, H.R., *Extrapulmonary Tuberculosis: An Overview*. Am Fam Phys, 2005. 72(9): p. 1761-1768.
88. Clarridge, J.E., Shawar, R.M., Shinnick, T.M., Plikaytis, B.B., *Large-scale use of polymerase chain reaction for detection of Mycobacterium tuberculosis in a routine mycobacteriology laboratory.* J Clin Microbiol, 1993. 31(8): p. 2049-2056.
89. Kolk, A.H.J., Schuitema, A.R.J., Kuijper, S., van Leeuwen, J., Hermans, P.W.M., van Embden, J.D.A., Hartskeerl, R.A., *Detection of Mycobacterium tuberculosis in clinical samples by using polymerase chain reaction and a nonradioactive detection system.* J Clin Microbiol, 1992. 30(10): p. 2567-2575.
90. Koh, D.M., Bell, J.R.G., Burkill, G.J.C., Padley, S.P.G., Healy, J.C., *Mycobacterial Infections: Still a Millennium Bug - the Imaging Features of Mycobacterial Infections.* Clin Radiol, 2001. 56(7): p. 535-544.
91. Pombo, F., Rodriguez, E., Mato, J., Perez-Fontán, J., Rivera, E., Valvuena, L., *Patterns of contrast enhancement of tuberculous lymph nodes demonstrated by computed tomography.* Clin Radiol, 1992. 46(1): p. 13-17.
92. Im, J.G., Itoh, H., Shim, Y.S., Lee, J.H., Ahn, J., Han, M.C., Noma, S., *Pulmonary tuberculosis: CT findings--early active disease and sequential change with antituberculous therapy.* Radiology, 1993. 186(3): p. 653-660.

93. Hatipoglu, O.N., Osma, E., Manisali, M., Ucan, E.S., Balci, P., Akkoclu, A., Akpinar, O., Karlikaya, C., Yuksel, C., *High resolution computed tomographic findings in pulmonary tuberculosis.* Thorax, 1996. 51(4): p. 397-402.

94. Hara, T., Kosaka, N., Suzuki, T., Kudo, K., Niino, H., *Uptake rates of ^{18}F-fluorodeoxyglucose and ^{11}C-choline in lung cancer and pulmonary tuberculosis: A positron emission tomography study.* Chest, 2003. 124(3): p. 893-901.

95. Goo, J.M., Im, J.-G., Do, K.-H., Yeo, J.S., Seo, J.B., Kim, H.Y., Chung, J.-K., *Pulmonary Tuberculoma Evaluated by Means of FDG PET: Findings in 10 Cases.* Radiology, 2000. 216(1): p. 117-121.

96. Sharma, M.P., Bhatia, V., *Abdominal tuberculosis.* Indian J Med Res, 2004. 120: p. 305-315.

97. Hustinx, R., Smith, R.J., Benard, F., Rosenthal, D.I., Machtay, M., Farber, L.A., Abass, A., *Dual time point fluorine-18 fluorodeoxyglucose positron emission tomography: a potential method to differentiate malignancy from inflammation and normal tissue in the head and neck.* Eur J Nucl Med Mol Imaging, 1999. 26(10): p. 1345-1348.

98. Nakamoto, Y., Higashi, T., Sakahara, H., Tamaki, N., Kogire, M., Doi, R., Hosotani, R., Imamura, M., Konishi, J., *Delayed 18F-fluoro-2-deoxy-D-glucose positron emission tomography scan for differentiation between malignant and benign lesions in the pancreas.* Cancer, 2000. 89(12): p. 2547-2554.

99. Kubota, K., Itoh, M., Ozaki, K., Ono, S., Tashiro, M., Yamaguchi, K., Akaizawa, T., Yamada, K., Fukuda, H., *Advantage of delayed whole-body FDG-PET imaging for tumour detection.* Eur J Nucl Med, 2001. 28(6): p. 696-703.

100. Zhuang, H., Pourdehnad, M., Lambright, E.S., Yamamoto, A.J., Lanuti, M., Li, P., Mozley, P.M., Rossman, M.D., Albelda, S.M., Abass, A., *Dual Time Point 18F-FDG PET Imaging for Differentiating Malignant from Inflammatory Processes.* J Nucl Med, 2001. 42(9): p. 1412-1417.

101. Matthies, A., Hickeson, M., Cuchiara, A., Abass, A, *Dual Time Point 18F-FDG PET for the Evaluation of Pulmonary Nodules.* J Nucl Med, 2002. 43(7): p. 871-875.

102. Demura, Y., Tsuchida, T., Ishizaki, T., Mizuno, S., Totani, Y., Ameshima, S., Miyamori, I., Sasaki, M., Yonekura, Y., *18F-FDG Accumulation with PET for Differentiation Between Benign and Malignant Lesions in the Thorax.* J Nucl Med, 2003. 44(4): p. 540-548.

103. Kumar, R., Loving, V.A., Chauhan, A., Zhuang, H., Mitchell, S., Alavi, A., *Potential of Dual-Time-Point Imaging to Improve Breast Cancer Diagnosis with 18F-FDG PET.* J Nucl Med, 2005. 46(11): p. 1819-1824.

104. Xiu, Y., Bhutani, C., Dhurairaj, T., Yu, J.Q., Dadparvar, S., Reddy, S., Kumar, R., Yang, H., Alavi, A., Zhuang, H., *Dual-Time Point FDG PET Imaging in the Evaluation of Pulmonary Nodules with Minimally Increased Metabolic Activity.* Clin Nucl Med, 2007. 32(2): p. 101-105.

105. Alkhawaldeh, K., Bural, G., Kumar, R., Alavi, A., *Impact of dual-time-point 18F-FDG PET imaging and partial volume correction in the assessment of solitary pulmonary nodules.* Eur J Nucl Med Mol Imaging, 2008. 35(2): p. 246-252.

106. Higashi, T., Saga, T., Nakamoto, Y., Ishimori, T., Mamede, M.H., Wada, M., Doi, R., Hosotani, R., Imamura, M., Konishi, J., *Relationship Between Retention Index in Dual-Phase 18F-FDG PET, and Hexokinase-II and Glucose Transporter-1 Expression in Pancreatic Cancer.* J Nucl Med, 2002. 43(2): p. 173-180.

107. Nishiyama, Y., Yamamoto, Y., Fukunaga, K., Kimura, N., Miki, A., Sasakawa, Y., Wakabayashi, H., Satoh, K., Ohkawa, M., *Dual-Time-Point 18F-FDG PET for the Evaluation of Gallbladder Carcinoma.* J Nucl Med, 2006. 47(4): p. 633-638.

108. Mavi, A., Urhan, M., Yu, J.Q., Zhuang, H., Houseni, M., Cermik, T.F., Thiruvenkatasamy, D., Czerniecki, B., Schnall, M., Alavi, A., *Dual Time Point 18F-FDG PET Imaging Detects Breast Cancer with High Sensitivity and Correlates Well with Histologic Subtypes.* J Nucl Med, 2006. 47(9): p. 1440-1446.

109. Kim, I.-J., Lee, J., Kim, S.-J., Kim, Y.-K., Jeong, Y., Jun, S., Nam, H., Kim, J., *Double-phase 18F-FDG PET–CT for determination of pulmonary tuberculoma activity.* Eur J Nucl Med Mol Imaging, 2008. 35(4): p. 808-814.

110. Nishiyama, Y., Yamamoto, Y., Kimura, N., Ishikawa, S., Sasakawa, Y., Ohkawa, M., *Dual-time-point FDG-PET for evaluation of lymph node metastasis in patients with non-small-cell lung cancer.* Ann Nucl Med, 2008. 22(4): p. 245-250.

111. Zytoon, A.A., Murakami, K., El-Kholy, M. R., El-Shorbagy, E., *Dual time point FDG-PET/CT imaging... Potential tool for diagnosis of breast cancer.* Clin Radiol, 2008. 63(11): p. 1213-1227.

112. Zytoon, A.A., Murakami, K., El-Kholy, M. R., El-Shorbagy, E., Ebied, O., *Breast cancer with low FDG uptake: Characterization by means of dual-time point FDG-PET/CT.* Eur J Radiol, 2009. 70(3): p. 530-538.

113. Yau, Y.-Y., Chan, W.-S., Tam, Y.-M., Vernon, P., Wong, S., Coel, M., Chu, S.K.-F., *Application of Intravenous Contrast in PET/CT: Does It Really Introduce Significant Attenuation Correction Error?* J Nucl Med, 2005. 46(2): p. 283-291.

114. Burgener, F.A., Hamlin, D.J., *Contrast enhancement of focal hepatic lesions in CT: effect of size and histology.* Am J Roentgenol, 1983. 140(2): p. 297-301.

115. Coleman, R.E., Delbeke, D., Guiberteau, M.J., Conti, P.S., Royal, H.D., Weinreb, J.C., Siegel, B.A., Federle, M.F., Townsend, D.W., Berland, L.L., *Concurrent PET/CT with an Integrated Imaging System: Intersociety Dialogue from the Joint Working Group of the American College of Radiology, the Society of Nuclear Medicine, and the Society of Computed Body Tomography and Magnetic Resonance.* J Nucl Med, 2005. 46(7): p. 1225-1239.

116. Carney, J., Beyer, T., Brasse, D., Yap, J.T., Townsend, D.W., *CT-based attenuation correction for PET/CT scanners in the presence of contrast agent.* IEEE Nuclear Science Symposium Conference Record, 2002. 3: p. 1443-1446.

117. Freedman, N.M.T., Moreno, R.M., Le Meunier, L., Bacharach, S.L., *Identification of Contrast Media in PET/CT Using Dual Energy CT.* IEEE Trans Nucl Sci, 2007. 54(3): p. 523-527.

118. Berthelsen, A.K., Holm, S., Loft, A., Klausen, T.L., Andersen, F., Højgaard, L., *PET/CT with intravenous contrast can be used for PET attenuation correction in cancer patients.* Eur J Nucl Med Mol Imaging, 2005. 32(10): p. 1167-1175.

119. An, Y.-S., Sheen, S.S., Oh, Y.J., Hwang, S.C., Yoon, J.-K., *Nonionic intravenous contrast agent does not cause clinically significant artifacts to 18F-FDG PET/CT in patients with lung cancer.* Ann Nucl Med, 2007. 21(10): p. 585-592.

120. Souvatzoglou, M., Ziegler, S.I., Martinez, M.J., Busch, R., Dzewas, G., Schwaiger, M., Bengel, F., *Standardised uptake values from PET/CT images: comparison with conventional attenuation-corrected PET.* Eur J Nucl Med Mol Imaging, 2007. 34(3): p. 405-412.

121. Mawlawi, O., Erasmus, J.J., Munden, R.F., Pan, T., Knight, A.E., Macapinlac, H.A., Podoloff, D.A., Chasen, M., *Quantifying the Effect of IV Contrast Media on Integrated PET/CT: Clinical Evaluation.* Am J Roentgenol, 2006. 186(2): p. 308-319.

122. Bunyaviroch, T., Turkington, T., Wong, T., Wilson, J., Colsher, J., Coleman, R., *Quantitative Effects of Contrast Enhanced CT Attenuation Correction on PET SUV Measurements.* Mol Imaging Biol, 2008. 10(2): p. 107-113.

123. Yen, R.-F., Chen, K.-C., Lee, J.-M., Chang, Y.-C., Wang, J., Cheng, M.-F., Wu, Y.-W., Lee, Y.-C., *18F-FDG PET for the lymph node staging of non-small cell lung cancer in a tuberculosis-endemic country: Is dual time point imaging worth the effort?* Eur J Nucl Med Mol Imaging, 2008. 35(7): p. 1305-1315.

124. Antoch, G., Kuehl, H., Kanja, J., Lauenstein, T.C., Schneemann, H., Hauth, E., Jentzen, W., Beyer, T., Goehde, S.C., Debatin, J.F., *Dual-Modality PET/CT Scanning with Negative Oral Contrast Agent to Avoid Artifacts: Introduction and Evaluation.* Radiology, 2004. 230(3): p. 879-885.

125. Burridge, N.A., Rowbottom, C.G., Burt, P.A., *Effect of contrast enhanced CT scans on heterogeneity corrected dose computations in the lung.* Journal of Applied Clinical Medical Physics, 2006. 7(4): p. 1-12.

126. Trebossen, R., Comtat, C., Brulon, V., Bailly, P., Meyer, M.-E., *Comparison of two commercial whole body PET systems based on LSO and BGO crystals respectively for brain imaging.* Med Phys, 2009. 36(4): p. 1399-1409.

127. Erdi, Y.E., Mawlawi, O., Larson, S.M., Imbriaco, M., Yeung, H., Finn, R., Humm, J.L., *Segmentation of lung lesion volume by adaptive positron emission tomography image thresholding.* Cancer, 1997. 80: p. 2505-2509.

128. Jacob, V., Astner, S.T., Bundschuh, R.A., Busch, R., Souvatzoglou, M., Wendl, C., Kneschaurek, P., Grosu, A.-L., *Evaluation of the SUV values calculation and 4D PET integration in the radiotherapy treatment planning system.* Radiotherapy and Oncology, 2011. 98(3): p. 323-329.

129. Berghmans, T., Dusart, M., Paesmans, M., Hossein-Foucher, C., Buvat, I., Castaigne, C., Scherpereel, A., Mascaux, C., Moreau, M., Roelandts, M., Alard, S., Meert, A.-P., Partz, E.F.Jr., Lafitte, J.-J., Sculier, J.-P., *Primary Tumor Standardized Uptake Value (SUVmax) Measured on Fluorodeoxyglucose Positron Emission Tomography (FDG-PET) is of Prognostic Value for Survival in Non-small Cell Lung Cancer (NSCLC): A Systematic Review and Meta-Analysis (MA) by the European Lung Cancer Working Party for the IASLC Lung Cancer Staging Project.* J Thorac Oncol, 2008. 3(1): p. 6-12.

130. Paquet, N., Adelin, A., Foidart, J., Hustinx, R., *Within-Patient Variability of ^{18}F-FDG: Standardized Uptake Values in Normal Tissues.* J Nucl Med, 2004. 45(5): p. 784-8.

131. Huang, Y.-E., Chen, C.-F., Huang, Y.-J., Konda, S.D., Appelbaum, D.E., Pu, Y., *Interobserver variability among measurements of the maximum and mean standardized uptake values on 18F-FDG PET/CT and measurements of tumor size on diagnostic CT in patients with pulmonary tumors.* Acta Radiologica, 2010. 51(7): p. 782-788.

132. Chen, C.-J., Lee, B.-F., Yao, W.-J., Cheng, L., Wu, P.-S., Chu, C.L., Chiu, N.-T., *Dual-Phase 18F-FDG PET in the Diagnosis of Pulmonary Nodules with an Initial Standard Uptake Value Less Than 2.5.* Am J Roentgenol, 2008. 191(2): p. 475-479.

133. Blodgett, T.M., Meltzer, C.C., Townsend, D.W., *PET/CT: Form and Function.* Radiology, 2007. 242(2): p. 360-385.

134. Obuchowski, N.A., *Receiver Operating Characteristic Curves and Their Use in Radiology.* Radiology, 2003. 229(1): p. 3-8.

135. Park, S.H., Goo, J.M., Jo, C.-H., *Receiver operating characteristic (ROC) curve: practical review for radiologists.* Korean J Radiol, 2004. 5(1): p. 11-18.

136. Son'kin, V.D., Kirdin, A.A., Andreev, R.S., Akimov, E.B., *Homeostatic Non-Shivering Thermogenesis in Humans Facts and Hypotheses.* Human Physiology, 2010. 36(5): p. 599-614.

137. Kim, J.K., Park, S.-Y., Ahn, H.J., Kim, C.S., Cho, K.-S., *Bladder Cancer: Analysis of Multi–Detector Row Helical CT Enhancement Pattern and Accuracy in Tumor Detection and Perivesical Staging.* Radiology, 2004. 231(3): p. 725-731.

138. Ichiya, Y., Kuwabara, Y., Sasaki, M., Yoshida, T., Akashi, Y., Murayama, S., Nakamura, K., Fukumura, T., Masuda, K., *FDG PET in infectious lesions: the detection and assessment of lesion activity.* Ann Nucl Med, 1996. 10(2): p. 185-191.

139. Tian, G., Xiao, Y., Chen, B., Xia, J., Guan, H., Deng, Q., *FDG PET/CT for therapeutic response monitoring in multi-site non-respiratory tuberculosis.* Acta Radiol, 2010. 51(9): p. 1002-1006.

140. Tian, G., Xiao, Y., Chen, B., Guan, H., Deng, Q.-Y., *Multi-site abdominal tuberculosis mimics malignancy on ^{18}F-FDG PET/CT: report of three cases.* World J Gastroenterol, 2010. 16(33): p. 4237-4242.

141. Schaefer, N.G., Hany, T.F., Taverna, C., Seifert, B., Stumpe, K.D.M., von Schulthess, G.K., Goerres, G.W., *Non-Hodgkin Lymphoma and Hodgkin Disease: Coregistered FDG PET and CT at Staging and Restaging-Do We Need Contrast-enhanced CT?* Radiology, 2004. 232(3): p. 823-829.

142. Rodriguez-Vigil, B., Gomez-Leon, N., Pinilla, I., Hernandez-Maraver, D., Coya, J., Martin-Curto, L., Madero, R., *PET/CT in Lymphoma: Prospective Study of Enhanced Full-Dose PET/CT Versus Unenhanced Low-Dose PET/CT.* J Nucl Med, 2006. 47(10): p. 1643-1648.

143. Strobel, K., Heinrich, S., Bhure, U., Soyka, J., Veit-Haibach, P., Pestalozzi, B., Clavien, P., Hany, T., *Contrast-Enhanced ^{18}F-FDG PET/CT: 1-Stop-Shop Imaging for Assessing the Resectability of Pancreatic Cancer.* J Nucl Med, 2008. 49(9): p. 1408-1413.

144. Mangili, G., Picchio, M., Sironi, S., Viganò, R., Rabaiotti, E., Bornaghi, D., Bettinardi, V., Crivellaro, C., Messa, C., Fazio, F., *Integrated PET/CT as a first-line re-staging modality in patients with suspected recurrence of ovarian cancer*. Eur J Nucl Med Mol Imaging, 2007. 34(5): p. 658-666.

145. Chung, H., Kang, W., Kim, J., Park, N.-H., Song, Y.-S., Chung, J.-K., Kang, S.-B., Lee, H.-P., *Role of [18F]FDG PET/CT in the assessment of suspected recurrent ovarian cancer: correlation with clinical or histological findings.* Eur J Nucl Med Mol Imaging, 2007. 34(4): p. 480-486.

146. Delbeke, D., Coleman, R.E., Guiberteau, M.J., Brown, M.L., Royal, H.D., Siegel, B.A., Townsend, D.W., Berland, L.L., Parker, J.A., Hubner, K., Stabin, M.G., Zubal, G., Kachelriess, M., Cronin, V., Holbrook, S., *Procedure Guideline for Tumor Imaging with 18F-FDG PET/CT 1.0*. J Nucl Med, 2006. 47(5): p. 885-895.

147. Goerres, G.W., Ziegler, S.I., Burger, C., Berthold, T., von Schulthess, G.K., Buck, A., *Artifacts at PET and PET/CT Caused by Metallic Hip Prosthetic Material.* Radiology, 2003. 226(2): p. 577-584.

148. Feng, Q., Yong, Y., Pan, T., Clark, J.W., Mawlawi, O., *Segmentation of contrast enhanced CT images for attenuation correction of PET/CT data*. IEEE Nuclear Science Symposium Conference Record, 2004. 5: p. 2686-2689.

149. Visvikis, D., Costa, D.C., Croasdale, I., Lonn, A.H.R., Bomanji, J., Gacinovic, S., Ell, P.J., *CT-based attenuation correction in the calculation of semi-quantitative indices of [18F]FDG uptake in PET.* Eur J Nucl Med Mol Imaging, 2003. 30(3): p. 344-353.

150. Nakamoto, Y., Osman, M., Cohade, C., Marshall, L.T., Links, J.M., Kohlmyer, S., Wahl, R.L., *PET/CT: Comparison of Quantitative Tracer Uptake Between Germanium and CT Transmission Attenuation-Corrected Images.* J Nucl Med, 2002. 43(9): p. 1137-1143.

151. Halls, S.B. *CT Scan Liver enhancement at different delay times*. 1999 [cited on 27th July 2009]; Available from: http://www.halls.md/ct/houns.htm.

152. Pallant, J., *SPSS survival manual: a step by step guide to data analysis using SPSS program*. 4th ed. 2010, Maidenhead: Open University Press.

153. Wang, Y., Chiu, E., Rosenberg, J., Gambhir, S., *Standardized Uptake Value Atlas: Characterization of Physiological 2-Deoxy-2-[18F]fluoro-d -glucose Uptake in Normal Tissues.* Mol Imaging Biol, 2007. 9(2): p. 83-90.

154. Nahmias, C., Wahl, L., *Reproducibility of Standardized Uptake Value Measurements Determined by ^{18}F-FDG PET in Malignant Tumors.* J Nucl Med, 2008. 49(11): p. 1804-1808.

155. Hairil Rashmizal, A.R., Geso, M., Noraini, A.R., Abdul Jalil, N., *The effect of integrating contrast enhanced CT in FDG PET/CT imaging of Extrapulmonary Tuberculosis patients: preliminary data.* ANZ Nuclear Medicine, 2010. 41(4): p. 19-23.

156. Brix, G., Beyer, T., *PET/CT: Dose-escalated image fusion?* Nuklearmedizin, 2005. 44: p. S51-S57.

157. Gelfand, M.J., Lemen, L.C., *PET/CT and SPECT/CT Dosimetry in Children: The Challenge to the Pediatric Imager.* Semin Nucl Med, 2007. 37(5): p. 391-398.

158. Huang, B., Law, M.W.-M., Khong, P.-L., *Whole-Body PET/CT Scanning: Estimation of Radiation Dose and Cancer Risk.* Radiology, 2009. 251(1): p. 166-174.

159. McCollough, C.H., Schueler, B.A., *Calculation of effective dose.* Med Phys, 2000. 27(5): p. 828-837.

160. Martin, C.J., *Effective dose: how should it be applied to medical exposures?* Br J Radiol, 2007. 80(956): p. 639-647.

161. Christner, J.A., Kofler, J.M., McCollough, C.H., *Estimating Effective Dose for CT Using Dose-Length Product Compared With Using Organ Doses: Consequences of Adopting International Commission on Radiological Protection Publication 103 or Dual-Energy Scanning.* Am J Roentgenol, 2010. 194(4): p. 881-889.

162. Stabin, M., *Internal Dosimetry*, in *Pediatric Nuclear Medicine/PET*, S.T. Treves, Editor. 2007, Springer: New York. p. 513-520.

163. International Commission on Radiological Protection, ICRP, *Recommendations of the International Commission on Radiological Protection. ICRP Publication 26.* Ann ICRP, 1977. 1(3).

164. International Commission on Radiological Protection, ICRP, *1990 recommendations of the International Commission on Radiological Protection. ICRP Publication 60.* Ann ICRP, 1991. 21(1-3).
165. International Commission on Radiological Protection, ICRP, *The 2007 recommendations of the International Commission on Radiological Protection. ICRP Publication 103.* Ann ICRP, 2007. 37(2-4).
166. International Commission on Radiological Protection, ICRP, *Radiation dose to patients from radiopharmaceuticals. ICRP Publication 53.* Ann ICRP, 1988. 18(1-4).
167. International Commission on Radiological Protection, ICRP, *Radiation Dose to Patients from Radiopharmaceuticals (Addendum to ICRP Publication 53). ICRP Publication 80.* Ann ICRP, 1998. 28(3).
168. International Commission on Radiological Protection, ICRP, *Radiation Dose to Patients from Radiopharmaceuticals - Addendum 3 to ICRP Publication 53. ICRP Publication 106.* Ann ICRP, 2008. 38(1-2).
169. Brix, G., Lechel, U., Glatting, G., Ziegler, S.I., Munzing, W., Muller, S.P., Beyer, T., *Radiation Exposure of Patients Undergoing Whole-Body Dual-Modality 18F-FDG PET/CT Examinations.* J Nucl Med, 2005. 46(4): p. 608-613.
170. Arora, B., Parikh, P.M., *PET-CT scan in pediatric oncology: Where, when, how and at what price?* Indian Journal of Cancer, 2010. 47(4): p. 355-359.
171. Imhof, H., Schibany, N., Ba-Ssalamah, A., Czerny, C., Hojreh, A., Kainberger, F., Krestan, C., Kudler, H., Nöbauer, I., Nowotny, R., *Spiral CT and radiation dose.* Eur J Radiol, 2003. 47(1): p. 29-37.
172. Shope, T.B., Gagne, R.M., Johnson, G.C., *A method for describing the doses delivered by transmission x-ray computed tomography.* Med Phys, 1981. 8(4): p. 488-495.
173. McNitt-Gray, M.F., *AAPM/RSNA Physics Tutorial for Residents: Topics in CT.* Radiographics, 2002. 22(6): p. 1541-1553.
174. Shrimpton, P.C., Jessen, K.A., Geleijns, J., Panzer, W., Tosi, G., *Reference Doses in Computed Tomography.* Radiat Prot Dosim, 1998. 80(1-3): p. 55-59.

175. Huda, W., Ogden, K.M., Khorasani, M.R., *Converting Dose-Length Product to Effective Dose at CT*[1]. Radiology, 2008. 248(3): p. 995-1003.

176. Son, H.-K., Lee, S. H., Nam, S., Kim, H.-J., *Radiation dose during CT scan with PET/CT clinical protocols*. IEEE Nuclear Science Symposium Conference Record, 2006. 5: p. 2210-2214

177. Huda, W., Sterzik, A., Tipnis, S., Schoepf, U.J., *Organ doses to adult patients for chest CT.* Med Phys, 2010. 37(2): p. 842-847.

178. International Commission on Radiological Protection, ICRP, *Managing Patient Dose in Multi-Detector Computed Tomography (MDCT). ICRP Publication 102.* Ann ICRP, 2007. 37(1).

179. Elojeimy, S., Tipnis, S., Huda, W., *Relationship between radiographic techniques (kilovolt and milliampere-second) and* $CTDI_{vol}$. Radiat Prot Dosim, 2010. 141(1): p. 43-49.

180. Jessen, K.A., Shrimpton, P.C., Geleijns, J., Panzer, W., Tosi, G., *Dosimetry for optimisation of patient protection in computed tomography.* Appl Radiat Isot, 1999. 50(1): p. 165-172.

181. International Commission on Radiological Protection, ICRP, *Managing patient dose in computed tomography. ICRP Publication 87.* Ann ICRP, 2000. 30(4).

182. Gosling, O., Loader, R., Venables, P., Rowles, N., Morgan-Hughes, G., Roobottom, C., *Cardiac CT: are we underestimating the dose? A radiation dose study utilizing the 2007 ICRP tissue weighting factors and a cardiac specific scan volume.* Clin Radiol, 2010. 65(12): p. 1013-1017.

183. Khamwan, K., Krisanachinda, A., Pasawang, P., *The determination of patient dose from* ^{18}*F-FDG PET/CT examination.* Radiat Prot Dosim, 2010. 141(1): p. 50-55.

184. Chawla, S.C., Boechat, M.I., McNitt-Gray, M., *Estimated cumulative radiation dose from PET/CT in children with malignancies: a 5-year retrospective review.* Pediatr Radiol, 2010. 40(5): p. 681-686.

185. Stabin, M.G., Sparks, R.B., Crowe, E., *OLINDA/EXM: The Second-Generation Personal Computer Software for Internal Dose Assessment in Nuclear Medicine.* J Nucl Med, 2005. 46(6): p. 1023-1027.

186. Butson, M.J., Cheung, T., Yu, P.K.N., *Measurement of energy dependence for XRCT radiochromic film.* Med Phys, 2006. 33(8): p. 2923-2925.
187. International Atomic Energy Agency, IAEA, *Radiation Protection in Newer Medical Imaging Techniques: PET/CT*, in *Safety Reports Series No. 58*. 2008, IAEA: Vienna.
188. Brady, S., Yoshizumi, T., Toncheva, G., Frush, D., *Implementation of radiochromic film dosimetry protocol for volumetric dose assessments to various organs during diagnostic CT procedures.* Med Phys, 2010. 37(9): p. 4782-4792.
189. Butson, M.J., Cheung, T., Yu, P.K.N., *Absorption spectra of irradiated XRCT radiochromic film.* Phys Med Biol, 2006. 51: p. 3099-3103.
190. Butson, M.J., Cheung, T., Yu, P.K.N., Alnawaf, H., *Dose response of irradiated XRCT radiochromic film.* Iranian Journal of Science & Technology, Trans. A, 2008. 32: p. 161-165.
191. National Council on Radiation Protection and Measurements, NCRP, *Limitations of Exposure to Ionising Radiation*, in *Report No. 116*. 1993: Bethesda, Maryland.
192. Niroomand-Rad, A., Blackwell, C.R., Coursey, B.M., Gall, K.P., Galvin, J.M., McLaughlin, W.L., Meigooni, A.S., Nath, R., Rodgers, J.E., Soares, C.G., *Radiochromic film dosimetry: Recommendations of AAPM Radiation Therapy Committee Task Group 55.* Med Phys, 1998. 25(11): p. 2093-2115.
193. Cheung, T., Butson, M.J., Yu, P.K.N., *Post-irradiation colouration of Gafchromic EBT radiochromic film.* Phys Med Biol, 2005. 50(20): p. N281-N285.
194. Rampado, O., Garelli, E., Ropolo, R., *Computed tomography dose measurements with radiochromic films and a flatbed scanner.* Med Phys, 2010. 37(1): p. 189-196.
195. Guo, P.Y., Adamovics, J., Oldham, M., *Characterization of a new radiochromic three-dimensional dosimeter.* Med Phys, 2006. 33(5): p. 1338-1345.
196. Adamovics, J., Maryanski, M.J., *Characterisation of PRESAGE: A new 3-D radiochromic solid polymer dosemeter for ionising radiation.* Radiat Prot Dosim, 2006. 120(1-4): p. 107-112.

197. Guo, P., Adamovics, J., Oldham, M., *A practical three-dimensional dosimetry system for radiation therapy.* Med Phys, 2006. 33(10): p. 3962-3972.

198. Fahey, F.H., *Dosimetry of Pediatric PET/CT.* J Nucl Med, 2009. 50(9): p. 1483-1491.

199. Alessio, A.M., Kinahan, P.E., Manchanda, V., Ghioni, V., Aldape, L., Parisi, M.T., *Weight-Based, Low-Dose Pediatric Whole-Body PET/CT Protocols.* J Nucl Med, 2009. 50(10): p. 1570-1578.

200. Treves, S.T., Davis, R.T., Fahey, F.H., *Administered Radiopharmaceutical Doses in Children: A Survey of 13 Pediatric Hospitals in North America.* J Nucl Med, 2008. 49(6): p. 1024-1027.

201. Gutierrez, D., Schmidt, S., Denys, A., Schnyder, P., Bochud, F.O., Verdun, F.R., *CT-automatic exposure control devices: What are their performances?* Nuclear Instruments and Methods in Physics Research Section A: Accelerators, Spectrometers, Detectors and Associated Equipment, 2007. 580(2): p. 990-995.

202. Graser, A., Wintersperger, B.J., Suess, C., Reiser, M.F., Becker, C.R., *Dose Reduction and Image Quality in MDCT Colonography Using Tube Current Modulation.* Am J Roentgenol, 2006. 187(3): p. 695-701.